Alma Mater Studiorum – Università di Bologna

DOTTORATO DI RICERCA IN

TECNOLOGIE DELL'INFORMAZIONE

Ciclo XXV

Settore concorsuale di afferenza: 09/E3 - ELETTRONICA

Settore scientifico-disciplinare: ING-INF/01 - ELETTRONICA

TITOLO TESI

HYBRID PORTABLE SYSTEMS

FOR BIO-NANOSENSORS

Presentata da: Michele Rossi

Coordinatore Dottorato   **Relatore**

Prof. Claudio Fiegna   **Prof. Marco Tartagni**

Esame finale anno 2013

II

Hybrid portable systems for bio-nanosensors

I

Abstract

The promising development in the routine nanofabrication and the increasing knowledge of the working principles of new classes of highly sensitive, label-free and possibly cost-effective bio-nanosensors for the detection of molecules in liquid environment, has rapidly increased the possibility to develop portable sensor devices that could have a great impact on many application fields, such as health-care, environment and food production, thanks to the intrinsic ability of these biosensors to detect, monitor and study events at the nanoscale.

Moreover, there is a growing demand for low-cost, compact readout structures able to perform accurate preliminary tests on biosensors and/or to perform routine tests with respect to experimental conditions avoiding skilled personnel and bulky laboratory instruments.

This thesis focuses on analysing, designing and testing novel implementation of bio-nanosensors in layered hybrid systems where microfluidic devices and microelectronic systems are fused in compact printed circuit board (PCB) technology. In particular the manuscript presents hybrid systems in two validating cases using nanopore and nanowire technology, demonstrating new features not covered by state of the art technologies and based on the use of two custom integrated circuits (ICs).

As far as the nanopores interface system is concerned, an automatic setup has been developed for the concurrent formation of bilayer lipid membranes combined with a custom parallel readout electronic system creating a complete portable platform for nanopores or ion channels studies.

On the other hand, referring to the nanowire readout hybrid interface, two systems enabling to perform parallel, real-time, complex impedance measurements based on lock-in technique, as well as impedance spectroscopy measurements have been developed. This feature enable to experimentally investigate the possibility to enrich informations on the bio-nanosensors concurrently acquiring impedance magnitude and phase thus investigating capacitive contributions of bioanalytical interactions on biosensor surface.

Contents

VI

Introduction

In the last decade, the convergence of nanotechnology with biology and medicine and the ability to fabricate structures using standard wafer-scale semiconductor processing techniques has shown an emerging and evolving interest in the development of new classes of rapid, sensitive and reliable biosensors devices, such as nanopores, nanowires and carbon nanotubes. These devices could have a great impact on many application fields related to our life: from health-care and environment, to food production and bio-warfare thanks to their properties of electrical, label-free and real-time readout. Moreover, the possibility of integration of this class of sensors with the readout structure makes them even more interesting. However, the integration of sensors with integrated electronics interfaces demands a quick although accurate knowledge of electrical parameters depending upon the specific structure and fabrication process and their related behaviours to target stimulus. For the above reasons, there is a demand for low cost, portable readout structures able to perform accurate preliminary tests on biosensors and/or to perform routine tests with respect to experimental conditions avoiding skilled personnel and bulky laboratory instruments.

In order to design specific systems, an accurate analysis of real-word experimental needs and the successive performances test is needed. This thesis focuses in analysing, designing and testing hybrid systems in which bio-nanosensors such as nanopores and nanowires are interfaced with advanced electronic circuits for signal acquisition. This leads to achieve very high sensitive and selective detection devices, using the great potentiality of microelectronics to develop miniaturized acquisition systems.

The objective of this thesis is to:

- Design novel implementation of nanosensors in layered hybrid systems where microfluidic devices and microelectronic systems are fused in compact printed circuit board (PCB) technology.
- Validate the above approaches in two cases using nanopore and nanowire technology, demonstrating new features not covered by state of the art technologies.

More specifically, after a brief introduction on biosensors and the benefits of the electronic readout, Chapter 1 reviews the two kinds of label-free bio-nanosensors considered and experimentally tested in this manuscript, the nanopores (in particular the biological ones) and the nanowires field effects devices.

As far as the nanopores are concerned, Chapter 2 presents an automatic setup for the concurrent formation of bilayer lipid membranes combined with a custom parallel readout electronic system creating a complete portable platform for nanopores or ion channels study. The automatic system, combined with the dedicated low cost and disposable microfluidics, represents an important step to meet experimental real-world needs related to this field of

research, since in many cases the unavoidable physical support for biological nanopores or ion channels studies, the bilayer lipid membrane, is created by means of manual approaches, which are strictly related to the ability of the specific operator, resulting in lack of reproducibility and time consuming experiments. The fine-tuned formation protocol achieved with the automation of the process and the possibility to concurrently readout the very low currents coming from these bio-nanosensors, enabled to easily demonstrate the capabilities of the system performing parallel real time ion channel recordings on multiple sites, without the use of highly expensive laboratories instrumentations and the need of highly skilled personnel.

Considering the nanowires biosensors, Chapter 3 presents a discrete component portable electronic readout board directly interfaced with the microfluidic system, able to host different nanowires-based sensor chips and controlled by a custom LabView based control interface also implementing the digital signal conditioning process. The system was designed to be as much versatile as possible, enabling to perform parallel, real-time, lock-in technique based complex impedance measurements, as well as impedance spectroscopy measurements and it was used to perform experiments on silicon nanowires.

Furthermore, this chapter presents experimental studies on the possibility to acquire characteristic information on the functionalization layer on nanowires sensors, which would be very important to qualitatively control the created functional layer, as well as on the possibility to achieve information about the specific electrolytic solution involved, such as concentration and pH, concurrently acquiring impedance magnitude and phase.

This could be performed by impedimetric analysis using the implemented AC lock-in detection at different frequencies, conversely to standard studies on nanowires, which normally involve conductance measurements. The lock-in technique, indeed, in addition to the well-known noise reduction property generally used, enable to measure the complex impedance and thus to obtain resistive and capacitive information on nanowires impedance.

Nanowires FET conductance variations are indeed based on a variation of the surface potential and thus either on variations of surface charges or of the total surface capacitance according to the well-known equation $V=Q/C$. In fact one could decouple these two contributions by measuring the resistance in DC and using impedimetric methods to measure the total surface capacitance, for instance to create miniaturized pHmeters able to concurrently read the ionic concentration (related to the surface capacitance) of the bulk solution and its pH (related to the surface charge).

Chapter 4 presents a simplified nanowires semi-empirical model, developed starting from the physical and geometrical characteristics of the silicon nanowires chips considered and easily implemented using electronic analog circuit simulation program, with the aim to catch the overall response of nanowires based sensors under an alternate current regime, with particular interest

on the different contributions given by the surface capacitive effects affecting the nanowires, as a function of the different operating frequency.

Finally, Chapter 5 presents a compact standalone hybrid system based on an Application Specific Integrated Circuit (ASIC) impedimetric interface (which integrates the lock-in detection architecture) developed by the research group and directly pluggable to the laptop (and power supplied by USB) for real time impedimetric studies on nanowires chips, which can be easily embedded in the platform thanks to the designed specific holder. The system is controlled by a custom software interface and an FPGA, which also executes the digital signal conditioning, and performs complex impedance measurements stimulating the nanowires with an AC current signal while reading the voltage signal response.

Thanks to these two systems it is possible to perform impedimetric measurements either using current sensing or voltage sensing methods and investigate how the measurement technique is differently affected by parasitic effects.

It must be pointed out that this work has been framed into a highly interdisciplinary teamwork, where the designed and tested hybrid platforms are the results of the combination of knowledge in bioengineering, silicon integrated technology, data processing and packaging design, unavoidable requisite to achieve the needed results.

Chapter 1   Electrochemical bio-nanosensors

1.1   Biosensor devices and benefits of electronic readout

A biosensor is an integrated device providing quantitative or semi-quantitative analytical information using a biological recognition system usually composed by two basic components connected in series: a chemical/molecular sensing element (receptor) and a physico-chemical transducer [1–3].

A typical biosensor signal chain front-end is shown in Figure 1.1
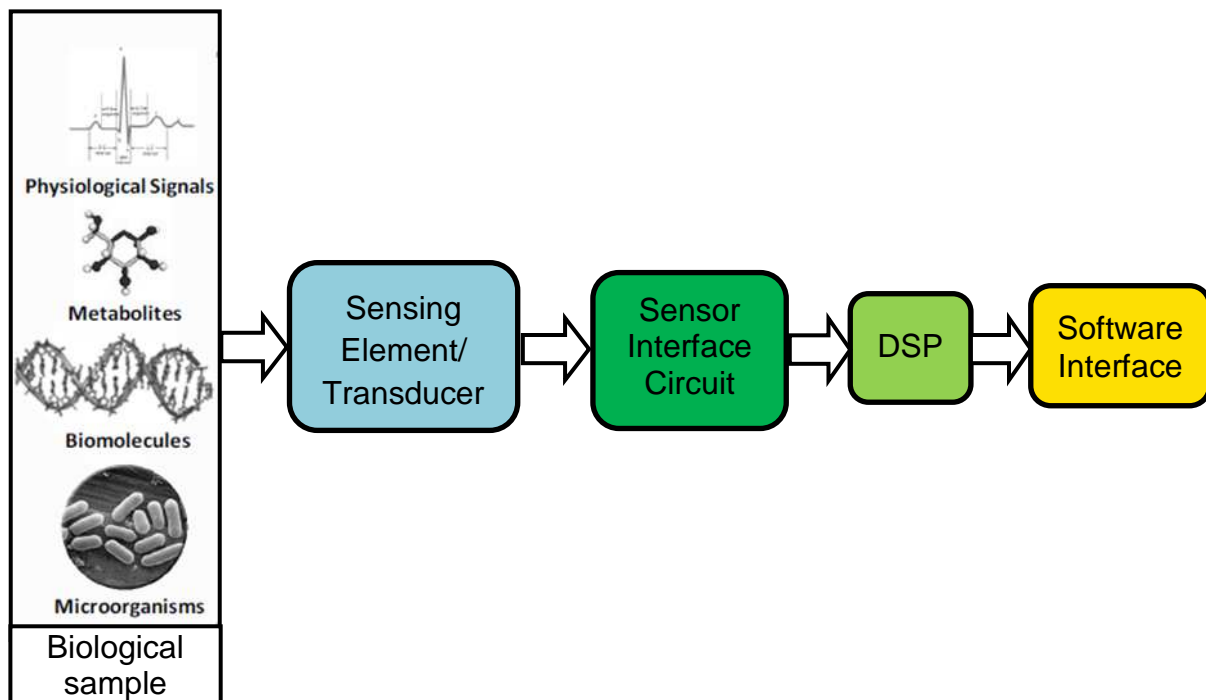
Figure 1.1 - Typical biosensor signal chain. The second block can be further divided in an analog frontend sensor circuit and an analog-to-digital conversion step. These, as well as the Digital Signal Processing (DSP), can be integrated thanks to the microelectronic approach.
It must be considered that in the hybrid systems presented in this manuscript the whole signal chain has been developed.

In general the transducer is a device that converts energy from one form to another. The most common output energy in the electrical, but any other form of energy, mechanical, electromagnetic, chemical, acoustic or thermal, can be the outputs signals. In this thesis, sensors based on optical readout (e.g. fluorescence or surface plasmon resonance), mechanical motion (e.g. quartz crystal microbalance or resonant cantilever), or the use of magnetic particles, etc. will not be considered, while the focus is on electrochemical transducers which extract information from biological systems transforming them into electrical signals.

Electrochemical transducers generally consist of electrodes where electrons are charge carriers and electrolyte where ions are charge carriers. This interaction alters the electrical characteristics of the electrode-electrolyte systems such as potential, current, impedance, and I–V curves [4].

A slightly different and very interesting class of transducers, usually called field-effect devices (ISFETs and their relatives EnFET,BioFET, etc), has attracted the researcher's attention in the last decade since they showed very promising performance. Such sensors rely on the field effect created by the interaction of external charges with carriers in a semiconductor structure, thus properly working at a low ionic strength, where counter-ion shielding is reduced [5], [6].

In general, there are some drawbacks of electroanalytic methods, such as the instability of the electrode-electrolyte interface, the high level of ionic background noise in the system, electrochemical interferers which can contribute to a not easily readable output signal.

On the other hand the key advantages of the electro analytical detection methods compared to other detection methods are straightforward and can be summarized in:

- the ability to monitor interactions in real-time,
- at low-cost,
- the possibility to miniaturize the transductor element and readout circuit,
- no requirement for molecular labels (label-free devices).

Besides these properties, combining the electrochemical transducer with the proper electronic readout allows creating real-time and label-free devices for inline production or rapid test diagnostic systems where the output of the sensor as to be as much immediate as possible. Moreover advantages of integrated electronics has started a revolution in this field allowing very complex electronic systems to be shrunk to millimetre square sizes enabling great improvements in terms of performances, reduction of parasitic effects and systems portability.

From a system point of view (see Figure 1.1), indeed integrated electronic circuits enable to merge the analog frontend sensor circuit and an analog-to-digital conversion (ADC) step, which usually follows the first readout stage, as well as the Digital Signal Processing (DSP) in a tiny microchip allowing to develop miniaturized acquisition systems. These can be easily controlled by specific software interfaces, which also usually display data to the final users.

The whole signal chain must be carefully considered and optimized in designing electrochemical biosensors. In particular, it must be pointed out that in the three hybrid systems presented in this manuscript the whole signal chain has been designed and custom made, as well as calibrated and tested.

1.2 **Bio-nanosensor**

Shrinking the dimensions of the transducer element to the nanometer dimensions, thanks to new and promising technologies and nanofabrication processes, enables to achieve highly sensitive devices able to detect and transduce information about nanoparticles, such as biomolecules or chemical compounds.

Besides the performances in terms of signal-to-noise ratio (SNR) due to increased signal variations vs. dimensions, the use of nanosensors gives advantages in terms of cost, and parallelization, since they require very low quantitative of reagents.

For these reasons electrochemical bio-nanosensors find applications in many fields, from medicine to biology and environment, where minimizing size and cost is essential, such as point-of-care diagnostics and bio-warfare agent detection. Here are listed, as example, some interesting applications:

- Biomarkers detection in diagnostic point-of-care applications.
- DNA-based analysis for genetic and epigenetic studies.
- Drug testing and discovering in pharmaceutical research.
- Detection of toxins and other agents in bio-warfare applications.
- Detection of pollutants nanoparticles in environmental monitoring.
- Water screening applications and oceans monitoring.

Although these tremendous possibilities, bio-nanosensor systems have not successfully made the transition to compact point-of-care devices yet, because their detection platforms still consist of fluidic systems and bulky detectors. Great efforts have been made recently by researchers to address these challenges of portable biosensor systems using semiconductor fabrication technologies and microfluidic chips (lab-on a-chip) to build high-performance systems [7].

An equally important, if often overlooked, factor is that research tools and instruments must be easy to use and cost-effective. The importance of these characteristics will grow as industry employment grows. Sometimes of the present commercial tools are unnecessarily complex, with too many unnecessarily functions [8].

Moreover, a sensitive instrument has limited value if it can't be connected to a device under test properly. In particular for bio-nanosensors, the electronic readout system must be

connected to the nanoscale device through a high quality signal path that allows rapid, low noise measurements.

Therefore, many practical aspects must be considered in the design of an electrochemical bio-nanosensor-based system and alliances between instrumentation designers and users of nanodevices are essential in constructing a complete measurement solution [8]. For these reasons the testing of these devices has to be considered an integrating part of the design of such systems in order to successfully address the experimental needs, as done in this thesis work.

Today, a multitude of instruments referred to as bio-nanosensors can be found in labs around the world and there is a growing number of bio-nanosensors being used as diagnostic tools in point-of-care testing. Also new commercial products based on bio-nanosensors are becoming available to the market, thanks to the rapid growing of new devices, such as these hand-held devices developed by QuantuMDX [9]. In many cases, however, these bio-nanosensors have to be confined to expert users of high-cost equipment in a lab environment and cannot be used e.g. by patients themselves or doctors in the field [10].

In this manuscript two kinds of bio-nanosensors are considered, the nanopores based and the field effects devices (FEDs) [11], in particular the nanowires. Both are label-free sensors but the working principle is very different: the formers are based on the creation of a hole in a septum or membrane that physically blocks the ion flux between two compartments filled with electrolytic solution and the readout is based on the real time monitoring of the current flowing through the pore either in response to a stimulus or as a result of the temporary clogging of the nanopore. The latters operate by field-effect modulation of carriers in a semiconductor by nearby charged target particles, thus the signal is given by the variation of the resistance of the device. To achieve the desired specificity, the surface of the device is functionalized by a layer of probe molecules usually antibody, nucleic acid sequence or biomimetic materials which are able to bind only the chosen target molecules. For this reason these nanosensors can be considered as a subgroup of affinity-based biosensors [2], [5]. Their inherent compatibility with advanced microfabrication technology makes them very attractive for the integration into the readout system [7] and, combined to microfluidic platforms, can lead to the creation of miniaturized analytical systems, like μTAS (micro total analysis system). This very tempting approach is however associated to many practical issues, such as the manufacturability of the transducer with the appropriate properties and, primarily, the lifetime when the aqueous biological solution is applied to the device, which make the whole system generally not reusable [12].
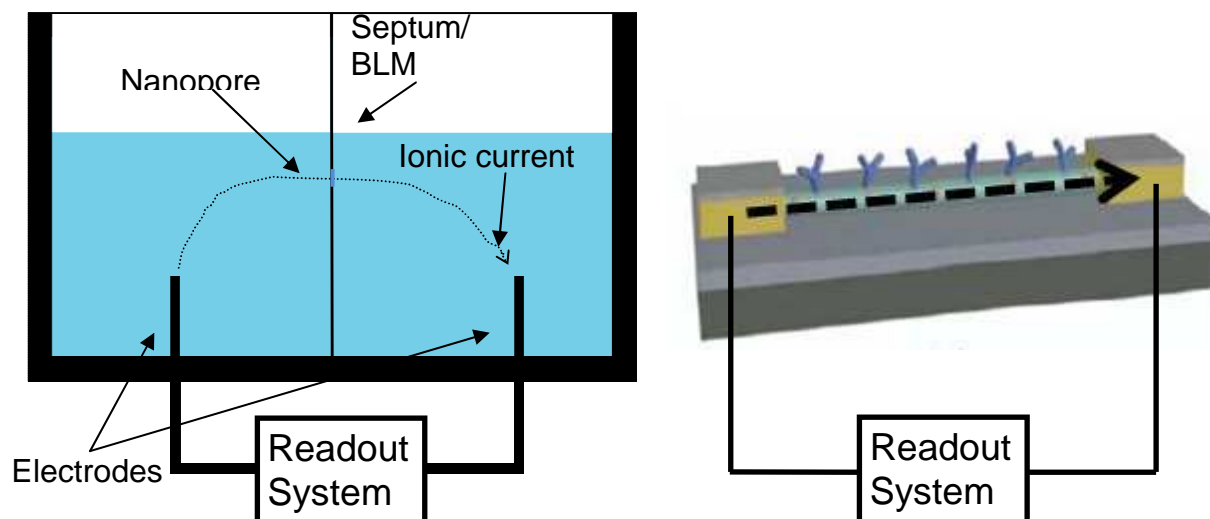
Figure 1.2 – Representation of the two different electrochemical bio-nanosensors considered and experimentally tested in this manuscript

1.3 Nanopores

A nanopore is a nanoscale aperture formed in an insulating membrane separating two chambers filled with conductive electrolyte. It can be a hole in a synthetic material like silicon or the graphene, or a pore-forming protein in a high electrical resistance bilayer lipid membrane (BLM).

The working principle of nanopores based sensors is analogous to that of the Coulter counter [13], [14], where charged molecules are driven through the pore under an applied electric potential, thereby modulating the ionic current through the nanopore. This current reveals useful information about the structure and dynamic motion of the molecule, as well as the concentration in solution. [15] For this reason membranes that contain nanopores are attracting a rapidly increasing interest from a broad community of scientists in nanotechnology, chemistry, physics, engineering, and the life sciences [16].

Even if the driving application for nanopores based sensor is undoubtedly the tempting opportunity to sequence a DNA in a rapid, label- and amplification-free fashion, combined to the possibility to scale the approach for high-throughput DNA analysis [15], [17], [18], the ability of these pores to act as a sensitive transducer that can detect nanoparticles, individual macromolecules, and even individual small molecules in solution is equally interesting [19–21].

From a readout system point of view, two parameters are of critical importance for pore-based sensing [16], [22], [23]:

- the acquisition bandwidth, that determines the temporal accuracy with which an instantaneous change in the current flowing through the pore is detected; the latter indeed is related, for instance, to the velocity of translocation of the target molecule through the pore.

- the current noise, that directly influences the sensitivity of a given pore; for instance in the specific detection of DNA bases or in the limit of detection of the dimensions of particles in solution.

1.3.1   Biological nanopores

Ion channels are biological protein nanopores formed by transmembrane proteins that regulate the ions exchange from intra and extra-cellular solution in a cell. Ion channels play an essential role in many biological processes and their malfunctions are involved in several diseases or severe pathologies. As a result, ion channels are targets of numerous pharmaceutical compounds [24] and therefore there is the need to understand their functioning the response to these artificial stimuli.

Moreover the capability of ion channels to respond to different chemical-physical stimuli has inspired the design of hybrid sensors where they are adopted as sensing units [25].

This can be achieved thanks to the possibility to artificially create the conditions present in natural cells environment by the formation of lipid bilayers on mechanical supports. Particular ion channels, or more specifically, some kinds of pore forming toxins [26], [27] can thus be embedded in biological membranes maintaining their natural behaviour and acting as sensor devices either responding to target stimuli (such as transmembrane voltage, pH variations and specific ligand binding) or acting as passive pore through which target molecules can pass.

Even if pioneering work on recording of single-ion channels started decades ago with electrophysiology experiments measuring the behaviour of single pores in cell membranes [28], in the 1990s, it was proposed that it might be possible to use natural nanopores to sense translocations of single-stranded DNA fragments through some particular protein nanopores [18]. Later on the same heptameric protein, the α-hemolysin, was used by Bayley's research group as single-molecule stochastic sensors, for identification and quantification of analytes, according to the conductance changes of the pore [19] and more recently as single-DNA base identification using an exonuclease enzyme coupled to it [17].

Integrating ion channels with electronic systems performing accurate ionic current readout it is possible to create molecular detection systems for specific targets in solution and for DNA sequencing [16], [20], [29–35].

One of the main issues of this approach is the unavoidable need to recreate the physiological condition and mechanical support to these kinds of bio-nanosensors; in particular one the most

challenging task is the creation of long term stable bilayer lipid membranes, eventually in a parallel and simultaneous fashion for the development of high throughput analysis [15], possibly in a rapid and cost-effective way [10], [36]. This is the main topic of the Chapter 2, in which an automatic setup for the concurrent formation of bilayer lipid membranes combined to the custom parallel readout electronic system is presented.

1.3.2 Solid state nanopores

Even if biological pores can be used fundamentally as transducers formed by biological matter and thus are intrinsically compatible with the target molecules of interest and have proven to be very useful for a wide range of interesting translocation experiments, they do exhibit a number of disadvantages. Some examples are the fixed size and physical properties given by nature and the limited stability [17].

Thanks to new and increasingly reliable nanofabrication processes a tempting alternative to biological nanopore is becoming the use of nanopores artificially formed in solid-state materials. This indeed presents many advantages over their biological counterpart such as very high stability, control of diameter and channel length, adjustable surface properties and higher potential for easy integration into devices, eventually in high-density arrays of nanopores [15]. On the other hand, they also exhibit higher noise level [23] and unwanted effects, such as the creation of nanobubbles [37] related to the strong dependence on the surface charges [38], [39]

The first report of DNA sensing using solid-state nanopores was published in 2001 by Golovchenko's group which was able to fabricate nanopores with well-defined sizes in thin silicon nitride membranes [40]. Then, the routinely creation of solid state nanopores and the demonstrated possibility investigate a wide range of phenomena involving DNA, RNA and protein have generated a dramatic increase in the number of applications [41]. More recently the growing studies on graphene and its fabrication make it to be considered the ultimate nanopore membrane, thanks to its thickness of only a single carbon atom [42–45]

Finally, a hybrid approach is presented in some literature examples in which solid state nanopores are used as mechanical support for bilayer lipid membranes creation, merging the advantages of the both structures [32], [35], [46]. In particular this enables to increase the stability of the lipid membranes, to reduce the sensor device capacitance (and thus the noise [16], [47]) and opens the possibility to use genetically engineered biological pores for the specific detection of biomolecules or for studies on DNA translocations [35].

1.4   Nanowires & Nanoribbons

Nanowires (NWs) are nanodevices characterized by two dimensions in the nanometer scale (i.e. the height and the width), while the other one (i.e.the length) could be in the range of tens to hundreds of micrometers. This high aspect ratio (length to width ratio of 1000 or more) makes the NWs to be considered as a one-dimensional (1-D) device. For instance, ultra-thin NWs, with diameters as small as 2-3 nm and of different materials [48], can be actually fabricated. In these devices quantum effects are very important, leading to many properties that are not seen in standard three-dimensional devices. For instance, the electrons become laterally quantum confined, thus they occupy discrete energy levels, leading to discrete values of the electrical conductance [49]. However, NWs with such reduced dimensions are difficult to physically realize and are not usually used as nanosensors due to practical mechanical issues [50], [51]. The term nanoribbons (NRs) is usually related to devices with bigger dimensions, in the order of some hundreds of nanometers to micrometers in height and width which are directly formed on a silicon substrate using standard microfabrication techniques [52–55].

In this section we will limit the analysis on nanowires and nanoribbons made of silicon. These kind of biosensors demonstrated high potential in sensing and promise highly sensitive real-time and label-free electrical detection of biomolecules, even in complex physiological media [54], [56–58].

Moreover in contrast to carbon nanotubes [59], [60], which are characterized by metallic or semiconducting properties and graphene [45], [61], which have no bandgap due to the fact that is composed of a single layer of carbon atom, silicon nanowires have the advantage of being only semiconducting and may be more easily integrated into CMOS industry fabrication and processing.

The fundamental principle for detection with semiconductor nanowires is their configuration as field-effect transistors (FETs), which use electrostatic interaction between charged molecules at the surface and the conductive channel, leading to a depletion or accumulation of carriers in the 'bulk' of the device when a species binds to the surface [62], [63] or properties of the electrolytic solution change. The chemical interactions between the FET and the molecules in the solution are therefore converted into electrical signals by device conductivity changes.

These devices are in principle MOSFETs where the gate metal of the MOSFET is replaced by an electrolyte solution and the gate oxide is in direct contact with the solution (which can be contacted by an electrode immersed into it). The main difference to the conventional MOSFET channel is due to the fact that the nanowire itself is a physically created conductive channel, connected by source and drain contacts. The substrate underneath the nanowire can be used as back gate, electrically isolated by an insulator.

A selective sensor can generally be achieved from silicon nanowire devices by linking recognition receptor groups to the surface of the nanowire. When the sensor device with surface receptors is exposed to a solution containing a macromolecule such as a protein, which has a net negative (or positive) charge in aqueous solution at a fixed pH, specific binding will lead to an increase (or decrease) in the surface negative charge and an increase (or decrease) in conductance for a p-type nanowire device [56], [64].

The first demonstration of the use of NW FET to sense analytes in solution occurred in 2001 with the sensing of pH concentration [62]; then, thanks to the one-dimensional morphology and nanometre-scale cross-section yielding an extremely high surface-to-volume ratio, nanowires demonstrated sufficient sensitivity to detect single particles, such as viruses [65], [66].

In the past years, the use of NWs has been widespread in many other applications, from sensing applications in biological systems to environments and gas sensors, as explained in recent reviews [56], [67–69], however there are still many challenges related both to the device aspects such as fabrication and the creation of stable and reliable contacts to sensitivity and selectivity issues relate to the particular probe receptors and the particular buffer solution [51].

The main limitation in the use of these nanosensors, indeed, is undoubtedly the need to perform measurements in a low salt concentrations buffer and the need to develop desalting methods in close contact with the transducer device [54], [58] since it was demonstrated that binding event must occur within electrical double layer (EDL), where counter-ion shielding is reduced, in order to maximize sensitivity [6], [55]. However it is difficult to realize immunosensors with immobilized antibodies that can lie within the EDL in physiological buffers.

Even if this strongly limited the possibility to have working products outside the research laboratories, new commercial products based on nanowires sensors are starting to come to the market of point-of care devices [9].

Moreover new readout methods where studied to overcome this practical issue [68], [70], [71] and, in particular, one of the focuses of this manuscript handles with this theme.

Many NWs characteristics depend upon the fabrication process, which can be classified as either bottom-up or top-down.

The former uses the vapour-liquid-solid (VLS) growing mechanism to realize in a cost-effective way and with a relatively easy control of the diameter, high crystallinity and with designated dopant density nanowires. This approach provides high-quality nanocomponents; however without a deliberate alignment for the randomly orientated SiNWs on the silicon substrate, the device fabrication would suffer from inefficient fabrication yields, which could also limit their development in the industrial applications. Therefore, the success of producing high-quality SiNW-FETs using this method calls for developing suitable techniques for accurate NWs alignment and electrical contact formation, in order to achieve mechanically and electrically robust contacts.

The latter, much more promising for commercial applications, starts from a silicon-on-insulator (SOI) wafer and uses micro- and nanofabrication techniques, such as photolithography and etching, to obtain the designed NW structure which results intrinsically embedded in the device structure and thus easily contacted in a mechanically robust manner. This technique also enables to better integrate the nanosensors with other electronics components and is less affected by contacts issues thanks to the generally bigger and fine-tuneable contacts area [66], [72]. Moreover this approach has the great advantage of having the possibility to precisely design a desired device-array pattern without problems of positioning Si-NWs.

Compared with the bottom-up method, the top-down approach itself is more complex because usually the process relies on high-resolution lithography instrumentations. Indeed, even if these technologies are currently the standard for semiconductor manufacturing, they are extremely expensive and accessible only to large-scale integrated circuit manufacturers.

Recently however it was demonstrated that the top-down approach enable to fabricate low-cost nanowires using simple and mature photolithography, thin film technology, and plasma etching, as the ones considered and tested in this manuscript [73].

Moreover one of the main challenges to the top-down method is that the physical limits of photolitography are beginning to be reached and minimum width of the produced Si-NWs is around 100 nm. To overcome this barrier, NWs of triangular cross-section can be fabricated to reach the transverse dimension of about 10nm [74]. A complete review of the two method is presented in [56]. In general it can be summed up that if ultra-high sensitivity is the main aim of the device, bottom-up approach can yield better results for applications tailored to laboratory research studies, however considering the desired main aim of achieving label free, low cost and portable devices, eventually for point of care applications and looking towards mass production the top-down approach is undoubtedly better.

As a further confirmation, in order to better meet the many practical aspects related to the possibility to achieve industrial mass production devices working in real word experimental conditions with less issues, a general trend is to moving through nanoribbons devices which anyway demonstrated a sufficient sensitivity and limit of detection for the sensing of biomolecules [52] or biomarkers [54], [58].
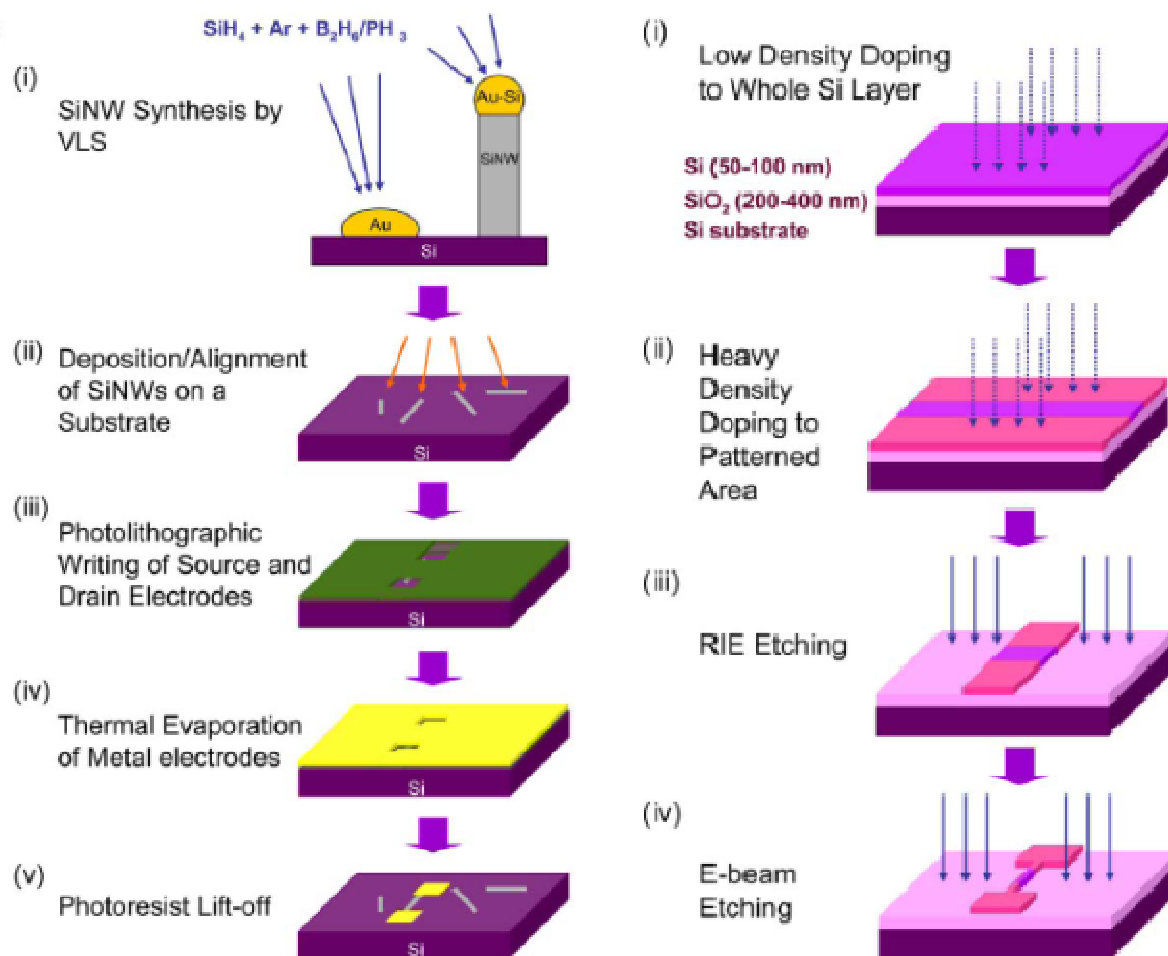
Figure 1.3 – Comparison between the typical bottom-up and top-down approaches for silicon nanowires fabrication [56].

Figure 1.4 shows the typical experimental setup used in experiments on nanowires sensors, where the sinusoidal or constant voltage stimulus is applied at the source contact and the resulting current is read by the transimpedance frontend at the drain contact, which is kept at virtual ground.

Contemporarily, the electrolyte potential solution and/or the back-gate potential in order to modulate the nanowire current [75–80].

Considering this readout setup, when using the sinusoidal input, this measurement approach results in a mixed acquisition method in which impedentiometry can be performed through the nanowires length, instead of through solid liquid interface as is done in typically impedance spectroscopy setup [11]. For this reason the thesis also focuses on the study of the possibility to use the AC stimulus in order to study the behaviour of the capacitive effects at the nanowires-electrolyte interface while measuring the sensors transconductance variations as usually done in field effect-based sensors. It must be noted that these investigations can be done exclusively

if the readout is performed in AC, while the standard FET DC analysis [6], [58], [66], [81] are not able to directly catch the capacitive effects that can occur at nanowires surface, these indeed are normally observed indirectly as the result of the transduction of the variations of FET surface potential.

Moreover it is well known that the 1/f noise main source in standard MOSFET devices is considered the conductivity fluctuations caused by charge traps at silicon/insulator interfaces. This phenomenon is highly dependent upon device fabrication process and it is even more critical considering nanowires devices, where the surface to volume ratio is usually very high [79], [82], [83].

For these two reasons the lock-in detection technique [47], [84], [85] has been implemented in the developed hybrid systems presented in Chapter 3 and Chapter 5.
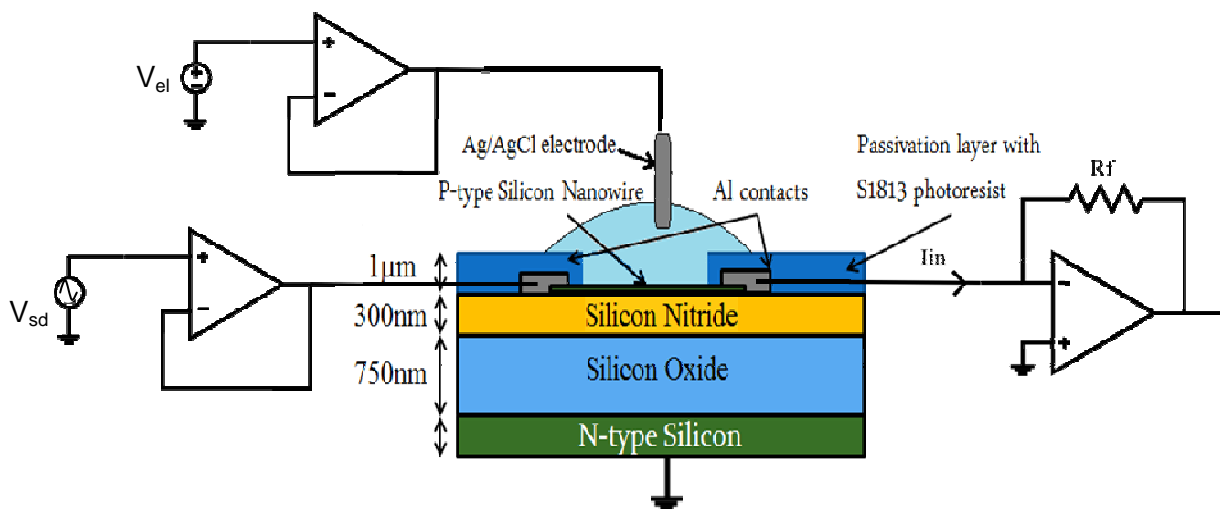
Figure 1.4 – Typical experimental setup used in experiments on nanowires sensors and implemented in the developed hybrid system presented in Chapter 3

Finally, Table 1.1 lists recent publications on nanowires sensors studies, highlighting the electrical readout method, the used readout system (where known) and, in case of AC detection, the used working frequency. As can be seen usually very low operating frequencies are used in order to reduce the 1/f noise.

Table 1.1: Key references of Si-NW devices highlighting measurement method and the readout system used.

Measurement Method/ Operating Frequency	Readout system	Reference
DC	Agilent 4156 parameter analyser/ Custom ASIC	[81]
DC	-	[6]
DC	Agilent Systems 4156B controlled by Lview	[66]
DC	Custom – 64 channels	[58]
DC / AC 79 Hz	Keithley 2636A / National Instruments PXI-8810 - PXI-4461	[86]
AC 79 Hz	-	[63], [64]
AC 30 Hz	Stanford Research Systems SR830	[74]
AC 30 Hz	Data acquisition board and LabView interface	[75]
AC 320 Hz	-	[77]
EIS 0.01 Hz-100 kHz	Gamry Instruments Reference 600	[87]

Chapter 2   A fully automatic parallel ion channel recording system

2.1   Introduction - A hybrid ion channel acquisition system

Typically electrophysiological system setups for ion channels investigations are based on two methods: the patch clamp technique [22], [88], in wich the cell membrane and the ion channels embedded in it are directly studied, and bilayer lipid membranes (BLMs), in which an artificial membrane is formed by means of various techniques reported in the literature on systems that mechanically support the bilayer, usually composed of a thin septum containing a small hole ranging from tens to hundreds of µm. This septum is usually created in a hydrophobic material foil such as Teflon or Delrin [89].

As shown in Figure 2.1, in both cases a membrane containing ion channels separates two compartments which simulate the intra and extracellular environment and the ions flowing across the membrane, under an electrochemical gradient, can be detected and converted into a tiny electrical current by means of electrodes (usually made of silver/silver chloride, Ag/AgCl) and measured using appropriate amperometric readouts.
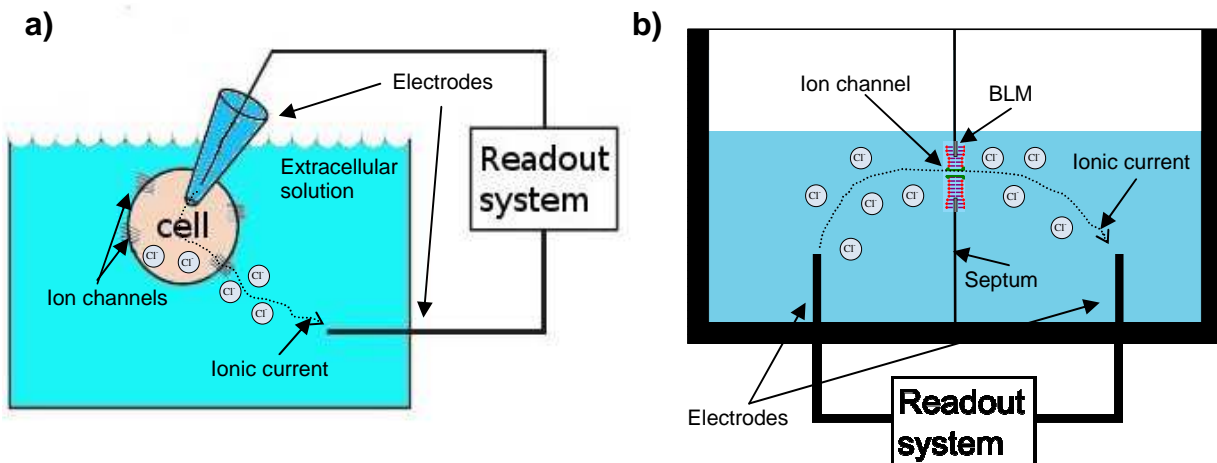
Figure 2.1 – Two typical electrophysiological setups: a) patch clamp technique, where the ionic current flows through ion channels embedded into the cell membrane; b) Bilayer lipid membrane technique, where a lipid membrane incorporating ion channels is artificially created over a thin septum, containing a microhole, that separates the two resevoirs which simulate the intra and extracellular compartments.

BLMs are widely used artificial biological substrates composed of phospholipid mixtures suspended into different organic solvents that self-assemble to form bilayers under specific

conditions and are used to host ion channel proteins since they well approximate the natural behaviour of cell membranes, with the advantage of a full control of the artificial physiological environment created, which contains exclusively the ion channels subject of studies under preset conditions and without spurious effect due to the cellular complex environment [89]. On the other hand, real cell physiological conditions cannot be achieved in such artificial systems.

Ion channels are involved into a large amount of processes of the cell life, regulating ion exchange between intra and extra cellular environment and they are involved into all the cellular life process [90]. Because of their key role in the physiologic process, ion channels behaviour can be altered or compromised from several diseases [91]. Morever novel biosensors able to detect low concentrations of target molecules [19] or even identify differences between different DNA bases [15], [17], [42], can be developed by integrating ion channels with electronic systems performing accurate ionic current readout.

For these reasons, simple and versatile systems that allow verifying and screening drugs interaction with ion channels are required to reduce time consuming in the drugs discovery and validation processes [24], as well as simply and quickly creating the physiological support for ion channel-based sensors.

Currently, it is possible to monitor ionic current flowing through ion channels embedded into bilayer lipid membranes (BLMs), cells or giant lipid vesicles, by characterizing the electrical transmembrane protein behaviour using laboratory techniques and low noise equipment for signal acquisition. State-of-the-art equipments offer high precision recording amplifiers that are able to sense single ion channels currents [22], [92]. These can be easily interfaced to laboratory-scale "craft" setups which require trained and sophisticated manual skills.

On the other hand, High Throughput Screening (HTS) systems require high data volumes implemented with automatic procedures and at the moment, they are available only for patch-clamp techniques with several drawbacks, such as the high overall running costs of advanced automated operations [24], [93].

A multichannel electrophysiology system for single ion channel recording, based on a modular system embedded into a hybrid architecture that is able to record single ion channels currents on an arbitrary number of spots was previously presented [94]. The system is composed of:

- an array of disposable microfluidic chambers [95] with embedded Silver/SilverChloride electrodes, for manual or automatic formation of BLMs to host single ion channel experiments, tightly interfaced with low noise electronics front-end;
- an array of low noise integrated microelectronic interfaces for signal amplification and analog to digital conversion [96];
- digital data elaboration performed by an embedded FPGA and link to PC by means of a USB interface;

- a graphical user interface (GUI) for data display and storage.

The flexibility of the proposed architecture allows different configurations, ranging from a limited number of data channels to be monitored, suitable for manual experiments, to thousands of data channels, coping with automatic HTS requirements [97].

As an example, Figure 2.2 shows a parallel readout hybrid electronic system [16] arrangement with 8 channels; the PCB acquisition board is composed of the top "wet" side and the bottom "electronic" side connected only by the electrode sockets. Moreover each disposable and independent Delrin block is directly interfaced with a dedicated low noise ADC converter [96] for ion channel recordings. This design allows assembling the single Delrin blocks on the acquisition board to realize arrays of any size depending on the final user's requirements.
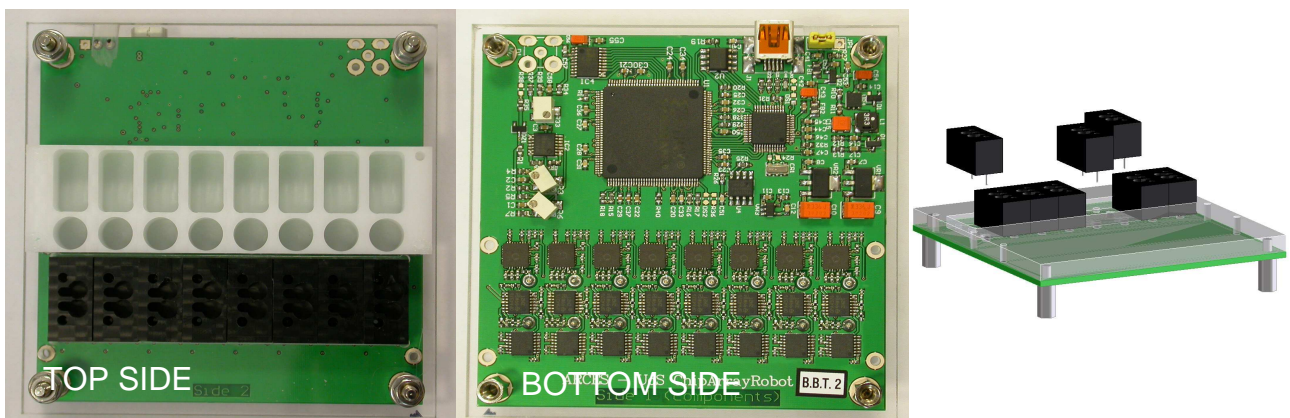
Figure 2.2: Top and bottom views of the 8 channels hybrid platform developed.
Black Delrin blocks are illustrated in section 2.3, while the white ones work as reservoirs for buffer and lipid solutions.
The Drawing on the right shows the disposable and flexible characteristics of the approach.

In any case, an open issue using the artificial BLMs method is given by the difficulty to obtain stable and long lasting membranes which are usually formed by means of standard techniques. Moreover the manual approach is strictly related to the ability of the specific operator resulting in lack of reproducibility and time consuming experiments.

For these reasons in this chapter a low cost, fully automated system able to mimic bulky and expensive liquid handling robot is presented. The complete and accurate description of the readout system interface was already reported by the colleague Thei [16], however the system presented here is an important step to meet experimental real-world needs related to this field of research and to obtain a complete, compact automatic hybrid system for ion channels investigations in artificial bilayer lipid membranes without the use of highly expensive laboratories instrumentations and the need of highly skilled personnel.

2.2   Montal Mueller method

As already mentioned, the most common and one of the first developed technique to create artificial bilayer is the painting method. It consists in manually applying a small quantity of lipid-solution dissolved in an organic, heavy and non-volatile solvent, such as decane and squalene using a borosilicate rod or a paintbrush over the septum aperture immersed in electrophysiological solution. A lipid monolayer is then constituted on each side of the septum, thanks to the amphiphilic properties of lipids. The lipid-solvent solution wets the hydrophobic walls of the aperture, resulting in a thinning of the solvent solution in the center of the aperture, until a completely fusion of the two monolayers into a single bilayer. A small quantity of solvent remains at the aperture perimeter (the annulus), increasing the BLM stability and acting as connection between the hydrophobic septum and the nanometric thickness of the BLM [89]. On the other hand, these pockets of solvent can interact with the physiological ion channel function. To overcome these limitations, several other techniques were developed following different approaches: some are based on droplets of water inside lipid solution [34]; others use the solvent evaporation and resulting thinning of the bilayer [98], or are based on the liquid infusion through a microfluidic chip which spreads lipids over small Teflon apertures [99]. All these techniques aim to obtain a high yield and the possibility to be automated; however other issues such as the stability of electrochemical connection and the related electrodes positioning, the working temperature, the differential pressure between the two chambers and the transmembrane potential applied have to be considered in order to obtain a really operative and compact experimental setup. Moreover, despite the tremendous potentials of BLM techniques, one of the main drawbacks of these approaches is the difficulty in integrating biological systems into large-scale arrays [15].

In this studies the Montal-Mueller approach was selected by our group, since it presents some characteristics procedures that can be automated [100]. As illustrated in Figure 2.3, the Montal-Mueller technique consists of the formation of two lipid monolayers at the lipid-aqueous interface of two separated chambers by applying a lipid solution in a volatile solvent, such as hexane or chloroform eliminating the use of a heavy, non-volatile solvent. The microhole on the thin septum is kept out from the aqueous surface during the monolayer formation and, after waiting for solvent evaporation time, the microhole is lowered (or the buffer level raised) and the two monolayers formed into the chambers aqueous surfaces are folded against each other, forming a bilayer across the aperture [100].
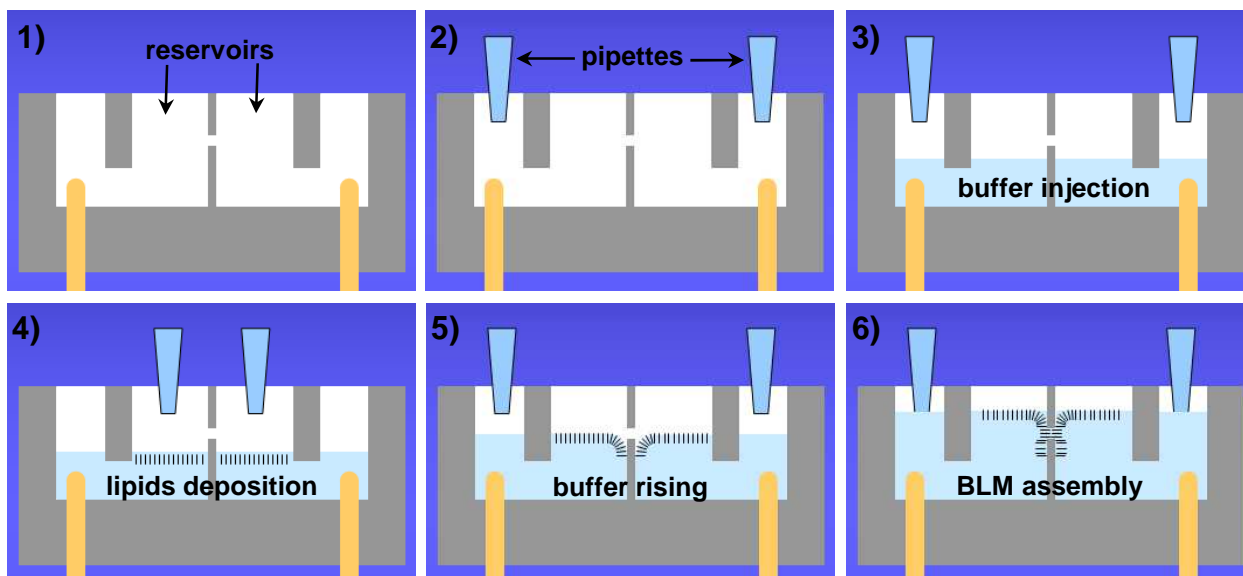
Figure 2.3 - Montal Muller technique for BLM formation on a small hole on a Teflon or Delrin septum that separate two chambers. 1) device empty; 2) pipette positioning on the inlet channels; 3) injection of buffer solution; 4) deposition of lipids for monolayer assembly on the two solution surfaces; 5) rising solution level to 6) the final bilayer assembly.

In order to real-time monitor membrane formation, a voltage triangular wave is usually applied across the membrane and the resulting current signal is visualized and recorded by the readout electronic system[94] and software interface.

Indeed, if the lipid bilayer is not formed, the microhole, filled by a conductive buffer solution acts as an electrical resistor and the current wave has the same triangular shape as the voltage stimulus. On the contrary, when a BLM is formed, it acts as a capacitor and the current is given by the derivative of voltage stimulus resulting in a square current waveform proportional to the membrane capacitance, as illustrated in Figure 2.4. This method allows to known the dimensions of the bilayer, since different BLM have different square wave amplitudes. Typically the equivalent membrane capacitance is in the order of 100-200 pF; however this value is highly dependent both on the dimensions of the microhole in the septum of the supporting device and on the composition of the lipid solution used to create the BLM [89]. In any case, the membrane capacitance is much higher than the septum capacitance (in the ten pF range), which can be usually neglected.
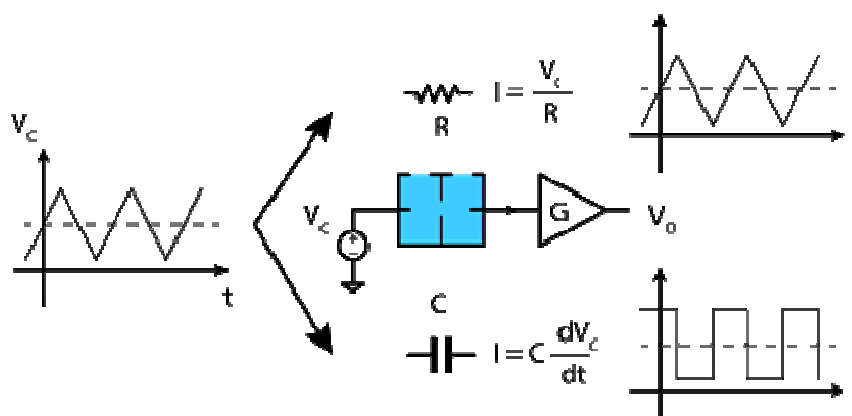
*Figure 2.4 - Equivalent electrical circuit of the septum. If BLM is not present,
the microhole can be represented by a resistor. In the presence of a bilayer
lipid membrane it can be modeled by a capacitor.*

2.3 Independent and disposable BLM support blocks

Few examples of parallel ion channels, embedded in BLMs, recording platform are present in literature [33], [34], [46], [101]. All of them have some common problems given by the fact that the above approaches are based on monolithic microfluidic structures, this cause that the yield of the array is linked to that of single microfluidic device and the fact that the whole systems, frequently relying on microfluidic routing channels, do not scale efficiently with respect to the dimension of the array. In this paragraph is presented the versatile and low-cost BLM support structure designed and realized using a micromilling process fabrication of polyoxymethilene homopolymer (Delrin™) substrates. The devices are suitable to support bilayer lipid membranes for ion channel investigations and are designed to be easily interfaces to the fully automated system approach described in the next section.

The section view of a single disposable monolithic block is shown in Figure 2.5 (left). The dimensions of the block are 9 mm x 18 mm x 10 mm (WxLxH), designed to meet the 96 well microplate standard ANSI/SLAS 2004 [102] allowing a limit-free scalable interface with multi-pipette or liquid handling robot in both planar directions. The device is composed of two "operating chambers" (6 mm depth) separated by a thin (50 μm) septum containing a microhole (at 4 mm from the bottom) and two "inlet/outlet chambers" (at 9 mm of distance each other) for the infusion/withdrawal of buffer. The total volume of the chambers is 120 μl.

The fabrication process is based on four steps and is accomplished by means of a computer numerical control (CNC) milling machine (Figure 2.5 right):

1. A Delrin™ block is initially milled on top and bottom surfaces for engraving the inlet/outlet and operating chambers on the top side and the electrode slots on the bottom one (Figure 2.5a);

2. Then, the small side face is drilled using a drill bit of 2mm (Figure 2.5b), in order to realize the interconnecting fluidic channels and the access hole for the creation of the microhole.

3. The latter is then drilled using a 200 µm diameter drill bit (Figure 2.5c).

4. The fabrication process ends by sealing the constructions holes with Delrin cylinders, previously opportunely fabricated by micromilling (Figure 2.5d).

Finally, two Ag/AgCl electrodes are stuck into the bottom slots as illustrated; the electrodes are fabricated by soldering a 0.5 mm diameter Ag wire into a female socket connector and by immersing the Ag wire into a fused AgCl solution (Sigma-Aldrich) to create a uniform coating.
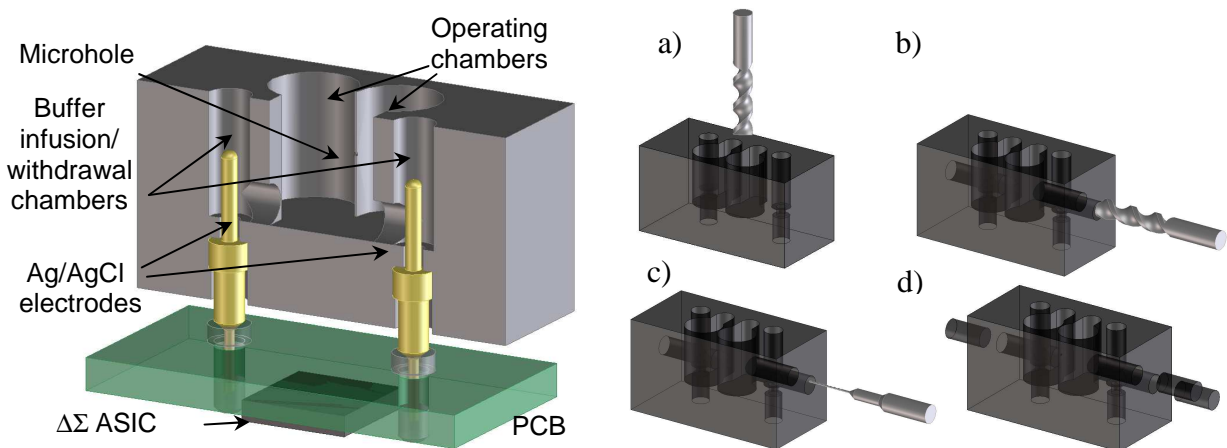
Figure 2.5 - Section view of the Delrin block assembled on the PCB (left) and the four fabrication process steps (right)

The main advantages of the proposed approach over the state-of-the-art systems can be summarized in the fact that:

- the overall structure is selectively disposable at single spot level and faulty elements can be easily revealed and removed;
- different array arrangements of the devices can be interfaced to any generic micropipetting machine and is fully scalable to any array size;
- each spot is directly interfaced with a dedicated electronic ASIC for a truly parallel readout signal acquisition.

2.4 Automatic liquid handling system structure and calibration

The presented automatic liquid handling system (Figure 2.6) is mainly composed of three parts:

1. 3-axis micromanipulator for pipette automatic movements in the 3D space (Sutter Instrument MP-285);
2. Single-axis micromanipulator for multipipette flux control (Newport NSA12);
3. Channel Pipette (20-200 µL) (Anachem Ltd 8);

The whole system is easily controlled by a user-friendly, custom interface developed in LabVIEW and described in the next section.

Thanks to the MP-285 micromanipulator, the multipipette used to handle liquids and to create BLMs can operate in a range of movement of 25 mm in the three directions of the space, enough to span over the whole readout system developed by the research group [94].

The micromanipulator has two submicron movement resolutions of 0.2 mm (coarse range) and of 40 nm (fine range) selectable by means of the control software interface.

Newport NSA12 provides a motorized, linear plunger, whose position can be controlled with sub-micron (0.1 µm - µSTEP) resolution, called over 11 mm of travel, with a minimum incremental motion of 0.3 µm (3 µSTEPs). Each µSTEP is 1/64 of the full-step (FS) of 6.4 µm.

The NSA is mounted in a fixed aluminum bracket (screwed in the MP-285 vertical plate) that provides both a rigid coupling between NSA12 plunger and the pipette one along the vertical axis and the rigid coupling between the MP-285 and the multipipette.
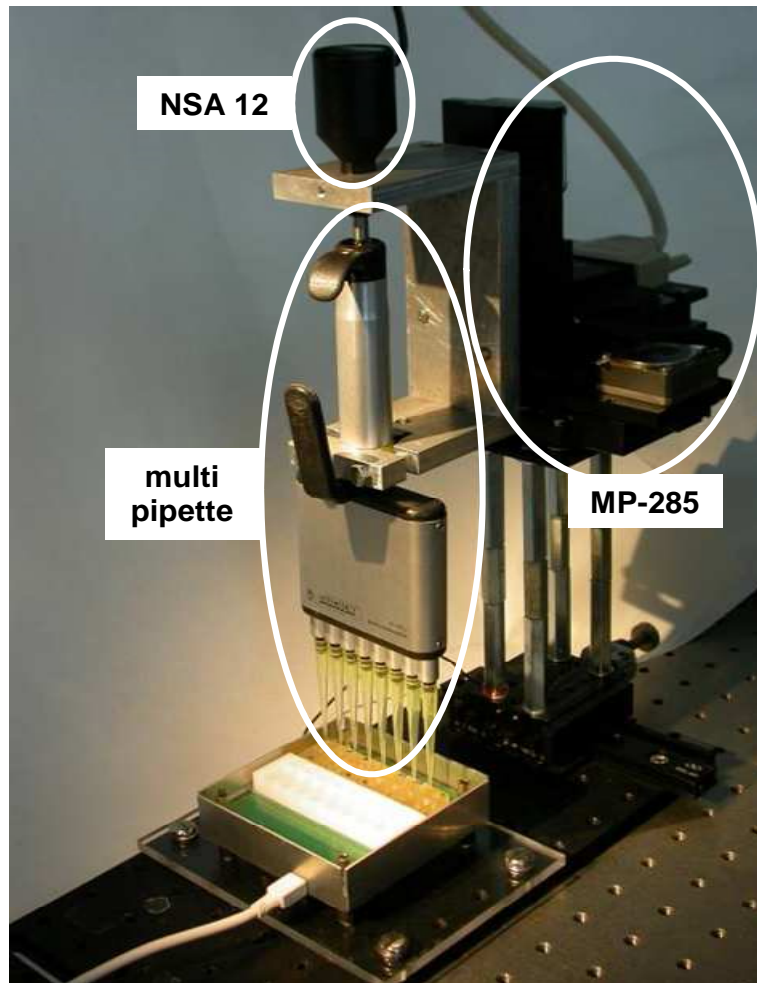
*Figure 2.6 - Details of the the compact automatic liquid handling
system composed of the two micromanipulators and the 8 tips
multipipette.*

In order to get the maximum pipette volume range, the NSA12 plunger is fully retracted when
the pipette plunger is fully extended and vice-versa. The mechanical interface is compatible with
any kind of pipettes.

The calibration procedure is performed measuring a quantity of water using a precision scale
(±0.1 mg resolution) on the basis of the following experimental relationships, which are
dependent on the particular pipette tips used:

$$8100\,\mu STEPS = 100\,\mu L \Rightarrow 810\,\frac{\mu STEPS}{\mu L} = 12.66\,\frac{FS}{\mu L} \tag{2.1}$$

$$1\frac{mm}{s} = 156.25\,\frac{FS}{s} \Rightarrow \left.156.25\frac{FS}{s}\middle/12.66\frac{FS}{\mu L}\right. = 12.34\frac{\mu L}{s} \tag{2.2}$$

Using the above experimental relationships and manufacturer's specifications, the volume can be related to the linear movement of the NSA12 plunger as in equation (2.1) and its velocity to the infusion/withdrawal flow rate as in equation (2.2). The implementation of these relationships in the LabVIEW control interface allowed having a final accuracy of ±1µL. This allows an extreme repeatability of experimental conditions in contrast to standard hand-made procedures.

Both the micromanipulators are connected to a PC using RS-232 interface and are simultaneously controlled by the LabVIEW control interface obtaining a extremely modular and versatile system for different applications.

2.5   LabVIEW Control Interface

The described system has been designed with the particular aim to create a compact automatic liquid handling robot for BLM formation able to be interfaced with a BLM array platform [95]. The system is controlled by a user-friendly LabVIEW control panel interface (see Figure 2.7), which has been designed following a modular and reusable approach starting from elementary operations, implemented in different subroutines and associated with single independent controls.
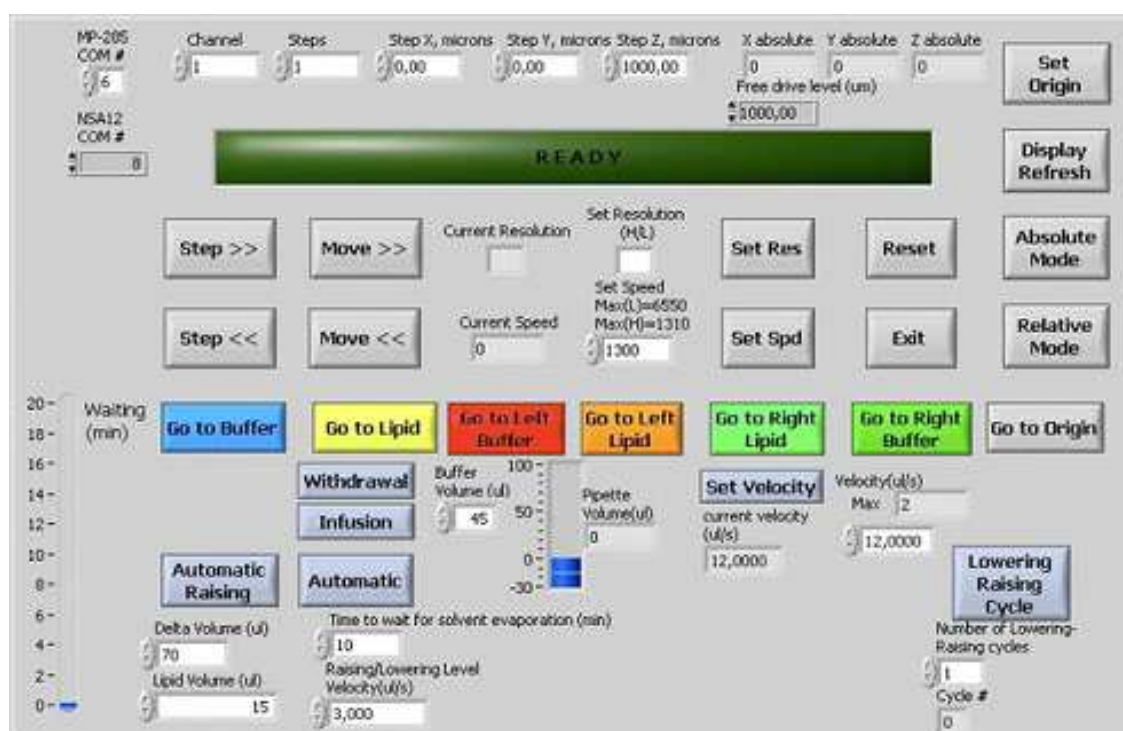
Figure 2.7 - LabVIEW Control Panel interface for automatic liquid handling

The operations are referred to the reference system fixed to the array platform [95].

Several elementary operations are implemented and available to the user, more specifically:

- move the multipipette to buffer reservoir;
- move the multipipette to lipid reservoir;
- shift left/right the multipipette on the bottom of left/right chamber;
- move the multipipette on the bottom of left/right chamber at the air-buffer interface level where lipids are deposited;
- return to origin: move the multipipette to the reference system origin;
- withdraw a fixed amount of buffer selected by the user (µL);
- inject a fixed amount of buffer selected by the user (µL).

Furthermore, several important parameters for BLM formation can be set, in order to test different BLM protocols, in particular:

- volume of buffer/lipids injected/withdrawal (µL);
- infusion/withdrawal flow rate (µL/s);
- number of lowering/raising buffer level cycles in both chambers;
- waiting time for lipid solvent evaporation (minutes).

Finally, stacking and synchronizing the different elementary operations, two automatic BLM formation protocols (both using the Montal-Müller method) have been implemented as described in the next section, in order to standardize the formation protocol and to achieve an high reproducibility of the BLMs.

2.6   Standardization of the protocols for parallel BLM formation

In order to demonstrate the versatility of the approach and to study the best experimental procedure in terms of yield and BLMs mechanical stability, aiming at obtaining a standardized BLM formation protocol, two protocols for automatic BLM formation have been implemented. Both are based on the Montal-Mueller technique [100], however, slightly different procedures are implemented.

They were called "Automatic Raising" and "Automatic" and are described below.

1. <u>Automatic raising:</u> The system withdraws a quantity of buffer from the reservoir and then fills the two chambers beneath the microhole (buffer volume ≤ 70µl). Then, a selected quantity of lipids is injected in the two chambers and, after a selectable waiting time for solvent evaporation, the buffer level in the two chambers is raised by a fixed quantity at a fixed velocity. At the end the pipette is moved to the reference system origin.

2. <u>Automatic</u> (the sequence is illustrated in Figure 2.8): The system withdraws a quantity of buffer (1) from the reservoirs and fills the two chambers above the microhole (2) (3) in order to allow using the offset correction (4) functionality implemented in the readout interface [103]. Then a selected quantity (5) of lipid is infused (6) (7) in both the chambers. After a selectable delay time for solvent evaporation, the buffer level in the two chambers is lowered and immediately raised (8) (9) by a selected quantity of buffer.

Moreover, in order to better spread the lipid over the microhole, the "lowering/raising cycle" functionality has also been implemented. This procedure automatically moves alternatively the pipette to both the chambers, withdraws and then injects a selected quantity of buffer in the two chambers using a fixed pipette flow rate (selected in "raising/lowering level velocity" option). The user can set several automatic cycles, for a proper lipid spreading, as well.
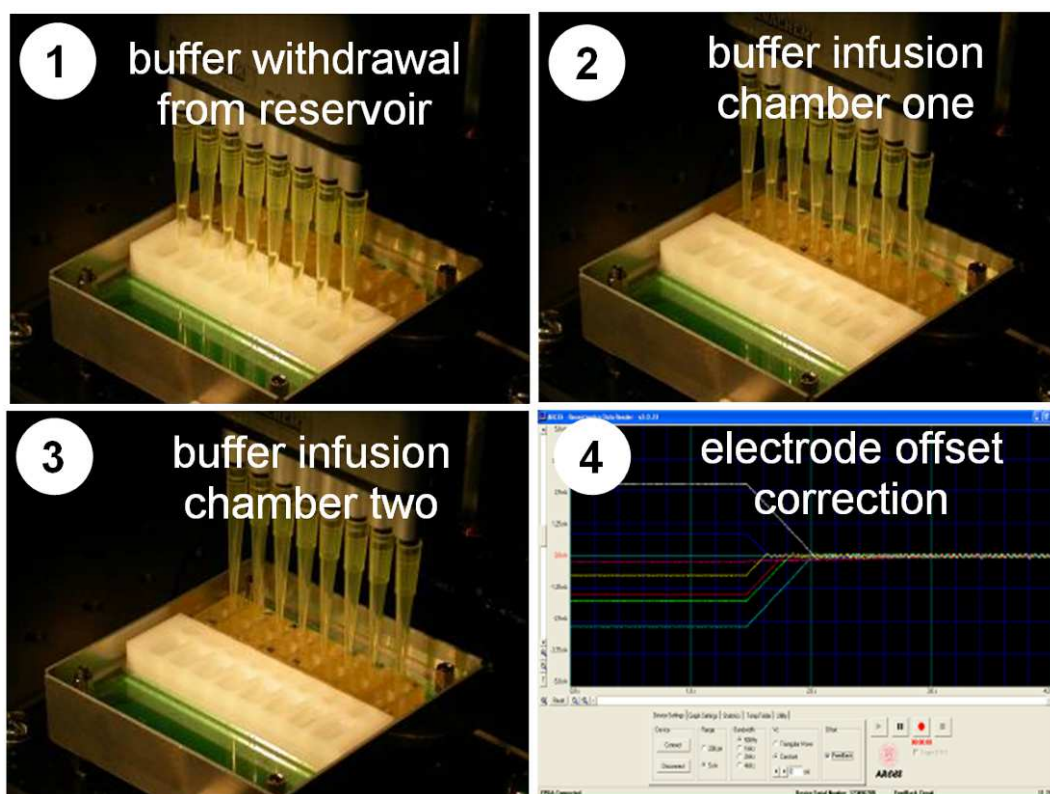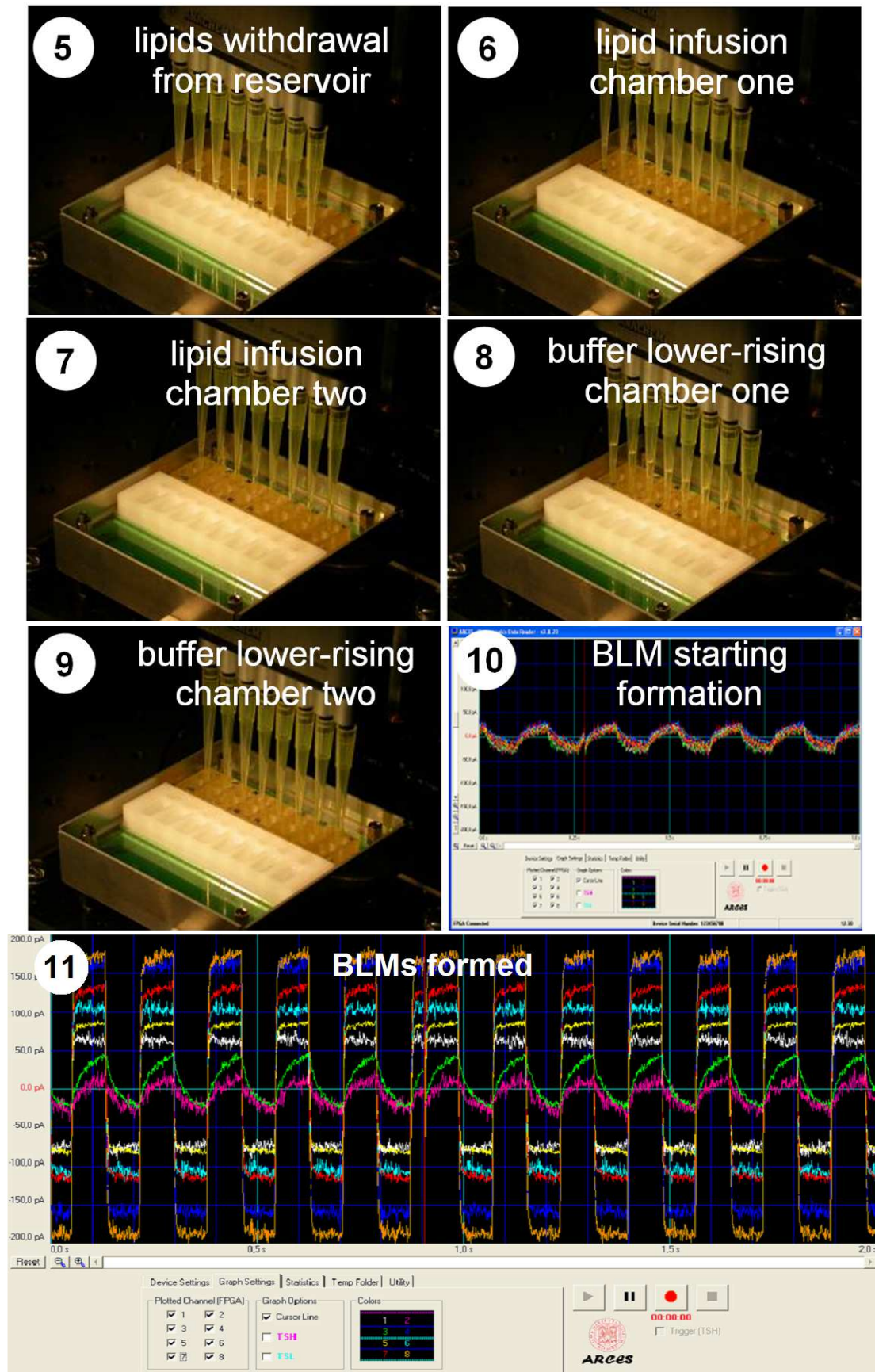
Figure 2.8 – Steps involved in the "Automatic" BLM formation procedure.

Steps4, 10 and 11 are screenshots taken from the GUI interface.

The six square-wave signals (orange, blue, red, cyan, yellow and white) in Figure 2.8 (step 11) demonstrate the concurrent formation of six independent BLMs of different dimensions on different BLM support blocks. Conversely, the magenta signal is related to and early stage of the membrane formation where a lipid agglomerate is present and behaves as a very small capacitance between the two chambers; whilst the green signal is result of a leaking membrane during formation, causing a response current wave in between the triangular and square wave shapes.

The result showed in Figure 2.8 (step 11) is achieved after several tests on the automatic BLM formation protocol, changing the main parameters affecting the BLM formation and stability, such as the lipid solution concentration, lipid solution solvent (hexane, heptane, octane, nonane were tested), lipid solution quantity injected in the chambers, infusion/withdrawal flow rate and waiting time for lipid solvent evaporation. In particular a trade-off between solvent volatility, BLM formation yield and solvent handling issues using standard pipette tips was found in the use of octane as lipid solution solvent.

The final protocol used for bilayer formation is constituted by:

- an initial pre-treatment of both sides of the microhole with a droplet (about 5 μl) of lipid solution composed of 1,2-diphytanoyl-sn-glycero-3-phosphocholine (DPhPC, Avanti Polar Lipids) in octane at a concentration of 1 mg/ml.

- Both chambers are then filled with 90 μl of buffer solution, composed of 1M KCl, 10mM HEPES, and 1mM ethylenediaminetetraacetic acid (EDTA) (Sigma–Aldrich) in ultrapure water, at pH 7

- The electrodes offsets in the different devices are automatically and simultaneously corrected.

- 10 μl of lipid solution are added to the chambers and two lowering/raising cycles are immediately performed using a raising flow rate of 13 μl/s corresponding to a buffer level raising velocity of about 1 mm/s.

- Waiting for spontaneous membrane arrangement and a complete formation within few minutes.

Bilayers lipid membranes in the range of 120-180pF and stable for 3-5 hours were achieved, with a yield of automatic BLM formation higher than 50%. This value is however strictly dependent on the quality of the Delrin support block used and, in particular, on the quality of the microhole and the thickness of the septum. Procedures to better control both these parameters have to be studied and improved in order to increase the BLM formation yield and make the automatic procedure yield independent of the particular BLM supporting device, however the modularity of the approach make the system fully operational by easily removing the unformed membranes spot, as described in section 2.3.

Finally, *Figure* 2.9 shows the overall system highlighting the three fundamental parts by which it is composed.
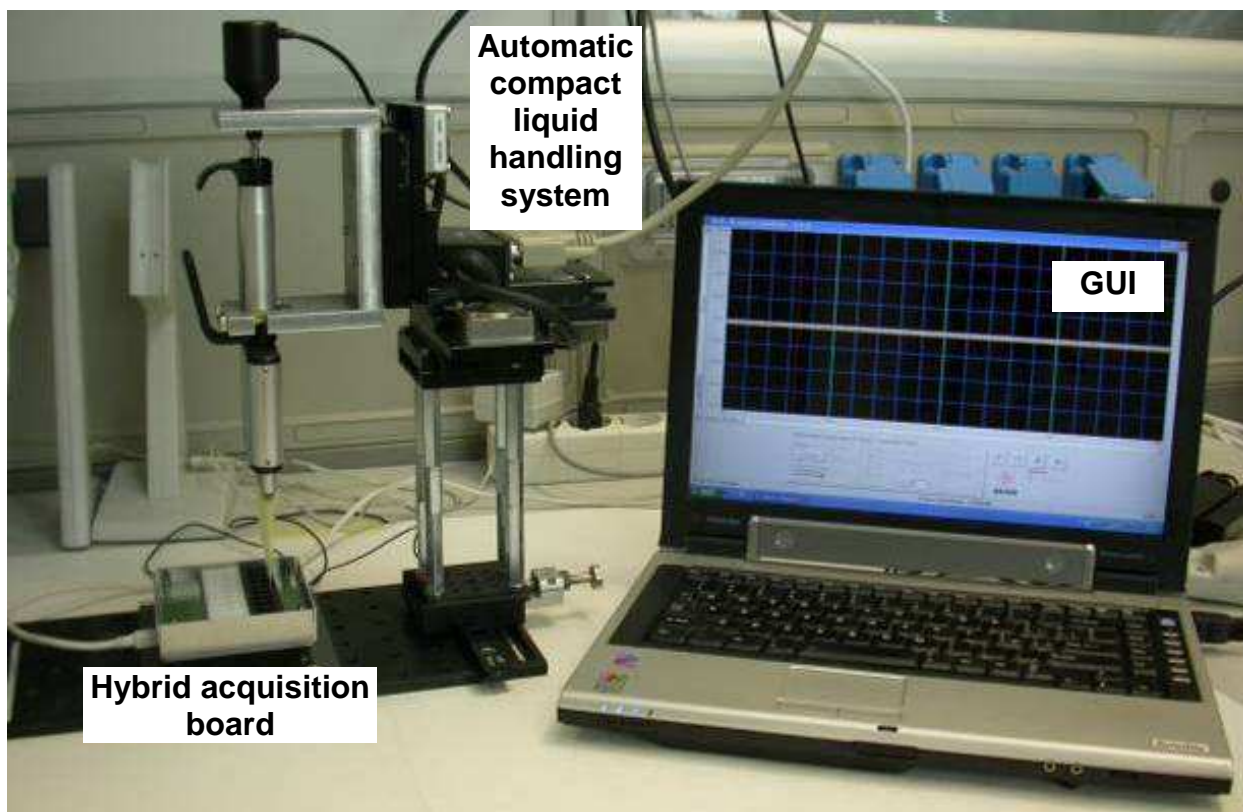
Figure 2.9 – Picture of the developed hybrid portable system for automatic and parallel recording of single ion channels inserted in bilayer lipid membranes.

2.7 Applications to biological nanopores and single channel recordings

In order to effectively demonstrate the formations of bilayers structure using the proposed approach, protein ion channels were embedded into the membranes and signal were concurrently recorded by the developed system. As model systems for proof of concept experiments, α-hemolysin (αHL) protein and gramicidin (gA) were chosen, see Figure 2.10.
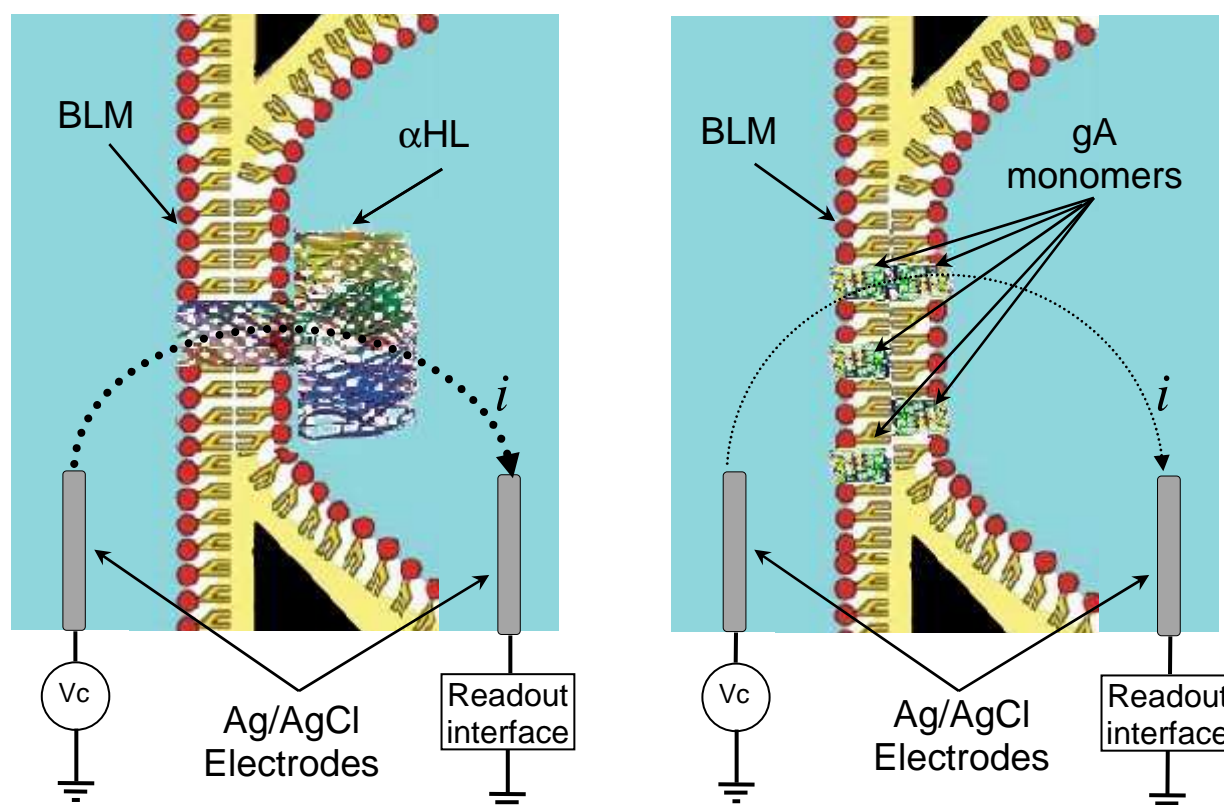
Figure 2.10 – Representation (not to scale) of the two different protein channels used in the experiments and the resulting ionic current, measured by the readout interface, relative to pore formations into the BLMs at a fixed control signal (Vc).

αHL is a 33 kDa exotoxin secreted by the bacterium *Staphylococcus aureus* that spontaneously forms relatively large beta-barrel pores, with an heptameric or hexameric structure [104], allowing ions and molecules to pass through the membranes inducing osmotic lysis of the target cell membranes. Thanks to the highly studied and well known three-dimensional structure at high resolution [26] and its large single channel conductance, it has a wide and common usage as base for stochastic sensors [19] and for DNA sequencing applications [18], [42].
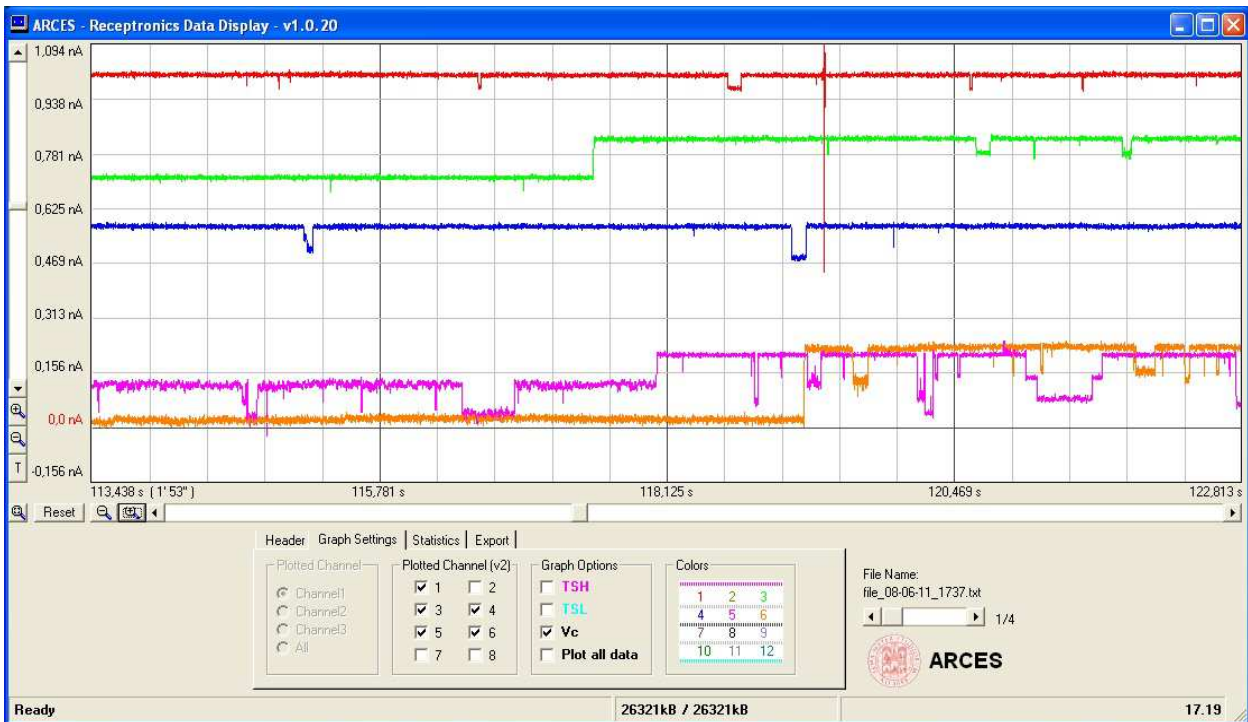
Figure 2.11 – αHL pore insertions into five different and independent BLMs spots. Applying a transmembrane constant

voltage stimulus of 80mV results in a step of about 80pA for each ion channel inserted.

Figure 2.11 shows a typical acquisition in which five membranes are formed in five different independent Delrin blocks. A relatively high quantity (50 ng/ml) of α-hemolysin monomers (Sigma-Aldrich) was added in the cis-chambers (the ones connected to the vitual ground of the readout system) in order to accelerate pore formations in membranes regardless the number of αHL channels inserted in each formed BLMs. As expected, after few minutes characteristic current steps related to αHL heptameric pores formations in membranes occurred. Indeed, applying a constant transmembrane potential of 80 mV in each spot, no current passage occurs if ion channels are not embedded into BLM due to the high electrical resistance (several Gigaohms) of the membrane with respect to ions, whilst a step of about 80 pA is observed every time a αHL pore forms, corresponding to the typical α-hemolysin heptameric channel ionic conductance of about 1nS for 1M KCl buffer solution [19]. If a more precise control of the number of αHL pores in membranes is required and only one or two channels have to be embedded in the BLMs (e.g. for translocations experiments [15], [18]), a much lower concentration (2-5 ng/ml) is usually used and an automatic flushing of the cis compartments is made after the first channel insertion in order to remove the monomers in solution with fresh buffer solution.

As a further confirmation of the well-formed BLM-αHL assembly, we also added a high concentration (80 μM) of β-cyclodextrin (βCD, Sigma-Aldrich) in the trans-chamber. This cyclic oligosaccharide molecule is able to get into the lumen of the pore from the stem side and to

bind the α-hemolysin protein, partially blocking the channel and significantly reducing the ionic channel conductance and thus the measured current, causing stochastic current spikes, as reported in literature [105] and illustrated in Figure 2.12

Figure 2.12 – Example of βCD single molecules binding activity in three different and independent BLMs. Each spike is caused by the interaction and the partial blockade of the αHL pore by a single βCD molecule lodged in the lumen of the pore.

As previously mentioned, experiments using another commonly used model membrane protein, the gramicidin A (gA) [106–108], were performed to demonstrate the capabilities of the developed automatic multichannel portable system in common electrophysiological experiments or in sensoristic applications [20], [25], [29], [30].

The gA is a small (1.9 kDa) pore forming toxin, secreted by the bacterium *Bacillus brevis*, which spontaneously incorporates into bilayers and creates pores allowing a transmembrane flux of monovalent cations upon transient dimerization. Once in the membrane as nonconducting monomeric subunit, indeed, gA temporarily self-assembles into a functional dimeric structure with characteristic conductance of about 5.8 pS in 100 mM NaCl [109] and about 21 pS in 1 M KCl [110].

Thanks to its well-studied and deeply modelled ion channel conductance [111] and the possibility to directly dissolve it in buffer solutions for the spontaneous incorporation in BLMs (without the need of proteoliposome fusion required for most ion channel proteins embedding into artificial membranes), gA is well suited for biosensor applications comfortably performed by means of the presented automatic system.

On the other hand, due to its low conductance (much lower than the αHL one), the readout of signals coming from this kind of channel is much more challenging, from the electronic interface point of view, since the typical current signal is in the few pA range and in the KHz range

bandwidth. Ultra low-noise current amplifier architectures, such as the developed one [96], are strictly required.

Figure 2.13 shows a representative acquisition (at 1KHz bandwidth) of performed experiments obtained automatically adding gA (Sigma-Aldrich) to both chambers at a final concentration of 50pM, demonstrating the possibly to concurrently and automatically create different, independent BLMs and acquire data coming from gA ion channels in a parallel fashion using the developed fully automatic ion channel recording system.

Data were obtained setting a high transmembrane potential of 200 mV and using a relatively highly concentrated buffer solution of 1M KCl (which is usually used for bio-nanosensors applications, but not for studies of ion channels in electrophysiological conditions) in order to have current steps of about 4pA, easily detectable by the developed integrated readout interface.

These results experimentally have shown that the developed unique readout system has edge performances, demonstrating on one hand the possibility to perform automatic and concurrent experiments on different biological nanopore-based biosensors, on the other that some improvements to the integrated readout interface had to be done in order to use the system for real electrophysiological studies on ion channels. It must be noted that the conductance of gA channel is similar to the conductance of the widely studied sodium channel in biological conditions, typically in the range of 4-18pS [90]. For these reasons great efforts have been made by the research group in order to overcome these limitations and to increase the system performances in terms of noise and signal bandwidth [47], allowing a step further towards the creation of a high performance fully automatic system that is currently under development.

Figure 2.13 - Example of gramicidin A single ion channels activity in three different and independent BLMs. Each time a gA dimer is temporarily formed a single current step of about 4 pA (resulting in a single channel conductance of about 21 pS) is recorded.

Multichannel events cause a characteristic staircase-like current signal.

Chapter 3   Hybrid, low-cost, compact system for Impedance sensing of Nanowires

3.1   Introduction

Biosensors based on silicon nanowires (Si-NWs) demonstrated high potential in sensing and promise highly sensitive real-time and label-free electrical detection of biomolecules[56], [67], [68], [112], even in complex physiological media [54], [57], [113], [114].

The electronic properties of nanowires (see section 1.4) offer high sensitivity and have the potential to revolutionize the field of Point-of-Care (POC) medical diagnosis since the fabrication can be performed using very low cost nanofabrication processes, based on simple and mature photolithography, thin film technology, and plasma etching [73], [74].

This chapter focuses on the design and test of a portable and compact hybrid interface comprising the electronic readout and the microfluidic system for nanowire based sensors. Indeed, even if literature presents many works on nanowires based sensors, typically the readout apparatus for these sensors is bulky and expensive and require skilled personnel (see Figure 3.1). To enable the routine application of predictive, preventive and personalized healthcare, these biochemical test sensors will have to work at a much larger scale, at much lower cost, and preferably also in point-of-care locations rather than exclusively into clinical laboratories.
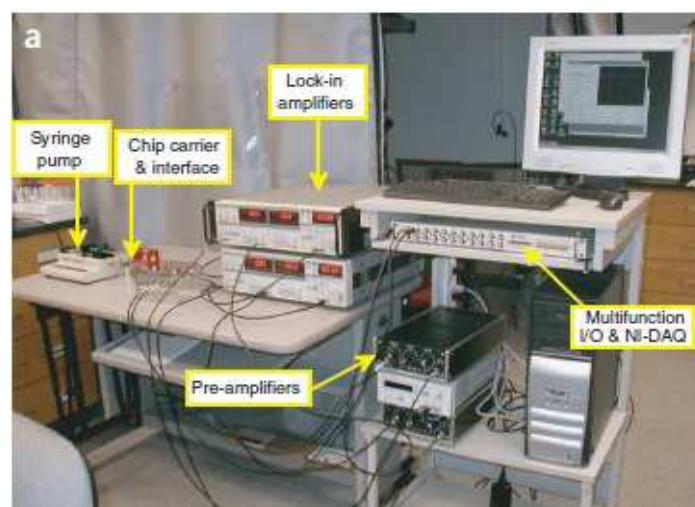
Figure 3.1 – Example of a typical nanowires readout apparatus

With these purposes, integrated sensor systems are emerging as important candidates for the development of point of care devices because of their intensive use in portable applications and lower price compared to the commercial instruments [115–118]. Integration of the sensor chips with custom electronics into a user friendly package would provide a new approach to decentralised healthcare management. However fully integrated biosensing systems have the drawback of tremendously high testing costs, not compatible with preliminary tests on biosensors in experimental conditions. Moreover affinity based bionsensors, such as the nanowires, need a functionalization step which create the necessity to have a good knowledge of the optimized functionalization procedures, requiring maintaining a separation between the "wet" biosensor, which can be disposable, and the electronic readout. On the other hand the possibility to have the custom readout system as tight as possible reduces parasitic interconnection effects.

For these reasons the integration of the nanowire sensors on a standard CMOS substrate has to be considered a long term goal, only after many tests on these kinds of sensors are performed and once many features are known on the exact response of nanowire sensors and on the best measurement technique to be used.

The sensing mechanism typically used for detection suffers from the ionic screening due to mobile ions present in the solution [6]. The idea was to investigate if the fundamental ionic screening effect can be measured by operating Si-NWs as an amplitude and phase shift detector, eventually in order to achieve information on the specific electrolytic solution used, such as concentration and ph.

Studies on nanowires that change conductivities involve normally resistance measurements, however since not much features are yet known on the exact response of the nanowire sensors, we believe the lock-in amplifier technique could be able to measure the complex impedances and possibly enrich information on the bio-analytical events occurring at the nanowires transducers surface, such as molecular interactions between the receptors layer and targets biomolecules.

Moreover, there is a lack of instrumentation able to perform both impedance spectroscopy and real-time impedance measurements in order to identify the electrical parameters model and real time behaviours of the nanowires depending upon the specific structure and fabrication process.

This would help the integration of the biosensor with the interface giving a quick thought accurate knowledge of electrical parameters (such as impedance, noise and bandwidth) [119] and their related behaviours to target stimulus, enabling an understanding of the design constraints for the next generation integrated readout systems.

In this chapter, the design and measurement of a low cost lock-in amplifier-based system, which realizes complex impedance measurements, is described. The implementation of the system was developed by three main steps:

1. Designing a discrete component parallel electronic readout interface
2. Interfacing the developed electronics with the nanowires sensors and designing appropriate microfluidics.
3. Experimental testing and improvements of the designed readout system.

Summing up, the characteristics needed by the readout system are:

- to be compact (eventually for point-of-care applications);
- to be flexible for different nanowires or nanoribbons based sensors, which can have different layouts and a wide range of transimpedances;
- to be able to perform parallel acquisitions, in order to enable sensing by multiple NWs in the same device, for instance functionalized to sense different molecules;
- to have the possibility to perform differential measurements in order to increased sensitivity and selectivity, eliminating all the "common mode" effects caused by the particular environment in which the sensors are immersed or by specific sensors parasitics;
- to be able to measure sensors impedance magnitude and phase, since the latter could offer better understanding of the surface molecular interaction (e.g. NW functionalization control or analysis of device parasitics at different frequencies)

3.2   The overall readout system

Literature analysis (see section 1.4) on nanowires based sensors resulted in observing quite relaxed requirements from the electronic interface point of view, since typical current signals responses are in the order of tens to hundreds of nA (Typical nanowire resistances are in the range of 100KΩ to 100MΩ [6], [58], [63], [64], [66], [74], [75], [77], [81], [120]), requiring current readout system with an input referred noise less than about 200fA/√Hz. However the great variance of nanowires impedance, strongly dependent on technology and realization process, requires a very flexible interface capable to span over a big range of full scale current values.

For these reasons the aim was to create a simple, versatile, easy-to-use and low cost compact system that enables to perform tests on nanowires chips and to investigate if phase shift in current response can effectively enrich information on NWs-electrolyte interface.

With this purposes, an analogue acquisition board able to perform real-time amperometric measurements both in AC and DC regimes, along with DC voltage sweeps (for voltammetric studies) and AC impedance spectroscopy, implementing a two electrode potentiostat,

conjugated with a lock-in technique, using commercially available integrated circuits, was developed.

The system (represented in Figure 3.2) comprises a custom printed circuit board (PCB) called "Nanowires Acquisition Board" and powered at ±12 V DC (described in the next section) hosting both the NW chip array DUT and the readout interface. The latter performs the readout of the current signal coming out of the sensors in response to a sinusoidal or DC V_{ref} signal generated by an external waveform generator (Tektronix AFG 3102). The amplified and demodulated analogue signals are then digitized by a National Instruments 6009 DAQ [121] whose output is sent to a laptop for storing and online (or post) processing using a custom implemented LabView interface.

The above approach, based on performing the filtering and data manipulations in the digital domain, allows the system to be particularly flexible, maintaining a simple analog front-end for different applications with respect to the system required performances.
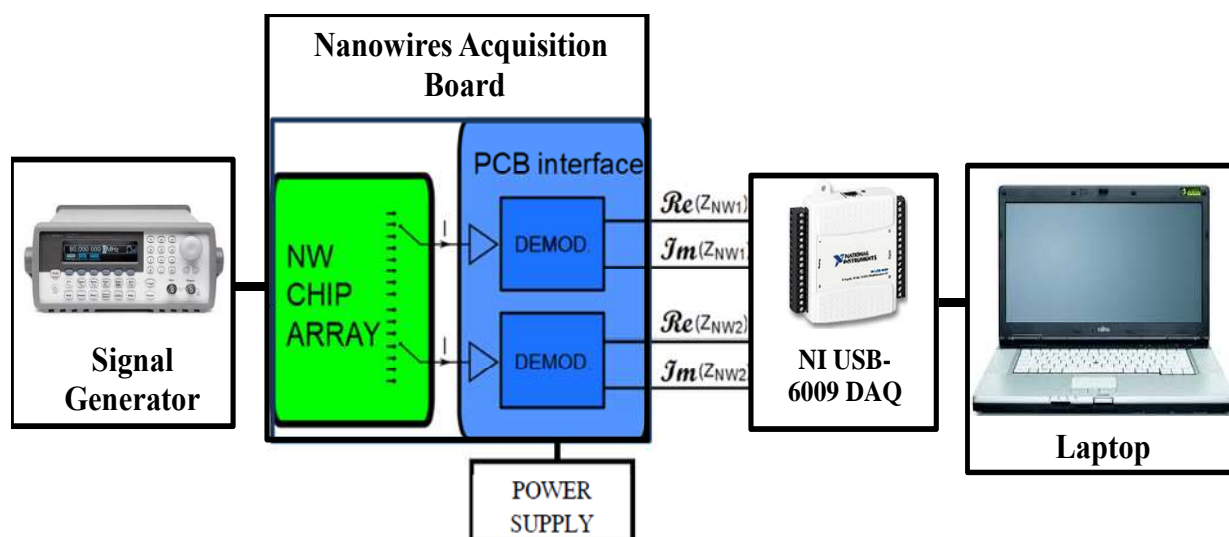
Figure 3.2 - Block diagram of the whole developed readout system

3.3   Nanowires acquisition board design

The designed "Nanowires Acquisition Board", block diagram is shown in Figure 3.3, where two identical and independent readout branches enable differential measurements of different

nanowires (or nanowires set) from an array (illustrated as Z-ref and Z-sens). These can be selected, independently on the two branches, by means of an an addressable switching system (see Figure 3.2).
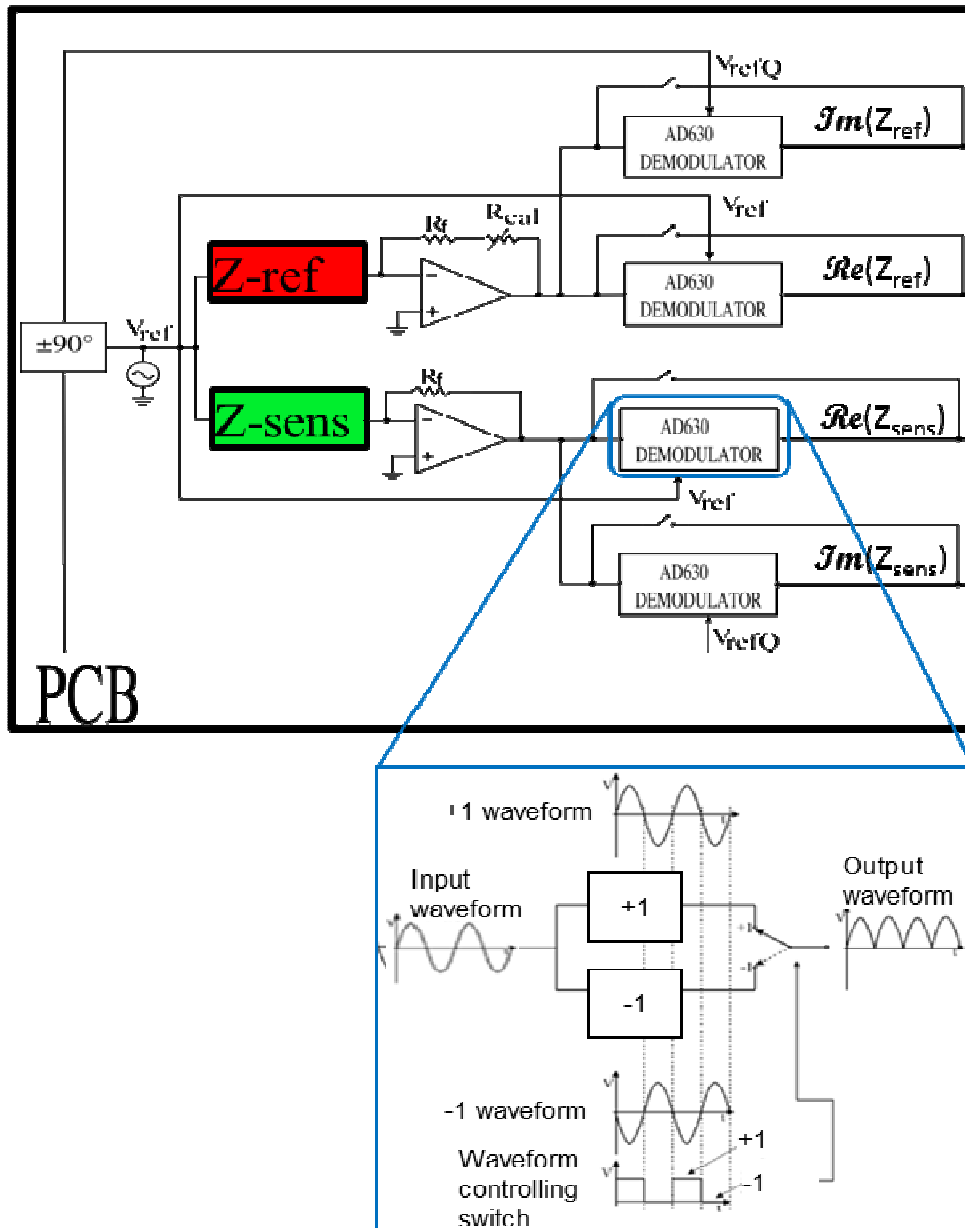
Figure 3.3 – Block diagram of the designed Nanowires Acquisition Board.
The inset shows the working principle of the AD 630 demodulator. The switch is driven by a
comparator that compares the reference signal (V_{ref} and V_{refQ}) with its DC offset level, resulting in a
square wave in-phase with the reference signal.

Each branch of the circuit can be roughly broken down into two parts: a transimpedance input amplifier that converts the current signal coming from nanowires based sensors to an amplified voltage signal prior to it being sent to the integrated circuit (the AD630) that performs the phase-sensitive detection.

In accordance with the aim of simple and low cost approach, a simple classical resistive feedback operational amplifier was chosen as preamplification stage due to the relatively high currents involved and since the the typical literature frequency range of lock-in based measurements on nanowires sensors span from few Hz to few KHz (as reported in Table 1.1).

On the other hand, the well-known gain-bandwidth trade-off must be considered if highly resistive nanowires (and thus as low currents as few nA) have to be studied; indeed in this case a high value discrete feedback resistors, strongly affected by stray capacitances, has to be used and a parasitics phase shift and magnitude compensation has to be done. This task is accomplished in the digital domain by the developed software interface (as reported below).

As operational amplifier the AD822 was chosen in particular thanks to its low power rail to rail FET input op amp with low noise performances (13 nV/√Hz @ 10 KHz) and low input bias current [122]. Four different feedback resistors of 1 MΩ, 10 MΩ, 100 MΩ, 1 GΩ enable to select the four different current working ranges of ±7.85 µA, ±785 nA, ±78.5 nA, ±7.85 nA by means of mechanical switches.

The demodulation is implemented by using an AD630, usually used in precision signal processing and instrumentation applications requiring wide dynamic range. It is working properly in the bandwidth of interest of this application [123].

The reference waveform sent to the nanowires chip DUT is:

$$V_{ref} = V_i \cdot \sin(\omega_i t) \tag{3.1}$$

and the AD630 demodulator is configured to have a gain of ±1 and, since the gain is controlled by a switch driven by a comparator (see inset of Figure 3.3), it fundamentally multiplies the input waveform for a unitary square wave whose Fourier series is given by:

$$V_{square}(t) = \frac{4}{\pi} \cdot \sum_{k=1}^{\infty} \left(\frac{\sin((2k-1) \cdot \omega_i t)}{2k-1} \right) \tag{3.2}$$

the output of the in-phase branches of the circuit is then:

$$V_o(t) = -V_i \cdot \left(\frac{R_f}{Z_{sens}} \right) \cdot \sin(\omega_i t + \varphi) \cdot \left(\frac{4}{\pi} \right) \cdot \sum_{k=1}^{\infty} \left(\frac{\sin((2k-1) \cdot \omega_i t)}{2k-1} \right) \tag{3.3}$$

where R_f and Z_{sens} are respectively the selected feedback resistance, which sets the range of measurements of the system, and the sensor impedance. Using Werner formulas we obtain:

$$V_o(t) = -V_i \cdot \left(\frac{R_f}{Z_{sens}} \right) \cdot \left(\frac{2}{\pi} \right) \cdot \sum_{k=1}^{\infty} \left[\left(\frac{\cos((2-2k) \cdot \omega_i t + \varphi)}{2k-1} \right) - \left(\frac{\cos(2k \cdot \omega_i t + \varphi)}{2k-1} \right) \right] \tag{3.4}$$

As can be better seen in equation (3.4), the output signal presents a high harmonic content associated to the square wave components of the signal.

The two "real part" branches of the PCB are then are externally digitized and low pass filtered (see below) to obtain only the DC component:

$$V_o(t) = -V_i \cdot \left(\frac{R_f}{Z_{sens}} \right) \cdot \left(\frac{2}{\pi} \right) \cdot \cos(\varphi) = \alpha \cdot \Re e(Y_{sens}) \tag{3.5}$$

Similarly, the output of the quadrature branches, in which the comparator input is shifted of 90°(V_{refQ} in Figure 3.3), of the circuit is:

$$V_o(t) = -V_i \cdot \left(\frac{R_f}{Z_{sens}} \right) \cdot \sin(\omega_i t + \varphi) \cdot \left(\frac{4}{\pi} \right) \cdot \sum_{k=1}^{\infty} \left(\frac{\cos((2k-1) \cdot \omega t)}{2k-1} \right) \tag{3.6}$$

Again using Werner formulas we obtain:

$$V_o(t) = -V_i \cdot \left(\frac{R_f}{Z_{sens}} \right) \cdot \left(\frac{2}{\pi} \right) \cdot \sum_{k=1}^{\infty} \left[\left(\frac{\sin((2-2k) \cdot \omega_i t + \varphi)}{2k-1} \right) + \left(\frac{\sin(2k \cdot \omega_i t + \varphi)}{2k-1} \right) \right] \tag{3.7}$$

That again digitized and filtered gives the output of the two "imaginary part" branches of the PCB:

$$V_o(t) = -V_i \cdot \left(\frac{R_f}{Z_{sens}} \right) \cdot \left(\frac{2}{\pi} \right) \cdot \sin(\varphi) = \alpha \cdot \Im m(Y_{sens}) \tag{3.8}$$

The operating frequency is selectable within 0.1 Hz-2 KHz range in accordance with previous work frequency detection range (see Table 1.1) and the main limitations are given by the real time data conditioning performed by the LabView interface (see below).

The implemented solution also enables to perform DC measurements by bypassing the demodulation stage (this possibility is represented with switches on each branch of Figure 3.2) and setting a constant V_{ref} signal by means of the LabView interface;

Moreover, an auxiliary potential (V_{bulk}) control circuit is designed to set the back-gate and/or liquid gate potential of nanowires. Indeed, as reported in several literature studies, the control of these potentials can affect the nanowires conductivity, enhancing or reducing the signal and thus the sensor sensitivity by modulating the current flowing through it [75–80].

Figure 3.4 shows a picture of the realized Nanowires Acquisition Board where that presents, on the same side of the PCB:

- an input signal SMB connector for the V_{ref},

- the dual power supply connector,
- 4 SMB connectors for the 4 board outputs (Re1, Im1, Re2, Im2).

An industrial process was selected to produce this 10x10 cm Nanowires Acquisition Board and special attention was paid to the PCB layout , using a four metal layer PCB, especially to shield as much as possible the analog signals on the board from external noise sources.

Finally, the board is designed following a modular approach in order to be as much versatile as possible and to have only one electronic readout interface for different NW bionanosensors.

With this approach, indeed a custom "PCB plug interface" (4x4 cm), hosting the NWs chip with the specific microfluidics and pluggable in the proper designed socket (see Figure 3.4 top), can be designed separately and specifically for each individual NW chip layout and application. An implemented example for a specific nanowires array chip provided by University of Southampton is shown below in section 3.6.

The socket connectors provide the power supply, Ground, V_{ref} and V_{bulk} signals to the PCB plug interface for different (eventually based on active components) solutions and connects the selected NW to the selected branch of the circuit (see Figure 3.3)

SOCKET			
Left connector	Dir.	Right connector	Dir.
+12V	out	NW1	in
-12V	out	NW2	in
Gnd	out	NW3	in
V_{ref}	out	NW4	in
Gnd	out	NW5	in
NW10	in	NW6	in
NW9	in	NW7	in
V_{bulk}	out	NW8	in
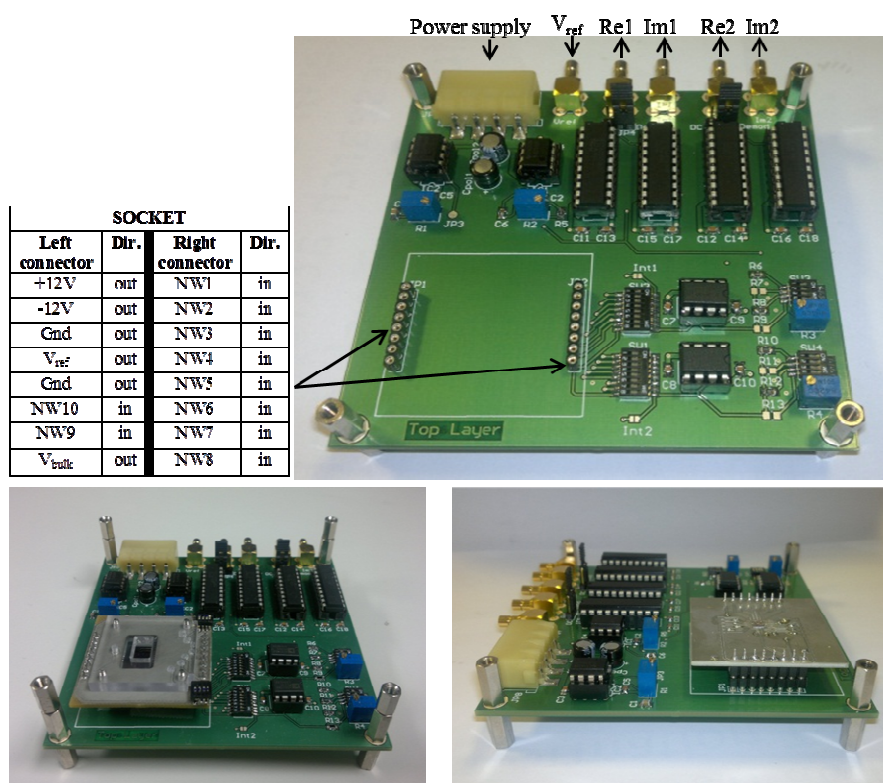
Figure 3.4 - Pictures of the realized Nanowire Acquisition Board.

The top figure shows the board without the 4x4 cm plug interface, the table lists the pinout of the two socket connectors and the two bottom pictures show two examples of realized "PCB plug interfaces".

Summing up the designed Nanowires Acquisition Board has the following main properties:

- Dimensions: 10 x 10 cm 4 layers PCB;

- Performs real time AC (in the range 0.1 Hz – 2 KHz) complex impedance measurements and amperometric DC measurements;

- Differential/parallel measurements are accomplished by means of the two identical readout branches;

- The addressable switching system enable to independently select single nanobiosensors from an array;

- Four different current ranges selectable by mechanical switch, in particular ±7.85 µA, ±785 nA, ±78.5 nA, ±7.85 nA,

- Possibility to set the potential of nanowires chip substrate and/or of the electrolyte in which nanowires are immersed (liquid gate).

- Modular and versatile design, which enables the board to be interfaced with different kinds of bionanosensors and applications by means of different specific "PCB plug interfaces" solutions.

3.4   LabView software interface and filter design

As already mentioned, the whole readout system is controlled by the implemented custom Labview interface. As represented in Figure 3.5, it enables to:

- set V_{ref} waveform properties (frequency, amplitude, DC offset) using the USB interface with the function generator;

- set the proper (adapted to the V_{ref} frequency) NI-DAQ sampling rate and acquisition voltage range;

- simultaneously and real time perform the signal conditioning (see below) of the four outputs of the Nanowire Acquisition Board to finally obtain the filtered real and imaginary voltage values of the two channels;

- display the real time Nyquist diagram of the bionanosensors admittance (or impedance), Magnitude and Phase values and calculate the equivalent values of simple RC circuit (as explained below).

- save data in user-specified text files, compatible with ZView data format.
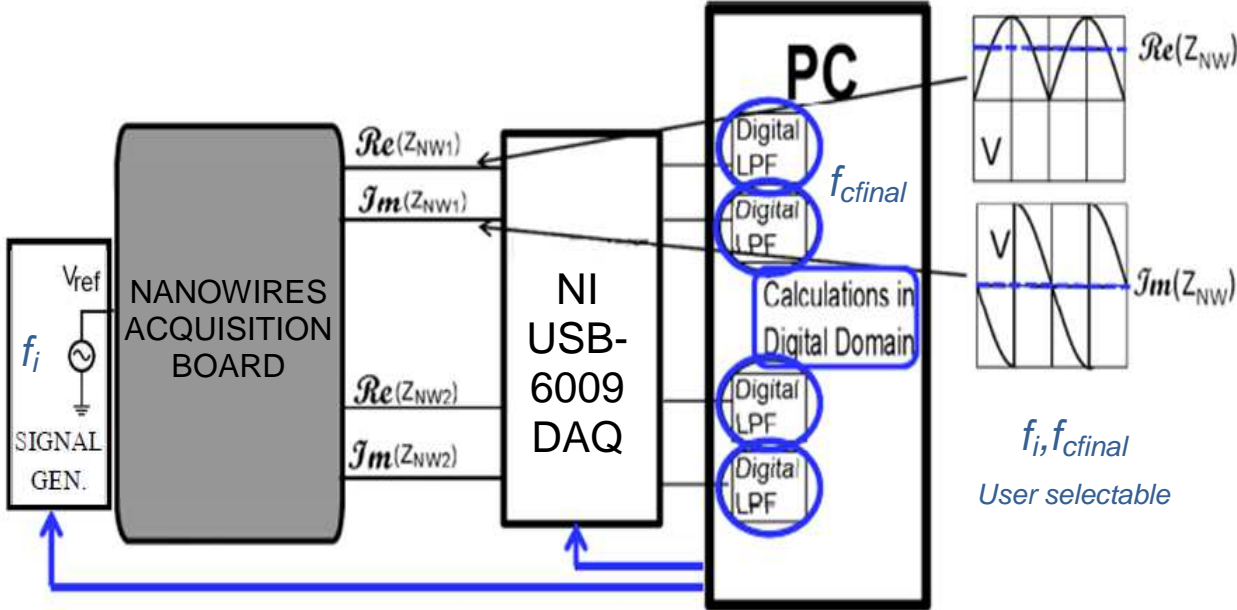
Figure 3.5 - Block diagram of whole acquisition chain with the implemented LabView software interface tasks and the user-selectable parameters, highlighted in blue,.

In order to optimize the computational resources for every working frequency selected, assuring a real time response of the system, an adaptive filter based on the (user selectable) V_{ref} input frequency (f_i) and the final signal band cut off frequency (f_{cfinal}) was implemented in the software interface.

The main signal conditioning process (represented in Figure 3.6) was segmented into 3 stages: two stages implementing finite impulse response digital low-pass filters (FIR Kaiser window) and one devoted to decimation. The two stages FIR was designed and simulated in MATLAB before Labview implementation. Weight taps have been calculated with MATLAB to have the best configuration for all the frequencies in the functioning range.
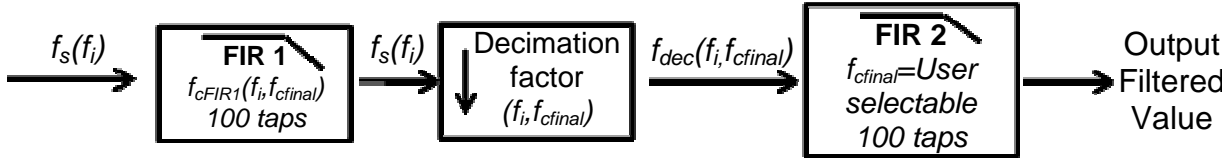
Figure 3.6 - Representation of the adaptive two stages low pass FIR filter implemented in the LabView software interface.

The NI-DAQ sampling rate f_s is automatically set once working frequency is selected, as well as the decimation factor and the cutoff frequency of the first stage filter, which also depend on the final bandwidth of the system.

The two stages are dimensioned to satisfy the condition of same ratio between cutoff frequencies and bandwidths:

$$\frac{f_{cFIR1}}{f_s} = \frac{f_{cfinal}}{f_{dec}}$$

(3.9)

whose expression, considering $f_{dec}=2* f_{c\,FIR1}$, allows calculating the first filter cutoff frequency (f_{cFIR1}) and the decimation ratio as:

$$f_{cFIR1} = \sqrt{\frac{f_{cfinal} \cdot f_s}{2}}$$

(3.10)

$$dec\ ratio = \frac{f_s}{f_{dec}} = \sqrt{\frac{f_s}{2 \cdot f_{cfinal}}}$$

(3.11)

Since the number of taps is the same for the two stages but the sampling rate is much lower for the second one (f_{dec}), the total delay can be written as:

$$Delay = \frac{1}{f_{dec}} \cdot nTAPs$$

(3.12)

where *nTAPs* is the number of FIR taps.

In order to perform real time, 4-channel measurements with a final very narrow bandwidth (to obtain the final mean value, usually f_{cfinal} =1 Hz or 0.1 Hz) and relatively limited computational resources (e.g., if using a laptop), a good trade-off between FIR performances, limited response delay and computational complexity has been found to be the cascade of two 100-taps adaptive filters.

Equation (3.12) shows that the delay is dependent on the sampling frequency; as higher is the sampling frequency, as faster is the system response, on the other hand a high sampling frequency requires much more efforts in terms of computing resources.

Moreover it must be noted that, since the needed final bandwidth is very narrow (usually f_{cfinal} =0.1 Hz or 1Hz) and in order to maintain the system as simplest and cost effective as possible, analysis of the nature of the output signals, that have to be sampled, allowed to consider the possibility to not implement anti-aliansing filters at Nanowire Acquisition Board outputs.

Indeed, selecting a proper sampling rate, it can be noted that the aliasing could be neglected, providing that the sampling frequency f_s is far enough from the harmonics of the output signals (see equations (3.4) and (3.7) and Figure 3.7).

Anti-aliasing filters implementations would have been possible either using passive RC filters or using active ones; however the latter would have complicated the system adding an opamp for every output channel (which would also have added noise to the whole acquisition chain),

while the RC solution, would have required the use of resistors in series to the outputs in the order of tens of KΩ (e.g. R=16 KΩ and C=1 µF to obtain a cutoff frequency fc=10Hz). These resistors would have been incompatible with the relatively low input impedance of the NI 6009 DAQ (only 144 KΩ [121]) resulting in a significant loading error (of about 10%), much higher than the folded noise and aliases contribution if the sampling frequency is selected properly.

For these reasons the interface also enables the selection of the highest harmonic of the signal to be considered following the Nyquist criterion, consequently changing the sampling rate (f_s) of the NI-DAQ in order to obtain for every application the best trade-off between accuracy of the measurement, response delay and computational resources demands.

As can be seen in Figure 3.7, as higher is the sampling frequency (f_s), as far from the DC component are the resulting high-amplitude square-wave-components aliases and the best situation is sampling at a frequency in between the input frequency (f_i) multiples. On the other hand, since the high sampling frequency requires more computing resources, it is possible to sample at a frequency as low as $2 \cdot f_{cfinal} + \varepsilon$ (where ε is a factor of safety for proper sampling rate) at the cost of an higher probability that a multiple of an harmonic of the signal is folded back in baseband.
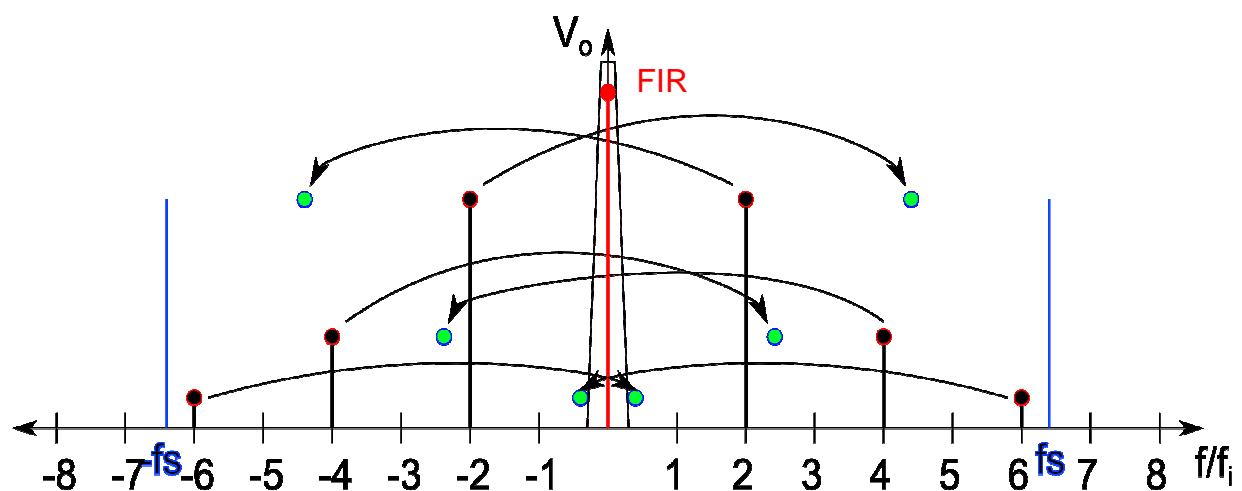
Figure 3.7 – Representation of the demodulated output signals and effect of the sampling which creates aliases of the harmonics at high frequency. However, since the final bandwidth (selectable by the second stage FIR implemented) is very narrow, aliases can be irrelevant if a proper sampling frequency is selected, as illustrated.
The x-axis represents the frequency normalized by the working frequency fi

The obtained filtered voltage signals are then real time manipulated to evaluate magnitude and phase from each branch of the circuit:

$$\left|V_o(t)\right| = \sqrt{\Re e^2\left\{V_o(t)\right\} + \Im m^2\left\{V_o(t)\right\}} = V_i \cdot \left(\frac{R_f}{\left|Z_{sens}\right|}\right) \cdot \left(\frac{2}{\pi}\right) \tag{3.13}$$

$$\varphi = \tan^{-1}\frac{\Im m\left\{V_o(t)\right\}}{\Re e\left\{V_o(t)\right\}} \tag{3.14}$$

In order to have a better representation of the acquired signals, voltage signals are manipulated to obtain, display and save directly the real and imaginary NW admittance values, properly dividing the voltage signal by the scale factor $\alpha = R_f \cdot V_i \cdot \dfrac{2}{\pi}$ (see equation (3.5) and (3.8));

Moreover, other data manipulation implemented in the LabView software interface allows to calculate in real-time the equivalent resistance and capacitance of the series and parallel RC models using the well-known relations [124]:

For RC series model

$$Z = R + jX = R - j\frac{1}{\omega C} \Rightarrow \begin{array}{l} R = R \\ X = -\dfrac{1}{\omega C} \end{array} \tag{3.15}$$

$$Y = \frac{1}{Z} = \left(\frac{R}{R^2 + X^2}\right) + j\left(\frac{-X}{R^2 + X^2}\right) = G + jB \Rightarrow \begin{array}{l} G = \dfrac{R\omega^2 C^2}{1 + \omega^2 R^2 C^2} \\ B = \dfrac{\omega C}{1 + \omega^2 R^2 C^2} \end{array} \tag{3.16}$$

For RC parallel model

$$Y = \frac{1}{R} + j\omega C \Rightarrow \begin{array}{l} G = \dfrac{1}{R} \\ B = \omega C \end{array} \tag{3.17}$$

$$Z = \frac{R}{1 + j\omega RC} = \left(\frac{R}{1 + \omega^2 R^2 C^2}\right) + j\left(\frac{-\omega R^2 C}{1 + \omega^2 R^2 C^2}\right) \Rightarrow \begin{array}{l} R = \dfrac{R}{1 + \omega^2 R^2 C^2} \\ X = \dfrac{-\omega R^2 C}{1 + \omega^2 R^2 C^2} \end{array} \tag{3.18}$$

Figure 3.8 shows the LabView interface which easily enable to perform real time AC measurements or automatic frequency sweeps for impedance spectroscopy characterization of

the bionanosensor hosted in the nanowires acquisition board, synchronously controlling the signal generator and the NI-DAQ card; as well as perform real time DC measurements and DC voltage (V_{sd}) sweeps for I/V bionanosensors characterizations.
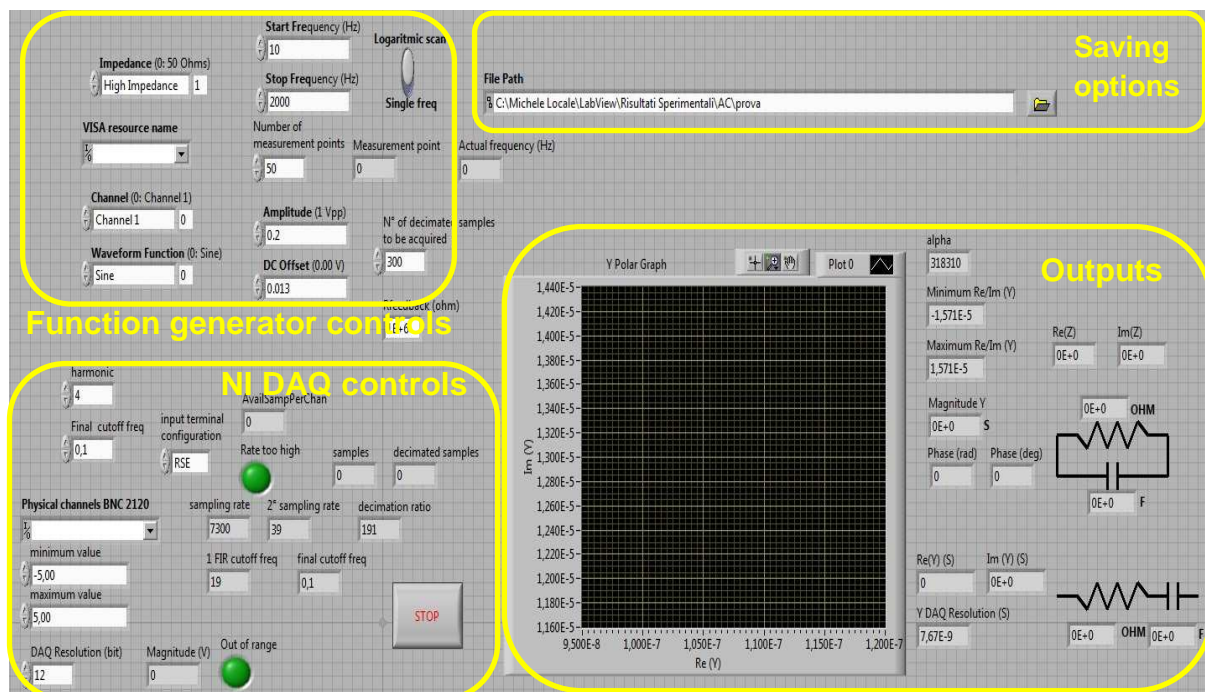
Figure 3.8 - Screenshot of the implemented LabView interface

3.5   System characterization, Calibration and Testing

Preliminary tests on simple DUT simulating nanowires behaviour, like resistors, capacitors and RC parallel circuit were performed to check the system performances, both in real time acquisitions and in frequency sweep mode, in terms of effective final resolution, accuracy and precision.

Matlab scripts were also implemented in order to automatically analyze saved data; next section shows some results obtained by preliminary tests.

3.5.1   Real-time preliminary tests on synthetic circuits

Preliminary tests on synthetic DUT (R, C and R-C combinations) in different measurement ranges and at different frequencies were performed connecting the DUT between V_{ref} and a selected NW socket (see Figure 3.4). In particular Vishay precision resistor of 1MΩ and 10MΩ,

0.005% tolerance and Dale RNX-3/8 100MΩ resistor, 1% tolerance and capacitors of 100pF and 1nF were used. Those resistors and capacitors values were selected since are the typical ranges of measurements involved in nanowires sensing [58], [64], [65], [68], [120].

In particular H8 precision resistor of 1MΩ, 0.1% tolerance (with R_f =1MΩ and 10MΩ) and Dale RNX-3/8 100MΩ Resistor, 1% tolerance (with R_f =100MΩ and 1GΩ) and Capacitor of 1nF were used.

For all the tests some systems parameter were fixed, in particular:

- V_{ref} sinusoidal input amplitude= 1 V_{pp} (V_i=0.5V).
- Sampling frequency fixed at $f_s=2*(5+ε)*f_i$, in order to sample at a quite high frequency but however allowing the acquisition of two data channels (48 KHz maximum sample rate of the NI DAQ 6009 to be divided for the used channels [121]).
- Digital filter final cutoff frequency f_{cfinal}= 0.1 Hz.

Table 3.1 sums up the different configurations for the four different selectable measurement ranges and shows the worst effective final resolution experimentally obtained for each configuration.

Table 3.1: Experimental performances at different measurement ranges

Selected $R_{feedback}$ [Ω] (Full Scale Current [A])	1 M (±7.85 μ)	10 M (±785 n)	100 M (±78.5 n)	1 G (±7.85 n)
Full Scale (Y) [S]	±1.57x10^{-5}	±1.57x10^{-6}	±1.57x10^{-7}	±1.57x10^{-8}
Minimum detectable Impedance [Ω]	6.37x10^4	6.37x10^5	6.37x10^6	6.37x10^7
Minimum experimental Dynamic Range - Worst case [dB] (ENOB)	68.03 (11.3)	54.18 (9)	68.63 (11.4)	51.17 (8.5)

Where:

- Full scale (Y) is the full scale in terms of admittance using a sinusoidal input amplitude fixed at 1V_{pp}
- Minimum readable Impedance is the minimum impedance that can be read by the system, it is simply the reciprocal of the Full Scale (Y) ;
- Minimum experimental Dynamic Range – worst case (ENOB) is the minimum effective final dynamic range experimentally obtained (considering all the experimental tests performed at different conditions) in terms of decibels and of Effective Numbers Of Bits (ENOB);

Hereafter are shown, as example, some of the results of tests done using resistors and RC parallel circuit. The first figure of each test shows a full scale view of performed real time AC measurements at different frequencies plotted in the same figure, while the zoomed version shows the details of the measurements. Each point is the result of 1 minute of acquisition at a fixed frequency.

As can be seen in the zoom view, parasitics affect the measurements highlighting the dependence of the measured data on the working frequency and consequently on the different contributions of parasitics either in the DUT or in the system acquisition chain. For this reason a phase shift and magnitude compensation was implemented in the LabView interface as reported in section 3.5.2.

Below each figure, tables show the obtained effective experimental resolutions (in terms of ENOB), as well as standard deviations (σ_{noise}) for Real and Imaginary parts, which give a measurement of the precision of the system, for each working frequency. Moreover a measurement of the absolute accuracy, related to the values of R_{DUT} (and C_{DUT}) measured using Agilent 34401A digital multimeter, for each considered frequency was calculated, in terms of percent error, as:

$$Accuracy\ Error(\%) = \left| \frac{actual\ value - measured\ value}{actual\ value} \right| \cdot 100 \qquad (3.19)$$

where the value read by the Agilent 34401A was considered as actual value and the measured value was the mean of the acquired data at a certain fixed frequency.
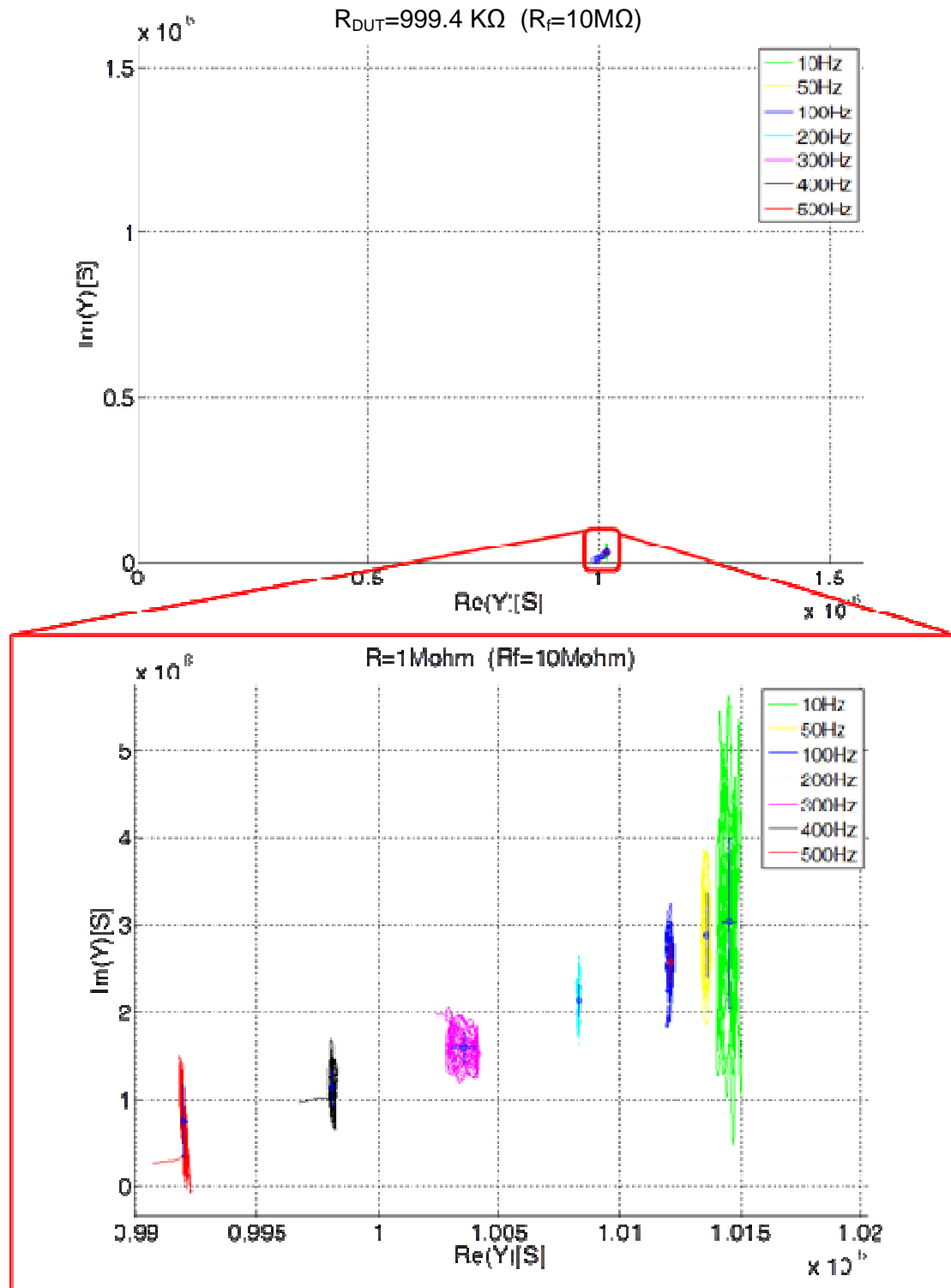
Figure 3.9 - System performances tests at different frequencies using a 1 MΩ Resistor as DUT.

Each point is the result of 1 minute of real- time acquisition at a fixed frequency.

Table 3.2: Experimental results at different frequencies using 1 MΩ Resistor as DUT
(Conductance actual value=1.0006 µS).

Frequency	10Hz	50Hz	100Hz	200Hz	300Hz	400Hz	500Hz
ENOB Re(Y)-G	13.6	9.4	15.3	16.2	12.8	15.2	14.6
ENOB Im(Y)-B	8.7	14.5	10.4	10.8	10.8	10.7	9.6
σRe (Y) [nS]	0.18	0.10	0.06	0.03	0.30	0.06	0.10
σIm (Y) [nS]	5.5	3.30	1.62	1.23	1.23	1.37	2.9
G Absolute Accuracy-Percent error	1.38%	1.3%	1.1%	0.76%	0.33%	0.25%	0.85%
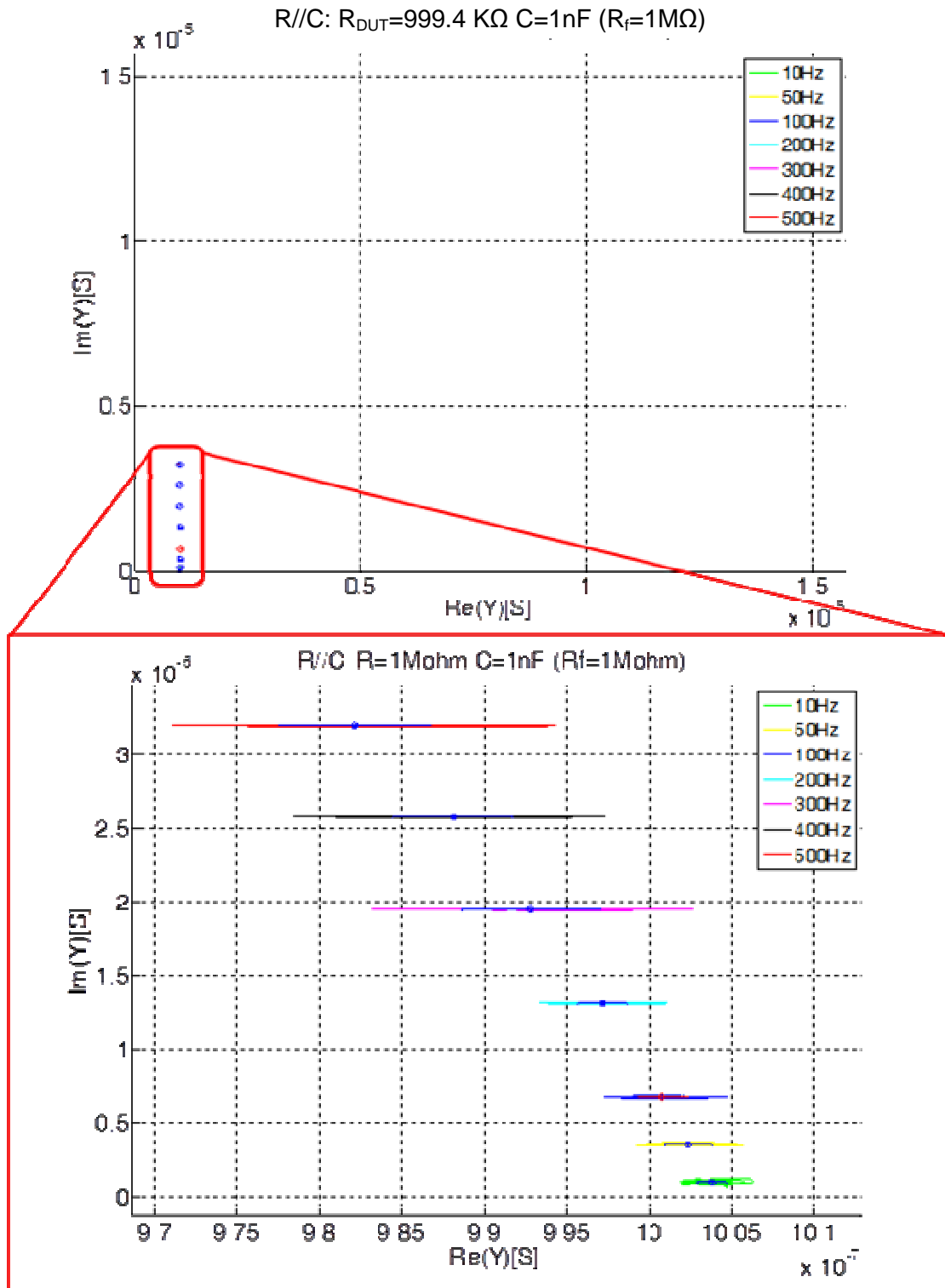
Figure 3.10 - System performances test at different frequencies using an R-C parallel circuit

(1 MΩ Resistor - 1nF Capacitor) as DUT.

Each point is the result of 1 minute of real- time acquisition at a fixed frequency.

Table 3.3: Experimental results at different frequencies using an R-C parallel circuit as DUT.

Frequency	10Hz	50Hz	100Hz	200Hz	300Hz	400Hz	500Hz
ENOB Re(Y)	15	14.5	14.3	14.3	12.9	13.1	12.7
ENOB Im(Y)	11.4	12.7	13.5	13.9	14.4	13.8	13.2
σRe (Y) [nS]	0.65	0.97	1.11	1.06	2.98	2.57	3.29
σIm (Y) [nS]	8.17	3.34	1.93	1.41	1.05	1.5	2.35
G Absolute Accuracy-Percent error	0.32%	0.18%	0.02%	0.34%	0.77%	1.24%	1.5%
B Accuracy-Percent error	11%	10.9%	6.8%	4.1%	3.2%	2.4%	1.8%

Susceptance (B) accuracy for each working frequency was calculated as:

$$B\ Accuracy(\%) = \left| \frac{B\ theoretical - measured\ value}{B\ theoretical} \right| \cdot 100 \qquad (3.20)$$

where $B\ theoretical = \Im m\{Y\}\ theoretical = 2\pi f C$.

3.5.2 Parasitics Phase shift and Magnitude compensation

As well known, the classical simple resistive feedback TIA front-end used has the drawback to be strongly affected by parasitics capacitances in parallel to the feedback resistor. In particular if the latter has high value as the one used for low current measurements ranges, a small parasitic capacitance as few pA can strongly affect the measurement.

Indeed in the real experimental world the situation of the front-end transimpedance amplifier is the one represented in Figure 3.11, thus the feedback network is given by the $R_f C_{par}$ parallel circuit and the transimpedance is given by:

$$Z_f = -\frac{V_{out}}{I_{in}} = \frac{R_f}{1 + j2\pi f_i R_f C_{par}}$$

(3.21)

Which substitutes the term R_f in the outputs of the nanowires acquisition board (see equations (3.5) and (3.8)).

This means that the "gain" (given by: $|Z_f| = \dfrac{R_f}{\sqrt{1 + \left(2\pi f_i R_f C_{par}\right)^2}}$) of the preamplifier stage

depends on the working frequency fi and on the $R_f C_{par}$ product and that the outputs significantly

decreases for frequencies higher than the cut-off frequency $f_c = \dfrac{1}{2\pi R_f C_{par}}$ (and by a factor of √2

at f_c).

For instance, considering a parasitic capacitance of 1 pF in parallel to the feedback resistor, we obtain a bandwidth that depends upon the specific feedback resistance used in the measurement giving a cut-off frequency varying from 159 Hz, for R_f= 1GΩ, to 159KHz for R_f=1MΩ as reported in Table 3.4 and close to the values experimentally obtained, as can be seen in Figure 3.12 and Figure 3.13.

Table 3.4: Estimated cut-off frequency for the different selectable feedback resistance considering a parasitic capacitance C_{par}=1pF

Selected $R_{feedback}$ [MΩ]	1	10	100	1000
f_C (KHz)	159.2	15.92	1.592	0.159
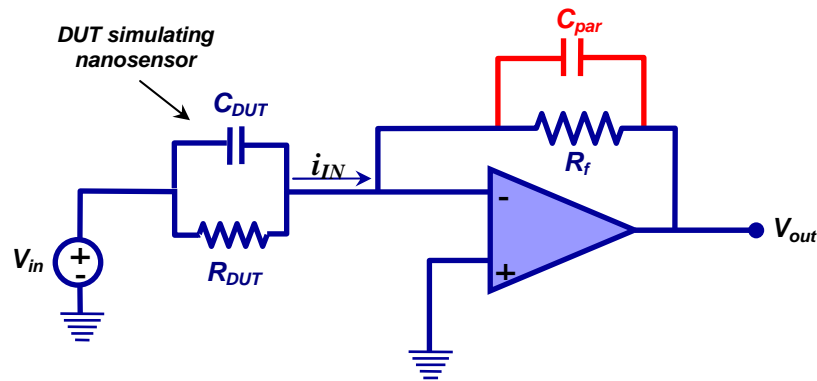
Figure 3.11 – Transimpedance preamplifier front-end. Unavoidable parasitic effects are highlighted.

This decrease in the real transimpedance value (and then in the output voltages), given by parasitics in parallel to the feedback resistor, is not considered in the implemented Labview interface when online calculating the real and imaginary NW impedance (or admittance) values (see section 3.4) resulting in a final (frequency dependent, but constant at a certain fixed frequency) overestimation of the impedance magnitude and a parasitic phase shift.

In particular for the highest values of R_f (100MΩ and 1GΩ) the cut-off frequency falls inside the measurement frequency range causing a high phase and impedance magnitude shifts as a function of frequency, as can be seen in Figure 3.12 where frequency sweeps are performed changing only the feedback resistors (respectively 10MΩ and 100MΩ) and measuring two different simple DUTs: a 10 MΩ resistor (blue and red lines) and an RC (10 MΩ-100pF) parallel circuit (green and magenta lines). Considering the simple resistor DUT case and using a feedback resistor up to 10 MΩ the system response is accurate, with a constant impedance magnitude over the whole frequency range and a maximum spurious phase shift of 4 degrees at 2 KHz. Conversely, using a feedback resistor of 100 MΩ a significant parasitic phase shift of 43 degrees at 2 KHz is obtained.

The same behaviour is observed when the RC parallel circuit is used as DUT. These results clearly demonstrate that effectively the phase shift is dependent on the parasitics coupled to the feedback resistance, which is the only parameter changed in these tests.
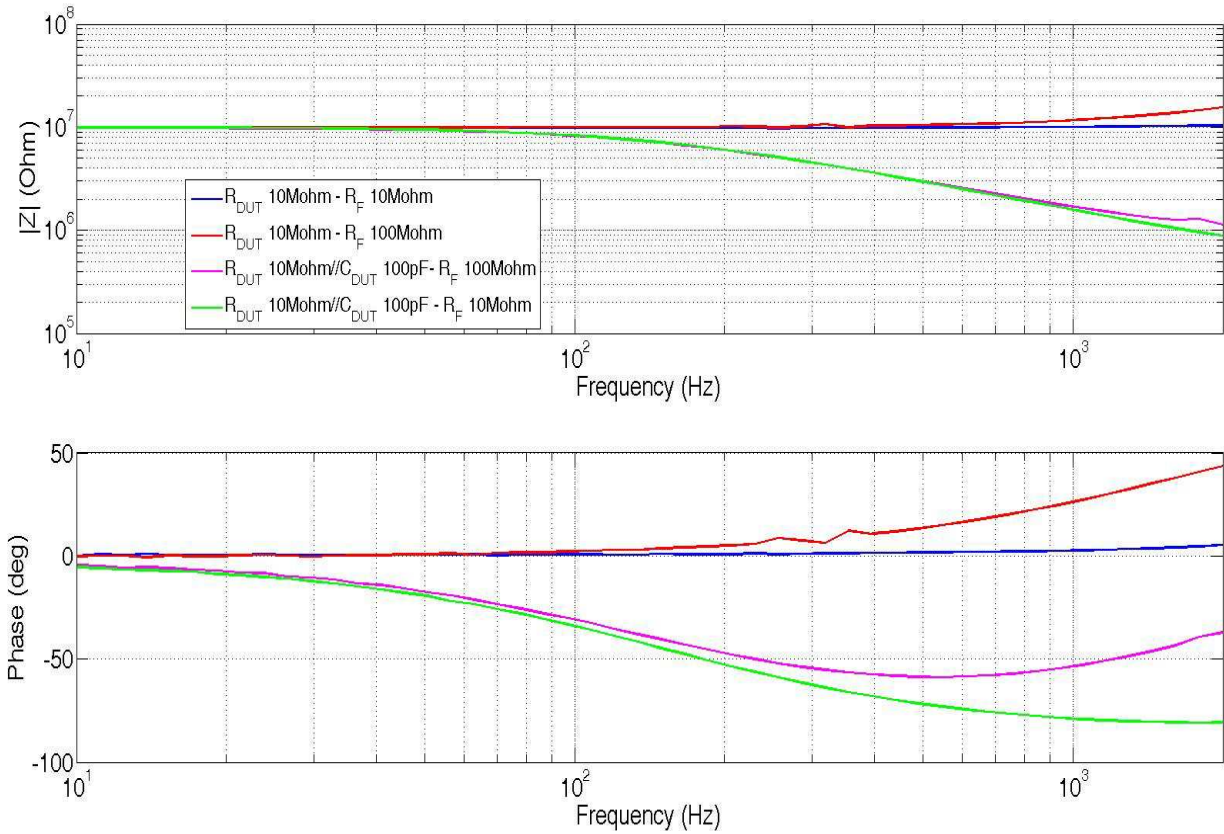
Figure 3.12 – Bode plots obtained using a 10 MΩ Resistor (blue and red lines) and an RC parallel circuit (green and magenta lines) DUT selecting two different measurements ranges, respectively using the 10 MΩ and 100 MΩ feedback resistors.

In particular, in order to quantify how much these shifts badly affect the accuracy of the system, the entire spectra were fitted with Zview software using the RC electrical circuit model to estimate the real components values. Results can be seen in Table 3.5, where the fitting error is directly calculated by ZView software, while accuracy error is calculated by:

$$Accuracy\ Error(\%) = \left| \frac{actual\ value - fitted\ value}{actual\ value} \right| \cdot 100 \qquad (3.22)$$

Table 3.5: Fitting results of RC (10 MΩ-100 pF) parallel circuit DUT with different transimpedance values.

	R_f=10 MΩ		R_f=100 MΩ	
	R_{DUT}	C_{DUT}	R_{DUT}	C_{DUT}
Fitting Error	0.6%	0.6%	3.7%	4.6%
Accuracy Error	1%	1.1%	17%	13.5%

To eliminate this unwanted behaviour of the system in a low cost and simple way, from the hardware point of view, the idea was to compensate these shifts in the digital domain, first only in post-processing and then directly implementing the method in the Labview interface.

The method consists in acquiring, for each preamplifier feedback resistor, the shifts given by parasitics using a calibration frequency sweep acquisiton of a precision resistor, which has a theoretical constant value of phase ($\varphi=0$) and a constant impedance magnitude ($|Z|=R_{cal}$, value of the calibration resistance used and before measured).

Then the obtained values for all the considered frequencies are used to compensate both the impedance magnitude and phase spectra of DUTs by subtracting the phase shift to the experimental acquisitions and by considering that the magnitude error at every certain frequency increases proportionally, thus calculating for each frequency the "overestimation ratio"$=\dfrac{|Z|_{cal}}{R_{cal}}$, where $|Z|_{cal}$ is the impedance magnitude obtained in the calibration frequency sweep.

The method was first implemented in a Matlab function wich has as input the experimental acquisiton, the calibration acquisition and the specific calibration resistance used for the calibration and as output the compensated experimental acquisistion.

This function calculates the compensated phase shift (φ_{comp}) and magnitude ($|Z|_{comp}$) respectively by subtracting the phase shift of the calibration acquisition from the input experimental acquisition and dividing, for each frequency, the experimental values by the "overestimation ratio".

Finally the values of $\Re e\{Z\}_{comp} = |Z|_{comp} \cdot \cos(\varphi_{comp})$ and $\Im m\{Z\}_{comp} = |Z|_{comp} \cdot \sin(\varphi_{comp})$ are calculated for every frequency and a file readable by ZView software is created as output.

To prove its effectiveness, the implemented method is applied to the previously presented experimental acquisition, in which 100 MΩ feedback resistor and an RC (10 MΩ-100pF) parallel circuit were used (magenta line of Figure 3.12).

As can be seen in Figure 3.13, a significant improvement is achieved and the values obtained after the compensation (blue line) are in well agreement with the values obtained using the lower feedback resistance of 10 MΩ (green line), which is much less affected by parasitic capacitances.
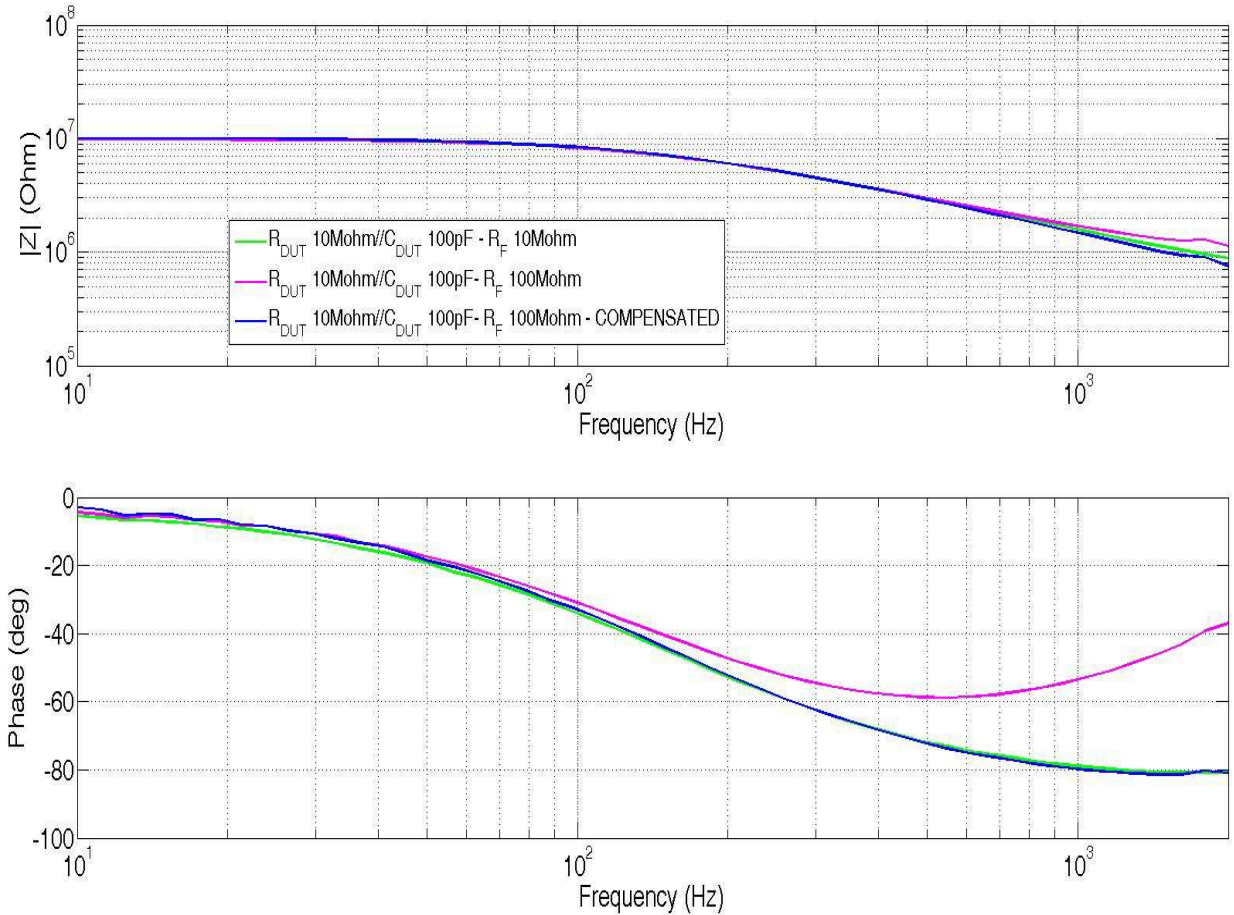
Figure 3.13 – Bode plots demonstrating the effectiveness of the implemented compensation method. Green and magenta lines are respectively obtained using the 10 MΩ and 100 MΩ feedback resistors and the RC parallel circuit DUT, as in Figure 3.12, while the blue line is obtained by the magenta data after the compensation method.

As done before, in order to quantify the improvements, the data were fitted to calculate the measurement accuracy after compensation. Data reported in Table 3.6 confirm the qualitative analysis demonstrating a good improvement in the accuracy of estimation of the real components values from the fitting of the spectrum.

Table 3.6: Fitting results of RC (10 MΩ-100 pF) parallel circuit DUT, using 100 MΩ feedback resistor, before and after the compensation.

R_F=100 MΩ	BEFORE COMPENSATION		AFTER COMPENSATION	
	R_{DUT}	C_{DUT}	R_{DUT}	C_{DUT}
Fitting Error	3.7%	4.6%	0.4%	0.4%
Accuracy Error	17%	13.5%	2%	2%

Similarly the method is applied to the most challenging transimpedance of 1 GΩ using once again an RC parallel circuit as DUT with R=100MΩ and C=100pF.

Experimental acquisition and data fitting accuracy are shown below respectively in Figure 3.14 and Table 3.7.
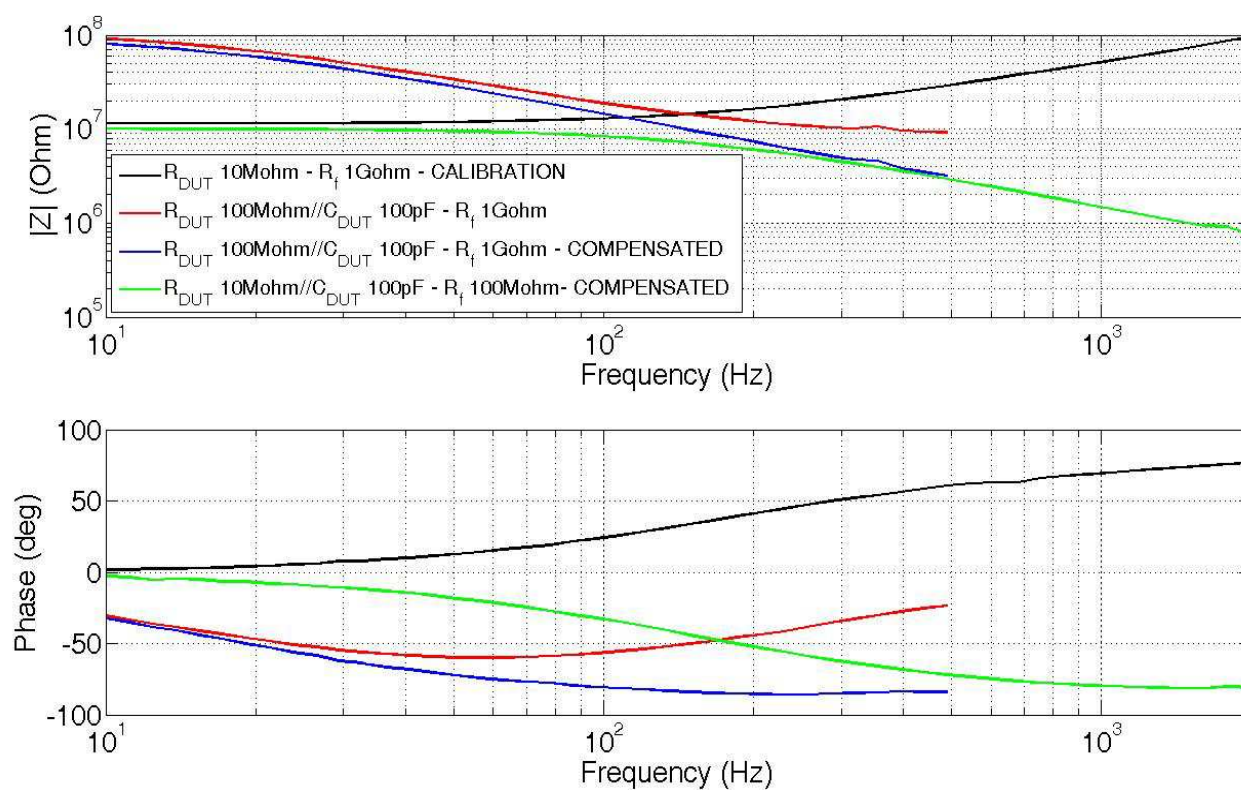
Figure 3.14 – Bode plots demonstrating good improvements of results using the compensation method also for the most challenging feedback resistor of 1GΩ. The blue line is the final result, obtained from the acquired red line, using the black one as calibration curve. Green line is reported for comparison and is obtained using a different DUT and the 100 MΩ feedback resistors after compensation, as in Figure 3.13.

Table 3.7: Fitting results of RC (100 MΩ-100 pF) parallel circuit DUT, using 1 GΩ feedback resistor, before and after the compensation.

R_f=1 GΩ	BEFORE COMPENSATION		AFTER COMPENSATION	
	R_{DUT}	C_{DUT}	R_{DUT}	C_{DUT}
Fitting Error	10.7%	9.6%	0.9%	0.4%
Accuracy Error	41%	32.3%	3.5%	4%

As already mentioned the compensation method was then implemented in the Labview interface in order to have a real time phase and magnitude shift compensation for every single frequency. Calibration data were stored and loaded from the software interface upon request and the calibration procedure for the selected working frequency is automatically performed in real-time.

3.5.1   Comparisons   with   commercial   Impedance Analyzer

As a final test, a comparison between the developed Nanowires Acquisition board interface and a specific commercial laboratory instrument such as Novocontrol Alpha-A Impedance analyser [125], using the "impedance spectroscopy mode" of the system and performing 50 points frequency scans in the range 10 Hz-2 KHz on different parallel RC test circuits, was performed.

Figure 3.15 shows the results obtained using two different RC parallel circuits, precisely using R=998 KΩ, C=1,022nF and R=10.19 MΩ, C=99pF (independently measured using Agilent 34401A high precision digital multimeter), and analysed with ZView software.

As can be seen the response of the commercial system seems noisier considering the higher impedance DUT; this can be explained considering that the Novocontrol impedance analyser is based on the frequency response analysis (FRA) method [125], [126], which ensure a very fast and broadband analysis at the cost of a limited noise removal as reported in [126], while in the developed system (based on the lock-in technique) each frequency point is obtained mediating (by the LabView software interface) the real time AC measurements of a selected number of acquired samples (usually 200 samples), thus reducing the final effective bandwidth of about ten times and thus strongly reducing the external noise at the cost of a slower acquisition.

Data fitting (see Table 3.8 and equation (3.22)) shows that the system demonstrates a fair accuracy, which is sufficient for many impedance biosensors applications [5], [127], [128], considering the much lower price and smaller sizes of the developed system in comparison with commercial instruments currently used for impedance spectroscopy and considering the system capability to perform real time AC measurements, feature offered only by a few commercial apparatuses.
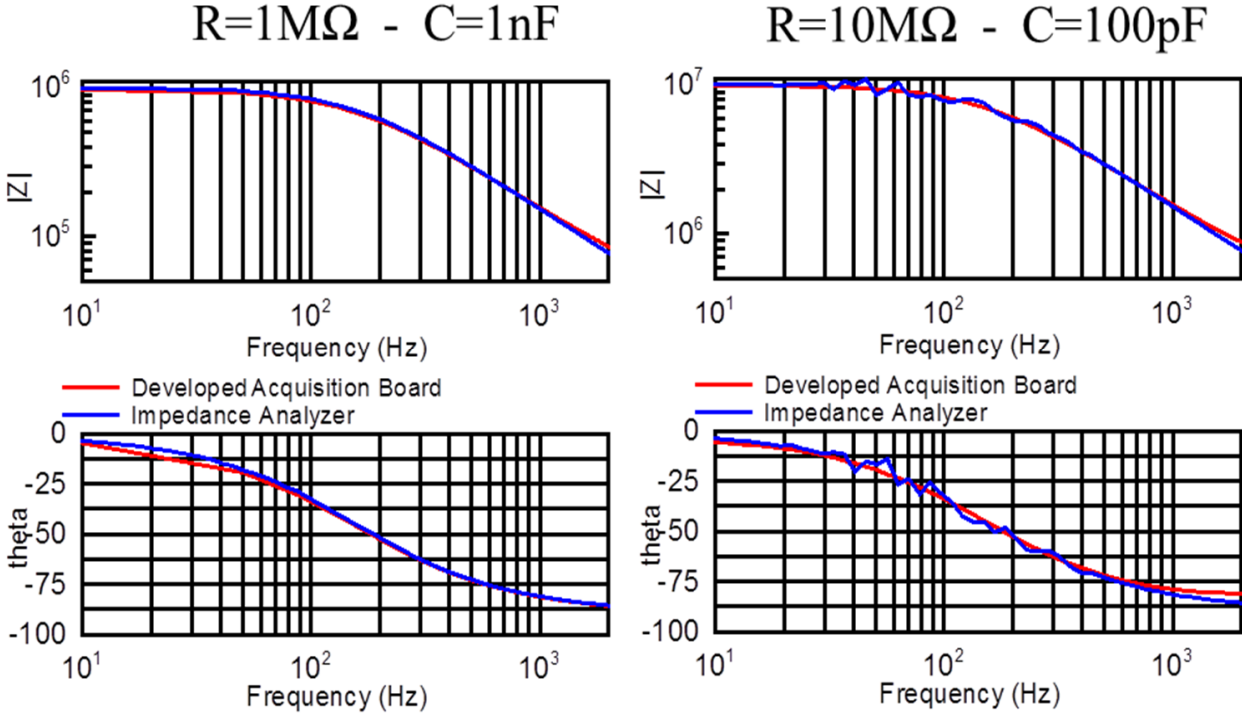
Figure 3.15 - Bode plots comparison obtained using the developed system interface and the commercial Novocontrol Alpha-A Impedance analyzer with two different parallel RC test circuits.

Table 3.8: Comparative fitting results of two different RC parallel circuits DUT, measured with the developed nanowires acquisition board and with a commercial impedance analyzer.

		R=998 KΩ - C=1,022nF			R=10.19 MΩ - C=99pF			
		Nanowires Acquisition Board		Alpha-A Impedance Analyzer		Nanowires Acquisition Board		Alpha-A Impedance Analyzer	
	R	C	R	C	R	C	R	C
Fitting error	0.5%	0.5%	0.06%	0.06%	0.6%	0.6%	0.8%	0.8%
Accuracy Error	0.6%	0.5%	0.04%	0.1%	1%	1.1%	0.04%	4.3%

3.6   Experiments on Si Nanowires sensors

The system was then interfaced with different NW chips tests by means of the design of the specific PCB plug interfaces, hosting the NW chip and eventually the microfluidics for each particular experimental need, pluggable in the proper designed socket of 4x4 cm.

In particular the interface for different NW chip provided by a partner research institute, the University of Southampton (UK), is presented below. It is a two layers PCB which has the aim to connect and physically hold the specific nanowires array chip to the readout system and was realized in an internal university facility, the LPKF Protomat micromilling machine, as well as the other plastic (delrin, polycarbonate) mechanical parts.

3.6.1   University of Southampton Nanowires chip

Nanowires (14.8 x 14.8 mm) chip provided by nano-research group of University of Southampton contains 8 different sets of p-type top-down fabricated nanowires (see Figure 3.16). These devices were fabricated using a very low cost nano fabrication process based on simple photolithography, thin film technology and a dry spacer etch technique suitable for low cost mass production [73].

The four outer sets have the same dimensions (sensing window length 40 µm and rectangular cross section of nominal 100nm x 100nm) and have the same number of nanowires in parallel (30) in all chips, while the center sets are variable from chip to chip in length (10 µm to 50 µm long) and number of nanowires in parallel (10 to 320) in order to perform conductivity tests and evaluate the best nanowire configurations.
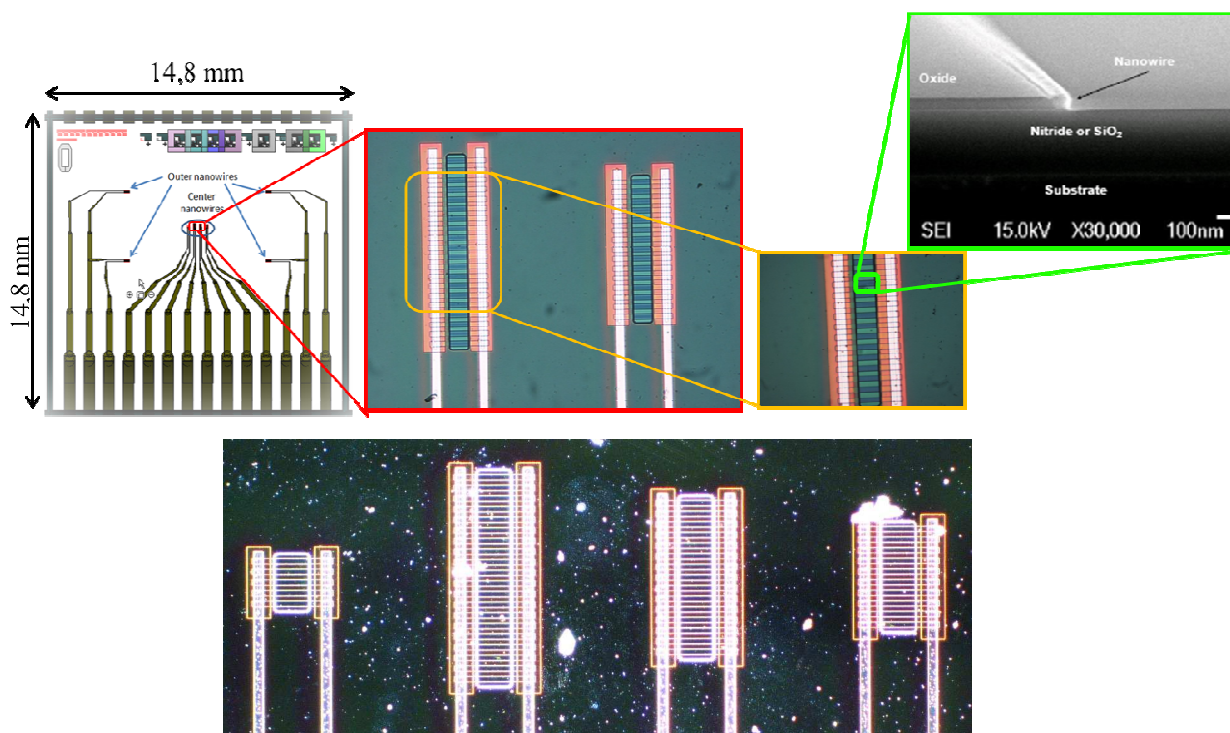
Figure 3.16 - University of Southampton Nanowires chip layout. The green-edged zoom shows a cross sectional detailed SEM pictures of a single nanowire and the dark field picture highlight the sensing region and nanowires edges.

Figure 3.18a shows the cross section of the device that is composed of the silicon substrate on which it is deposited by plasma enhanced chemical vapour deposition (PECVD) a 750 nm oxide layer followed by a 300 nm silicon nitride layer. Then oxide pillars are created (again by PECVD) and patterned using 3 μm photolithography and anisotropic etching. On these pillars a 100 nm amorphous silicon (α-Si) film is deposited by low pressure chemical vapor deposited (LPCVD) at 560°C and then doped by boron implantati on at a dose of $1 \times 10^{18}/cm^2$ and an energy of 25 keV. Rectangular-shaped nanowires are formed using a special anisotropic dry etch process performed using an Oxford Instruments Plasma Technology 80+ reactive ion etcher (RIE) system at 160 W input power, with a SF6 flow of 12 sccm, an O2 flow of 12 sccm and a pressure of 30 mT. A sketch of the main phases of the fabrication process is represented in Figure 3.17.
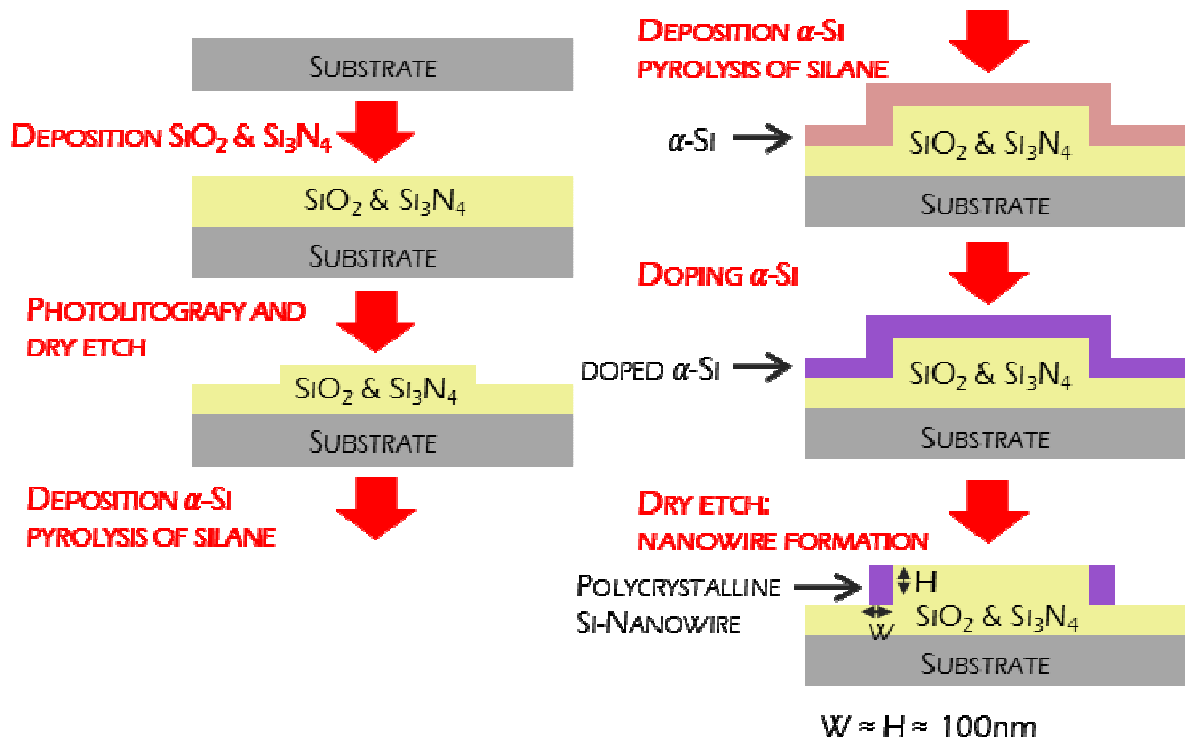
Figure 3.17 – Sketch of the nanowires top-down fabrication process.

At the end of the process, to create a stable surface for nanowire sensing, to crystallize the amorphous silicon to polycrystalline silicon and to activate the implanted dopant, a nominally 10 nm gate oxide was grown at 900 ℃. Finally, alumini um contacts at both end of the polysilicon nanowire were made by the creation of a heavily doped (with a dose of $1 \times 10^{21}/cm^2$) source/drain pad region, highlighted in red in Figure 3.18b. The figure also shows (in green) the sensing window over the nanowire which is the only exposed region, while the rest of the all regions are covered with 1 µm thick layer of S1813 photoresist.

Similarly, metal pads closed to the lower scribe lines (see Figure 3.16) also have exposed metal for measurements and are designed with a pitch of 1 mm to be compatible with standard commercial connectors (Samtec SEI series [129]). This feature allowed designing a PCB plug interface enabling the simple connection between the chip and the readout board, without the need of wire bonding and assuring the possibility to reuse the designed plug interface for different NW chips.
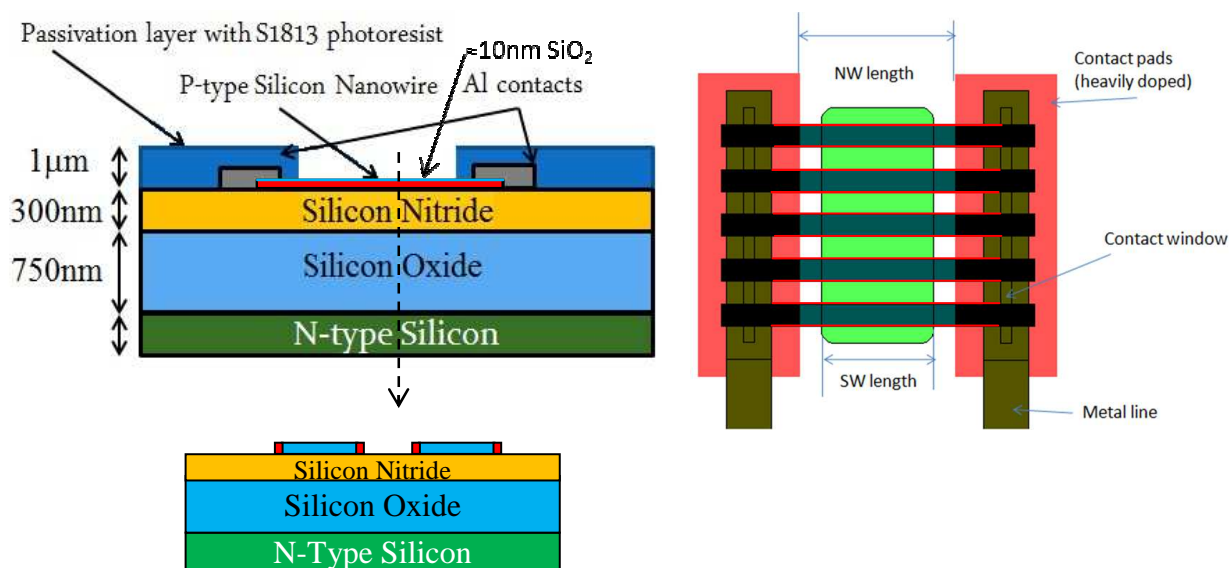
Figure 3.18 – Cross section and top view of the University of Southampton nanowires chip.

3.6.2 Design and realization of university of Southampton specific PCB plug interface

According to the possibility to use the commercial Samtec connector, a "sandwich approach", enabling the easy removal and connection of the NW chip, was used to design the plug interface (see Figure 3.19). It is composed mainly of four parts:

- the base, which perfectly hosts the NW chip and, underneath it, a small piece of aluminium foil to create a constant potential plate and ensure the back-gate contact. The proper cavity dimensions allow an automatic alignment of the metal pads of the NW chips (see Figure 3.16) with the connector.

- the windowed two-layers PCB, which hosts Samtec SEI connector [129], a Mill Max spring connector [130] and two 4-way SMD switches These three elements are used respectively to connect inbound and outbound signals from the NW chip to the dedicated socket connector pins (see Figure 3.4), to assure the bulk contact connecting the aluminium foil in the base to the and to address the V_{ref} signal coming from the acquisition board to the selected Silicon NWs under test;

- the rectangular PDMS microfluidics gasket (see below), which can be designed and moulded as required by the specific application or test (e.g. with or without microchannels for solution flow) and ensure a tight seal between the sensitive NW chip surface and the bottom layer of the PCB avoiding electrolyte leakage;

- the lid, which is used to package the microfluidic gasket as well as the whole device by means of four screws, screwed in the threaded holes at the four corners.
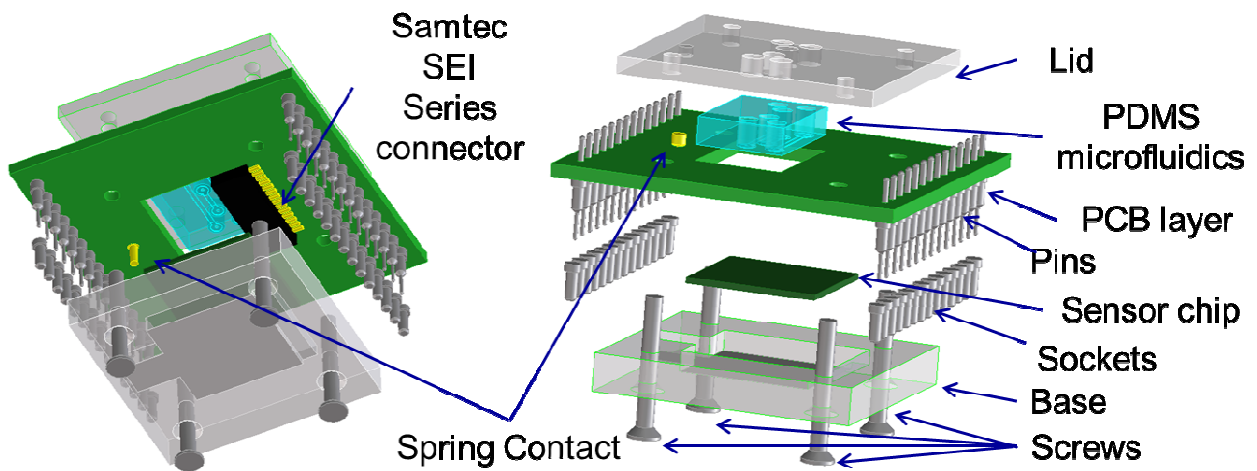
Figure 3.19 - : Design drawings of the Southampton chip specific plug interface highlighting the different components stacked in a "sandwich approach".

Figure 3.20 shows some pictures of the realized modular PCB plug interface; disassembled, after the clamping of the NWs chip and assembled in the nanowires acquisition board.
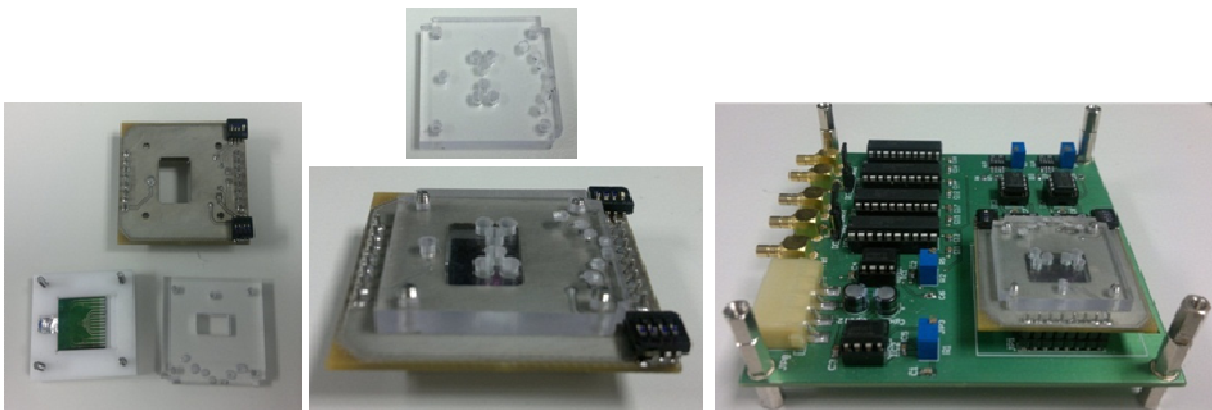
Figure 3.20 - : Pictures of the realized plug interface specific for the university of Southampton nanowires chips.

As an example, in order to meet experimental needs, in particular to facilitate the repeatability of alignments between the microfluidic gaskets and the NW chip, a PDMS mould (Figure 3.21) was designed and realized using the Objet Connex350 3D Printer of University of Southampton. It presents an array of 4 x 4 identical (rectangular 15x10 mm) features each containing five pillars of 2.5 mm of diameter for the creation of five independents microfluidic

chambers (each with a volume of ~10μl) aligned with the different NWs sets of the NW chip (see Figure 3.16), in which test solutions can be directly injected.

To create the microfluidic PDMS gasket, the PDMS Sylgard 184 (Dow Corning, mixture 10:1 [131]) was placed in a vacuum chamber to outgas for 15 minutes; then the mix was directly poured in the mould and baked for 2 hours at 75℃ in oven. Once removed the array of gaskets was peeled out from the mould and single gaskets are created by cutting using a scalpel along the moulded lines.
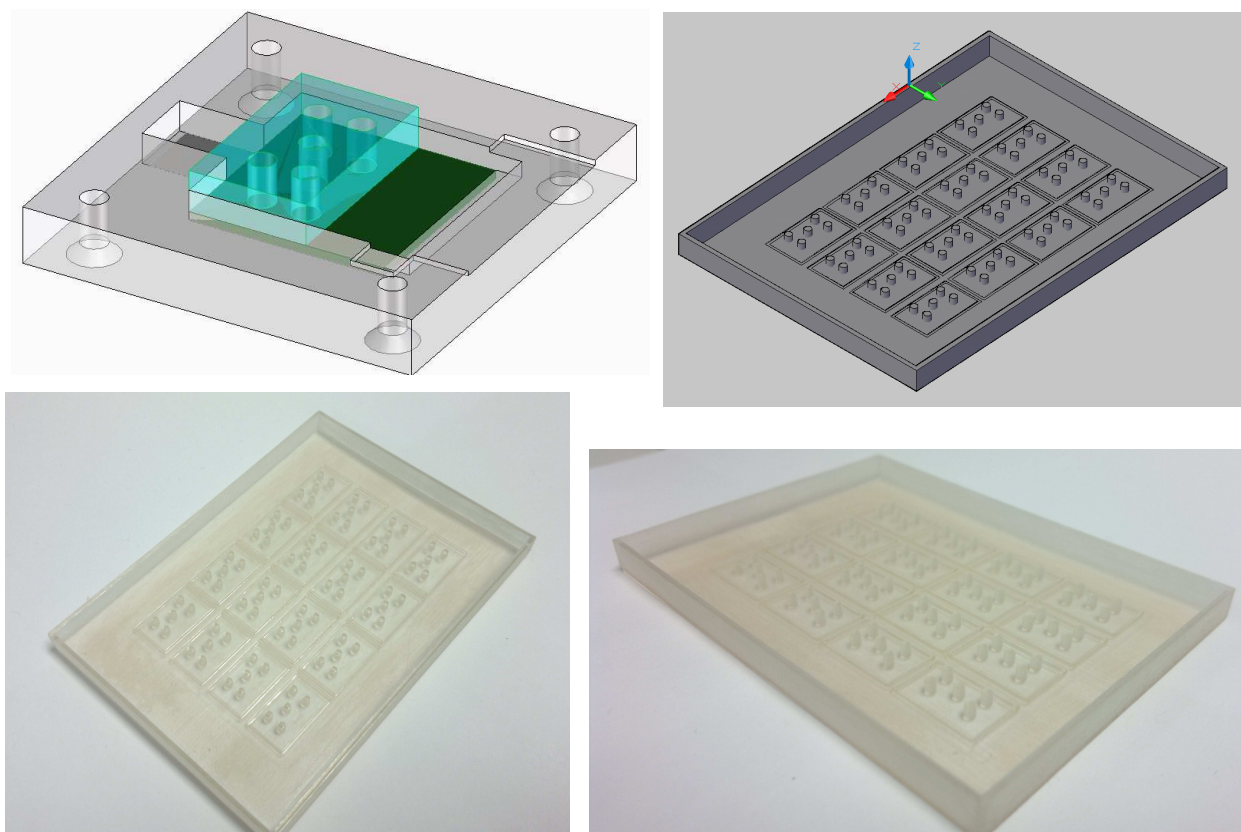
Figure 3.21 - PDMS mould for microfluidic chambers design and pictures.

3.7   Preliminary tests on nanowire chips

Once calibrated the system using tests on synthetic DUT, preliminary tests on nanowire chips were performed in order to characterize nanowires sensors using the developed system and to effectively prove the effective accuracy of the whole system with the PCB plug interface.

In particular automatic I_{sd}/V_{sd} (DC) at different back-gate potentials and I_{sd}/V_g (DC) characterization in air and buffer were performed, as previously reported [73].

Indeed, even if the research group of university of Southampton had already characterized and studied the first batch fabrication in a previous work [73], using a standard bulky laboratory readout setup, a new devices batch was fabricated during the last year and it was characterized and studied using the developed nanowires acquisition board.

In order to improve nanowires performance, this new nanowires batch was fabricated with the fabrication process and characteristics reported above in section 3.6.1. In particular some modifications were done to the first batch reported in [73]. These are an higher doping rate resulting in a higher conductivity and threshold voltage of the nanowires and a thicker insulating layer between the nanowires and the silicon substrate, in order to achieve a better temporal stability, since the experiments performed in previous work were affected by a systematic drift, as reported in supplementary information of [73], probably caused by the creation of pinholes in the insulating layer .

3.7.1   Comparison   with   standard   electrical characterization setup and nanowires characterization

Figure 3.22 shows, as proof of concept, the I_{sd}/V_{sd} characteristic of one chip sample for two different back-gate (V_g) potentials of 0 and -5 V measured in air using a standard probe station-based setup (in particular the Cascade R32 REL3200 Probe Station associated with a Agilent 4155C) and the developed Nanowires Acquisition Board. Consistent results and good accuracy of the developed system demonstrated the possibility to substitute the previously used bulky probe station with the presented developed compact system.

The I_{sd}/V_{sd} characteristics also show, as expected, a higher conductivity of the new batch nanowires chip and a very linear response even for low absolute values of back gate potential unlike Hakim's first results, where I_{sd}/V_{sd} characteristics presented a nonlinear response, probably given by Schottky barriers at the metal contacts-silicon NW junction [73].
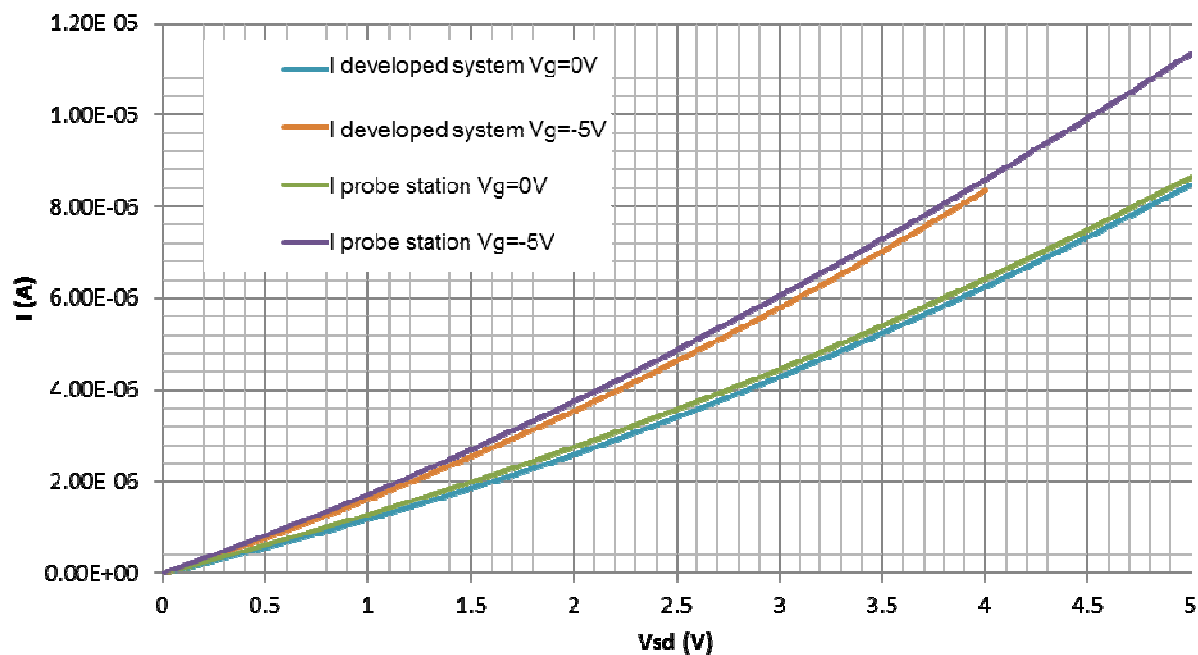
Figure 3.22 - I_{sd}/V_{sd} output characteristic of a representative nanowires chip for two different back-gate voltages acquired using a standard probe station setup and the developed system.

Nanowires DC characterizations were then performed using the developed nanowires acquisition board. In particular the transfer characteristic of I_{sd} as a function of the back-gate potential V_g for different V_{sd} values.
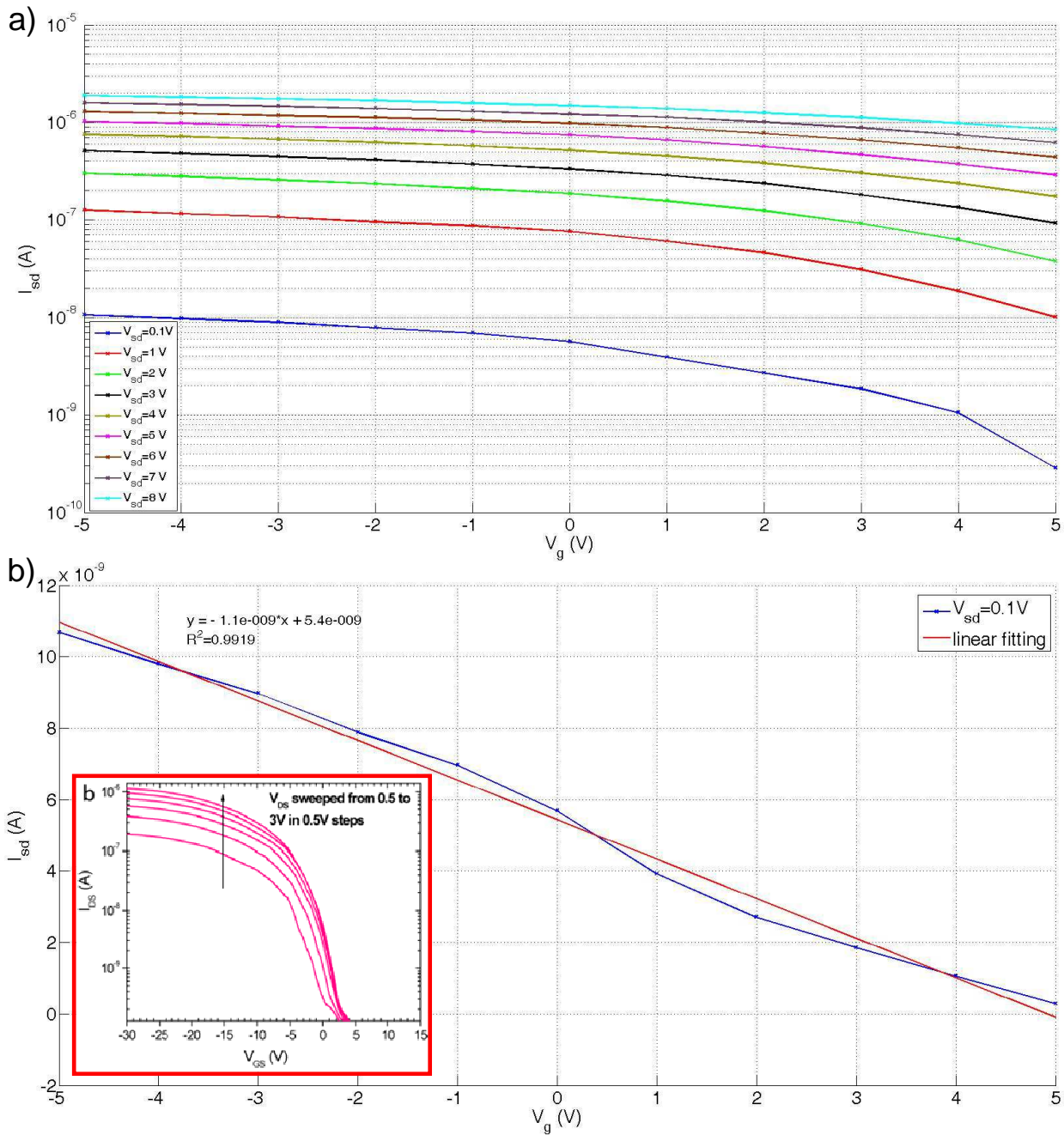
Figure 3.23 – a) I_{sd}/V_g transfer characteristic of a representative nanowires chip for different source-drain potentials as a function of V_g. b) Magnification of the low V_{sd} voltage condition as the one usually used in the experiments and relative linear fitting, in this representative case the $g_{m=}\Delta I_{sd}/\Delta V_g$ results 1.1nS. The inset shows a representative transfer characteristic of the first nanowires batch reported in [78].

The electrical characterization demonstrates that the provided nanowires have a positive backgate threshold voltage, as previously reported [73]. This means that the conduction (holes carriers) channel is conductive also for V_g=0V since it is physically implanted in the device.

The higher doping dose used in this nanowires batch resulted in an shift of the threshold voltage towards more positive values (outside the range of measurements of Figure 3.23 and

higher than the one reported in [73], which fell in the 0 - 5V range, as shown in the inset of Figure 3.23).

Moreover, as expected, the higher doping dose used in this nanowires batch resulted in a quite high transconductance value, given by the slope of the linear transfer characteristic:

$$g_m = \left.\frac{\Delta I_{ds}}{\Delta V_g}\right|_{V_{ds}}$$

(3.23)

For instance, in the case reported in the figure (V_{sd}=0.1V, the typically used range of applied voltage) results in a transconductance value g_m of 1.1nS

Usually the experiments were performed setting the back gate voltage at ground, in order to work in the linear regime using a low V_{sd}, the while the effects of the liquid gating on nanowires response were studied and described below.

The well-known general expressions for the MOSFET in linear accumulation regime for small V_{ds} (for p-type devices the condition (3.24) is valid) can be also used for an ISFET and therefore for a nanowire.

$$V_{ds} > V_{gs} - V_{th}$$

(3.24)

$$I_{ds} = \mu C_{OX} \frac{W}{L}\left(V_{gs} - V_{th}\right)V_{ds}$$

(3.25)

with C_{OX} is the oxide capacity per unit area, W and L the width and the length of the channel, respectively, and μ is the holes mobility in the channel [132].

3.7.2   Reproducibility after disassembling from plug interface

In order to verify that the developed system contacts and the assembly of the chip into the designed plug interface do not affect the measurements, the reproducibility of the results was also tested. In particular real-time measurements on the same chip and at the same condition (V_{sd}=0.5V, V_g=0V), switching progressively between all nanowires sets present in the chip, were performed in different days and after removing the nanowire chip from the plug interface (see Figure 3.19).

Figure 3.24 shows the measurements overlapped, demonstrating the same current levels for all the different nanowire sets, both considering the acquisition done after one day and after the disassembly of the plug interface.
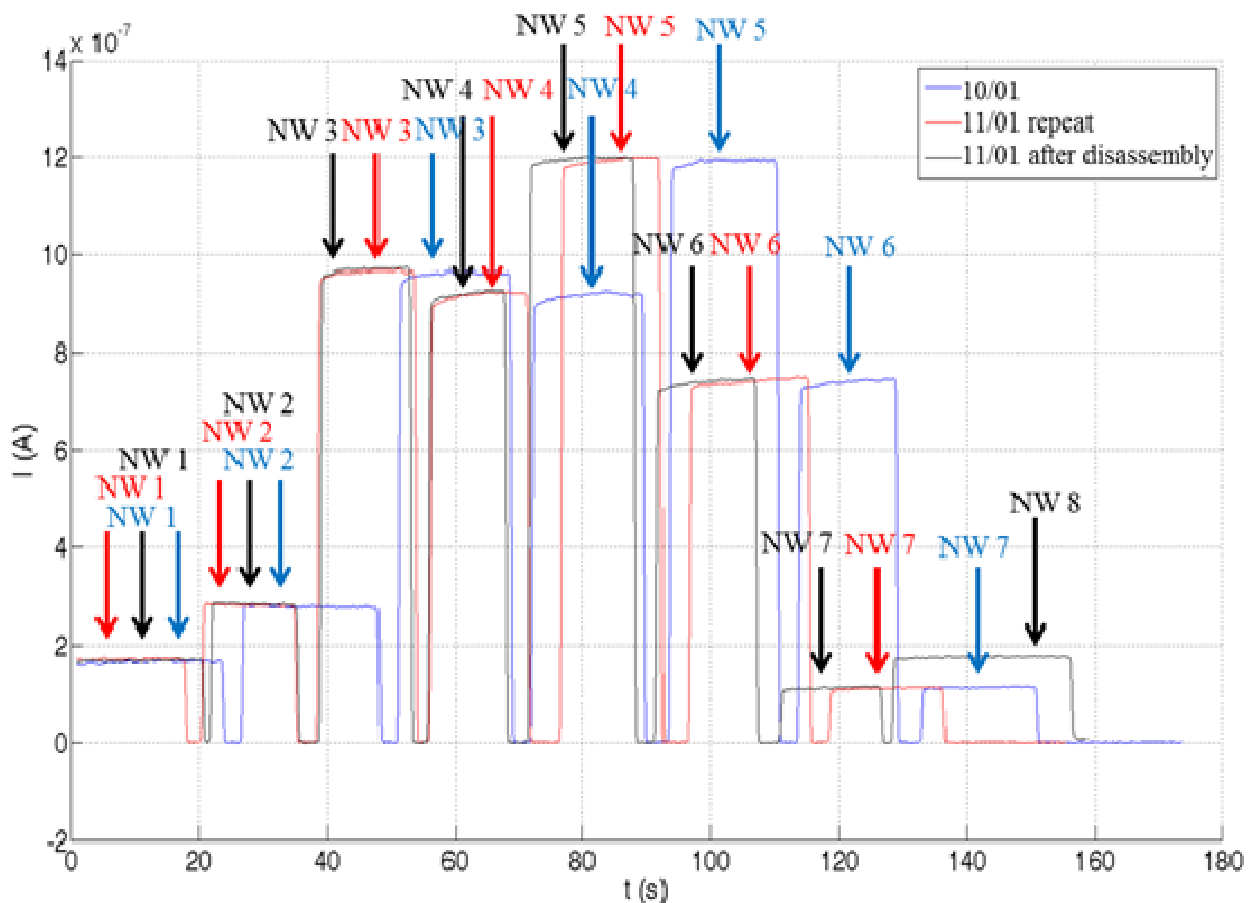
Figure 3.24 - Reproducibility test on the same nanowire chip in different measurement days and after disassembly from the holder.

As can be seen the same current levels, considering the same nanowires set in the chip, are obtained after one day (red) and after disassembling the chip from the plug interface (blue).

3.7.3   Stable measurements in liquid solutions

Since stability in liquid solution is a known issue of NW based sensors [72], [75], temporal stability of new batch of nanowires was tested performing real time DC measurements in phosphate buffer solution 1mM, pH 7 and calculating the slope of the current during a period of some hours.
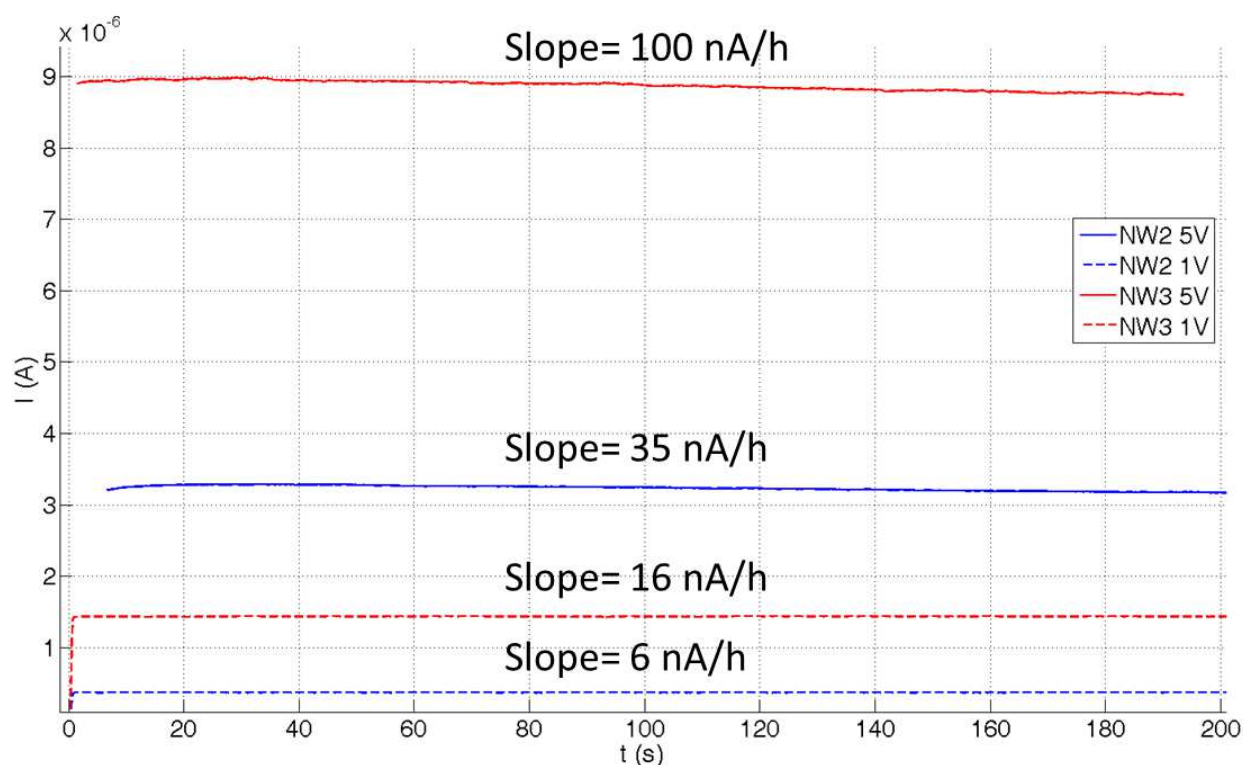
Figure 3.25 - Temporal stability in liquid solution. The legend indicates the nanowire set used and the applied V_{sd} voltage.

Nanowires chips demonstrated a very good stability during the time of the experiment and for different back-gate voltages. It was noticed that higher V_{sd} potentials (and nanowire set conductivity) give a higher current drift, as shown in Figure 3.25; for this reason, during experiments for the detection of different pH solutions and specific target molecules, lower V_{sd} potentials (usually of 0.2 V) were used.

3.8   pH measurements

The concept of the measurement of the proton concentration (pH) of an electrolyte using the surface potential changes of an ISFET is not new and was demonstrated for the first time by Bergveld starting from 1970 [133].

Merging this idea with the fact that silicon nanowires FET can achieve a high sensitivity thanks to their large surface/volume ratio [134], Cui et al. reported for the first time the possibility to use a nanowire as a highly sensitive pH sensor [62].

After that, the measurement of the pH causing the gating of the nanowire FET device is one of the most common tests to prove the nanowire sensitivity [72], [75], [77], [79], [135].

It is based on the property of the modulation of the conductivity by means of different charged groups on nanowire surface. Indeed the Si-oxide layer created on the device acts as a surface site in which the amphoteric silanol groups (Si-OH) can be protonated or deprotonated resulting in a positively or negatively charged surface depending on the pH of the solution and on the isoelectric point (IEP) of the surface, either as:

$$SiOH_2^+ \leftrightarrow SiOH + H^+$$
$$SiOH \leftrightarrow SiO^- + H^+$$

(3.26)

If the pH of the solution is higher than the IEP the surface results deprotonated and acts as adding negative surface charges, increasing the holes carrier concentration and thus increasing the nanowires conductance, while if the pH is lower the situation is the opposite, with an increase of positive surface charges and thus a depletion of carriers in the nanowires resulting in a lower device conductivity.

In particular, covalently linking APTES (3-aminopropyltriethoxysilane) to Si-NW oxide surface results in a surface terminating in both amino (-NH$_2$) and silanol (-SiOH) groups [136], [137], which have different dissociation constants, pKa (respectively of about 9 and 6.8).

As represented in Figure 3.26, at low pH, both the -NH$_2$ groups of the APTES molecules are protonated to -NH$_3^+$ and silanols to -SiOH resulting in a positive gate, which depletes hole carriers in the p-type Si-NW and decreases the conductance. At neutral pH there is an intermediate situation with some protonated and some deprotonated groups resulting in a combined behaviour which results in a progressive linear conductance increase; while at high pH, both the amino and silanol groups are deprotonated, correspondingly causing an high conductivity of the nanowires [62].
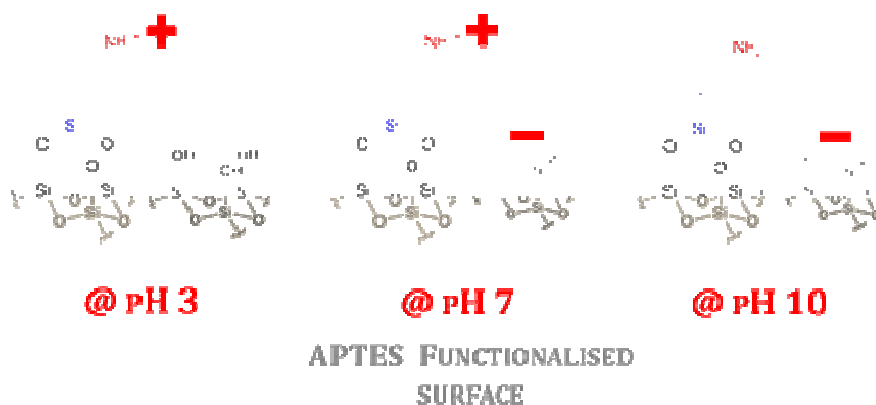
Figure 3.26 - pH detection mechanism with APTES functionalized nanowires.

3.8.1   DC analysis

To test the nanowires behaviour DC and AC real time measurements were performed using the developed system on bare (unmodified, only -SiOH functional groups) Si-NWs and on APTES treated ones. A representative result is shown in Figure 3.27, where a constant Vsd of 500mV was applied and the back-gate and liquid gate contacts were fixed at ground.

Different pH levels (pH 3-10) sodium phosphate buffer solutions at 10mM concentration were used as electrolyte solutions.
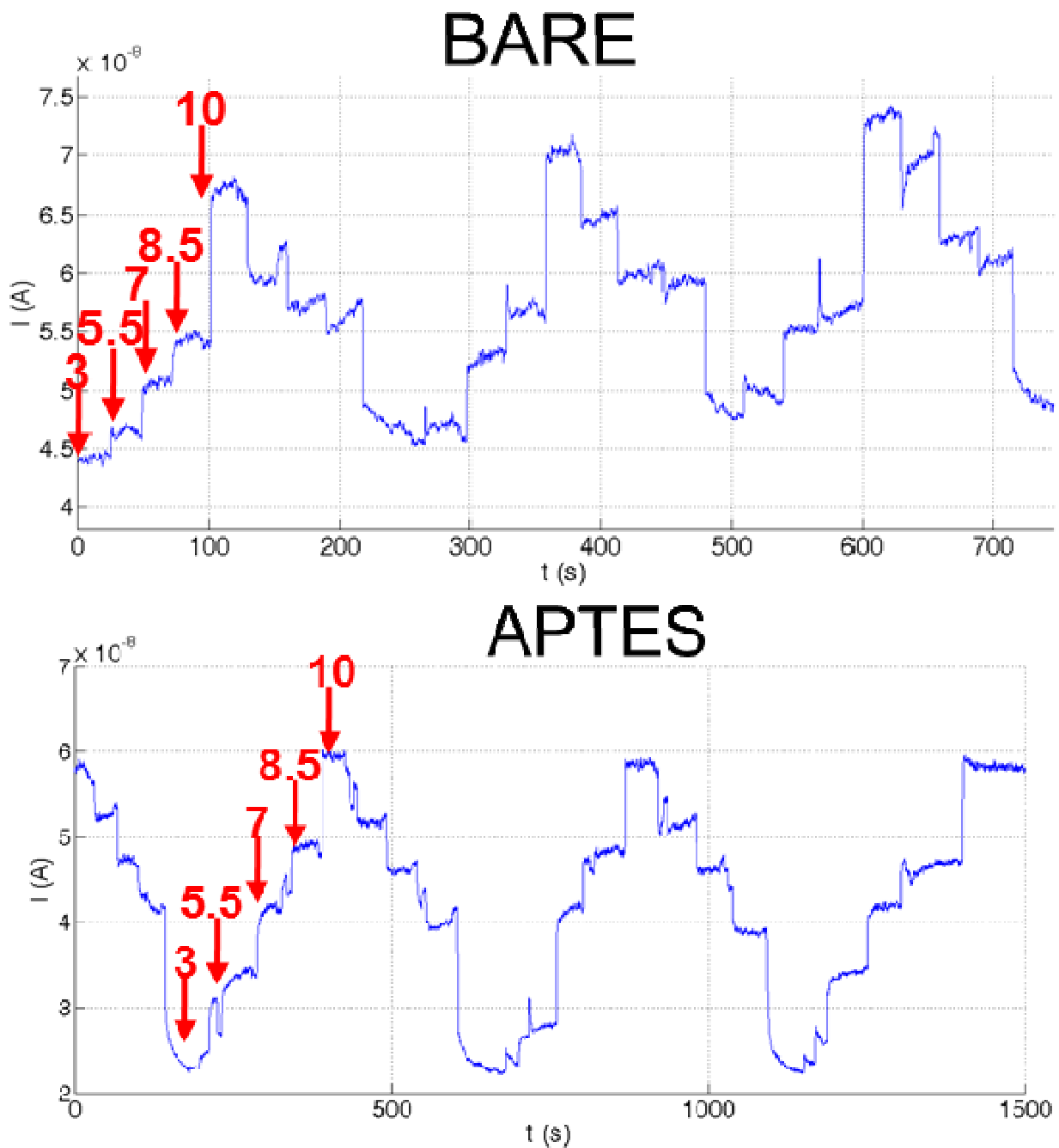
Figure 3.27 - DC real-time current measurements of different pH level buffer solutions, using bare and APTES functionalized nanowires. Arrows show when the solution with the indicated pH level was changed.

As expected and previously reported [62], current measurements on bare NWs show a nonlinear (polynomial) pH dependence; indeed the current change is small at low pH but large at high pH range, while APTES functionalized ones show a linear response. Moreover a good repeatability over time of current levels for different pH level variation cycles was achieved, as can be seen from the reported figures.

Finally, linear fitting the data for APTES treated NWs resulted in a sensitivity ($\Delta G/G$)/(ΔpH) of approximately 22%, with $\Delta pH=7$, almost one order of magnitude better than other data reported for nanowires fabricated using top-down processes [72] (see Figure 3.28).
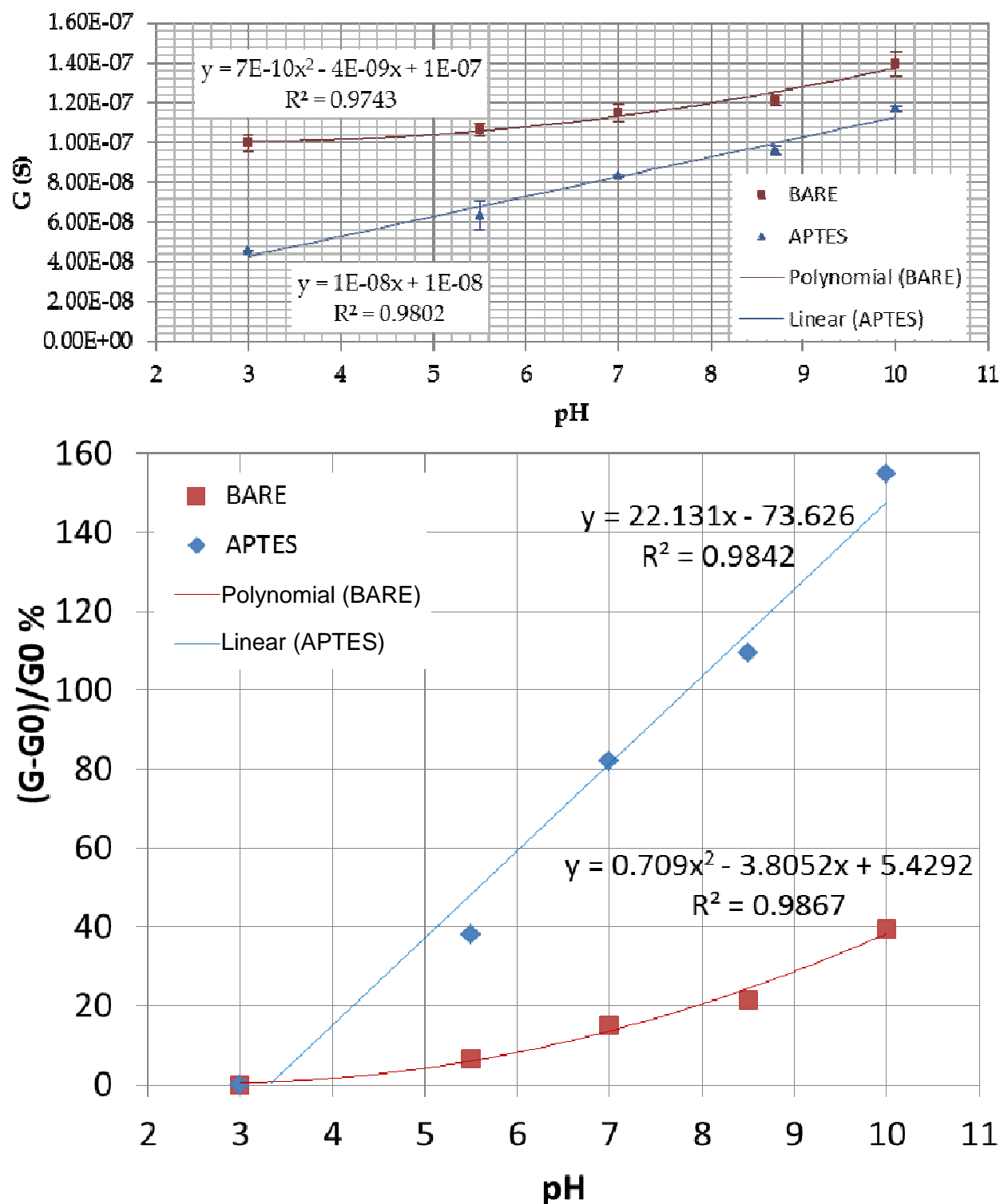
Figure 3.28 – Conductance of bare and APTES functionalized NWs versus pH and relative fitting curves Absolute conductance values (above) shows the decreasing of NW conductance upon APTES functionalization, as explained below in section 3.9

3.8.2   AC analysis

Using the other features of the developed readout system, it was also possible to analyse the response to pH level variations in AC. In particular AC real time measurements on APTES treated NWs using sinusoidal inputs at different frequencies were performed focusing the attention on phase shift data.

Figure 3.29 shows acquired data (admittance magnitude and phase) for different pH level variation cycles using respectively sinusoidal inputs at 100 and 500Hz (V_i=100 mV).

First of all, considering admittance magnitude compared to DC measurements, we can notice a lower noise thanks to the use of the lock-in technique. Data analysis yields a noise of about 400pS rms at a final bandwidth (given by the sampling frequency) of 10Hz considering the DC measurements and 70pS rms at a final bandwidth of 1Hz (given by the selectable FIR cut-off frequency) considering the AC measurements.

Moreover, the data show that depending on the chosen frequency it is possible to detect a signal change related to different pH levels in the phase shift data. This, as reported for instance, can be detected at 500 Hz but not at 100 Hz due to the frequency dependence of the response of the device (see below). Anyway these results allow observing that a specific working frequency can be chosen to increase the sensitivity towards a particular detection range.
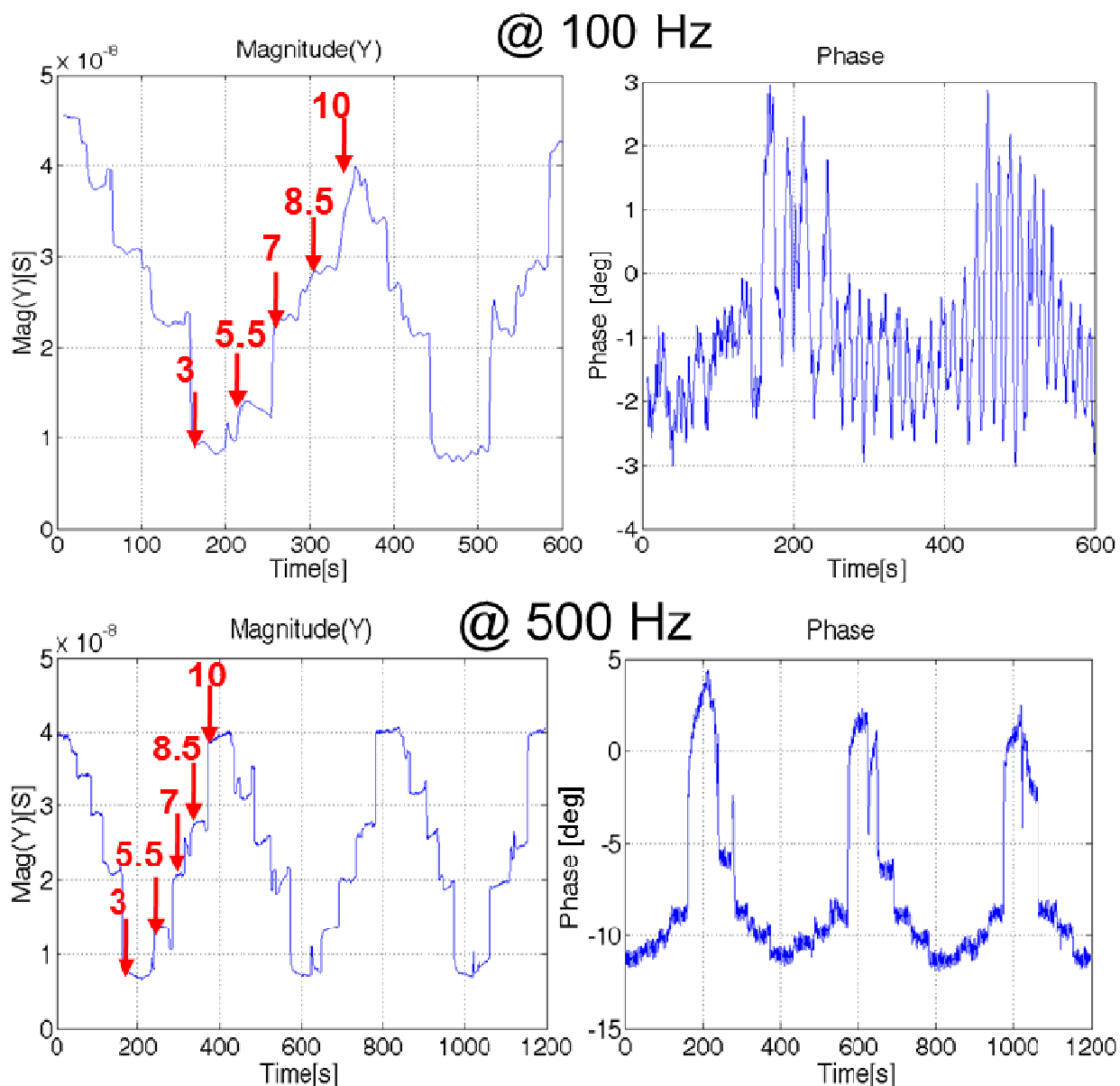
Figure 3.29 - AC real-time measurements of different pH level buffer solutions at two different working frequencies, using APTES functionalized nanowires. Arrows show when the solution with the indicated pH level was inserted in the microfluidic chamber.

To analyze this phenomenon, AC frequency sweeps for impedance characterization in the range 10 Hz- 2 KHz, using the same nanowires set used before in pH 3-7-10 buffer solutions were performed.

As can be seen in Figure 3.30, nanowires immersed in different pH level solutions have different impedance magnitude values (as expected and confirmed by DC measurements) and these differences can be seen in the whole range of frequencies considered; however these differences are reduced at higher frequencies, where the main pole dominates, see below in Chapter 4 for further details. On the contrary, differences on phase levels related to different pH level solutions increase at higher frequencies closer to dominant pole frequency. These

experimental data confirm the possibility to have different and more information on pH levels detection adding the phase shift data to the standardly used nanowires conductivity ones depending on the particular working frequency used and on the position of the dominant pole of the nanowires device. For these reasons an AC frequency sweep characterization can give important indication on the best working frequency in order to get real time phase information on NWs sensitivity and this can be easily performed with the developed system selecting the proper acquisition method from the implemented software interface.
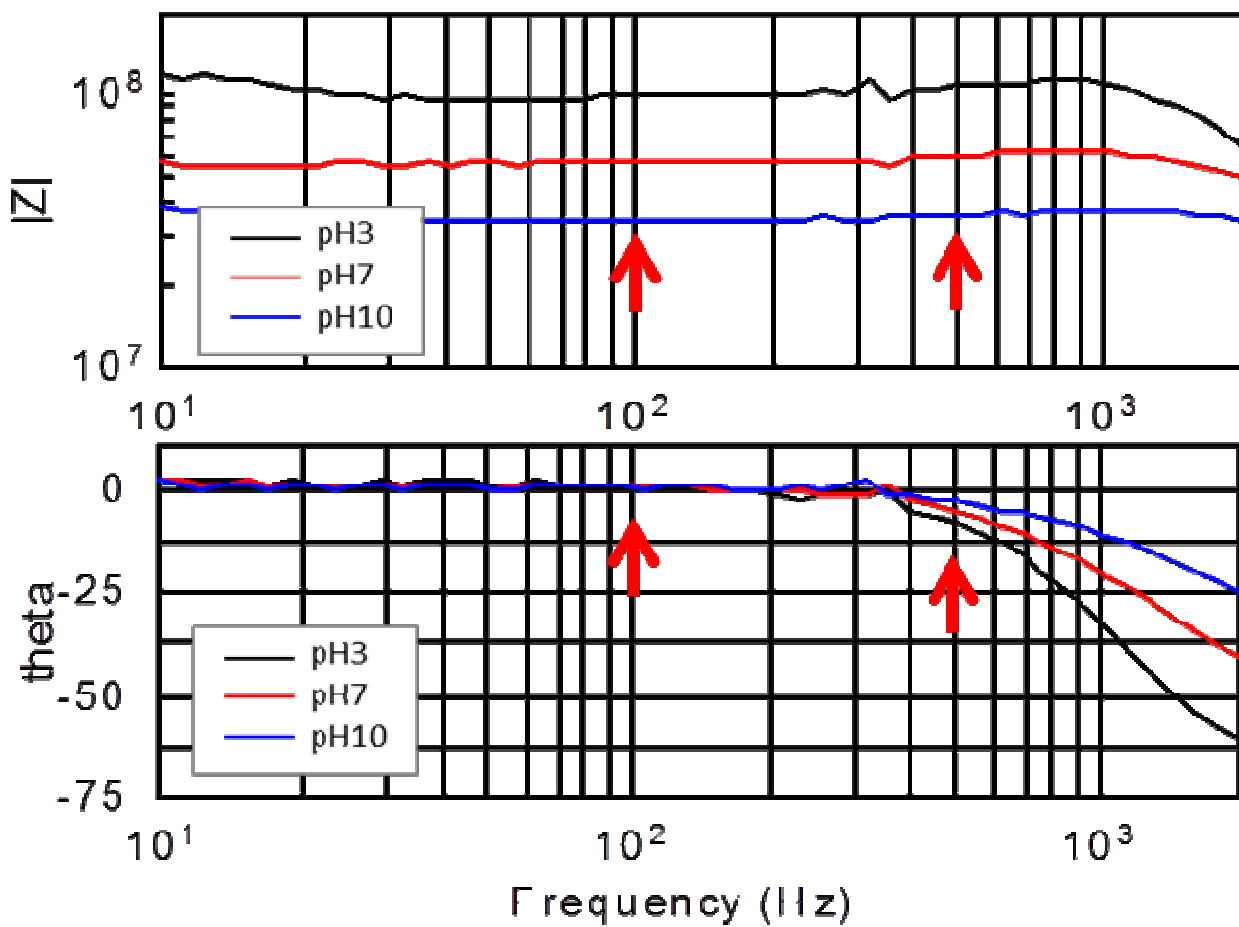
Figure 3.30 - AC frequency characterization of the previously used APTES treated nanowires set, for different pH buffer solutions. In particular, arrows indicate the two working frequencies of the acquisitions reported in Figure 3.29.

3.9   Nanowires functionalization

By attaching antibodies to the nanowire surface, it is possible to properly use these devices as specific biosensors able to detect specific target molecules. In particular one of the aims of our studies was to convert the polysilicon nanowires into sensors for inflammatory biomarkers, such as IL-8 and TNF-α [73].

The functionalization of the nanowire surface was performed in three steps as represented in Figure 3.31:

    1. APTES treatment

The surface was functionalised by a vapour deposition of 3-aminopropyltriethoxysilane (APTES), which is known to give smooth, reproducible films of a monolayer character [138].

Nanowires were cleaned and activated by oxygen plasma and then exposed overnight at 25 ℃ to APTES vapour. To complete the silane cross-po lymerisation the wires were dried at 70℃ for 2 hours. This process enables to create a layer (ideally a self-assembled monolayer, SAM) and to form siloxane bonds between the surface silanols and the APTES resulting in a substitution of some of the surface silanol groups (-OH) by amino groups (-NH2) [136–139].

PH sensing measurements described above where performed after this step.

    2. Succinic Acid treatment

In order to create a linker terminating in a carboxyl group for the creation of peptide bonds with the specific selected antibodies, the nanowire surface was then functionalized with succinic acid. This was done by exposing the nanowires to a solution of N-(3-Dimethylaminopropyl)-N′-ethylcarbodiimide hydrochloride, (EDC-HCl, 100mM, Sigma-Aldrich), N-hydroxysulfosuccinimide sodium salt (Sulfo-NHS, 100mM, Sigma-Aldrich) and succinic acid (1M, Sigma-Aldrich) in phosphate buffer (PBS) with pH 8. After 2 hours at 25 ℃ the nanowires chip was washed with Milli-Q water and dried.

    3. Antibody coupling

Finally the nanowires were functionalised with two different antibodies, anti-TNF-α (from ELISA kit human-TNF-α, Duoset R&D) or anti-IL-8 (ELISA kit human IL-8 CytoSet, Biosource Invitrogen). The antibodies were covalently bound to the nanowires by first activating the surface by exposure to EDC-HCl and Sulfo-NHS for 2 hours at 25 ºC in a phosphate buffer with pH 6. Coupling of the antibodies was achieved by overnight incubation at 4 ºC in a phosphate buffer pH 8.

As experimentally tested and known from literature [64], one of the main problems in specific biosensing lies in excluding unspecific binding or spontaneous surface adsorption of molecules, which results in a change of surface potential and consequently in an undesired charge of nanowires conductance, since it is not related to the concentration of specific target. For this reason, at the end of the functionalization process and before using the device for biosensing, the nanowires were treated for 30 min with 200mM ethanolamine (Sigma-Aldrich) in PBS pH 8.
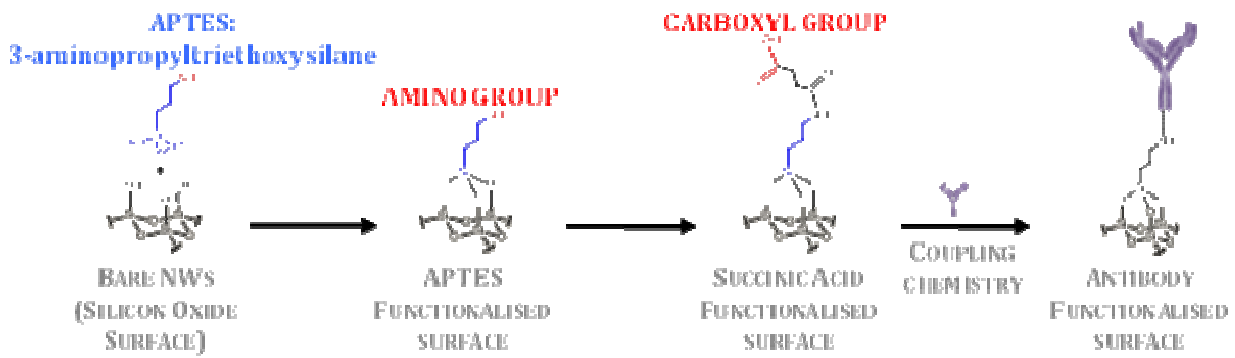
Figure 3.31 – Sketch of the three steps nanowires functionalization. APTES molecules create a layer terminating with amino groups by bonding to the silicon oxide surface. Succinic acid act as a linker terminating in a carboxyl group needed for the final antibody binding.

3.9.1   Functionalization steps control

Thanks to the different dissociation constants (pKa) of the different ending groups, the functionalization process could be controlled and confirmed by electrical DC measurements at a fixed pH 7 buffer solution by the developed board. In particular nanowires conductivity decreases after APTES functionalization due to the amino group (pKa~9) that protonates at pH 7, reducing the local concentration of holes (carriers) in the p-type nanowire. Conversely it increases after succinic acid treatment, since the terminal carboxyl group (pKa~5) deprotonates at pH 7, resulting in a conductance similar to the bare nanowires one as recently reported by Hakim [73] (see Figure 3.32).
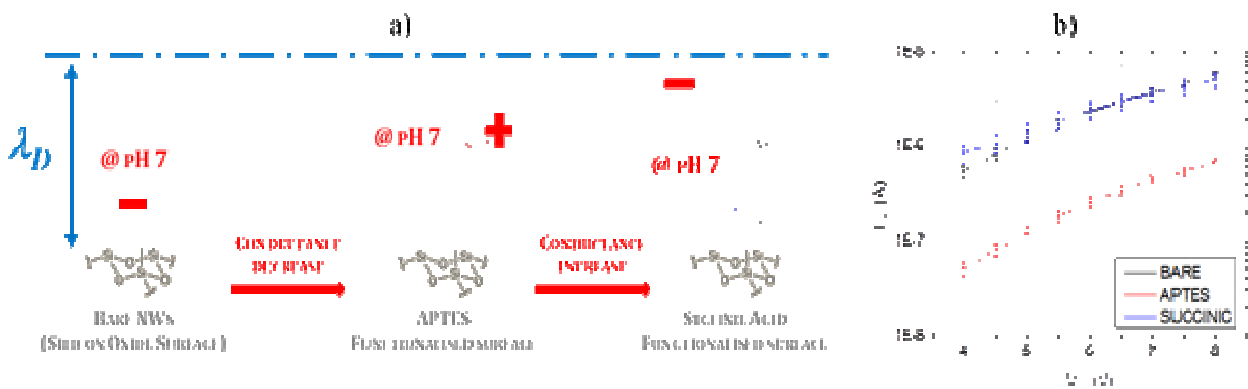
Figure 3.32 - Electrical functionalization steps control. a) Sketch of functionalization steps and relative charged ending groups (in pH 7 solution). b) Nanowire I/V characteristics after different functionalization steps.

Previously obtained DC results were confirmed performing AC frequency sweeps of nanowires immersed in a pH 7 buffer solutions at 1mM concentration using the developed readout system. Figure 3.33 shows admittance magnitude and phase. In particular the

magnitude data are in well agreement with the DC measurements confirming the expected behaviour of the modulation of conductivity in response to changes of isoelectric points of nanowires surface typical of the in the whole range of frequencies considered.

Conversely, phase plot shows unexpected and interesting results since APTES and succinic acid treated nanowires seem to behave in the same manner and differently to bare nanowires, in which no molecular layer is present, suggesting the possibility to have information on the position of different ending groups (that modulate the capacitance on the surface of nanowires) using nanowires impedance phase data. Indeed, considering only admittance magnitude data, bare and succinic acid treated nanowires behave in a very similar manner coherently with the standard nanowires FET principle [11], while, considering also the phase data, it is clearly possible to distinguish between the two different functionalization steps. This result demonstrates the effective possibility to also use phase shift data to obtain more details on the positions of charges compared to the ones obtained considering only DC conductance data.
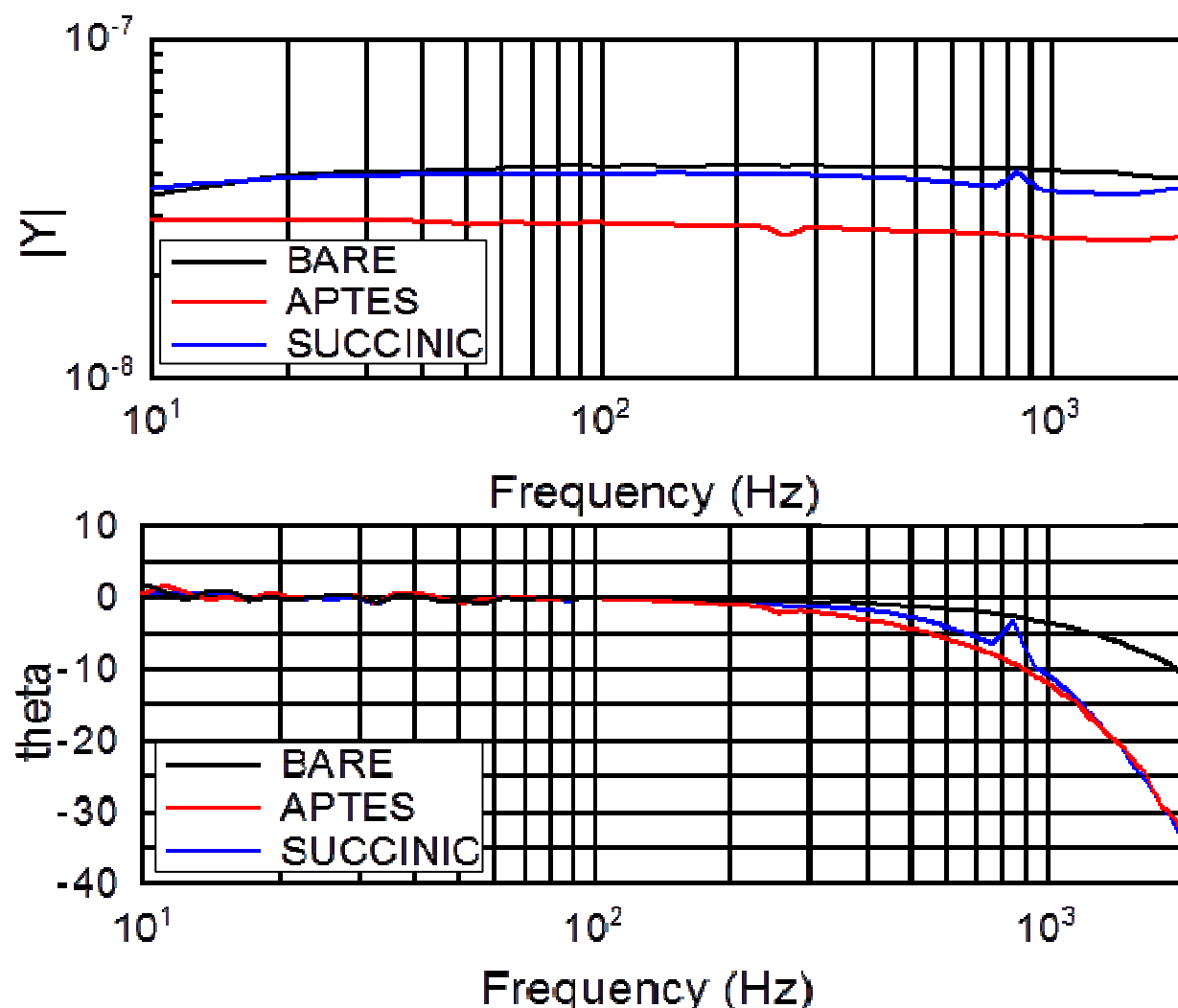
Figure 3.33 - Admittance magnitude and phase versus frequency after different functionalization steps, obtained performing AC frequency sweeps in 1mM, pH7 buffer solution using the developed system.

3.10   Cytokine detection with nanowires sensors

Finally, tests on antibody functionalized new batch nanowires were performed using the developed system to experimentally verify the detection of specific target biomarker molecules. In particular interleukin-8 (IL-8) and tumour necrosis factor-alpha (TNF-α) over a wide range of concentrations were used, as previously done by the research group of University of Southampton [73].

TNF-α is a cytokine involved in systemic inflammation. Relevant concentrations of TNF-α for clinical diagnostic in serum range from 0.004-0.5 mg/l [140] and thus in terms of molarity a range of 230 fM-29pM.

Figure 3.34 shows, as proof of concept, DC real time current measurements of anti-TNF-α functionalized nanowires after the insertion of increasing quantities of target TNF-α protein, the subsequent washing using low pH phosphate buffer solution to unbind the target from the antibody and the insertion of IL-8 non-target protein at high concentration.
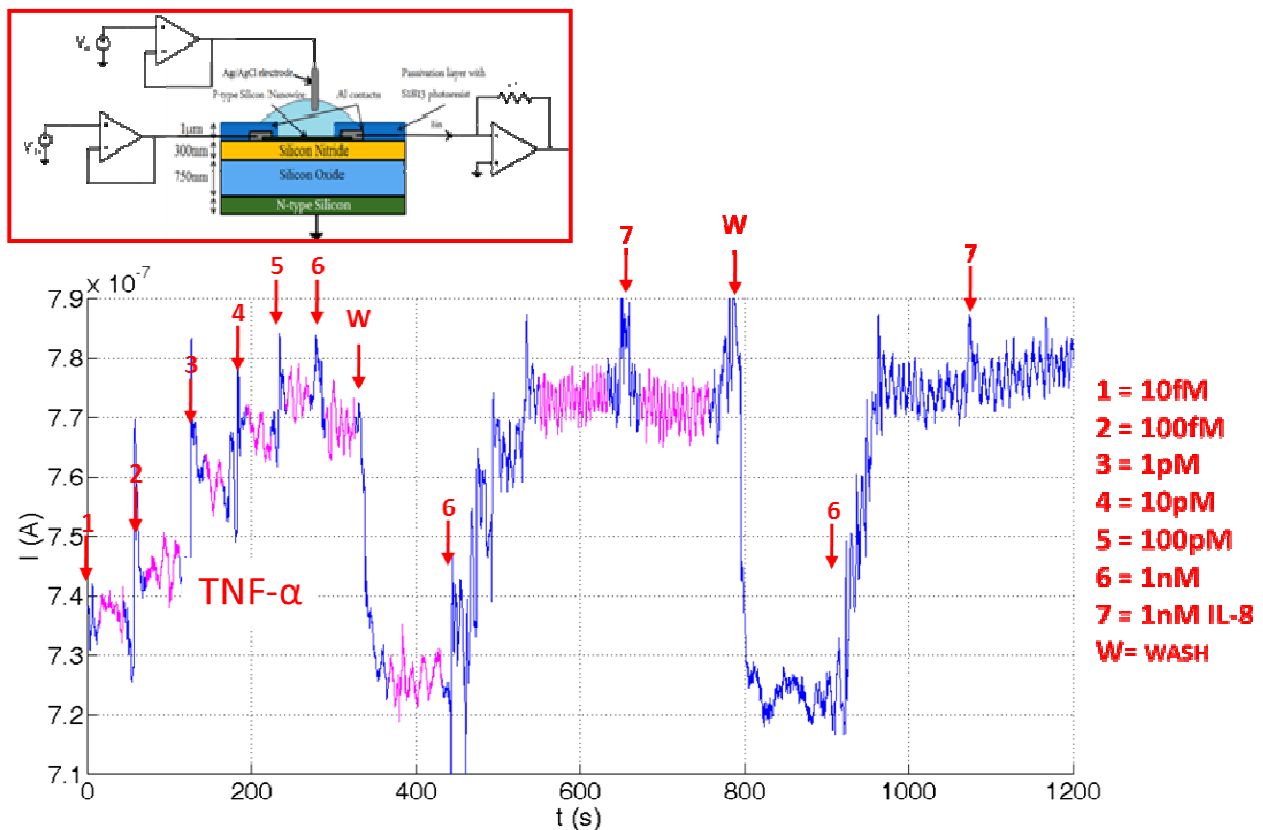
Figure 3.34 - DC real time current measurements of increased quantity of specific TNF-α protein followed by negative control of unspecific IL-8 protein at high concentration performed using the developed nanowires acquisition board. Arrows show when solution with the indicated (on the right) concentration of protein was inserted in the microfluidic chamber. The inset shows the experimental readout setup with the gating electrode inserted in the buffer solution.

The results show a limit of detection (LOD) as low as 10fM and a good specificity demonstrated by the unchanged nanowire current level after the insertion (arrows 7 in Figure 3.34) of the negative control IL-8 non-target proteins at high concentration (100000 fold higher the LOD), as previously reported [73]. Moreover it is reported (and repeated to confirm) that interestingly, inserting high concentration (1nM) of target protein, the current level decreases (instead of continue increasing) suggesting a change of the net charge seen by the nanowire surface after reaching a saturation limit of about 100pM. This phenomenon has to be better investigated in future experiments, but it is probably due to unspecific bindings between the target molecules and the silicon nanowires surfaces and relative possible charge inversion [141], [142].

The same experiment was also performed without the gating electrode inserted in the buffer solution in order to analyse its effect. As reported in Figure 3.35, the measurement setup is noisier and less sensitive to specific target biomarker molecules with a sensitivity that is halved compared to the liquid gated case. Moreover and interestingly, the protein concentration at which the current level starts decreasing is reached at a higher value (above 1nM), suggesting an influence of the forced external potential in the above reported behaviour.
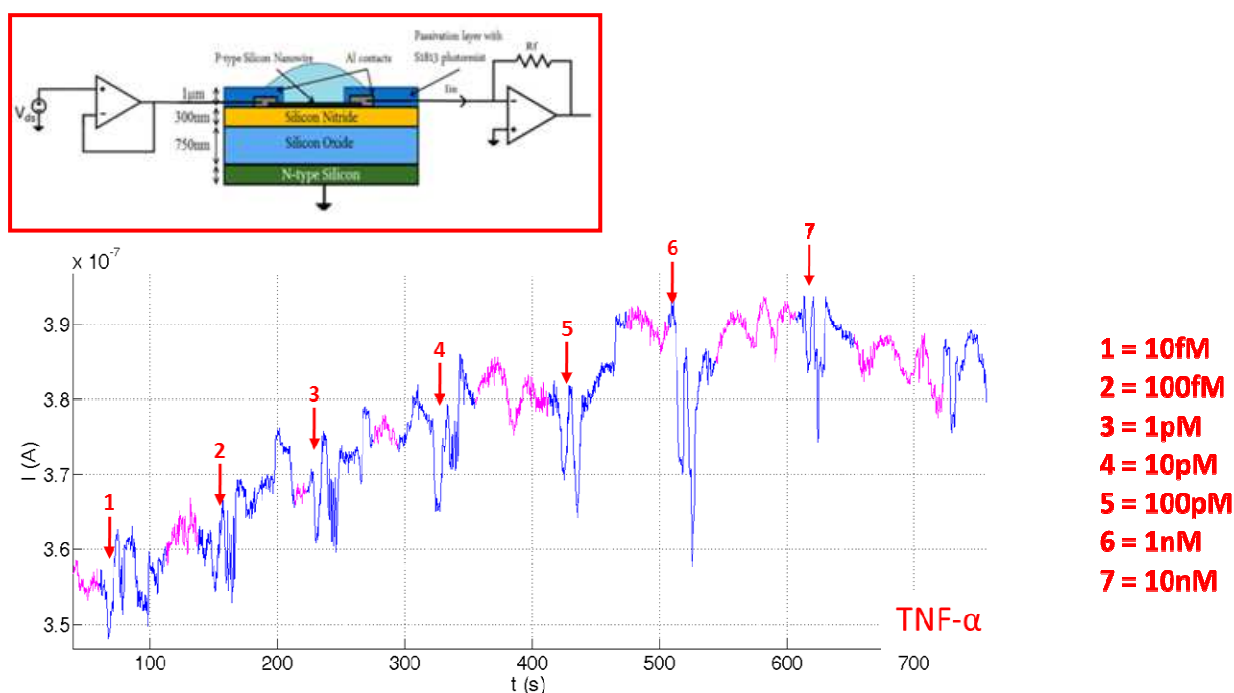
Figure 3.35 - DC real time current measurements of increased quantity of specific TNF-α protein. Measurements are performed without liquid gating electrode immersed in solution, as represented in the inset, to investigate the effect of liquid gating. Arrows show when solution with the indicated (on the right) concentration of protein was inserted in the microfluidic chamber.

These results, performed during the period spent at the centre for hybrid bio-devices of University of Southampton, demonstrated the possibility to perform specific biomolecules detection by the use of the developed hybrid system embedding the provided nanowires chip.

Chapter 4   Nanowires equivalent model

4.1   Introduction

One of the main advantages of developing models of the devices under test is the possibility to infer the experimental results in an easy way achieving sufficiently accurate results which catch the overall behaviour of the system in the different possible experimental conditions.

However, in order to achieve a reliable model, experimental results are useful to verify and validate the results of the simulations under particular conditions, these can be easily obtained by the use of versatile portable hybrid devices as the one developed and presented in this thesis.

Many models on nanowires FET were developed [143–145] considering different level of approximation and implementation; from the modelling of the transport conditions inside the nanowires device [146], to the modelling of the sensitivity of the device upon molecular bindings of target charged molecules considering the charge distribution of the biomolecules and the effect of screening related to the Debye length of the electrolyte solution [142], [145], [147].

Moreover the possibility to easily implement the model using a standard electronic simulation tool is a very tempting aspect. This was already considered by Martinoia [148] for the modelling of ISFET based sensors. However to our knowledge all the models on nanowires or ISFET sensors are aiming at precisely explain the DC response or FET transfer characteristics.

Since in many cases it is useful to perform AC conductance measurements of the NWs (see Table 1.1), in particular using the liquid gating electrode [76], and given the experimental results obtained using the developed nanowires acquisition board, effectively demonstrating the possibility to achieve interesting information from phase shift data, a simplified electric equivalent model starting from physical considerations of the particular provided device would be very useful in order to try to understand how different capacitive effects affect the nanowires complex impedance response and to relate them to the detection of biomolecules at the nanowire interface or to the physical parts of the device.

For these reasons, in this chapter a simplified semi-empirical model, easily implemented using a common electronic analog circuit simulation program, PSpice, is presented with the aim to catch the overall response of nanowires based sensors under an alternate current regime, with particular interest on the different contributions given by the capacitive effects affecting the nanowires, as a function of the different measurement frequencies used. Given the affinity based principle of the nanowires biosensors, finding a simple method to model the overall capacitive effects at the interface between the nanowires and the liquid solution while

measuring the conductance variations of the nanowire would be an important step to understand the nanowire sensors functioning and to analyse if phase shift data can give complementary information and at which particular frequencies. For instance try to understand how organic charged molecules inside the double layer affect the characteristics of the double layer modulating the resulting capacitance, which effects can be read by the phase shift changes.

As a first step it was needed to determine the appropriate simplified equivalent circuit and to estimate parameter values, then, analysing the simulations responses and comparing them with experimental results we could understand which parameters are affecting more the nanowires based sensors AC response in order to also elucidate the critical points in the fabrication process, in the device geometric properties or in the functionalization steps.

As stated above the model considers nanowire chip as a whole, trying to reproduce the experimental response of the system; however it must be noted that this type of representation and simulations do not consider other "physics based" transient effects (e.g. charge trapping / de-trapping at interfaces, ion drift in solution etc.) [141], [149], [150]

4.2   Electrical Double Layer

Usually bio-sensing experiment are performed in electrolytic solution in order to artificially create the proper wet environment and ensure the natural living and functioning properties of the biomolecules. For this reason the electrolyte solution is an unavoidable component of biosensors which has to be accurately taken into account, in particular for FET devices where the sensing principle is strictly based on the effect of charged molecules at device surface [11].

The processes taking place at the solid/liquid interface when a metal or semiconductor is immersed in an electrolytic solution are complex and some of them not yet fully understood; we remand to popular electrochemistry textbook, such as the one by Bockris and Reddy [151], by Bard and Faulkner [4] or by Morgan and Green [152] for a complete description.

However, here we give few notions useful to understand the argumentations and observations discussed in the next sections as well as the functioning principles and challenges in the using of nanowires based biosensors.

When a metal or a semiconductor, which in general has a surface that carries a net charge resulting either from an external potential applied or from the dissociation of chemical groups at the surface, is immersed in an electrolytic solution, ions of opposite charge (counter-ions) are attracted by the electrostatic potential while ions of like charge (co-ions) are repelled resulting in the creation of compact layers of ions that balance the excess charge of the surface. This region of counter charges from the solution that screens the surface charge to give an overall charge of zero is called electrical double layer (EDL). The double layer plays a fundamental role

in the behaviour of molecules and particles close the surface influencing electrical forces acting on them and also changing their effective charge.

The structure of this region have been studied starting from the 1879 by Helmholtz [153], who was the first who modelled the electric double layer structure as a compact layer of counter-ions adsorbed at the electrode surface, resulting in a structure analogous to the conventional solid-state capacitor with two layers of charges of opposite signs separated by a dielectric material. Therefore in this model the potential drop across the interface is linear and the specific capacitance (per unit surface area) is simply given by the parallel plate capacitor formula:

$$C_{dl}^{H} = \frac{\varepsilon}{d}$$
(4.1)

where ε is the absolute permittivity of the electrolytic solution and d the thickness of the layer that can be approximated as the radius of solvated ions.

Other models on the EDL were then developed in the following years [154], [155] to take into account that experimentally the differential capacitance varies with the potential as a function of distance from the surface and considering that the ions are able to move in the in the electric double layer and are subject to electrical and thermal forces according to the Maxwell-Boltzmann distribution. However the resulting Gouy-Chapman double layer model could not fully describe the resulting experimental potential drop and in particular it overestimates the interface charge (and the capacitance) for high concentration electrolytes.

The Gouy-Chapman diffuse layer model was then improved by Stern who realized that ions cannot approach the electrode surface closer than their ionic radius (known as outer Helmholtz plane, OHP) and also that a single layer of counter ions are not enough to screen all the charges of the surface. For these reasons the current thinking and most commonly used model is given by the combination of the above two models, with a compact first layer (Stern layer) in which counter-ions are bound to the surface and the potential falls linearly from the surface value ϕ_0, and by the diffuse layer in which ions are free to move and the potential decays exponentially with a characteristic distance given by the Debye length λ_D. Moreover, to take into account the possibility of specific and non-specific absorption of ions at the surface, the model can be further refined in the Gouy–Chapman–Stern–Graham model where the Stern layer is subdivided into two regions adding a very compact layer, the inner Helmholtz plane (IHP), which comprises the adsorbed unsolvated ions. Figure 4.1 shows a sketch of the double layer composed of the above mentioned layers.

Considering the diffuse layer, since the capacitance is potential dependent, it is possible to define the differential capacitance:

$$C_{dl}^{G} = \frac{d\sigma_{d}}{d\phi_{d}} = \frac{\varepsilon}{\lambda_{D}} \cosh\left(\frac{ze\phi_{d}}{2K_{B}T}\right) \qquad (4.2)$$

Where σ_{d} is the equivalent surface charge density of the diffuse layer, ϕ_{d} is the diffuse layer potential (see Figure 4.1), z is the charge of the ion in solution, e is the elementary charge, K_{B} is the Boltzmann constant, T is the absolute temperature. For low surface potential the dependence of capacitance on the potential becomes negligible and the specific capacitance of the diffusive layer becomes:

$$C_{dl}^{G} = \frac{\varepsilon}{\lambda_{D}} \qquad (4.3)$$

that is also called the integral capacitance of the diffusive layer corresponding to that of a parallel plate capacitor of thickness λ_{D}.

Considering the series combination of the Helmholz, C_{H} and the diffuse layer capacitance (also known as Gouy-Chapman capacitance), C_{G} it is possible to calculate the total double layer capacitance. In particular, considering the case of low surface potential and considering the integral capacitance of diffusive layer:

$$\frac{1}{C_{dl}} = \frac{1}{C_{H}} + \frac{1}{C_{G}} = \frac{d_{OHP}}{\varepsilon} + \frac{\lambda_{D}}{\varepsilon} \qquad (4.4)$$

where d_{OHP} is the thickness of the Stern layer (typically 0.5nm).

Since the diffuse layer capacitance depends on the Debye length, it is most influential at low ionic concentrations, as the one typically used in nanowires based sensing, while for high ionic concentrations the diffuse layer collapses and its thickness approaches that of the Stern layer [152].
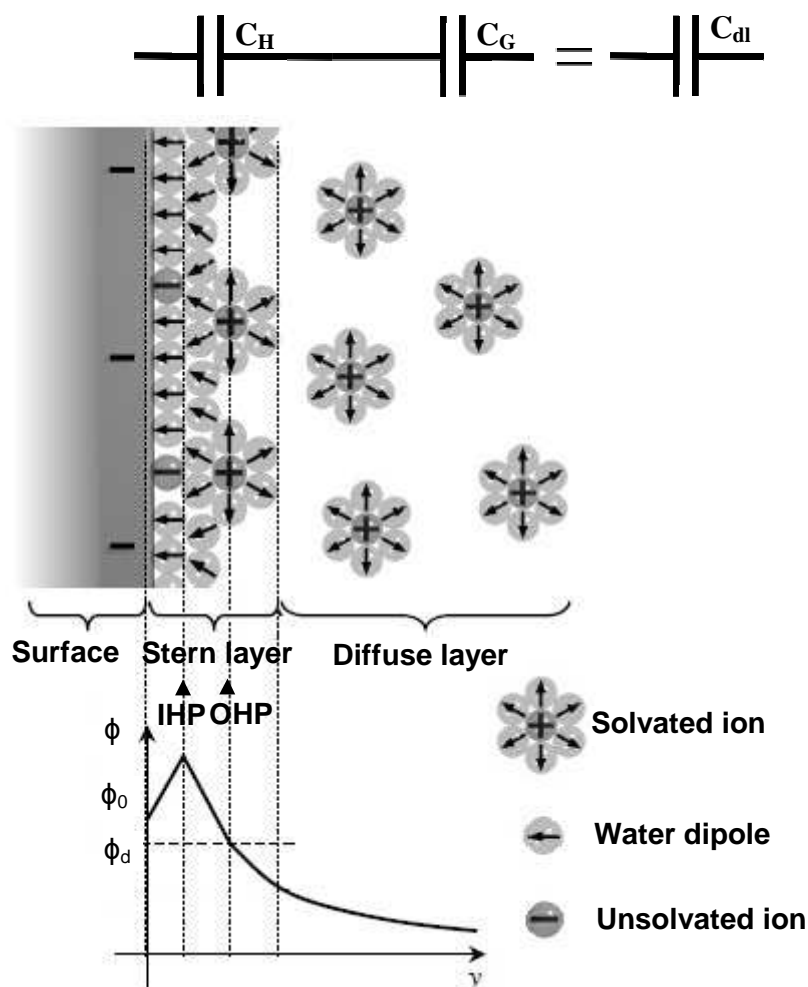
Figure 4.1 – Complete Gouy–Chapman–Stern–Graham model, adapted from [108]

As mentioned above, the Debye length is a measure of the thickness of the ionic solution region that screens the charge of the surface, is typically a few nm thick and it is possible to estimate its value by:

$$\lambda_D = \sqrt{\frac{\varepsilon_0 \varepsilon_{rH_2O} K_B T}{2 N_A e^2 I}}$$ (4.5)

where ε_0 is the vacuum permittivity, ε_{rH2O} is the relative permittivity of water, K_B is the Boltzmann constant, T is the absolute temperature, N_A is the Avogadro number, e is the elementary charge and I is the ionic strength of the solution, which depends on the molar concentration C_i and charge z_i of all ionic species present in the buffer:

$$I = \frac{1}{2} \sum_{i=1}^{n} C_i z_i^2$$ (4.6)

Nanowires (and in general bio FED[11]) are strongly dependent on the Debye length of the solution used for sensing because only the charges within this distance from the nanosensor are not screened and can be sensed since affect the surface potential and modulates the current flowing in the device. [6], [55], [147]

This is one of the main limitation of the nanowires based sensing; in general the sensing need a step of dilution of the electrolyte solution in which experiments are performed and much effort has been made in recent years to overcome these limitations [54], [58], [68], [70].

In our experiments low ionic strength sodium phosphate buffer solutions were used and Table 4.1 lists the calculated values of Debye length for the two different concentrations used, in particular these are selected in order to be as much constant in Debye length as possible upon pH variations.

Table 4.1: Buffer solutions used for pH measurement experiments.

Solution	pH	1mM - λ_D	10mM - λ_D
H_3PO_4	~3	3.9nm	1.25nm
$Na_2HPO_4+H_3PO_4$	~5.5	4.6nm	1.3nm
Na_2HPO_4	~7	4.8nm	1.4nm
$Na_2HPO_4+K_3PO_4$	~8.5	4.6nm	1.3nm
K_3PO_4	~10	3.9nm	1.25nm

4.3   Nanowires simplified semiempirical model

In order to investigate if current phase information can enrich information from nanowires based sensors and, eventually, in which range of frequency, a nanowire (in buffer solution) model has been proposed considering the physical characteristic of the University of Southampton nanowires arrays and simulated using PSpice software, by performing AC sweeps from 1Hz to 1 MHz:

In particular, for all the calculations the characteristics of the outer set of nanowires (see section 3.6.1 and Figure 3.16) were considered, since they are nominally identical in all different chips.

The following table indicates the nominal dimensions and the number of parallel NWs in a set.

Table 4.2: Nominal characteristics of the nanowires set considered in the model.

Name	NW length (L) (seeFigure 3.18)	SW length (seeFigure 3.18)	N° of NWs in parallel
Outer NW	48 μm	40 μm	30

Considering the linear output and transfer characteristics of the provided nanowires and since our measurements are always performed in the linear accumulation regime ($V_{DS}>V_{GS}-V_{th}$), it is possible to model the nanowire device with a varying resistor which is modulated by nanowires surface charges and analyse the other capacitive contributions related to the device structure. Moreover the accumulation regime, in which measurements are performed, enable to neglect the semiconductor depletion capacitance, usually considered in modelling of FET devices [128], [143], thus enabling to consider variable only the capacitive contribution on the semiconductor interface [156], hereafter called surface capacitance (C_s).

Lumped elements are used to model the electrodes parasitic capacitances shown in Figure 4.2

In particular, the values of those capacitances were directly measured on several different nanowires test chips using a probe station (the Cascade Microtech prober, associated with Agilent 4279A 1MHz CV meter) both in air and in buffer conditions. Measured values are listed in the following table:

Table 4.3: Measured values of lumped capacitances considered in the model.

	In air	In Buffer (10mM PH7)
Track-Track(C_{line})	2 - 4pF	2 - 5pF
Track-Bulk (C_{stray})	15-20pF	18- 25pF

The nanowires set was modelled as a distributed network composed of a series of identical RCR T-network elements surrounded by lumped parasitic capacitances as shown in Figure 4.2b.

a)

b)
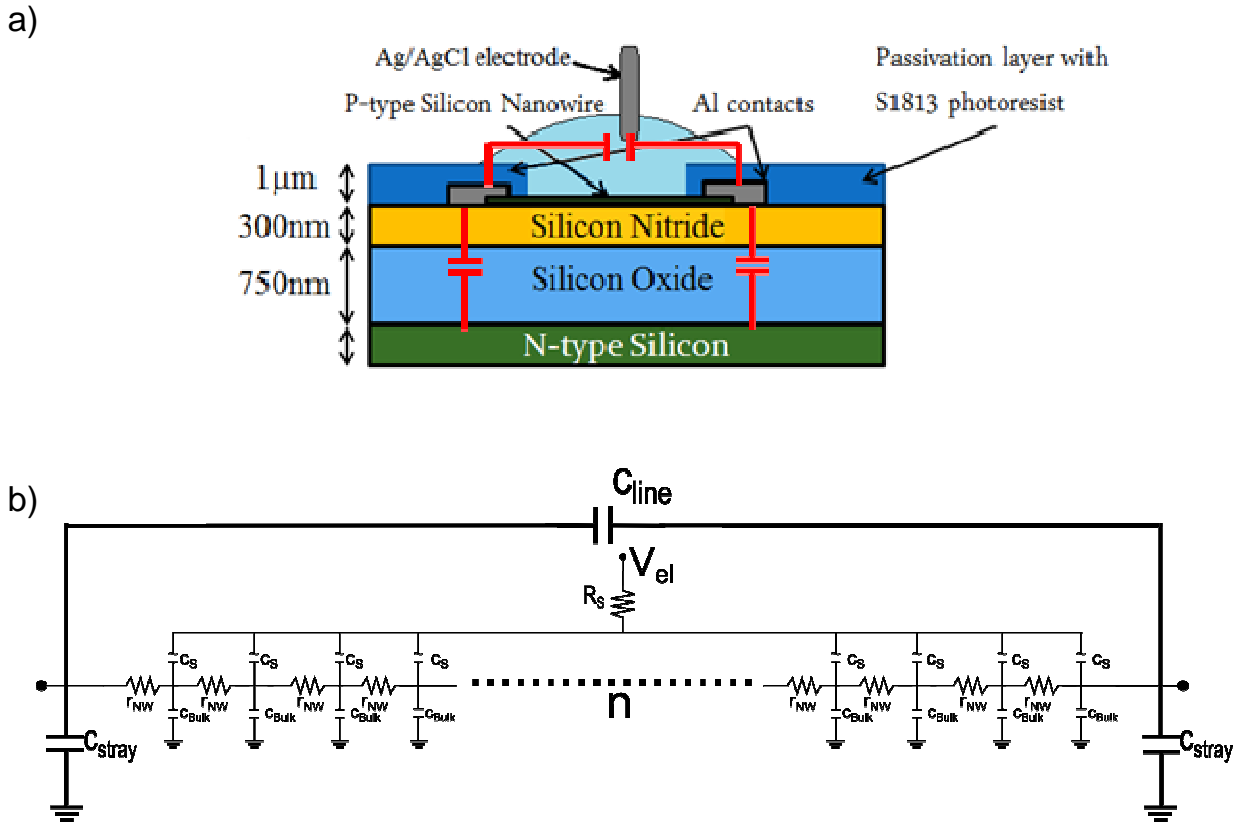
Figure 4.2 – a) Nanowire biosensor cross section and contacts parasitic capacitances.

b) Proposed distributed nanowire model with lumped contact capacitances.

In particular, given the non-faradaic conditions thanks to the insulating oxide layer created at the end of the fabrication process on top of nanowires surfaces (10 nm nominal thickness), we neglected the leakage resistance ($R_{leakage}$) contribution usually considered in electrode-electrolyte interface model [4], [5], and only the total surface capacitive effect given by the series between the oxide capacitance, the double layer capacitance and eventually the capacitance given by the insulating molecular layer after the different nanowires functionalization steps [5], [77], [157] was considered.

As a further confirmation of this hypothesis we measured the current flowing between the liquid gate electrode and the nanowires drain contact resulting in a very small leakage current (of about 10pA) with respect to the I_{ds} current (of some tens of nA) setting the liquid gate potential at 100mV, thus resulting in a leakage resistance of about 10GΩ that we neglected in our model.

Another contribution that was neglected is the one given by the device contact resistances, which are orders of magnitude lower than the NW set resistance.

Finally it must be noted that also all the impedance contributions of the electrode/electrolyte interface [4], [5] at the liquid gate electrode were neglected due to its very large dimensions

compared to the nanowires ones and it was considered as an ideal electrode used to set the potential of the buffer solution.

4.4 PSpice Implementation

The presented model can be implemented into commonly used circuit simulation software, such as PSpice, which allowed to easily investigate the impedance response of the three electrode setup, in which the impedance spectroscopy can be performed through the nanowires biosensors instead of performing the common EIS analysis through the liquid/solid interface, and focus the attention on the information that phase shift data can give.

In order to have a better representation of the real physical system a distributed model was chosen to simulate the nanowire set behaviour in response to an applied AC voltage (or current) signal at the different frequencies.

First of all, to determine the appropriate equivalent circuit, the contribution of the number of repeated elements of the RCR T-network on the system response was considered, implementing in PSpice different nanowires array models containing a different number of repeated elements, respectively a 3, 5 and 50. The impedance response was then compared to the lumped T network.
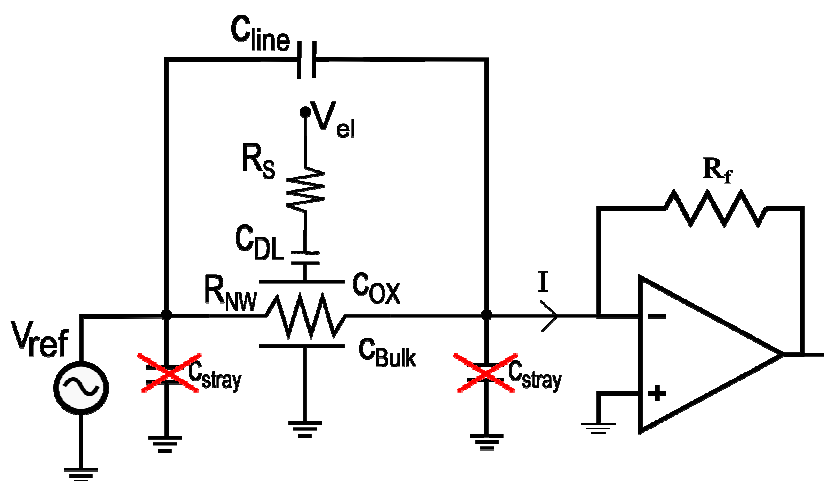
Figure 4.3 – Sketch of the proposed nanowires simplified model and readout setup. The C_{stray} capacitance is negligible in the represented measurement setup considering the fixed input node and the ideal virtual short circuit of the amplifier, as confirmed by performed simulations.

Performed simulations (see Figure 4.4) have shown that the 5-elements distributed model well approaches the response of the 50-elements one, which is considered the best representation of the real physical device; for this reason the 5-elements model appeared to be a good trade-off between model response accuracy and device model simplicity.
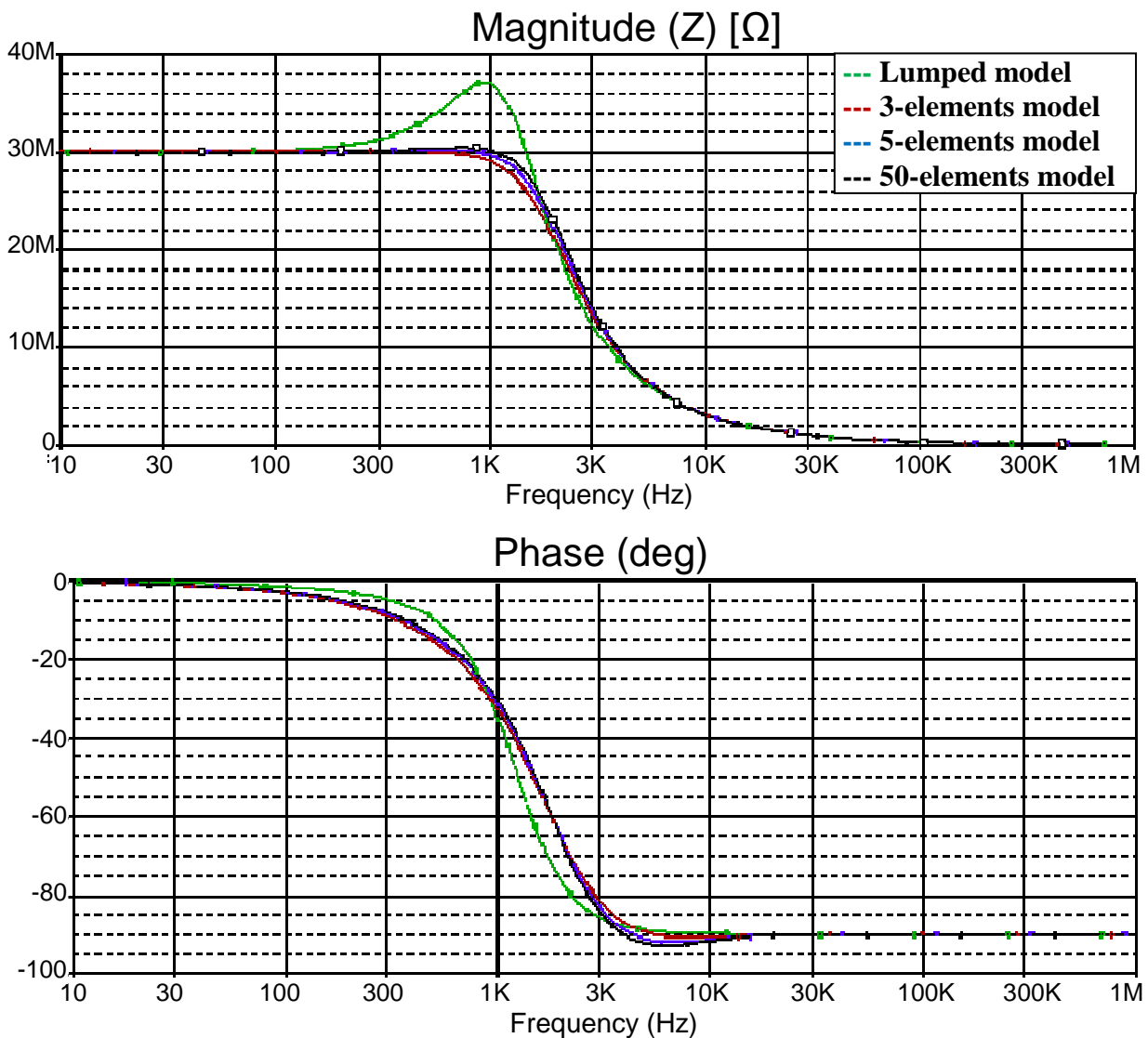
Figure 4.4 – Effects of number of elements in the considered distributed RCR T network compared to lumped model response. The following parameters were used in simulation:
R=30MΩ C_s=15pF C_{line}=2.5pF C_{stray}=18pF C_{bulk}=100fF R_s=2MΩ

The selected 5-elements model was then considered for the simulations reported below, where parametric AC Sweeps in the range 10 Hz -1 MHz varying the different parameters one by one over a range of reasonable experimental values were performed, as illustrated in next sections.

In must be noted that one of the main limitation of this approach is that every parameter is considered independent from the other, since only one parameter at a time can be varied performing parametric sweep simulations, whilst in the real experimental world the different model parameters are dependent each other; for instance the bulk liquid resistance with double layer capacitance, or the nanowires resistance which vary at a response of the different solutions (and thus of double layer capacitance) due to the FET principle. These effects have to be taken into account during simulation data analysis, however the main aim of the performed

simulations is to understand how the modelled components, related to physical and geometrical considerations of the biosensor device under test comprising the predictable parasitic elements, affect the impedance response of the system, in order to predict the behaviour for different biosensor working environments (e.g. different nanowires functionalization treatments) or different physical device characteristics (e.g. different oxide passivation layer).

4.5　Parameters values calculation and variations effect

The values of the parameters other than the directly measurable NW resistance and lumped electrodes parasitic capacitances were estimated considering the physical structure of the NW arrays (see Figure 3.18).

4.5.1　C_{BULK}

The specific capacitance between the set of nanowire and the bulk (called C_{Bulk} in the shown model) was estimated for the devices under study using a microstrip impedance calculator [158], which implements the following formula [159] :

$$C_o = \frac{0.67(\varepsilon_r + 1.41)}{\ln\left(\dfrac{5.98T}{0.8W + H}\right)} \qquad (4.7)$$

The value of the specific capacitance per unit length C_0 was obtained considering for simplicity the worst case of a single material substrate, composed unically by Si_3N_4 (which has the higher relative permittivity ε_r of 7.5 compared to SiO_2 which has 3.9). For the parameters H and W were used both the nominal lateral dimensions of the nanowires of 100 nm (see Figure 3.17). As value of T was considered the sum of the Si_3N_4 and SiO_2 layers of about 1μm (see Figure 3.18)
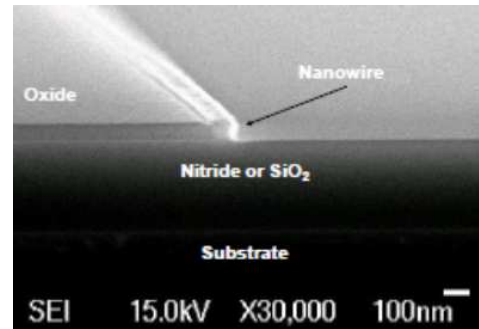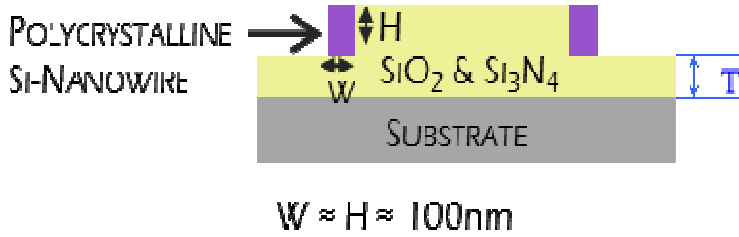
Figure 4.5 – Sketch of the cross section (left) and SEM picture (right) of the provided nanowires

The obtained value of 0.671 pF/cm was then multiplied by the NW length (L =48μm) obtaining the value of the capacitance for a single NW in the array (3.22fF). Finally, since capacitance between the single nanowire and the bulk is in parallel with the one of all the other NW of the array, this value was multiplied by the number of NW in the outer set of nanowires considered in this model (30), obtaining the value of the $C_{BulkTOT}$=96.6fF used for the simulations. It must be noted that this value is constant during the experiments, since it depends on the fabrication process; however performed simulations show that it does not have a significant effect on the nanowires response, even for large variations (up to 2500%) from the estimated value.
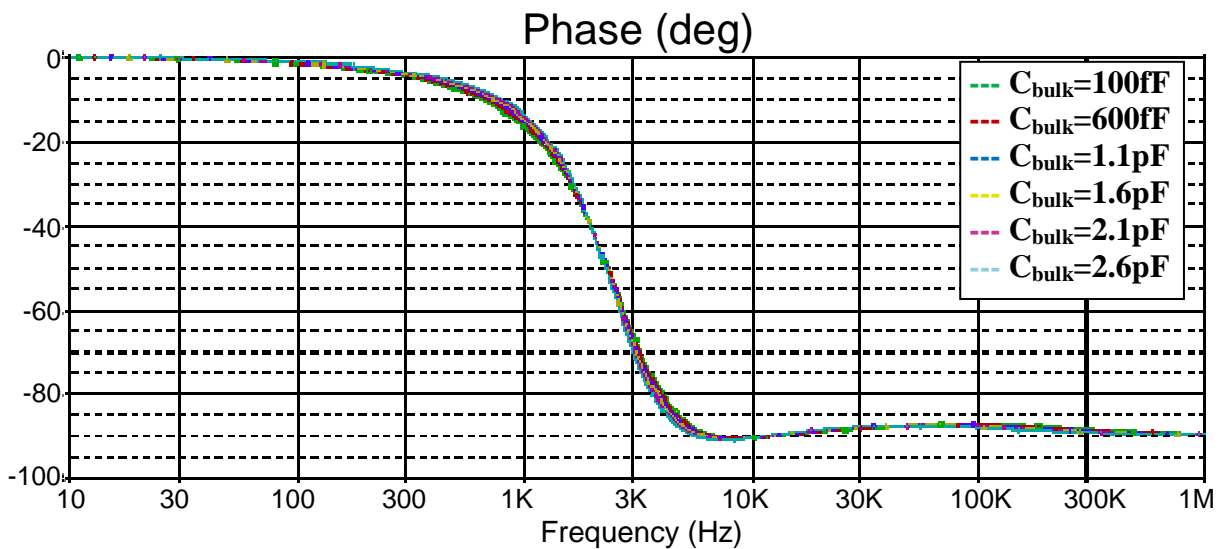
Figure 4.6 – Effect of bulk capacitance variations.
The following parameters were used in simulation:
R=30MΩ C_s=10pF C_{line}=2.5pF C_{stray}=18pF R_s=2MΩ

4.5.2 C_{DL} & C_{OX}

Contrary to C_{Bulk}, the double layer capacitance that arises at the nanowire-electrolyte interface could have a high impact on the phase of the acquired current. The possibility to acquire the phase angle between the modulated applied voltage and the resultant current could then enables the detection of the double layer capacitance variations, which are function of the concentration of the electrolytic solution and thus of surface charge density and potential difference across it.

For simplicity, in the presented simulations, the double layer was treated in the Debye-Hückel limit as simple parallel plate Helmholtz capacitor with a thickness equal to λ_D and the C_{dl} was calculated by the equation [152]:

$$C_{dl} = \frac{\varepsilon_0 \varepsilon_{rH_2O} A}{\lambda_D} \qquad (4.8)$$

where $\varepsilon_{rH2O}=80$ is the relative permittivity of the water, λ_D is the Debye length, A is the area of nanowires exposed to electrolyte solution (see Figure 4.5). For the calculations, 0.01X and 0.1X PBS solutions yielding Debye length values respectively of λ_D =7.3 nm and 2.3nm [6] were considered.

The total wet area is obtained by simple geometric considerations and summing the two sides contributions. This yields a value of A=8µm². The double layer capacitances for a single nanowire result respectively in 0.77 pF and 2.5pF. Multiplying these values for the number of nanowires in parallel in the set (30), it is possible to estimate the total double layer capacitance for the NWs set C_{dlTOT} in the two cases related to the two different phosphate buffer solution concentrations, respectively 23 pF and 74pF.

Performed simulations varying contribution of the total surface capacitance (C_s) show that increasing its value the phase plot becomes steeper; this also means that, by setting a single frequency comprised in the range of sensitive frequencies, important phase angle shifts could be recorded even for small changes in the double layer capacitance, as can be seen in Figure 4.7.

Phase (deg)
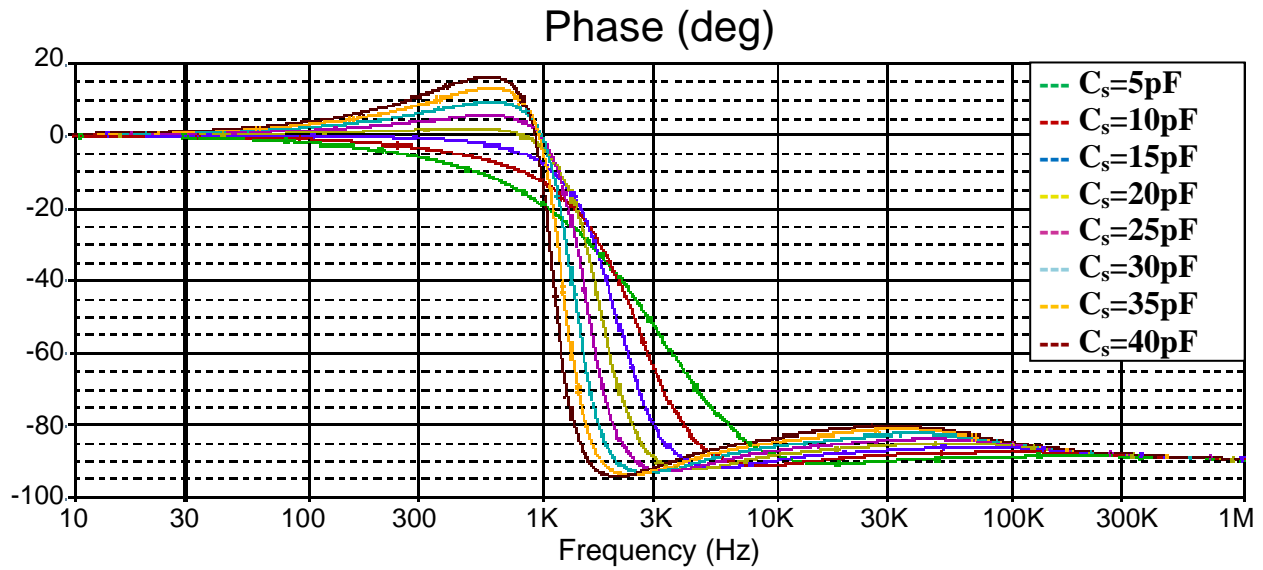
Figure 4.7 – Effect of surface capacitance variations.
The following parameters were used in simulation:
R=30MΩ C_{line}=2.5pF C_{stray}=18pF C_{bulk}=100fF R_s=2MΩ

However, an important and critical aspect of the biosensor is related to the SiO_2 layer at the nanowires surface, which gives rise to a small capacitance in series with the relatively large double layer capacitance. The thickness of the SiO_2 layer (d_{ox}) influences the magnitude of the total surface capacitance (C_s), which can be calculated at a first approximation as series of C_{dl} and C_{ox} as follows:

$$C_S = \frac{\varepsilon_0 \varepsilon_{rH_2O} \varepsilon_{rSiO_2} A}{\varepsilon_{rH_2O} d_{ox} + \varepsilon_{rSiO_2} \lambda_D} \tag{4.9}$$

Where ε_{rH20} and ε_{rSi02} are respectively the dielectric permittivity of the electrolyte and the silicon dioxide, A is the exposed surface area to the electrolyte, nNW is the number of the nanowires in parallel and λ_D is the Debye length.

As a proof of concept it is possible to estimate the sensitivity of the surface capacitance to double layer capacitance variations considering two experimental situations of thin native or created thermal oxide layer.

A 10nm thick SiO_2 layer (the nominal value of the thermal oxide on top of nanowires chip used for testing, see section 3.6.1 and [73]) yields a C_{ox} of about 0.9 pF for the given nanowires set geometry. Since this value is significantly smaller than the typical C_{dl} values (order of tens to hundred pF), the relative changes of the C_{dl} could not significantly influence the changes of the

total surface capacitance, resulting in an effect of screening of the double layer capacitance variations. Indeed in this case, if we consider for instance a $\Delta C_{dl} = 51pF$, that is due to a change in the PBS solution concentration of one order of magnitude (from 0.01X PBS to 0.1X PBS), the final relative ΔC_s is only 0.02pF and consequently $\Delta C_s/\Delta C_{dl}=0.045\%$. On the contrary, considering a thinner oxide layer (for instance native oxide of 1nm thickness), the estimated C_{ox} is about 9pF and sensitivity to the same $\Delta C_{dl} = 51pF$ would strongly increase, resulting in a relative $\Delta C_s=1.5pF$ and thus giving $\Delta C_s/\Delta C_{dl}=3\%$. Figure 4.8 shows the simulated results considering the two just mentioned situations.
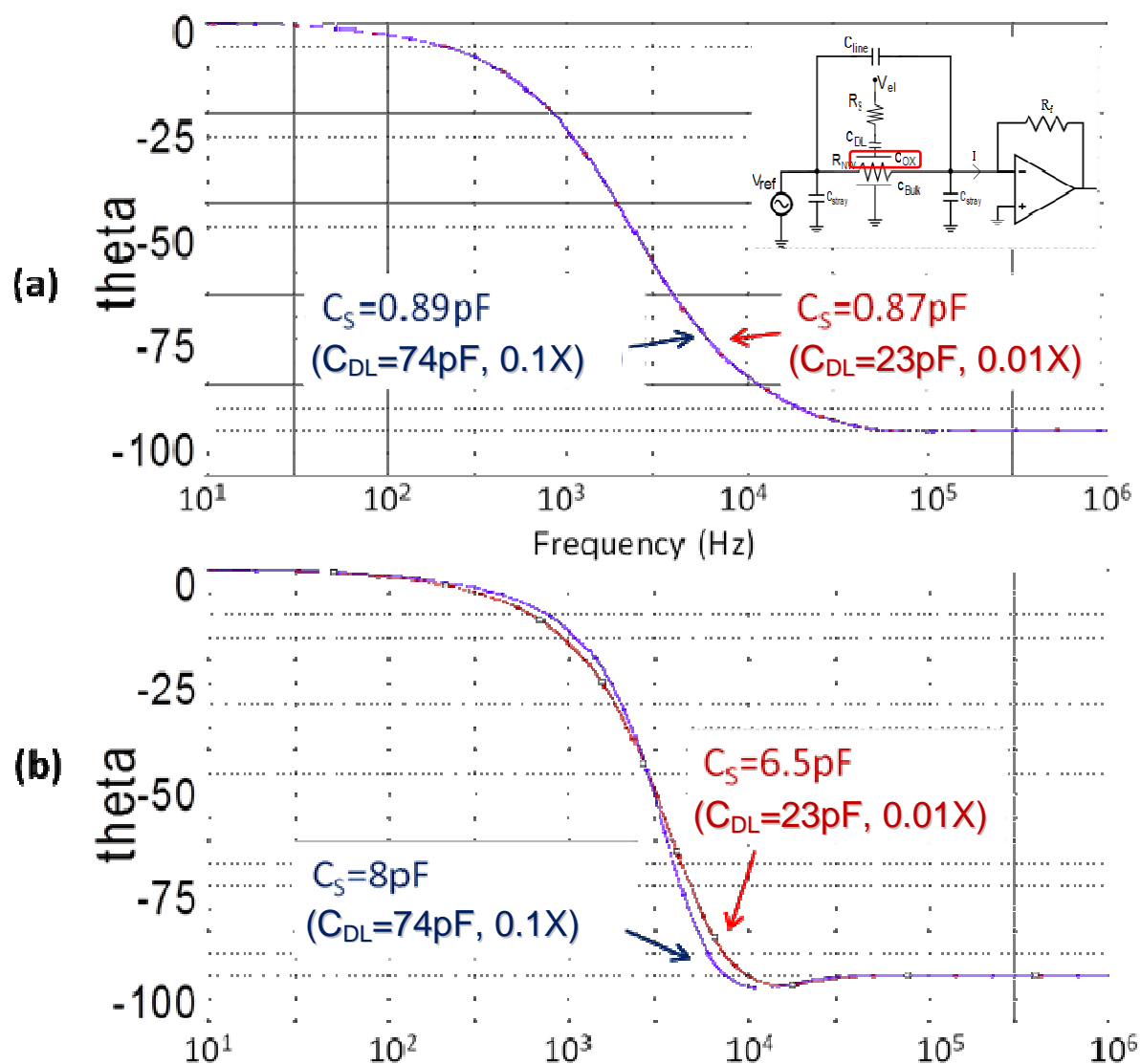
Figure 4.8 – Effects of silicon oxide layer capacitance. Simulations were performed considering estimated capacitance of (a) 10nm SiO₂ layer, Cox~0.9pF (b) 1nm SiO₂ layer, Cox~9pF using two different solution concentration, PBS 0.1X and PBS 0.01X.

These observations can explain and confirm the experimental literature results [72], [75], [147] highlighting the trade-off between the nanowires FET sensitivity and the temporal stability in liquid environment; indeed as higher is the thickness of the oxide layer as more stable is the

response over time, however this costs a lower sensitivity of the sensor to surface charge variations (which can be seen as changes of the surface capacitance considered in our model) and it is generally recognized that the passivation layer should be as thin as possible in order to not compromise the nanowire sensitivity [72], [75], [145], [160]. In simulations the lower and eventually imperfect insulation that arises from the thinning of the passivation layer can be modelled by inserting a leakage resistance ($R_{leakage}$) in parallel to the surface capacitance resulting in lower sensitivity in phase to changes of surface capacitance (see Figure 4.9) [5].

For these reasons instead of using a thinner silicon oxide passivation layer in order to have a higher C_{ox}, some recent literature works use different insulator material with higher dielectric constant, such as Al_2O_3 (ε_r=9 compared to SiO_2 ε_r=3.9) resulting both in a good stability of the response signal in liquid environment and a good sensor sensitivity [77], [135], [160].
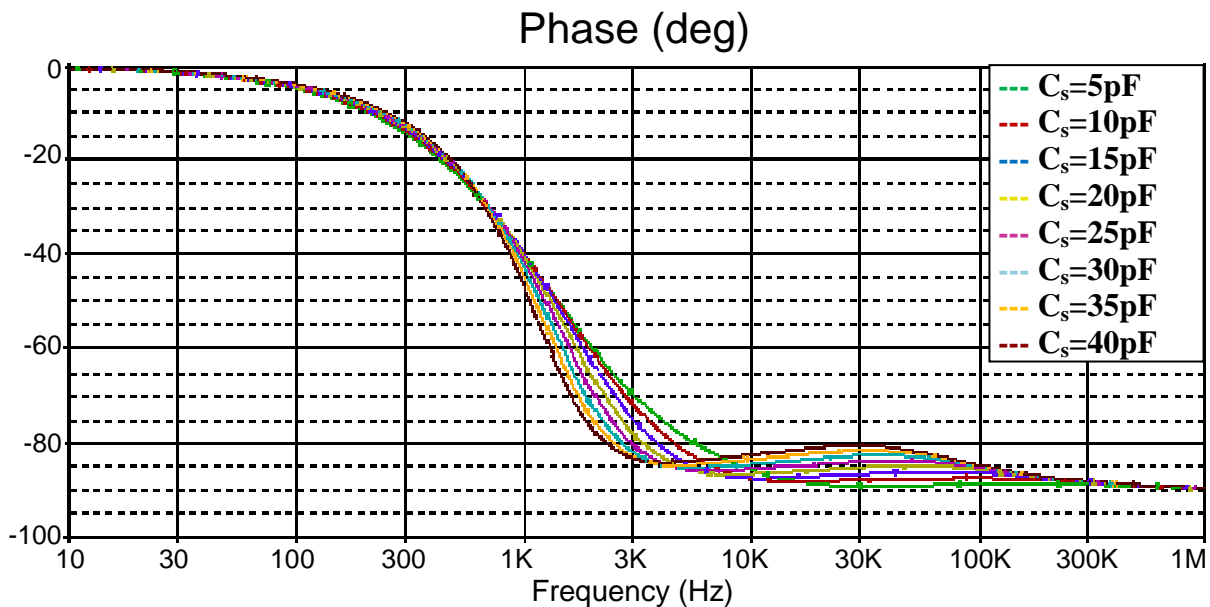
Figure 4.9 – Effect of surface capacitance variations with a leakage current between the liquid solution and the nanowires. The following parameters were used in simulation:
R=30MΩ C_{line}=2.5pF C_{stray}=18pF C_{bulk}=100fF R_s=2MΩ $R_{leakage}$=100MΩ

Finally the simulations demonstrate that in principle surface capacitive effects can be directly analysed (instead of indirectly as a response of the well-known FET principle of modulation of the current in the nanowires biosensors device) considering the phase shift response of the nanowires in the proper range of frequencies, provided that the insulating passivation layer capacitance is not too small compared to the resulting double layer or molecular layer capacitance on the nanowire surface.

4.5.3   R_S

The solution resistance is dictated by the conductivity of the solution and this is expected to have a very high value given the low concentrations of the solutions considered in nanowires sensing and thus it can have important effect on the developed model.

It has been shown that, in the case of microelectrodes, it becomes independent on the distance from the electrode and it depends only on the geometric area of the electrode [161]. Thus, under the assumption that the liquid gate electrode is infinitely large and the nanowires are surrounded by electrolyte and considering the nanowires as square electrodes with side equal to $\sqrt{A_{TOT}}$, it is possible to estimate the value of R_s as:

$$R_S = \rho \frac{\ln 4}{\pi l} \tag{4.10}$$

where ρ is the solution resistivity and l is the electrode side length [161].

Using equation (4.10) and considering the typical solution resistivity of PBS solution (~5 Ω*m for 0.1X and ~55 Ω*m for 0.01X [162]) and considering the total nanowires wet area, obtained summing the equal contributions for all the nanowires in the set, that yields a value of A=240μm^2 and thus a value of l=15.5μm, we estimated the R_s values for the two considered buffer solution concentrations respectively of 160KΩ and 1.6MΩ.

For these reasons and for simplicity usually the simulations were performed considering a worst case value of 2MΩ.

As higher is the solution resistance as lower is the sensitivity to surface capacitance as can be seen in Figure 4.10. Indeed, considering the series of the solution resistance R_s and the surface capacitance C_s, it must be noted that for low frequencies, smaller than f=1/(2πR$_s$C$_s$), the capacitive term dominates while for higher frequencies the impedance is purely resistive.
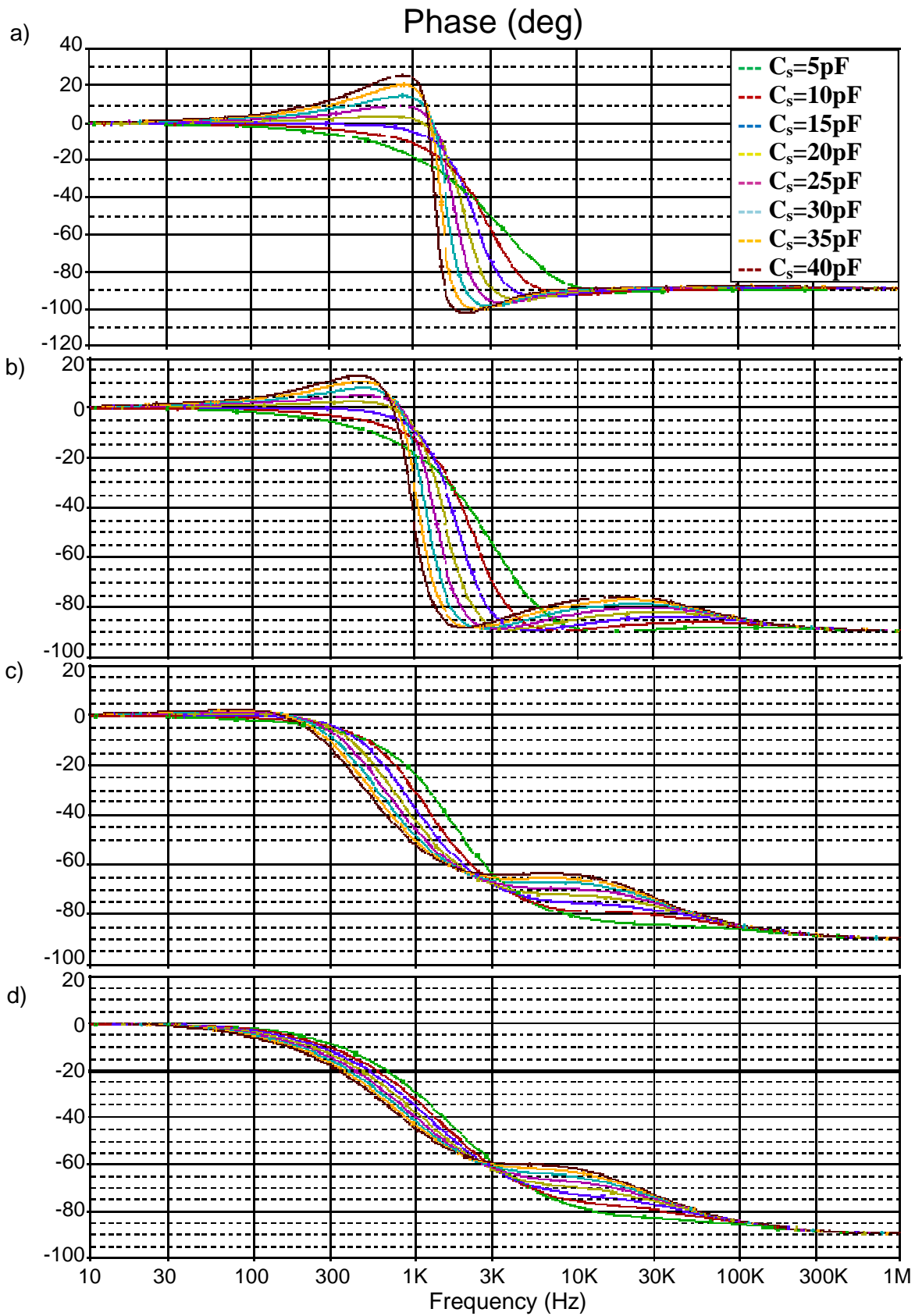
Figure 4.10 – Effects of surface capacitance variations for different solution resistances values:

(a) R_s=200KΩ (b) R_s=2MΩ (c) R_s=20MΩ (d) R_s=200MΩ.

The following other parameters were used in simulation:

R=30MΩ C_{line}=2.5pF C_{stray}=18pF C_{bulk}=100fF

4.5.4 R_{NW}

Simulations performed varying the nanowires set resistance in the typical range of values measured (1MΩ -100MΩ) allows to visualize the position of the main pole given by the parallel of R_{NW} and the measured parasitic pad-pad capacitance (C_{line}) that slightly vary from chip to chip in the range 2.5-5pF.

Consequently, in order to study the phase shift response to buffer and functionalization layer formation, usually highly resistive nanowires set (R_{NW}≥20MΩ) and the proper working frequency in the range of measurements of the developed system and possibly where the phase sensitivity is higher were selected.

As a proof of concept Figure 4.11 shows the results of simulation performed setting a C_{line}=2.5pF and a constant surface capacitance of 10pF. As can be seen, phase shift data can also be used to detect changes of nanowires resistance increasing the range of frequency where the system is sensitive to R_{NW} variations, in particular where the main pole (given by parasitic capacitances coupled to the nanowires resistance) dominates and the differences in magnitude are reduced. Indeed at some particular frequencies the changes in phase result higher in percentage with respect to the magnitude changes, as already reported with experimental results in section 3.8.2.

However, it must be noted that variations of nanowires resistance R_{NW} are given, for the FET working principle, as a consequence of variations of the nanowires surface potential upon variations of surface charges Q or of surface capacitance C_s according to the well-known equation $Q=C_sV$ [163], [164], resulting in a mixed behaviour between the simulations here reported and the aforementioned ones. In particular, the surface charge variation can be easily achieved by a change of the pH of the used solution, while the variation of the surface capacitance can be related to the variation of the electrolytic solution concentration. The creation of organic layers upon specific functionalization can give raise to both the effects depending on the pH of the liquid environment, since the molecules can have charged groups at a specific distance from the sensor device surface.

Moreover, as known from literature, the impact of the surface charge is dependent on the surface-to-volume ratio of the device and the sensitivity to variations of surface charge decreases with the increase of nanowires dimensions [134]; this would also mean that, considering bigger devices, such as nanoribbons, the variation of nanowires resistance R_{NW} would be more sensitive to surface capacitance variations (which are proportional to the exposed surface) than to the surface charge variations.

Magnitude (Z) [Ω]

Phase (deg)

Legend:
- R$_{NW}$=1MΩ
- R$_{NW}$=12MΩ
- R$_{NW}$=23MΩ
- R$_{NW}$=34MΩ
- R$_{NW}$=45MΩ
- R$_{NW}$=56MΩ
- R$_{NW}$=67MΩ
- R$_{NW}$=78MΩ
- R$_{NW}$=89MΩ
- R$_{NW}$=100MΩ
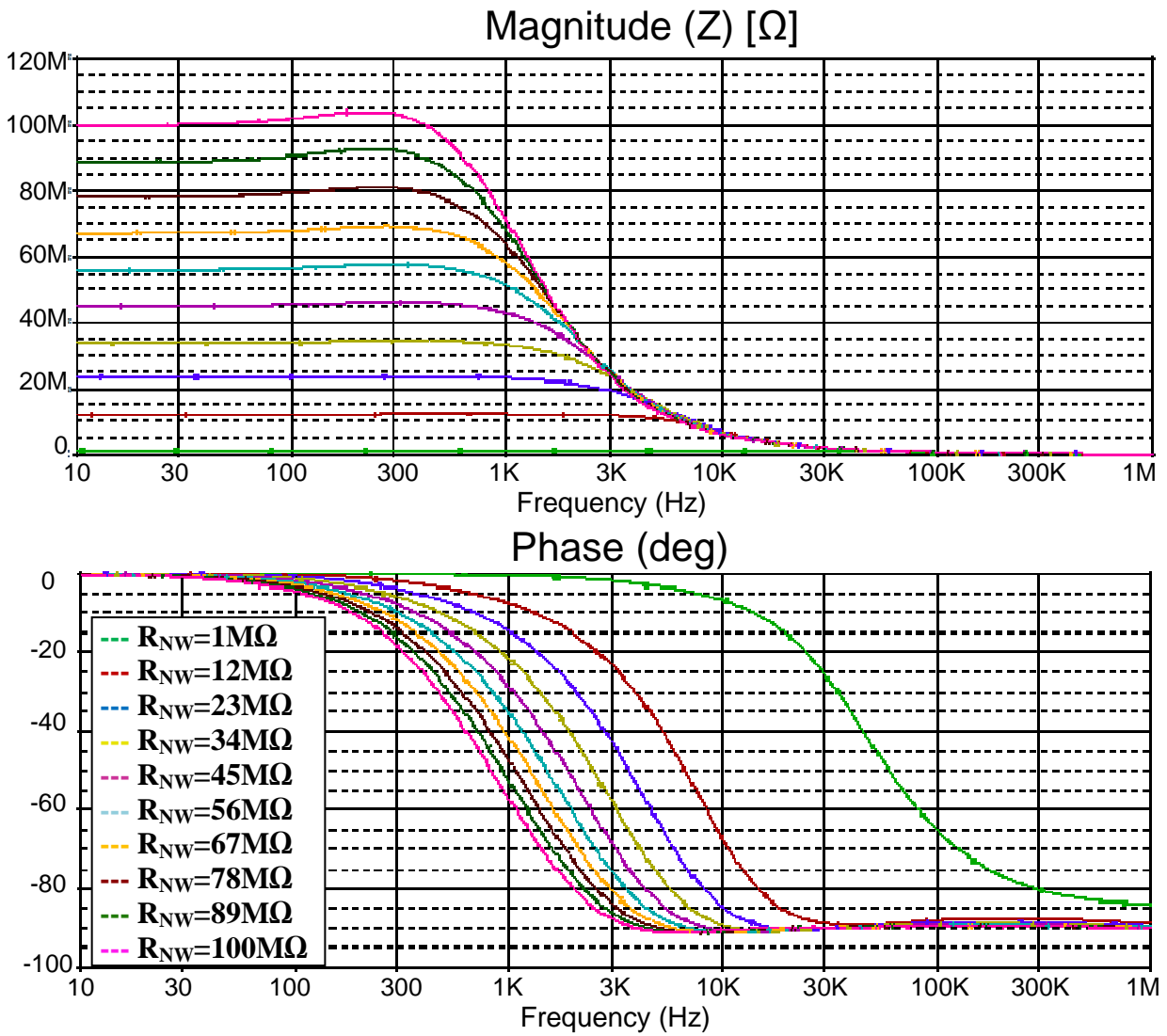
Figure 4.11 – Effects of nanowires resistance variations.The following parameters were used in simulation:

C_{line}=2.5pF C_{stray}=18pF C_{bulk}=100fF C_s=10pF R_s=2MΩ

4.6   Comparison with experimental results

As stated above, in principle a 10 nm thick SiO_2 resulting in a so small oxide capacitance should almost totally screen magnitude and phase shift variations of double layer capacitance as the ones estimated by the change of electrolytic solution concentration from 1mM to 10mM (variation of more than 200%). This predicted and simulated behaviour is confirmed by performing frequency sweeps, with the developed system, on bare nanowires devices immersed in phosphate buffer solution at the two different concentrations considered of 1mM and 10mM at the same pH7. Figure 4.12 shows representative results performed on a highly resistive nanowires set, selected in order to work in the range of sensitive frequencies compatible with the developed system measurement range, as mentioned before in section 4.5.4. As can be seen the changes of double layer capacitances are almost totally screened by the SiO_2 passivation layer and only a very slight sensitivity is achieved both in magnitude and phase shift data.

The result is coherent with work of Nikolaides et al. [165], in which only a slight sensitivity to solution concentration is achieved between 1mM and 10mM, although in that specific case the passivation layer is composed of 2-3 nm native oxide, while raise abruptly after the 10mM concentration. Similar results are achieved by Park et al.[72] and Clement et al.[166] who claim a sensitivity of the nanowire to electrolyte concentration but, analysing the experimental results, the changes are clear only for electrolyte concentration higher than 10 mM.

At such higher concentrations, indeed, our hypothesis is that other phenomenon (not directly considered in our capacitive model) occurs, such as the adsorption of ions to the nanowires surface, as discussed in a very recent work [150]. This would cause an accumulation of not screened charges at the nanowires interface resulting in a variation of the device resistance.

This hypothesis is also in line with the ISFET working principle and the fact that probably at such high concentrations the capacity of amphoteric surface groups to buffer the proton concentration, property related to the particular oxide material and known in literature as surface buffer capacity [163], is overcome, resulting in the presence of a net charge affecting the nanowires device.
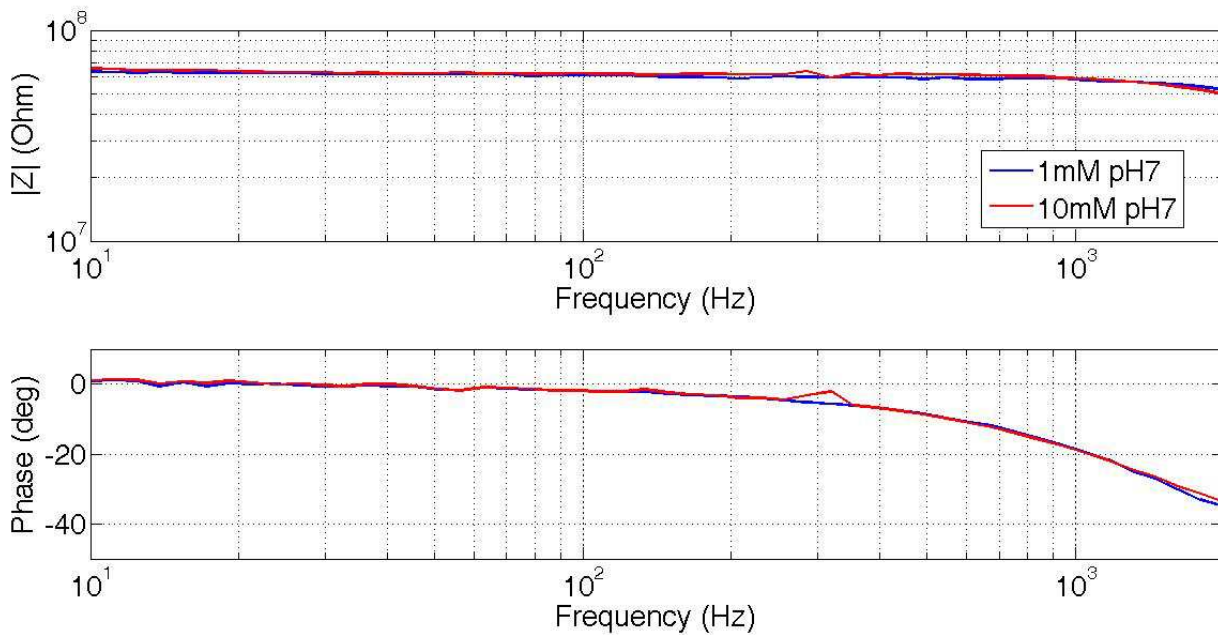
Figure 4.12 – Experimental bode plot demonstrating the effect of oxide passivation layer on bare nanowires.

However, if we consider the situation where a molecular layer is formed on the nanowire, such as after the APTES and succinic acid functionalization steps (see section 3.9), surface capacitance variations can be quantitatively enough to be recognized by phase shift data.

Indeed, it was previously demonstrated that the two aforementioned functionalization steps give significant changes due to different charge distributions at the surface.

In this case the situation is given by the series of different capacitances given by the oxide insulator layer (C_{ox}), the insulating molecular layer (C_{ins}) and the double layer capacitance influenced by the molecular terminal charged groups (C_{DL}) [143], [157]. The total value is given by $C_s = \left(\sum_i \frac{1}{C_i} \right)^{-1}$ and it is dominated by the smallest value, however it is not easy to understand how the charges of the adsorbed molecules affect the double layer structure and thus to estimate the value of the resulting equivalent surface capacitance [141], [151], [167].

The displacement of electrolytic solution from the surface upon functionalization layer assembling increases the thickness and also decreases the relative permittivity of the insulating layer on nanowires surface (considering the higher $\varepsilon_r=80$ of the water in comparison to the value of $\varepsilon_r=2$-5 typical for biomolecules) resulting in a significant variation of the surface capacitance [5]. Moreover the external potential applied by means of the liquid gate electrode can force the extra charges towards the nanowires surface and these non-screened charges, whose number is a function of the quantity of available counter-ions and thus on the buffer concentration, can affect the nanowires conductivity [77].

This is confirmed by data acquired, as previously done, with the nanowires acquisition board using two different concentrations of buffer solution of 1mM and 10mM at the same pH=7. In this case, as can be seen in Figure 4.13, the changes of electrolytic solution concentration (and thus of double layer capacitance) can be detected both in magnitude and in phase data despite the presence of the 10 nm SiO_2 layer, confirming the aforementioned observations.
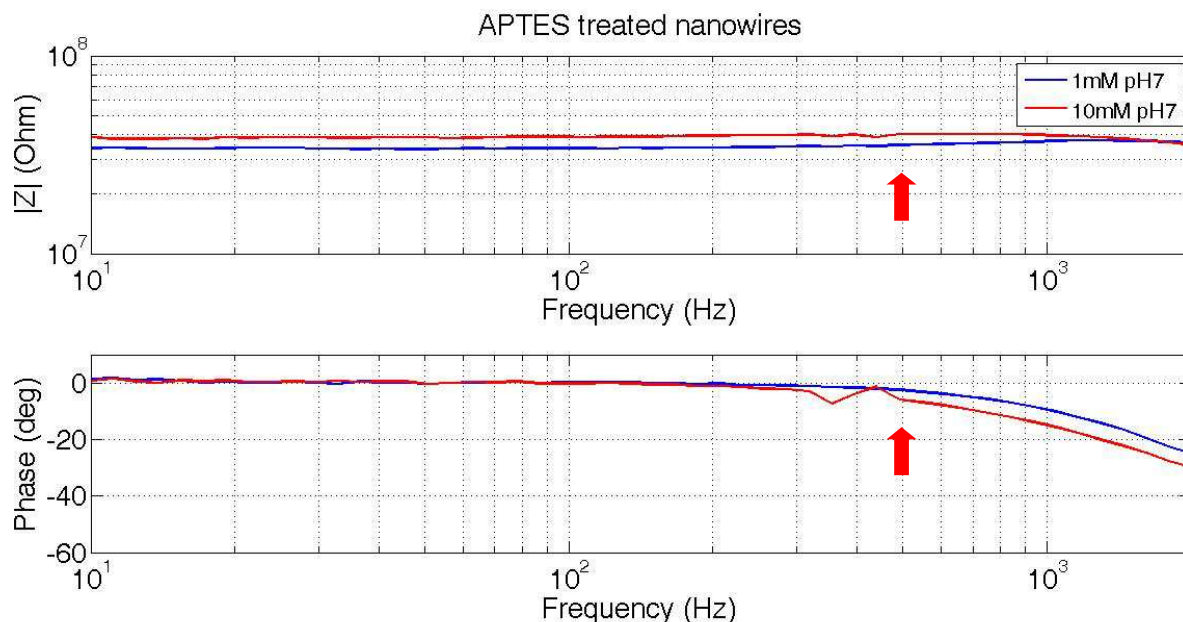
Figure 4.13 – Experimental bode plot demonstrating the effect of APTES functionalization in the detection of double layer capacitance variations. It must be noted that the nanowires set used for these experiments was different and intrinsically less resistive compared to the one used for experiments reported in Figure 4.12. The arrows indicate the operating point frequency used for real time measurement reported in Figure 4.14.

The same results were achieved performing real time AC measurements using a modulating frequency of 500Hz and confirming the slight sensitivity both in magnitude and in phase data to electrolyte solution concentration once the nanowires surface was treated by adding APTES molecules, as reported in Figure 4.14.
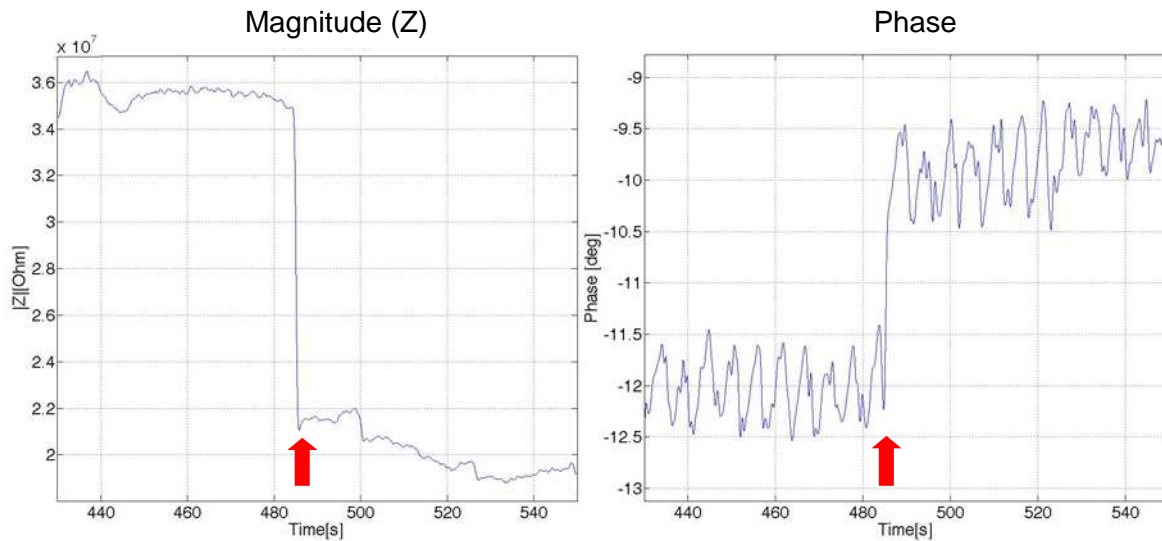
Figure 4.14 – Real time AC acquisition performed at 500Hz demonstrating the effect of APTES functionalization in the detection of double layer capacitance variations. Arrows show when the solution concentration was changed from 10mM to 1mM.

Moreover, in order to confirm the possibility of the simplified developed model to catch the main characteristics of magnitude and phase response at the variations of the resulting equivalent surface capacitance, a comparison between the PSPICE simulations of the electrical model of the system and the experimental data was done.

Two different surface treatments were considered: functionalization with 3-aminopropyltriethoxysilane (APTES) and a following succinic acid treatment. For these test we used the Novocontrol Alpha-A Impedance analyser [125] (see also section 3.5.1) to measure the response of the NW biosensors, in 1mM buffer solutions at pH7, within a wide range of frequency (1 KHz up to 1 MHz) and record the phase shift due to the change in the surface capacitance in relation to charge changes at the surface.

As clearly visible in Figure 4.15 the model well captures the experimental response in a qualitatively correct way; in particular the steeper slope of the phase shift response predicted by an increase of the equivalent surface capacitance experimentally achieved upon succinic acid treatment.
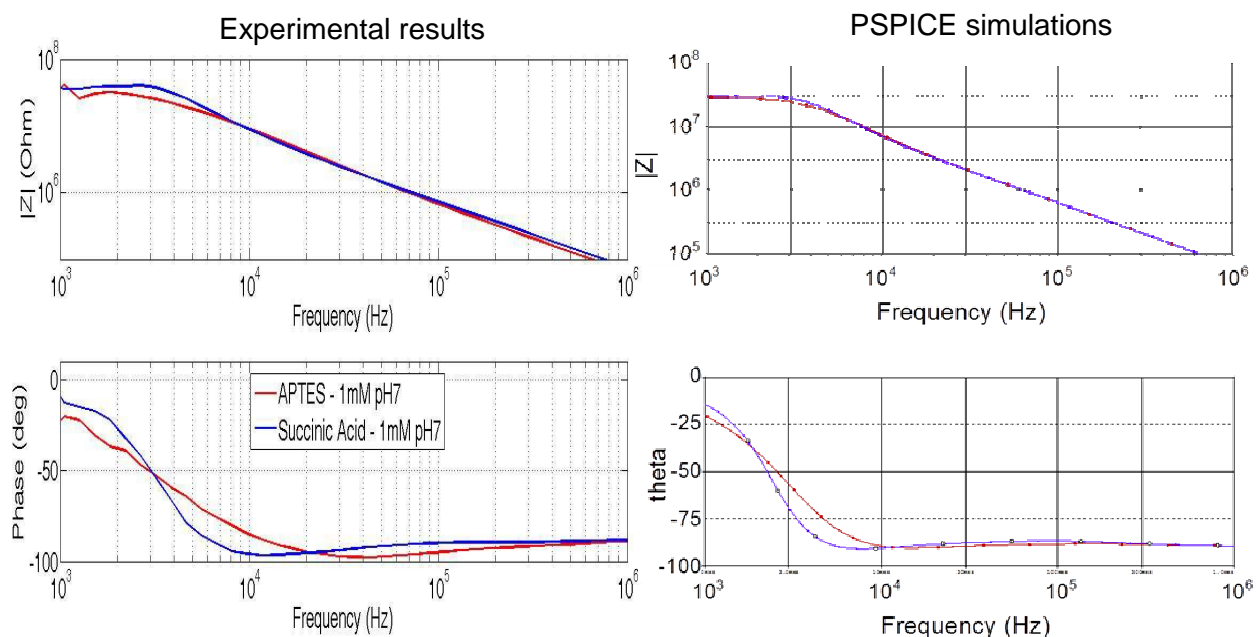
Figure 4.15 – Comparison between experimental bode plots of APTES and succinic acid treated nanowires (left) and PSpice simulations (right).

Interestingly the resulted behaviour seems counterintuitive; indeed one could expect a decreasing of the surface capacitance after succinic acid treatment due to the higher distance of terminal charges of the succinic acid molecule from the nanowire surface with respect to the APTES treated surface. On the contrary and surprisingly the equivalent surface capacitance C_s results higher upon succinic acid linkage compared to the APTES treated case, giving the reported steeper slope of phase shift data.

However the results can be explained considering the isoelectric point of the given molecules as explained before in section 3.9.1 and considering that the pKa of the succinic acid is lower (~5) compared to the APTES one (~9). This gives, at every pH, a less positively charged (or even negatively charged for pH>pKa) molecular layer after succinic acid treatment and thus the charges of the molecular layer will be less repulsed from the sensor surface compared to the case where APTES layer is present, resulting in a lower distance of the charges from the surface. This consequently causes an increase of the resulting equivalent surface capacitance C_s and thus the steeper phase shift response.

Finally the tests were repeated using a different buffer solution concentration of 10mM (at ph7), in order to both confirm the experimental observations and analyse the effect of the double layer capacitance variations.

Figure 4.16 confirms the repeatability of the aforementioned results and observations also using a more concentrated solution; moreover it highlights the slight sensitivity on double layer

capacitance variation upon the creation of the molecular layer on the nanowire surface both after APTES and succinic acid treatment as previously reported.
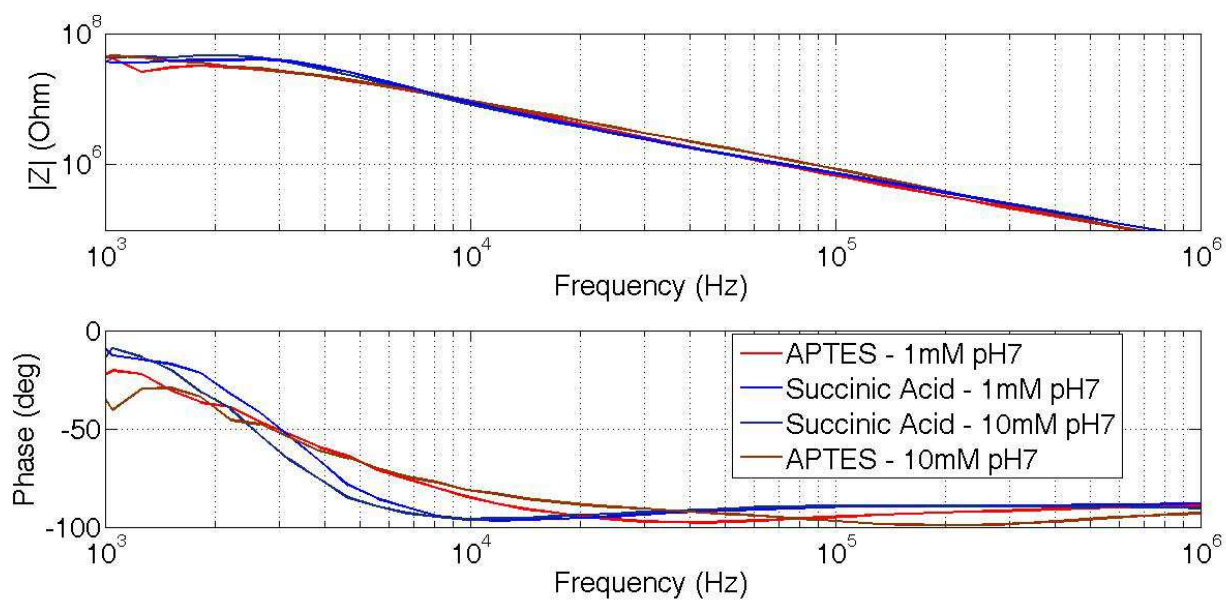
Figure 4.16 – Experimental bode plot of APTES and succinic acid treated nanowires demonstrating the effect of different electrolyte solution concentrations and the repeatability of the results.

Chapter 5   Hybrid, portable, integrated lock-in-amplifier-based system for real-time impedimetric measurements

5.1   Introduction

In this chapter a portable standalone system directly pluggable to the laptop for real time impedimetric measurements on nanowires biosensors is presented and tested.

The system is based on the low power fully integrated impedimetric system recently developed by the research group [47], [168], which integrates a band-pass delta-sigma and enables the real time complex nanowires impedance readout in the range 1 KHz -25KHz.

The high dynamic range IC is designed to perform four terminal measurements (also known as Kelvin sensing) and it is particularly tailored for low resistive conductivity-temperature-depth sensors, however few implemented adaptations made the system very versatile and suited to study nanowires based sensors, performing user friendly measurements at different working frequency in order to investigate capacitive effects related to bio-nanodevices.

As stated above, generally the voltage sensing methods yields the best results for low impedances devices since the low currents values needed to limit the voltage drop on the DUT are strongly affected by parasitic capacitances. However, considering the developed model, the small variations of surface capacitance on which we are interested can be considered as parasitic capacitances variations in parallel to the bulk capacitance, as represented in Figure 5.1. For this reason investigations on this measurement setup, in which the current reference signal is imposed to the DUT while measuring the voltage output, were performed.

In particular with this approach there is a different contribution of DUT capacitive effects as resulted from simulations using the previously presented model; this motivated the use of this sensing method on nanowires based sensors and in particular to investigate if the phase shift response can be more meaningful with respect to the standardly used magnitude impedance or simple DC conductance ones.

Simulations indeed have shown that for frequencies above the dominant pole cut-off frequency the constant parasitic capacitances drain more current and the resistive effect is progressively less influent; however the small variations of surface capacitance should be visible in a wide range of frequencies, as can be seen from Figure 5.2.
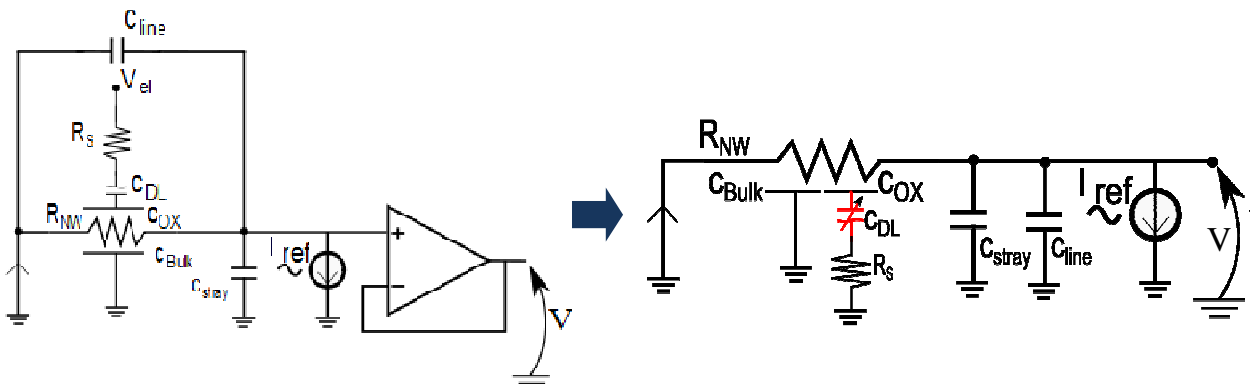
Figure 5.1 – Proposed nanowires simplified small-signal model with AC voltage sensing readout setup and rearranged version highlighting the variable capacitive effects of interest.
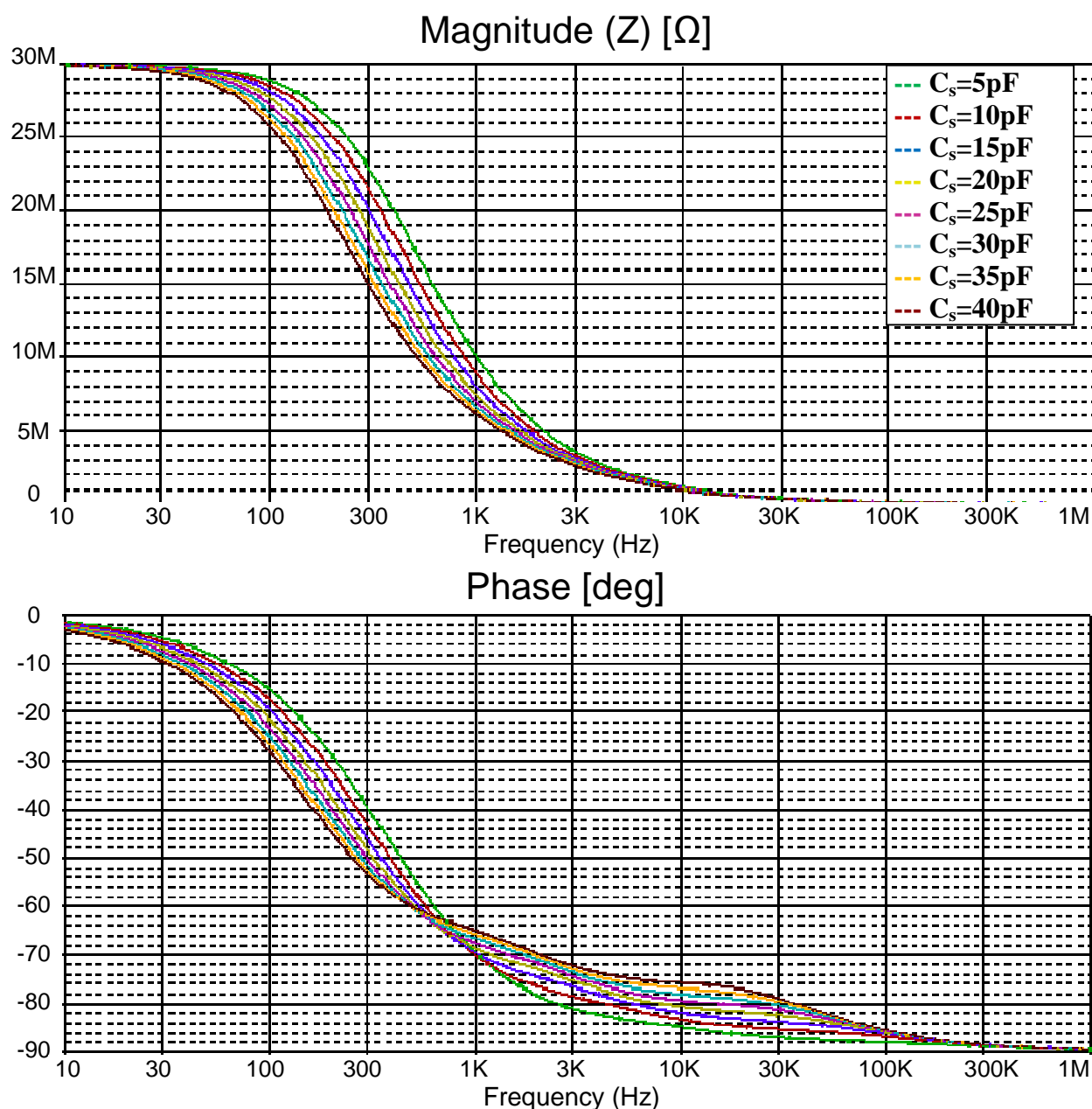
Figure 5.2 – Simulation performed using the simplified model stimulated by a current signal and performing the voltage sensing. These results demonstrate that the effect of surface capacitance could be read by phase shift data in a fixed range of measurements, corresponding to the frequencies where the impedance magnitude is attenuated, in particular enlarging the useful operating frequency of almost two decades with respect to magnitude data .

The following parameters were used in simulation:

$R=30M\Omega$ $C_{line}=2.5pF$ $C_{stray}=18pF$ $C_{bulk}=100fF$ $R_s=2M\Omega$ $R_{leakage=}100M\Omega$

Finally, some improvements were made from a system point of view, compared to the previously developed nanowires acquisition board; these are represented in Figure 5.3 and can be summarized in:

- Internal input voltage provided by the Field Programmable Gate Array (FPGA) module.
- A/D Conversion done by integrated $BP\Delta\Sigma$ Analog-to-Digital Converters in the developed integrated impedimetric system.
- USB power supply.
- Only visualization and data storage done by the PC, digital filtering done by FPGA.
- Working frequency selectable in the range 1 KHz- 25 KHz.
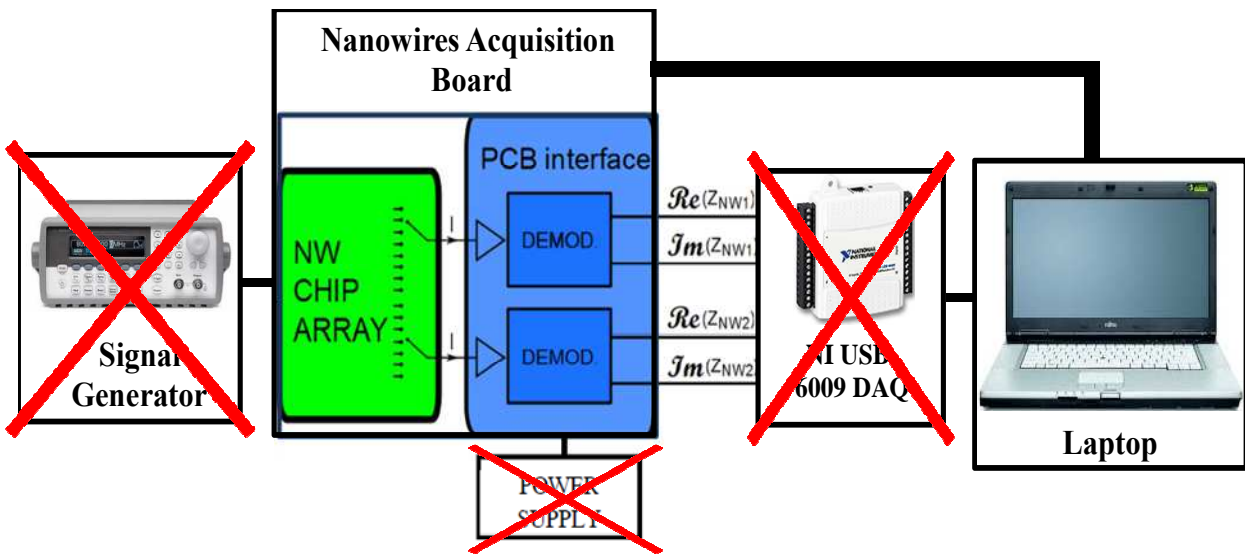
Figure 5.3 – Improvements of the system compared to the previously developed and presented nanowires acquisition board.

5.2   Integrated impedimetric interface

The integrated impedimetric interface used in the hybrid portable system have been designed and developed by the research group [47], [168]; it is specially tailored to high resolution impedance spectroscopy and it works by imposing a reference current at a certain frequency to the sensor under test and measuring the voltage response and then eventually sweeping the working frequency over a defined range of values.
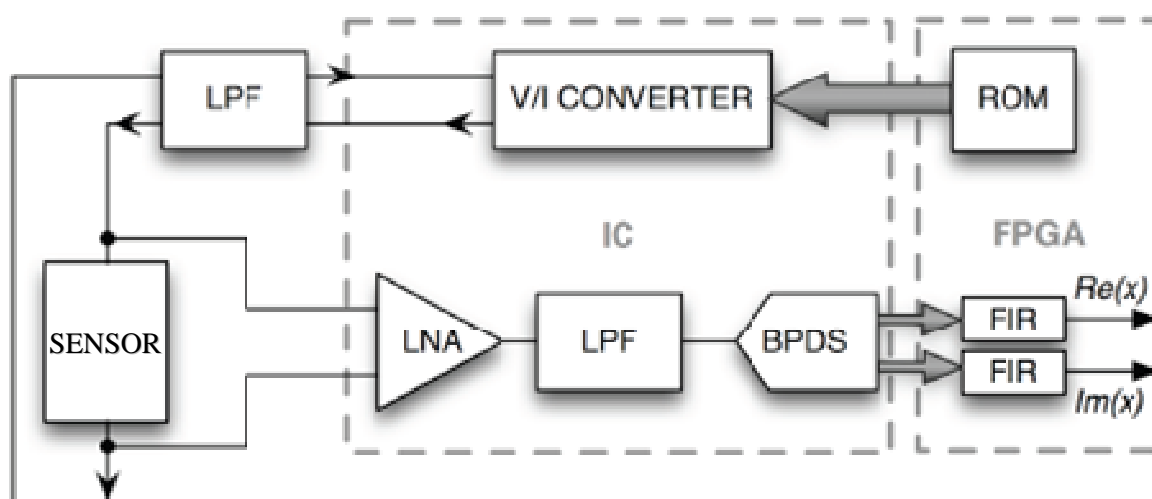
Figure 5.4 – Block diagram of the integrated impedimetric interface system developed by the research group [68].

The IC (block diagram shown in Figure 5.4, designed in 0.35 μm CMOS technology and 1.32mm^2 of area) host four identical cores and implements the lock-in technique based on a band-pass delta-sigma approach. Each core comprises an integrated fully-differential low-noise amplifier (LNA) followed by an anti-aliasing switched-capacitor filter and a band-pass delta-sigma (BPDS) analog-to-digital converter [169]; thus the demodulation is easily performed in digital domain by means of a couple of XOR gates, getting rid of the need of hard to design and sources of non-idealities and non-linearities analog multipliers, differently to other literature works where Gilbert cell mixers [170] or switched system [171] are used.

The delta-sigma converters are oversampling converter working at a sampling frequency much higher than the signal bandwidth. A delta sigma converter is generally composed of an integrator (which acts as a low pass filter), a comparator and a 1-bit DAC in the feedback loop. The main advantage of this circuit is the straight reduction of the in-band quantization noise thanks to the feedback loop and the oversampling operation, yielding a very high resolution [169], provided that the high frequency quantization noise resulting from the noise shaping is digitally filtered, usually using a cascade of finite impulse response (FIR) filters. This is

accomplished by the use of a field programmable gate array (FPGA) which digital filters and down-samples the 1-bit data streams to achieve the desired resolution.

Substituting the integrator with a band pass filter it is possible to implement a band pass delta sigma converter able to digitize narrowband signal modulated at a selectable frequency providing the real and imaginary part of the input signal. The developed solution implements a BPDS in the pseudo two path switched-capacitor architecture [172], [173], where the sampled in-phase and quadrature components of the sinusoidal input wave are sent alternatingly to two symmetric paths performing the multiplication by ±1, as shown in the working principle sketch represented in Figure 5.5.

In particular it must be noted that the sinusoidal input is sampled at a frequency $f_s=4 \cdot f_0$, thus the samples are exactly separated by a temporal shift of 1/4 of the sinusoidal input period, which is equivalent to 90° phase shift, between the samples going to one branch with respect to the other. This yields a single bit digital output given by the combination of the two digital data streams containing the in-phase and quadrature component of the input signal at a scalable frequency and proportional to the selectable modulating frequency; for instance with a working frequency of 1KHz the two real and imaginary parts streams have a frequency of 2KHz and are serialized in a unique output data stream of 4KHz frequency, which is sent to the FPGA.

The system can work using the scalability of the clock generated by a quartz oscillator embedded in the FPGA from 500 KHz to 12.5 MHz, enabling the possibility to select a modulating frequency in the range from 1 KHz to 25 KHz and thus resulting in output data streams in the range 4 KHz - 100 KHz.
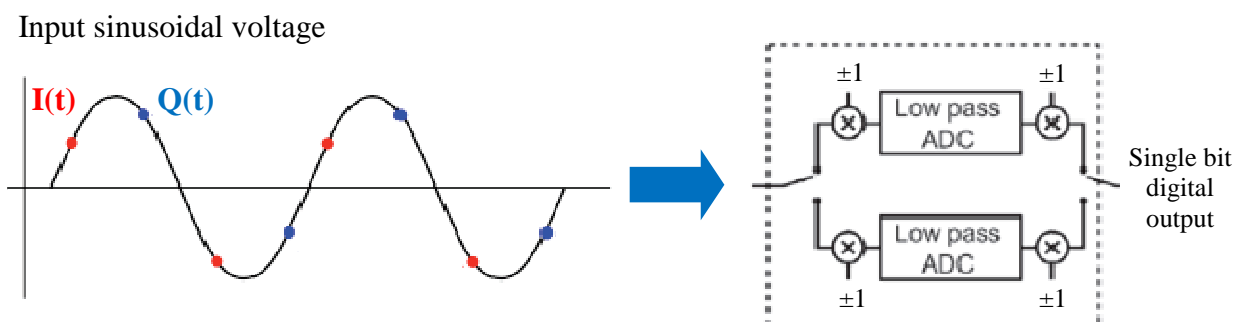
Figure 5.5 – Working principle sketch of the pseudo two path BPDS converter.

The input sinusoidal voltage signal is amplified by the frontend low noise amplifier (LNA) which uses a rather common capacitive fully differential architecture with the AC coupling at input pins that blocks the DC voltage and low voltage drift.

The implemented solution enables to select the gain among eight different values, respectively of 0.5, 1, 2, 5, 10, 20, 50, and 100, given by the ratio between the feedback and the

input capacitors, resulting in a high flexibility of the interface and enabling the use for different applications.

The gain is selectable by means of external control inputs which can be easily set by the developed software interface (see below). Usually, given the high variability of nanowires sensor impedance during the experiments, a gain of 1 was selected in order to achieve a high range of measurement.

Moreover as illustrated in Figure 5.4, in order to achieve a very high resolution of more than 15 bits [168], the designed IC is able to internally generate four sinusoidal stimulating-current signals of amplitude 10µA-150µA–300µA-1mA starting from the $\Delta\Sigma$ modulated signal stored in the ROM and using four replicated H-bridge based architectures to ensure the different amplitude current signal flowing across the DUT in both directions.

Given the high impedance values of the considered bio-nanosensor application this feature is not used in the developed portable system, which however uses the same basic principle of the generation of the current starting from the $\Delta\Sigma$ modulated signal, in order to maintain the synchronism with the readout architecture, as will be explained in next section.

Summing up the main features of the integrated impedimetric interface are:
- Internal generation of the input signal, in particular to achieve high resolution which is not strictly required for the considered application;
- AC voltage readout designed for Kelvin sensing;
- Integrated delta sigma modulation enabling the readout of sensor complex impedance;
- Demodulation easily performed in digital domain;
- Capability to operate in an array fashion thanks to the four cores layout;
- Flexible range of measurements to cope with different kind of sensors

5.3 Portable acquisition system design

As stated above, the minimum current amplitude internally generated by the developed integrated impedimetric interface is 10μA. Considering for instance a nanowire set with a resistance of 10 MΩ (typically the provided nanowires set resistance lie in the range 1 MΩ -100 MΩ) a 10μA amplitude input signal current would yield a voltage drop over the nanowires under test of 100 V_{AC}. In order to keep the voltage response low enough to be compatible to practical measurements, a discrete components-based off-chip current generator embedded in the PCB was thus needed to be implemented.

Moreover the frontend LNA of the integrated impedimetric interface has a maximum amplitude range of 900mV (considering the total system gain of 0.5). This means that a current as low as 90nA should be generated considering the same representative 10MΩ nanowires set and even lower if more resistive nanowires are considered. Designing such a low current generation circuit using discrete components is very challenging since parasitic effects strongly affect the performances of the circuit. Indeed in general high resistances are needed to obtain such low current values, but as higher is the resistance as higher is the probability that parasitics coupled to that resistance affect the system in the working bandwidth in the tens of KHz range.

Finally the signal at the input of the LNA has to be centered in the proper voltage bias (common mode voltage V_{cm}=1.65V)[168].

For these reasons the proposed trade off solution is based on the generation of a current in the order of some hundreds of nA to few μA (to ensure a limited voltage drop on the DUT) followed by a voltage level adapter stage which has the task to reduce the voltage signal coming from nanowires sensors and to adapt the signal to the proper DC voltage level compatible with the integrated impedimetric interface LNA input.

The developed solution is shown in Figure 5.6, which shows the complete block diagram of the developed PCB comprising the integrated impedimetric interface, the FPGA, the electronic circuit for off-chip current generation and voltage level adaptations and the module used to host and address the selectable nanowires set in the chip and the proper microfluidics, as presented above in section 3.6.2.

In particular the selected approach is based on the generation of the sinusoidal input signal starting from the ΔΣ modulated sine wave created using Matlab and memorized on a read only memory (ROM) in the FPGA. The squared wave voltage signal is then filtered, converted in the current signal and sent to the DUT. This ensures the perfect synchronization of the input signal frequency with the clock frequency that control the ΔΣ demodulation performed inside the microchip. This approach also enable to fine the initial phase shift during the calibration step,

which can be easily performed using a software interface controlling the FPGA, as explained below. The frequency synchronization indeed allows to be sure that the eventual initial phase shift between the input current and the output voltage is constant over the time and can be calibrated only once.

Finally, the system offers the possibility to perform parallel single-ended or differential measurements thanks to the two illustrated identical branches. For each of them a single nanowires set can be selected from the chip array and independently addressed by means of the switching system. The output voltage signal coming from each branch of the circuit is then read from one of the two AC coupled inputs of the integrated impedimetric interface fully differential LNA.

The developed measurement setup can be considered as a particular case of kelvin sensing in which one of the two terminals is kept at a fixed common voltage V_H while the other is sensed by the system (see Figure 5.7). This uncommon readout setup enables to perform either single ended (short-circuiting one of the two branches) or differential measurements for every core of the integrated impedimetric interface; thus, using this approach, one single integrated impedimetric interface chip composed of 4 cores is able to read up to eight nanowires sets in a differential fashion, or up to four in a single-ended parallel fashion.
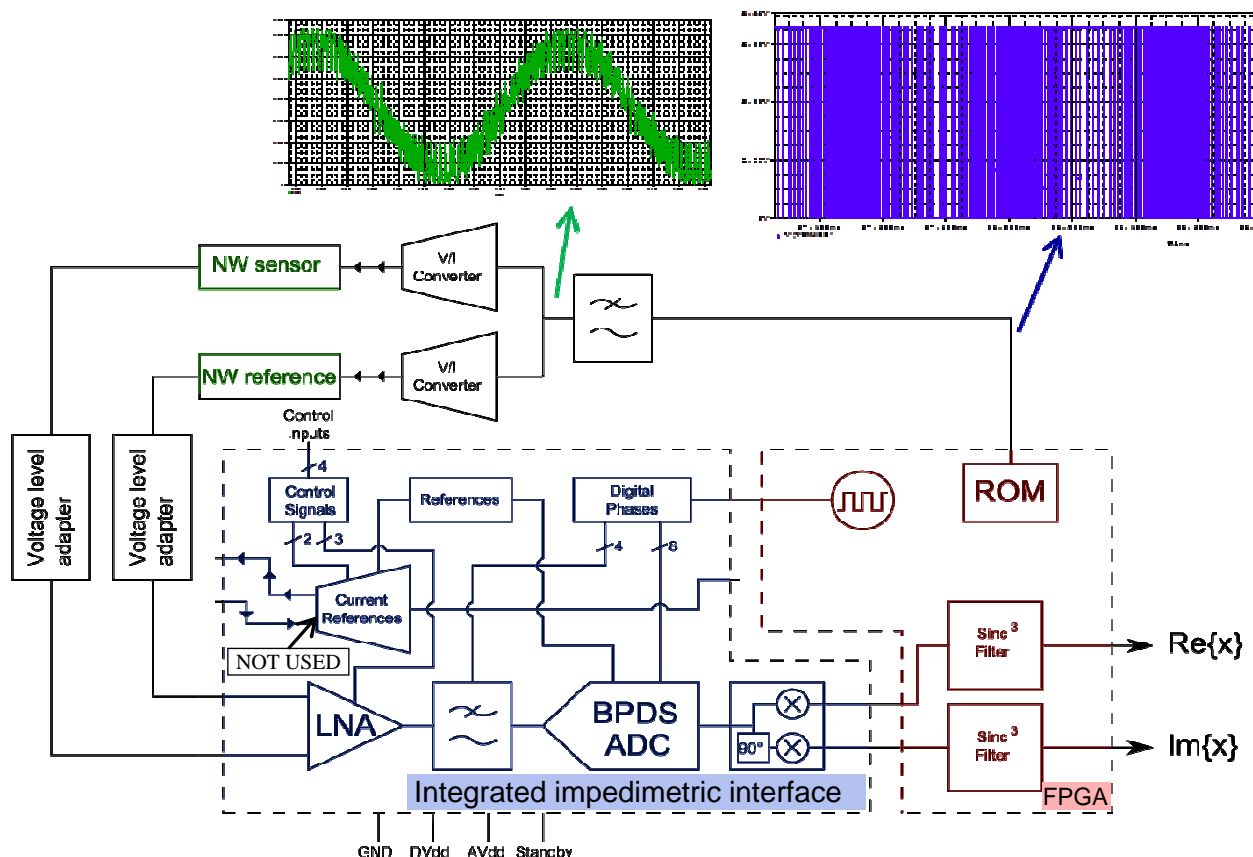
Figure 5.6 – Block diagram of the hybrid standalone portable system. The off-chip generation of the sinusoidal input signal starting from the ΔΣ modulated sine wave ensures the perfect synchronization of the input signal frequency with the clock frequency that control the ΔΣ demodulation.

The AC voltage-to-current converter enable to convert the input voltage signal to the selectable low current values to be send to the DUT.

Starting from the filtered ΔΣ modulated sine wave it generates a biased AC current given by:

$$I_{ref} = \frac{|V_I|}{R_I} + \frac{V_{ref}}{|Z_I|} \sin(\omega_0 t + \varphi) \qquad (5.1)$$

Where V_I is a user selectable negative voltage and V_{ref} is the amplitude of the filtered input sinusoidal wave, whose DC value is blocked by the coupling capacitor C_C and whose amplitude is selectable by means of the voltage divider (see Figure 5.7).
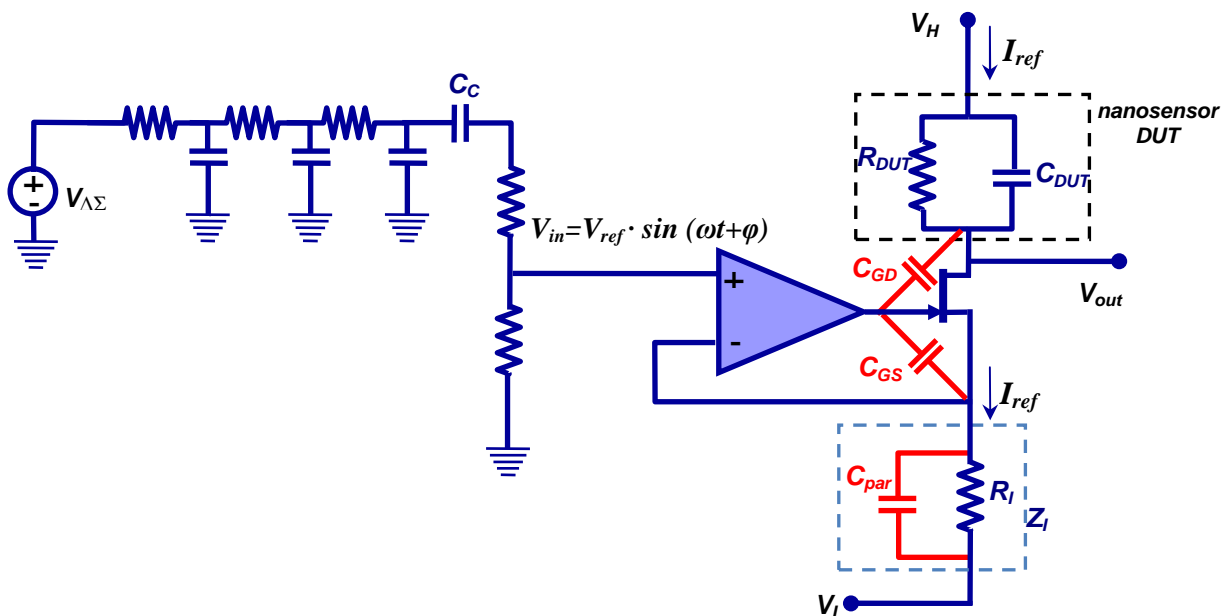
Figure 5.7 – Voltage to current converter and the related parasitics issues that have to be considered to maintain constant the low current amplitude value at the different frequencies.

As shown in the figure above, a rather common circuit was used; however some critical points must be pointed out.

Indeed, even if the simplest thing would be the use of a high R_I in order to achieve the needed low currents, an important aspect related to this kind of circuit using discrete components is to keep the R_I as lower as possible in order to reduce the effects given by parasitics in parallel to R_I. These parasitic capacitances indeed would affect the impedance Z_I, which sets the current amplitude value, resulting in a dependence of the amplitude on the frequency, with higher current flowing through the Z_I impedance at high frequencies.

On the other hand, in the implemented board, the negative voltage V_I is set by means of a potentiometer and thus cannot be too small in order to ensure a sufficient accuracy in the voltage (and thus in current) tuning.

For these reasons the value of R_I had to be dimensioned considering the maximum working frequency of 25KHz and a good trade-off value was found in the use of a R_I=100KΩ and setting a potential V_i=-100mV, thus resulting in a DC current of 1μA. Implementing, for instance, a voltage divider that yields a V_{ref} of 45mV, the current amplitude can be easily set to a constant value of 450nA.

The circuit was simulated using PSpice and experimentally tested with different transistors and the best trade-off was identified in the use of a JFET (in particular the BF245A [174]) thanks to its low gate-source and gate-drain capacitances, which can couple to the high values Z_{DUT}, and the high isolation between input and output given by the high input resistance.

Finally the voltage lever adapter stage attenuates the buffered output voltage signal V_{out} in order to maintain the signal inside the maximum allowed signal range of ±900mV and set the DC value at 1.65V as required by the LNA of the integrated impedimetric interface [168].

In particular, potentiometers in the two branches enable to accurately set the current levels and the gains of the voltage level adapters in order to achieve two perfectly identical branches during the calibration step.

The whole signal adapter chain was simulated using PSpice and implemented in the 4 layer PCB that composes a standalone hybrid portable system directly pluggable to the laptop for real time impedimetric measurements on nanowires biosensors using a kelvin sensing technique. Figure 5.8 shows a picture of the developed system whose main properties can be summarized in:

- Dimensions: 10 cm x 10 cm, 4 layers PCB;
- USB power supply, the board power supply is then raised to ±15 V_{DC} by means of a dual DC-DC converter [175] to ensure a high measurement range;
- pairs of identical and independent channels which enable differential (or single-ended) real time AC impedimetric measurements in the range 1 KHz- 25 KHz;
- eight different sinusoidal amplitude voltage ranges selectable by means of the developed custom software: 5.04V, 2.52V, 1.26V, 504mV, 252mV, 126mV, 50mV, 25mV;
- switching system to select single bio-nanosensors in a sensor array chip;
- modular approach with electronics separated by specific fluidics and enabling the easy interchangeability of different sensor chips;
- possibility to set both the potential of nanowires chip substrate and/or of the liquid gate electrode setting the potential of the electrolyte in which nanowires are immersed.
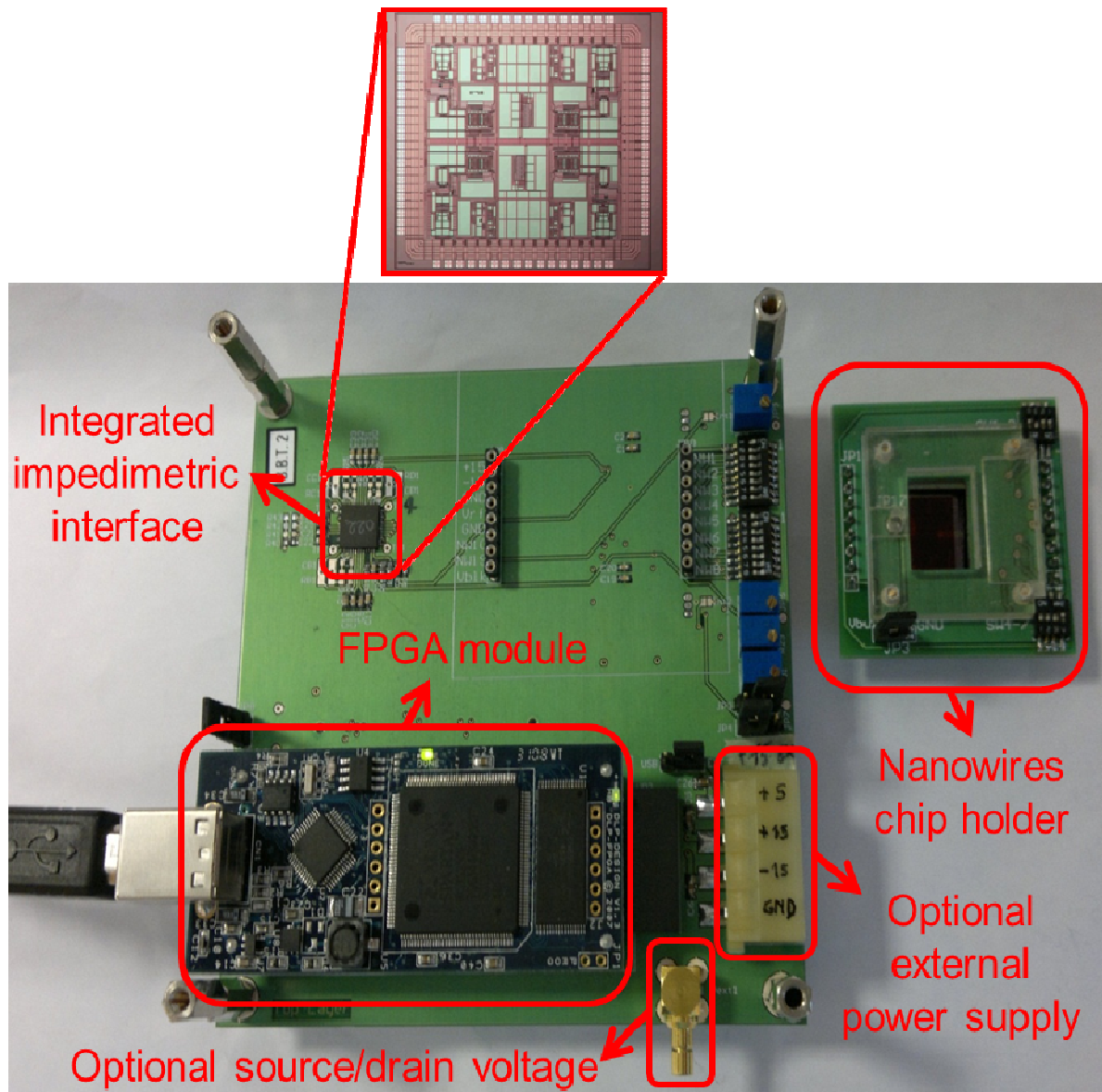
Figure 5.8 – Picture of the realized portable standalone acquisition system comprising the integrated impedimetric interface developed by the research group, the FPGA module and the nanosensor array holder module which connect the selectable bio-nanosensor to the readout electronics.

5.4   FPGA and Software interface

As explained above, to obtain the required resolution, the one bit data output of the BPDS converter has to be filtered and decimated by a digital elaboration system.

Given the possibility to implement in the system in a parallel approach [36], [113] thanks to the 4-cores integrated impedimetric interface the FPGA was selected as digital architecture thanks to its versatility and is suitability in applications were a potential high number of channel have to be elaborated simultaneously and at high frequency.

As illustrated in Figure 5.6 FPGA main tasks are:

- Generate the system clock using the embedded quartz oscillator at a selectable frequency in the range 500 KHz -12.5 MHz, which consequently changes the BPDS sampling frequency and the sinusoidal current stimulus frequency.

- Provide the 1 bit $\Delta\Sigma$ modulated sine wave generated using Matlab and memorized in the internal read only memory (ROM). This sine wave has a frequency that is proportional to the system clock, thus perfectly synchronized with the $\Delta\Sigma$ analog-to-digital converter.

- Real-time filter using an implemented Sinc^3 Filter for each data channel [176].
  The final bandwidth B of the output signal from the FPGA is given by:

$$B = \frac{f_s}{2 \cdot OSR} \tag{5.2}$$

  where f_s is the BPDS sampling frequency and the oversampling ration (OSR) is fixed at a value of 200 yielding a final signal bandwidth varying in the range 10 Hz – 250 Hz.

In particular, as stated above, the real and imaginary parts data streams are serialized by the BPDS and send as output in a unique data stream (OUT in Figure 5.9). In order to recover the two independent signal streams the FPGA read a synchronization signal (SYNC) provided by each core and samples the in-phase component during the rising edges of the SYNC signal and the quadrature component during the falling edges of SYNC signal, as represented in .
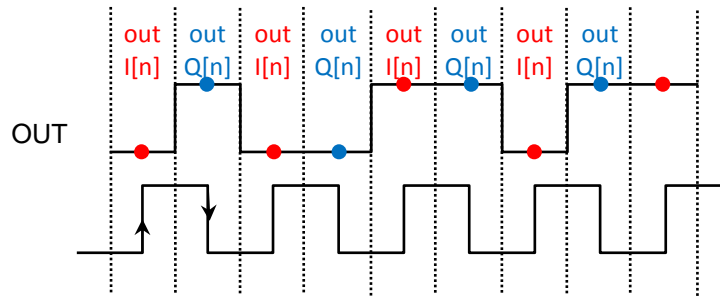
Figure 5.9 – Representation of the implemented protocol used by FPGA to recover the two serialized data streams coming from the BPDS and containing the in-phase (I) and quadrature (Q) components of the input signal, see Figure 5.5.

Moreover the integrated impedimetric interface is designed to be programmable using the SPI interface, which allows to enable and to program the four cores independently by means of control signals written by the FPGA to the selected core every time the user clicks on an option of the software interface, for instance to select the gain of the LNA.

The DLP-FPGA module [177] was selected as compact and low-cost device based on the Xilinx Spartan 3E FPGA, with a USB interface and a 50 pin connector for signals input/output. Figure 5.10 shows the picture and the block diagram of the module and the main features are listed below:
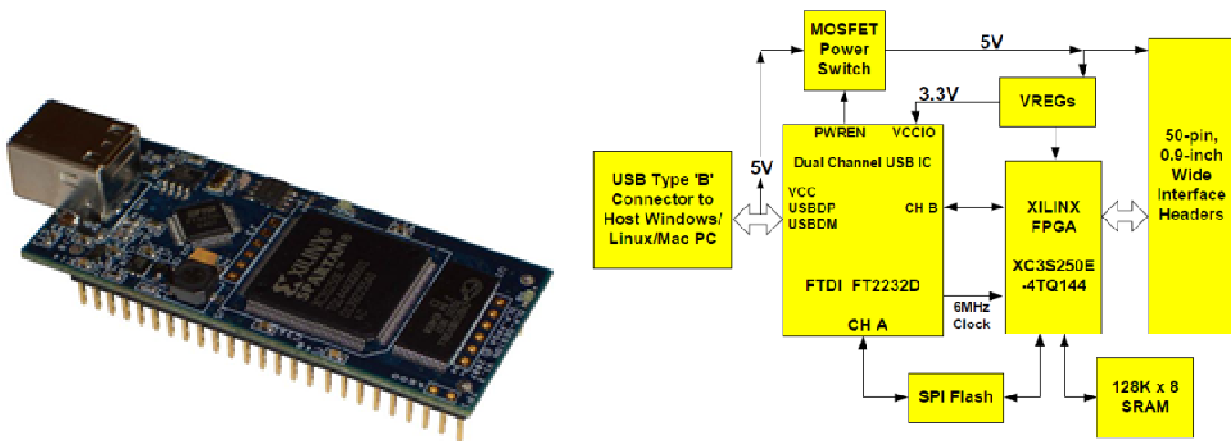
Figure 5.10 – Picture and block diagram of the DLP-FPGA module.

- FTDI FT2232D USB 2.0 full speed (12Mb/s) interface with 2 data ports;
- 250 kgate FPGA, 216 Kbit RAM (12x18 Kbit), 12 multipliers (18x18 bits), 4 DCMs clock resource;
- 40 I/O channels;
- SPI Flash for code download to self-programming;
- 128 KB SRAM;
- fully USB powered.

Moreover the manufacturer provides a configuration Loader which writes the .bit file directly to SPI Flash via full-speed USB interface for FPGA initialization, a screenshot of the interface is shown in Figure 5.11.
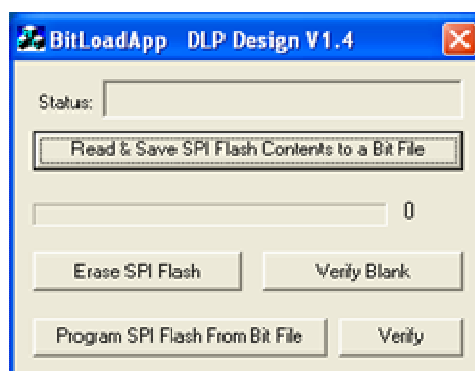
Figure 5.11 – Screenshot of the configuration loader software interface to program the SPI flash of the DLP-FPGA module.

The .bit file is created by means of development software tool ISE 10.1, provided by Xilinx, including all the simulation, mapping and routing tool to develop FPGA projects.

The whole standalone hybrid portable system is controlled by means of the developed custom data acquisition software designed in Java. It has a user-friendly interface, shown in Figure 5.12, enabling to easily control all the selectable options of the 4-cores integrated impedimetric interface, for instance the gain and the working frequency.
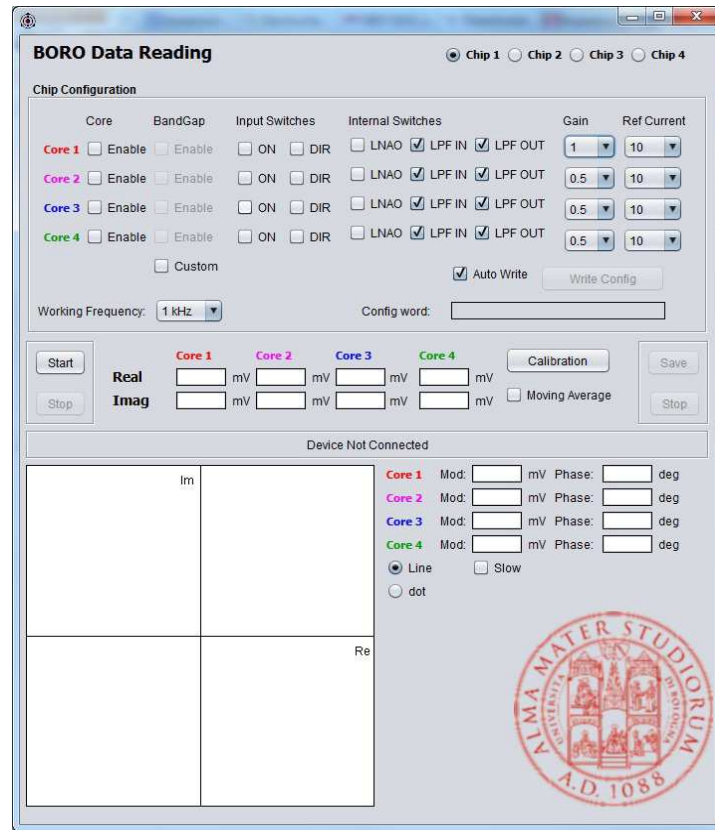
Figure 5.12 – Screenshot of the developed data acquisition software interface.

The start button opens the connection with the developed portable acquisition system connected to the USB port.

By means of dedicated buttons and scroll lists, each integrated impedimetric interface core can be configured and switched on independently by means of the configuration bytes sent via the USB connection to the FPGA, which writes them to the selected core by means of the SPI interface.

The software interface also collects and rescales to the correct voltage range the data streams from the impedimetric interface in order to graphically display them in a Nyquist plot and to calculate the modulus and the phase for real time analysis.

In particular, using an implemented feature, the initial phase shift can be calibrated to take into account the delays of the chip acquisition chain. This calibration is done practically by hardware by shifting the phase of the reference $\Delta\Sigma$ modulated sine wave bit stream generated by the FPGA, see Figure 5.6.

5.5   Calibration and testing

As first step, calibration of the system was performed using different values resistances, to test system performances and experimental ranges of measurements.

The reference current was set and experimentally measured as: $I_{ref} = 1\mu A + 0.45\mu A \cdot \sin(\omega_0 t + \varphi)$ and this value is the one used for all the experiments reported.

Moreover the two branches have to be calibrated in order to be sure that the two acquisition chains gains are exactly the same (see Figure 5.6). This is done performing single ended measurements on a selected resistance of 10 MΩ and short-circuiting one of the two branches alternatingly while setting the potentiometers in order to obtain the same magnitude value in the two cases.

In order to obtain a calibration curve, different resistances were connected to socket connector and measured by the system at a fixed frequency. Resistances values were previously measured using Keithley 6514 System Electrometer and the obtained values were considered as the actual ones.

Figure 5.13 shows, as an example, the calibration curve obtained by single-ended acquisitions of different resistor values using a working frequency of 1 KHz and setting the gain of the IC interface to 1. As can be clearly noted the measurements have the typical RC behaviour caused by parasitic capacitances in parallel to the DUT resistors.
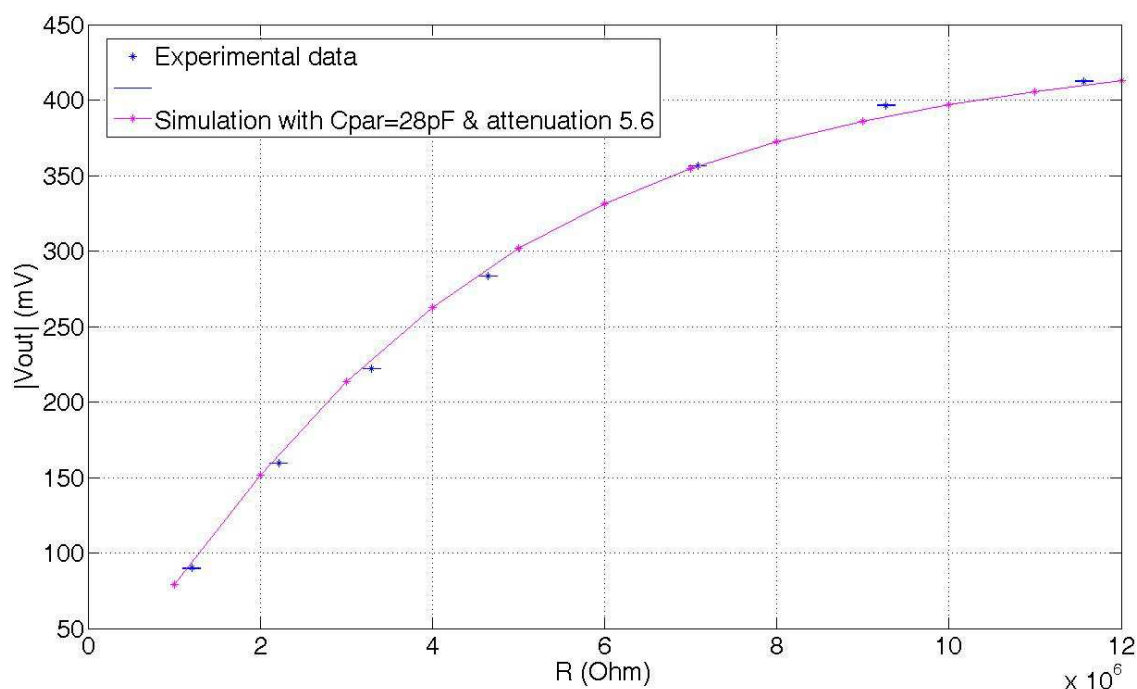
Figure 5.13 – Single ended measurements calibration curve at 1 KHz working frequency.

Performing PSpice simulations using a simple RC parallel equivalent circuit stimulated by a sinusoidal current signal of 450 nA of amplitude it was possible to obtain the magenta curve of the figure above that fit very well the experimental data, allowing to estimate the parasitics capacitance value of 28pF in parallel to the resistors under test.

By fitting the data with this method it was also possible to experimentally obtain the total acquisition chain attenuation of each branch, which resulted of 5.6 instead of the nominal value of 4.7.

In particular it must be noted that the 9.27 MΩ resistor used for the calibration was obtained soldering two resistors in series, therefore this particular DUT was affected differently from other single DUT resistors from parasitic capacitances. Accordingly, the experimental results clearly demonstrate a slight deviation of this point value from the curve obtained considering a parasitic capacitance of 28pF, demonstrating a very high sensitivity of the system.

Similarly, the calibration curve obtained performing differential measurements at 1 KHz, with an IC interface gain of 1 and using a 7.063 MΩ resistor as reference resistance while varying the other branch DUT is shown as example in Figure 5.14.
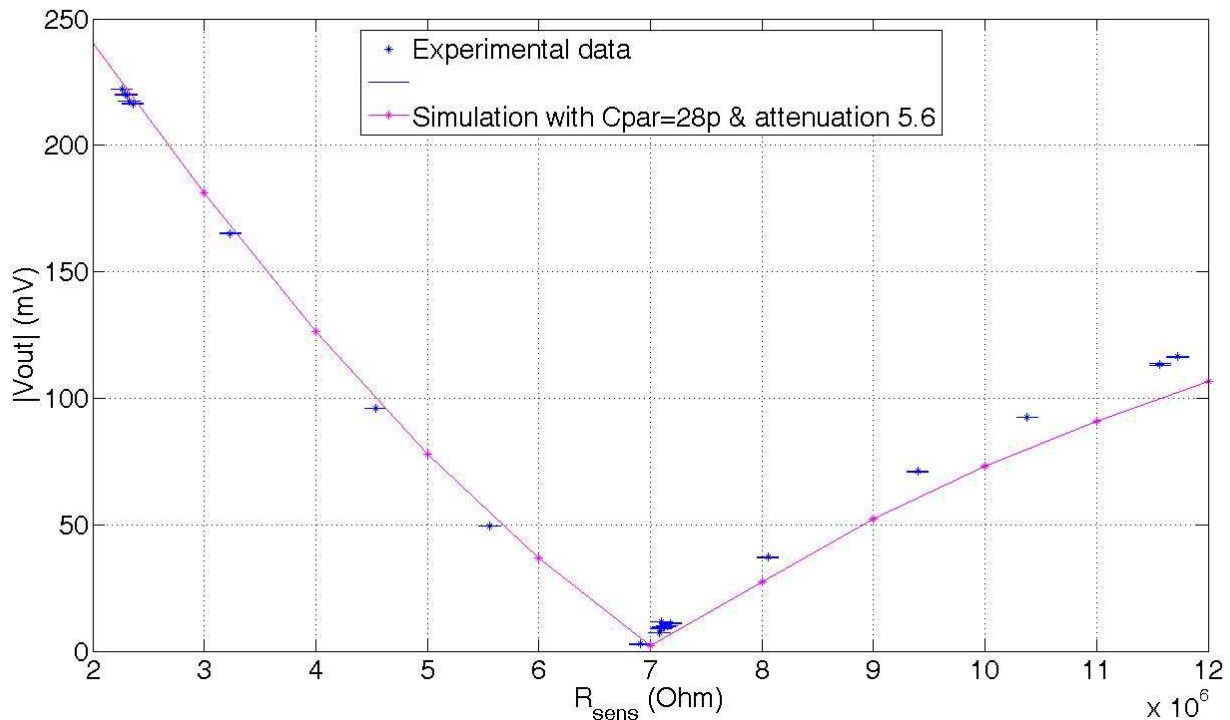
Figure 5.14 – Differential measurements calibration curve using a reference resistor of 7.063MΩ

The magenta curve of the figure above is obtained simply performing the differences between the simulation outputs of two RC parallel circuits maintaining fixed the resistance of one branch and sweeping the other and considering for both branches a parasitic capacitance

of 28pF. The slight deviation of the simulated results from the experimental ones for higher resistance values can be explained by a tiny parasitics effect differential value which is not considered in the simulations.

Moreover, as previously done for the nanowires acquisition board (see section 3.5.1), in order evaluate the system performances in terms of effective experimental resolutions (in ENOB) differential measurements using two nominally identical resistors of 7 MΩ (measurements of the two resistances using Keithley 6514 System Electrometer yielded values of 7.063 MΩ and 7.081 MΩ) in the two branches were performed at different working frequencies setting the gain of the LNA of the integrated circuit to 1.

Obtained values are reported in Table 5.1 and demonstrate, as expected, a lower accuracy compared to the very high one of 15-bits obtained in simulation [168] (and confirmed experimentally, data not yet published) considering the IC directly connected to low impedances and taking advantage of the capability of the internal generation of the reference current signal. This lower experimental resolution is attributed to the use of the off-chip signal adapter circuit, which however enable to use the integrated impedimetric interface to read high impedance values as the ones typical of nanowires biosensors maintaining a fair accuracy, sufficient for the purposes of the application. Moreover it must be noted that the experimentally considered case is the worst one, given to the fact that the noise of the two branches are summed in the differential measurement, while considering the single-ended measurement (short circuiting one of the two branches) the noise is lower, and thus an higher resolution is achieved.

Table 5.1: Experimental performances at different working frequencies

Frequency	1 KHz	2 KHz	4 KHz	8 KHz	16 KHz
ENOB Re	13.2	12.7	12.8	11.9	12
ENOB Im	13.3	12.6	12.7	11.8	11.6

As a proof of concept, Figure 5.15 shows the acquisition performed at 1 KHz, thus with a final signal bandwidth of 10 Hz.
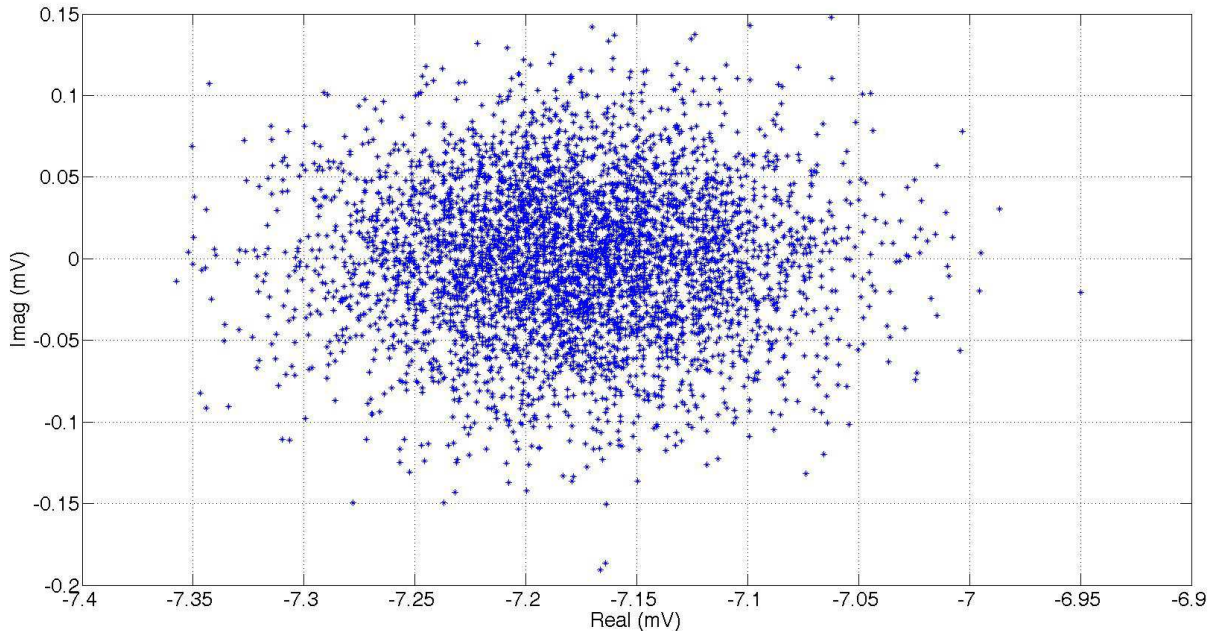
Figure 5.15 – Noise measurement performed in a differential fashion using two nominally identical resistors of 7 MΩ at 1 KHz working frequency and setting the LNA gain to 1.

5.6   Testing with Silicon NWs

After performing calibrations, it was possible to test the nanowires sensors with the developed portable system. First of all measurements in air were performed using the setup represented in Figure 5.16. The source was kept at a high constant voltage while the nanowire was stimulated by the reference AC current signal and the AC voltage at the drain contact was measured by the impedimetric interface. As stated above differential or single-ended measurements can be performed by the system, however in this thesis only the single ended case was considered.
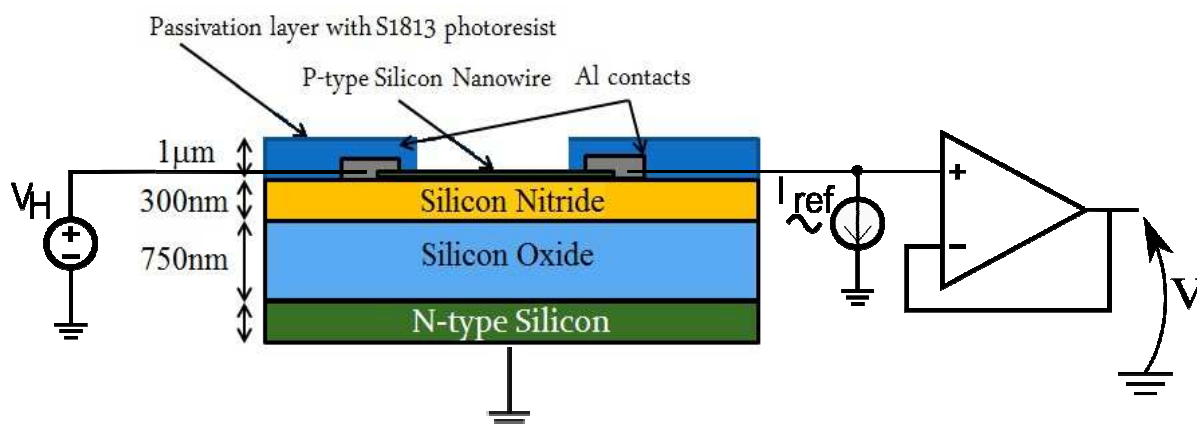
Figure 5.16 – Measurement setup using the developed portable system which can be considered as a particular case of kelvin sensing, in which one of the two terminals is kept at a fixed common voltage V_H while the other is sensed by the system and the nanowires are stimulated by an AC current signal.

In particular, considering the four central nanowires sets of the provided chips, an interesting result was noticed performing measurements at 1 KHz on the different nanowires set in air.

Indeed results show (Table 5.2 reports measurements on a representative test chip, as an example) as expected, a decrease in the nanowires set impedance for higher number of nanowires in parallel (which however do not decrease linearly, probably due to a non-homogeneous doping along the wafer or to a), but also and more interestingly a different phase shift depending on the particular nanowires set considered. As reported in table, the phase shifts are all referred to the phase shift measured by the system considering the first nanowires set (NW3).

Table 5.2: Experimental single-ended acquisitions of different central nanowires sets at 1 KHz working frequency

	NW 3	NW 4	NW 5	NW 6
Number of nanowires in parallel	50	80	70	60
Measured impedance (MΩ)	1.87	1.24	1.31	1.74
|Δ phase| (deg)	Reference	17	17	0

Differences in phases can be easily explained considering the layout of the provided nanowires chip and the fact that the more internal nanowires (called NW4 and NW5) are affected by the track-bulk capacitance, previously modelled as C_{stray}, by the track-track capacitance (C_{line}), but also by the coupling capacitance to the adjacent nanowires sets on both sides (represented in red in Figure 5.17), while conversely the external nanowires sets (called NW3 and NW6) are affected by this parasitic capacitance only on one side.

These results clearly demonstrate a high sensitivity of the system on parasitic capacitances, in particular since all result connected to bulk and, as noted, strongly affect the current source/voltage sensing measurements.

This effect, indeed, was not obtained using the nanowires acquisition board presented above in this thesis and considering the current sensing setup. This experimentally demonstrates that different device parasitic effect contributions can be measured, in particular using the phase shift data, depending on the sensing setup. Moreover, stating this effect, differential measurements can be performed in order to eliminate constant device parasitic effects.
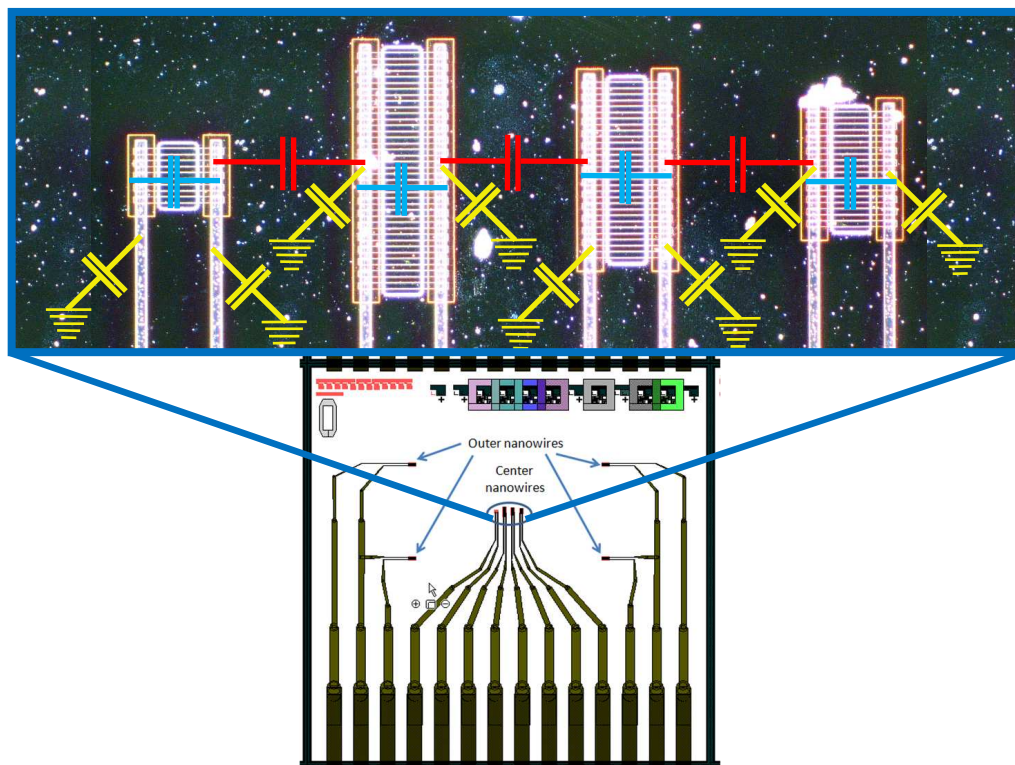
Figure 5.17 – Provided nanowires chips layout and detailed dark field picture of the central nanowires sets with overlapped the representation of parasitic capacitive contributions. The outer nanowires are not affected by the parasitic capacitance with the adjacent nanowires set (in red)

5.6.1   pH sensing

As previously done, pH measurements were performed on bare nanowires and real time AC measurements were performed using the developed portable standalone system, therefore stimulating the nanowires with a sinusoidal current and reading the output voltage.

A pseudo reference electrode was inserted in solution and the back gate and liquid gate contacts were fixed at V_H in order to maintain the same conditions ($V_{gs}=0$) of experiments performed using the previously described system based on current sensing.

A picture and a schematic representation of the experimental setup are shown in Figure 5.18.
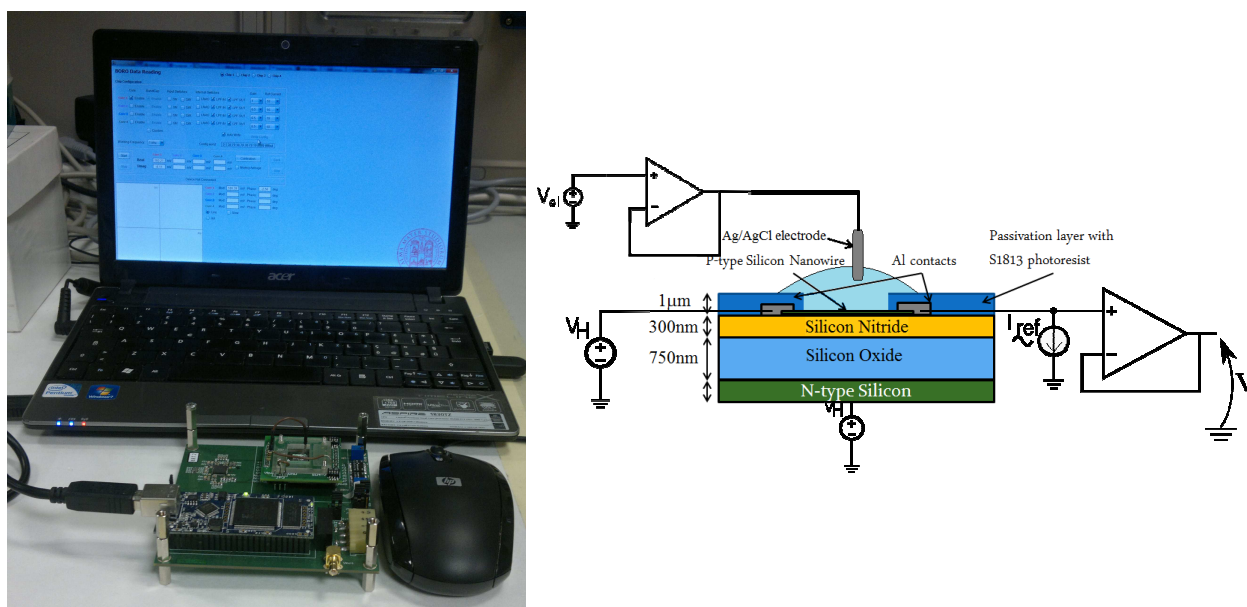
Figure 5.18 – Picture and schematic of the measurement setup for pH sensing experiments with constant liquid gating voltage that can be imposed by the developed portable system, while the nanowires are stimulated by an AC current signal.

Different pH levels (pH 4-11) sodium phosphate solutions at 10mM concentration were used. The final pH was obtained adding small concentrations (0.5-1 mM) of H_2SO_4 and NaOH.

In particular, these solutions were used in order to analyse if (and how) the Debye length affect the measurement of pH using the implemented AC kelvin sensing technique.
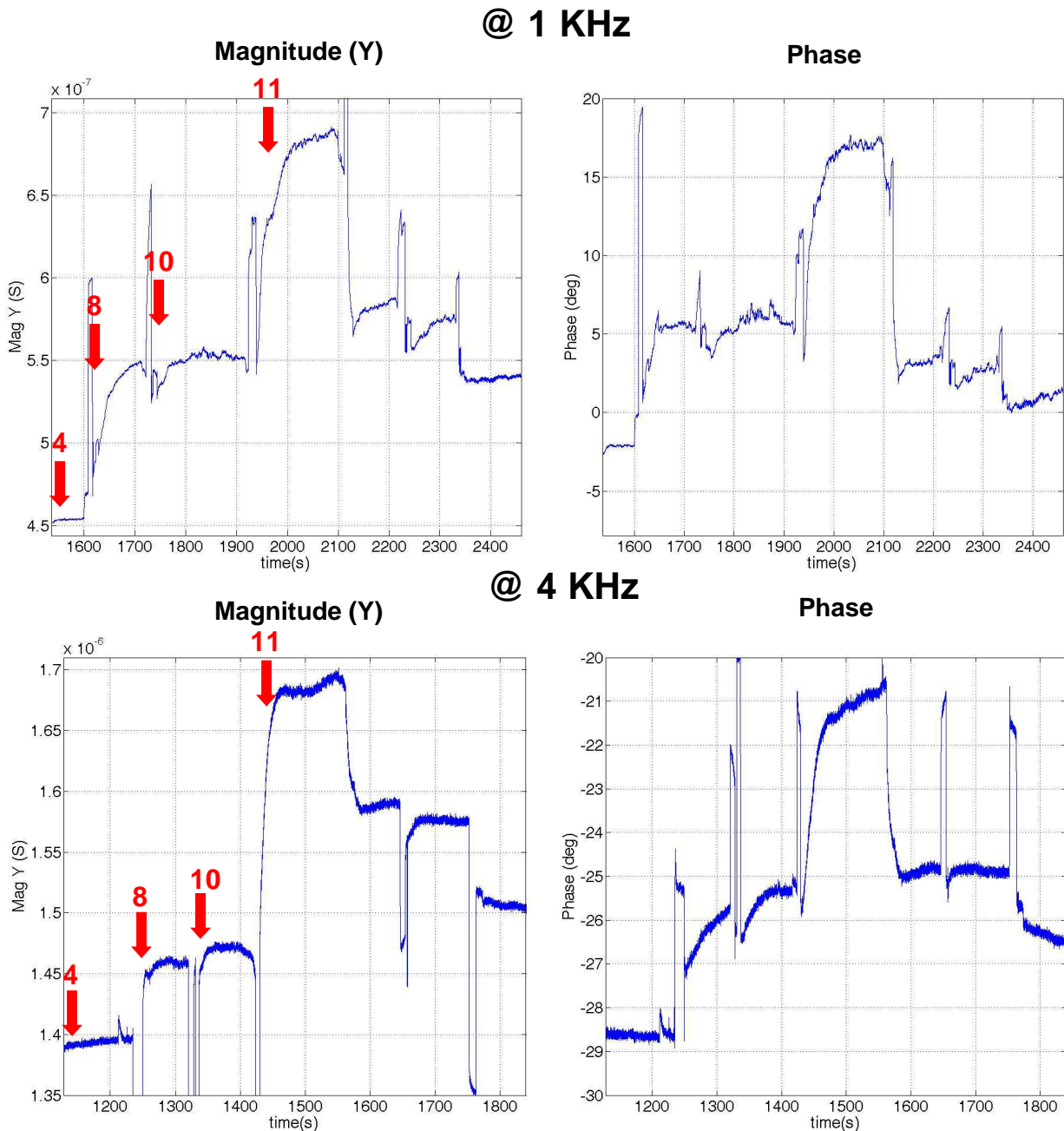
Figure 5.19 – AC real-time measurements of different pH level buffer solutions at two different working frequencies of 1 KHz and 4 KHz, using bare nanowires. Arrows show when the solution with the indicated pH level was changed.

As can be seen from figure, data are coherent with others previously obtained using the current sensing implemented before in the nanowires acquisition board (see section 3.8.2) and confirm the possibility to sense pH variations using the phase shift data as well as the impedance magnitude, even if the working point is dependent on the modulating frequency used.

The higher noise obtained setting the working frequency to 4 KHz is due to the fact that the final bandwidth at the output of the system is higher in this case compared to the 1 KHz case, respectively of 40 Hz and 10 Hz, as previously discussed.

Analysing the data and, in particular, referring the variations to the values obtained for the first pH value of 4 and normalizing the impedance magnitude and phase shift data for the respective full scale values (in order to calculate the comparable percentage variation), it was possible to obtain the values reported in Table 5.3. As observed qualitatively in section 3.8.2, considering the response at 1 KHz the percentage variations in magnitude results higher compared to the ones for phase shift; conversely, considering the data obtained using 4 KHz stimulating frequency, the behaviour is the opposite and the percentage variations, even if lower in absolute value due to attenuation given by the low pass filter behaviour, result higher for the phase shift data compared to the magnitude ones. This result indicates that the phase shift data can be effectively used to have similar information to the one obtained using the standard conductivity measurements; however there is a range of frequency in which the sensitivity is higher considering the phase shift data instead of the magnitude ones, as expected from simulations performed stimulating the developed equivalent model with an AC current signal.

Table 5.3: Experimental percentage variations for different pH solution

pH	1 KHz		4 KHz	
	$(|Z|-|Z_0|)/FS(Z)$ %	$(Ph-Ph_0)/FS(Ph)$ %	$(|Z|-|Z_0|)/FS(Z)$ %	$(Ph-Ph_0)/FS(Ph)$ %
4	0	0	0	0
8	6.5	4.3	0.6	1.3
10	7.1	4.6	0.7	1.8
11	13.2	10.6	2.2	4.2

Moreover, experimental data shown that only a slight variation is achieved between the pH 8 and pH 10 solutions, on the contrary to the one obtained previously using the nanowires acquisition board (see Figure 3.29). However this result is explainable calculating the Debye length of the used solutions and analysing the data considering also these values. The obtained values are reported in Table 5.4.

Table 5.4: Calculated Debye length for the different pH solutions 10mM used.

Solution	pH	λ_D
$Na_2HPO_4+H_2SO_4$	4.1	1.3 nm
Na_2HPO_4	8.3	1.5 nm
Na_2HPO_4+NaOH	10.3	1.6 nm
NaOH	11.3	3 nm

Figure 5.20 clearly shows the dependence of both the magnitude and phase shift to the Debye length of the electrolyte solutions and can easily explain the very slight sensitivity of the sensor to the variation between the pH 8 and pH10 levels.
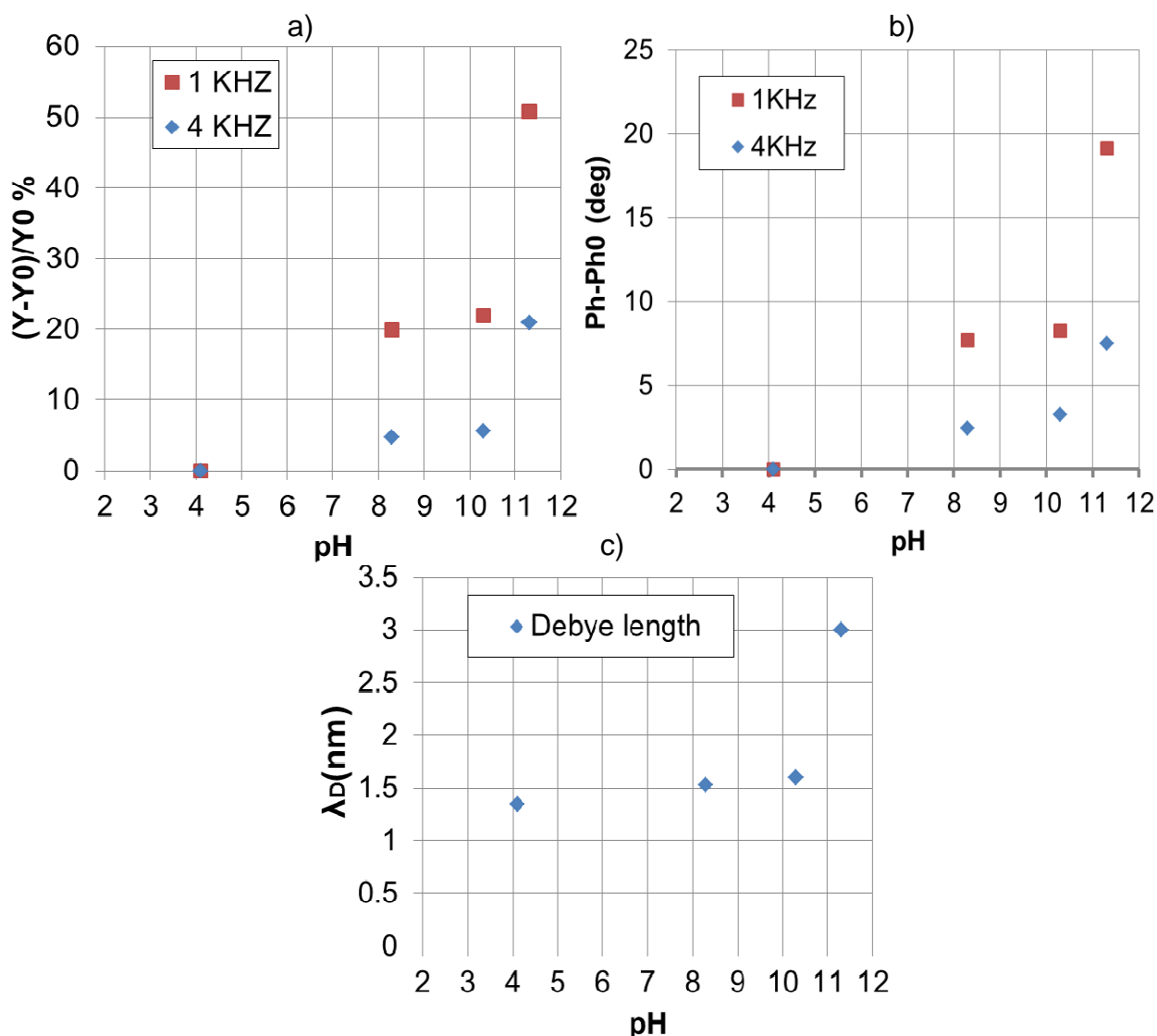
Figure 5.20 – Experimental values of different pH level buffer solutions, obtained by the mean levels of real time AC measurements once stabilized, at two different working frequencies of 1 KHz and 4 KHz, using bare nanowires. a) Percentage variation of admittance magnitude referred to the pH 4 value. b) Phase shift variations referred to the pH 4 value. c) Debye lengths of the different 10mM solutions.

Similar results, in terms of response to different pH and Debye lengths, were also obtained considering 1mM solutions with the pH adjusted by adding small concentrations of NaOH. Our hypothesis is that this stronger sensitivity to Debye length (and thus to the surface capacitance variations) than to the pH level, not shown using the current sensing method (as reported in section 4.6) can be attributed to the fact that in this case we stimulated the device with an AC current, while performing a voltage sensing. This measurement setup indeed is differently affected by capacitive contributions and thus, for instance, more sensitive to double layer

variations compared to the voltage applied/current sensing setup, as resulted from simulations performed using the simplified developed nanowires model.

Additional supporting experiments are currently performed to better investigate if the effective dependency of these results to particular solutions and Debye length used has to be attributed to the measurement setup or to the particular strong base (NaOH) used and to the possible related anions adsorption mechanism, very recently addressed by Tarasov et al. [150].

Conclusions and Future Perspectives

This thesis has been aimed at demonstrating real implementation of three examples of compact hybrid readout systems designed and developed for rapid and low cost analysis of different kind of bio-nanosensors. These custom systems merge a dedicated microfluidic and a custom electronic readout setup in order to perform tests in the experimental liquid environment using both DC and AC regimes.

The systems were calibrated and tested performing typical experimental studies to prove the effective response for the needs of new emerging and promising bio-nanosensor technologies.

The first system is a complete, compact hybrid system which enabled the automatic and simultaneous formation of arrays of bilayer lipid membranes for biological nanopores investigations by means of the developed low-cost programmable liquid handling system and the fine-tuned protocol. This addresses the needs of parallel readout on ion channels for drug screening and DNA sequencing, without the use of highly expensive laboratories instrumentations and the need of highly skilled personnel.

The two other compact and portable systems that have been presented are enable to perform tests on nanowires field effect devices in a user friendly and rapid fashion. In particular the two systems implementing the lock-in detection are based on complementary measurements techniques which enable to perform experiments stimulating the bio-nanosensors using a DC or a AC voltage or AC current signal and to investigate if and how the measurement technique affects the system response.

Experiments were performed to characterize the sensor response with respect to different environmental stimulus and for biosensing of specific detection of biomarkers molecules.

In particular the AC stimulation was used to investigate if phase shift data can be useful and enrich informations with respect to standard DC measurements, basically performing impedance analysis (in real time and in frequency sweeps mode) to sense capacitance variations on the surface of nanowires biosensors with the final aim to better understand the behaviour at sensor-electrolyte interface.

Experimental acquired data confirmed the effectiveness of phase shift data in the nanowire based sensing of different solution pH values and of specific molecular bindings depending on the particular input signal operating frequency used, adding information to the standardly used nanowires conductivity data.

144

In particular results have shown that phase shift data could be used to understand and characterize the structure of molecular functionalization layer on the surface of the nanosensor FET device which changes the resulting surface capacitance, suggesting that the method could be also used to directly probe biomolecular interaction, for instance the antigen-antibody binding or DNA hybridization close to the functionalized nanowires surface, giving informations on the distance of the charges from the surface.

A semi-empirical equivalent simplified nanowires model based on physical devices characteristics has been developed and implemented in PSpice in order to quickly analyse how the changes of different parameters related to physical device properties affect the response of the sensor and explain the obtained experimental results.

As demonstrated, it is able to qualitatively catch the overall behavioural response of the nanowires sensors and understand different contributions of the different physical parameters to phase shifts at the different frequencies

However, since FET devices are fundamentally transducers of surface potential variations it is not easy to experimentally decouple surface capacitive effects by the ones related to the changes of conductivity of the device. As known from literature, the impact of the surface charge is dependent on the surface-to-volume ratio of the device and the sensitivity to variations of surface charge decreases with the increase of nanowires dimensions; this would also mean that, considering bigger devices, the variation of nanowires resistance would be more sensitive to surface capacitance variations (which are proportional to the exposed surface) than to the surface charge variations. For this reason the analysis done on the surface capacitance variations could be even more effective for devices in which the surface exposed to liquid environment is bigger such, as nanoribbons.

The model also enabled to predict the response of the device at different working frequencies showing the strong dependence of the sensitivity to surface changes on the devices parasitics, and therefore on the particular measurement setup used, since parasitic capacitances affect the measurements in a different way thus moving the poles and zeros of the system.

Future perspectives are aimed at using the developed systems to better understand the device complex impedance response at different kinds of bio-chemical stimuli and validate the model with further experimental results, eventually changing some geometric and physical characteristics of the nanodevices under test.

Finally, further studies exploring the effectiveness of differential measurements on adjacent nanowires will be performed once nanowires sensors fabrication process yields less variability on nominally identical devices. All the presented bio-nanosensors indeed are very promising since can be easily investigated with the developed systems in an array fashion, however other

problem related to this kind of measurements arises such as the need of a strong uniformity over the biosensors, problem that increase as much as the sensor device becomes smaller and sensitive.

Moreover, from a system point of view, it should be noted that by adding a different analog front-end amplifier to the impedimetric impedance interface and maintaining the same analog-to-digital conversion architecture, for instance integrating a low noise current amplifier as the one previously developed by the research group, the same approach could be used to develop a complementary portable system able to stimulate the nanosensor device either with an AC voltage signal (and read the current signal) or with an AC current signal (and read the voltage signal), eventually switching between the current sensing and the voltage sensing method, in order to address a broader number of applications and nanosensor devices and better investigate how the particular readout technique can highlight devices response.

Acknowledgements

First and foremost I would like thank Prof. Marco Tartagni for his encouragement and availability during the entire Ph.D. course. He has been my guide and he always believed in me.

Secondly all my colleagues of the research group for their inestimable suggestions and fruitful and peaceful team work; in particular Federico for his initiative and support and Marco Bennati and Crescentini for their useful advices and guidelines on the electronic design.

A special thanks to Prof. Hywell Morgan for having me accommodated in his amazing laboratory at the University of Southampton. Working together with Marta Lombardini was really worthwhile and amusing at the same time, also when the experiments were disappointing.

A very important thank to my parents for their unconditional love and encouragement and to my few but good friends.

Last but not least I would like to thank a very special person, Isabella, with whom I have shared every good and bad moment of the last ten years.

Index of abbreviations

αHL	Alpha Hemolysin
ADC	Analog to Digital Converter
Ag/AgCl	Silver/Silver Chloride
ASIC	Application Specific Integrated Circuit
βCD	Beta Cyclodextrin
BLMs	Bilayer Lipid Membranes
CNC	Computer Numerical Control
CE	Counter Electrode
ΔΣ	Delta Sigma
DSP	Digital Signal Processing
EIS	Electrochemical Impedance Spectroscopy
FIR	Finite Impulse Response digital filter
FPGA	Field Programmable Gate Array
gA	Gramicidin A
GUI	Graphical User Interface
HTS	High Throughput Screening
IC	Integrated Circuit
ISFET	Ion-Sensitive Field-Effect-Transistor
KCl	Potassium Chloride buffer solution
LNA	Low Noise Amplifier
LPF	Low Pass Filter
NWs	Nanowires
OSR	Oversampling Ratio
PBS	Phosphate Buffered Saline
PCB	Printed Circuit Board
SNR	Signal to Noise Ratio
USB	Universal Serial Bus
WE	Working Electrode

Bibliography

[1]   E. A. H. Hall, *Biosensors*. Englewood Cliffs, N.J.: Prentice Hall, 1991.

[2]   J. Labuda, A. M. O. Brett, G. Evtugyn, M. Fojta, M. Mascini, M. Ozsoz, I. Palchetti, E. Paleček, and J. Wang, "Electrochemical nucleic acid-based biosensors: Concepts, terms, and methodology (IUPAC Technical Report)," *Pure and Applied Chemistry*, vol. 82, no. 5, pp. 1161–1187, Apr. 2010.

[3]   D. Thévenot, K. Toth, R. Durst, and G. Wilson, "Electrochemical biosensors: recommended definitions and classification," *Biosensors and Bioelectronics*, vol. 16, pp. 121–131, 2001.

[4]   A. J. Bard and L. J. Faulkner, *Electrochemical Methods: Fundamentals and Applications*, 2nd ed. New York: Wiley, 2001.

[5]   J. S. Daniels and N. Pourmand, "Label-Free Impedance Biosensors: Opportunities and Challenges," *Electroanalysis.*, vol. 19, no. 12, pp. 1239–1257, 2007.

[6]   E. Stern, R. Wagner, F. J. Sigworth, R. Breaker, T. M. Fahmy, and M. A. Reed, "Importance of the Debye Screening Length on Nanowire Field Effect Transistor Sensors," *Nano letters*, vol. 7, no. 11, pp. 3405–3409, 2007.

[7]   B. Jang, S. Member, and A. Hassibi, "Biosensor Systems in Standard CMOS Processes : Fact or Fiction ?," vol. 56, no. 4, pp. 979–985, 2009.

[8]   Keithley Instruments Inc., Ed., *Nanotechnology Measurement Handbook*, 1st ed. Keithley Instruments, 2010.

[9]   "QuantuMDx Devices." [Online]. Available: http://www.quantumdx.com/devices.html. [Accessed: 09-Mar-2013].

[10]   D. Grieshaber, R. MacKenzie, J. Voeroes, and E. Reimhult, "Electrochemical biosensors-Sensor principles and architectures," *Sensors*, no. January, pp. 1400–1458, 2008.

[11]   M. J. Schöning and A. Poghossian, "Bio FEDs (Field-Effect Devices): State-of-the-Art and New Directions," *Electroanalysis*, vol. 18, no. 19–20, pp. 1893–1900, Oct. 2006.

[12]   A. Hassibi and T. Lee, "A programmable 0.18-μm cmos electrochemical sensor microarray for biomolecular detection," *IEEE Sensors Journal*, vol. 6, no. 6, pp. 1380–1388, 2006.

[13]   W. H. Coulter, "Means for counting particles suspended in a fluid." 20-Oct-1953.

[14]   M. TARTAGNI, M. ROSSI, and N. MANARESI, "APPARATUS AND METHOD FOR COUNTING AND IDENTIFYING PARTICLES OF INTEREST IN A FLUID." 12-Jun-2009.

[15]   B. M. Venkatesan and R. Bashir, "Nanopore sensors for nucleic acid analysis.," *Nature nanotechnology*, vol. 6, no. 10, pp. 615–24, Oct. 2011.

[16]   F. Thei, "A Hybrid Technology for Parallel Recording of Single Ion Channels," *Ph.D. dissertation, ARCES, University of Bologna, Bologna, IT*, 2011.

[17]   J. Clarke, H. Wu, L. Jayasinghe, and A. Patel, "Continuous base identification for single-molecule nanopore DNA sequencing," *Nature …*, no. February, 2009.

[18]   J. J. Kasianowicz, E. Brandin, D. Branton, and D. W. Deamer, "Characterization of individual polynucleotide molecules using a membrane channel.," *Proceedings of the National Academy of Sciences of the United States of America*, vol. 93, no. 24, pp. 13770–3, Nov. 1996.

[19]   H. Bayley and P. S. Cremer, "Stochastic sensors inspired by biology.," *Nature*, vol. 413, no. 6852, pp. 226–30, Sep. 2001.

[20]   R. Capone, S. Blake, M. R. Restrepo, J. Yang, and M. Mayer, "Designing nanosensors based on charged derivatives of gramicidin A.," *Journal of the American Chemical Society*, vol. 129, no. 31, pp. 9737–45, Aug. 2007.

[21]   E. N. Ervin, R. J. White, and H. S. White, "Sensitivity and signal complexity as a function of the number of ion channels in a stochastic sensor.," *Analytical chemistry*, vol. 81, no. 2, pp. 533–7, Jan. 2009.

[22]   R. Sherman-Gold, *The Axon Guide*. Axon Instruments, 2008.

[23]   J. D. Uram, K. Ke, and M. Mayer, "Noise and bandwidth of current recordings from submicrometer pores and nanopores.," *ACS nano*, vol. 2, no. 5, pp. 857–72, May 2008.

[24]   J. J. Clare, "Targeting ion channels for drug discovery.," *Discovery medicine*, vol. 9, no. 46, pp. 253–60, Mar. 2010.

[25]   S. Blake, *Designing Nanosensors Based on Ion Channel-forming Derivatives of Gramicidin A*. ProQuest, 2008, p. 135.

[26]   L. Song, M. R. Hobaugh, C. Shustak, S. Cheley, H. Bayley, and J. E. Gouaux, "Structure of staphylococcal alpha-hemolysin, a heptameric transmembrane pore.," *Science (New York, N.Y.)*, vol. 274, no. 5294, pp. 1859–66, Dec. 1996.

[27]   R. J. C. Gilbert, "Pore-forming toxins.," *Cellular and molecular life sciences : CMLS*, vol. 59, no. 5, pp. 832–44, May 2002.

[28]   E. Neher and B. Sakmann, *Single-channel recording*, 2nd ed. New York :: Plenum Press,, 1995.

[29]   V. Krishnamurthy, K. Y. Luk, B. Cornell, J. Prashar, I. L. di Maio, H. Islam, A. R. Battle, S. M. Valenzuela, and D. K. Martin, "Gramicidin Ion Channel-Based Biosensors: Construction, Stochastic Dynamical Models, and Statistical Detection Algorithms," *IEEE Sensors Journal*, vol. 7, no. 9, pp. 1281–1288, Sep. 2007.

[30]   A. Hirano, M. Wakabayashi, Y. Matsuno, and M. Sugawara, "A single-channel sensor based on gramicidin controlled by molecular recognition at bilayer lipid membranes containing receptor.," *Biosensors & bioelectronics*, vol. 18, no. 8, pp. 973–83, Aug. 2003.

[31]   G. Baaken, N. Ankri, A.-K. Schuler, J. Rühe, and J. C. Behrends, "Nanopore-based single-molecule mass spectrometry on a lipid membrane microarray," *ACS Nano*, vol. 5, no. 10, pp. 8080–8088, Apr. 2011.

[32]   E. N. Ervin, R. Kawano, R. J. White, and H. S. White, "Simultaneous Alternating and Direct Current Readout of Protein Ion Channel Blocking Events Using Glass Nanopore Membranes," *Analytical Chemistry*, vol. 80, no. 6, pp. 2069–2076, Mar. 2008.

[33]   T. Osaki, H. Suzuki, B. Le Pioufle, and S. Takeuchi, "Multichannel simultaneous measurements of single-molecule translocation in alpha-hemolysin nanopore array," *Analytical chemistry*, vol. 81, no. 24, pp. 9866–70, Dec. 2009.

[34]   M. Zagnoni, M. E. Sandison, and H. Morgan, "Microfluidic array platform for simultaneous lipid bilayer membrane formation.," *Biosensors & bioelectronics*, vol. 24, no. 5, pp. 1235–40, Jan. 2009.

[35] M. Rincon-Restrepo, E. Mikhailova, H. Bayley, and G. Maglia, "Controlled translocation of individual DNA molecules through protein nanopores with engineered molecular brakes.," *Nano letters*, vol. 11, no. 2, pp. 746–50, Feb. 2011.

[36] M. Rossi, F. Thei, and M. Tartagni, "A parallel sensing technique for automatic bilayer lipid membrane arrays monitoring," *Sensors & Transducers*, vol. 14–1, pp. 185–196, 2012.

[37] R. Smeets, U. Keyser, M. Wu, N. Dekker, and C. Dekker, "Nanobubbles in Solid-State Nanopores," *Physical Review Letters*, vol. 97, no. 8, p. 088101, Aug. 2006.

[38] C. Ho, R. Qiao, J. B. Heng, A. Chatterjee, R. J. Timp, N. R. Aluru, and G. Timp, "Electrolytic transport through a synthetic nanometer-diameter pore.," *Proceedings of the National Academy of Sciences of the United States of America*, vol. 102, no. 30, pp. 10445–50, Jul. 2005.

[39] J. Liu, M. Kvetny, J. Feng, D. Wang, B. Wu, W. Brown, and G. Wang, "Surface charge density determination of single conical nanopores based on normalized ion current rectification.," *Langmuir : the ACS journal of surfaces and colloids*, vol. 28, no. 2, pp. 1588–95, Jan. 2012.

[40] J. Li, D. Stein, C. McMullan, D. Branton, M. J. Aziz, and J. A. Golovchenko, "Ion-beam sculpting at nanometre length scales.," *Nature*, vol. 412, no. 6843, pp. 166–9, Jul. 2001.

[41] C. Dekker, "Solid-state nanopores.," *Nature nanotechnology*, vol. 2, no. 4, pp. 209–15, Apr. 2007.

[42] G. F. Schneider and C. Dekker, "DNA sequencing with nanopores.," *Nature biotechnology*, vol. 30, no. 4, pp. 326–8, Apr. 2012.

[43] C. Sathe, X. Zou, J.-P. Leburton, and K. Schulten, "Computational investigation of DNA detection using graphene nanopores.," *ACS nano*, vol. 5, no. 11, pp. 8842–51, Nov. 2011.

[44] M. Drndic, "Nanopore Graphene-based Electronic Devices," *Bulletin of the American Physical Society*, vol. Volume 58,, Mar. 2013.

[45] A. K. Geim and K. S. Novoselov, "The rise of graphene.," *Nature Materials*, vol. 6, no. 3, pp. 183–191, 2007.

[46] A. Kleefen, D. Pedone, C. Grunwald, R. Wei, M. Firnkes, G. Abstreiter, U. Rant, and R. Tampé, "Multiplexed Parallel Single Transport Recordings on Nanopore Arrays," *Nano letters*, vol. 2025, pp. 5080–5087, Oct. 2010.

[47] M. Crescentini, "Advanced CMOS Interfaces for Bio-Nanosensors," *Ph.D. dissertation, ARCES, University of Bologna, Bologna, IT*, 2012.

[48] G. Shen, B. Liang, X. Wang, H. Huang, D. Chen, and Z. L. Wang, "Ultrathin In2O3 Nanowires with Diameters below 4 nm: Synthesis , Reversible Wettability Switching Transistor Applications," *ACS Nano*, no. 8, pp. 6148–6155, 2011.

[49] D. R. Khanal, J. W. L. Yim, W. Walukiewicz, and J. Wu, "Effects of quantum confinement on the doping limit of semiconductor nanowires.," *Nano letters*, vol. 7, no. 5, pp. 1186–90, May 2007.

[50] J. l. Arlett, E. b. Myers, and M. l. Roukes, "Comparative advantages of mechanical biosensors," *Nature Nanotechnology*, vol. 6, no. 4, pp. 203–215, Apr. 2011.

[51] K. Balasubramanian, "Challenges in the use of 1D nanostructures for on-chip biosensing and diagnostics: a review.," *Biosensors & bioelectronics*, vol. 26, no. 4, pp. 1195–204, Dec. 2010.

[52] N. Elfström, A. E. Karlström, and J. Linnros, "Silicon nanoribbons for electrical detection of biomolecules.," *Nano letters*, vol. 8, no. 3, pp. 945–9, Mar. 2008.

[53]   a. Tarasov, W. Fu, O. Knopfmacher, J. Brunner, M. Calame, and C. Schönenberger, "Signal-to-noise ratio in dual-gated silicon nanoribbon field-effect sensors," *Applied Physics Letters*, vol. 98, no. 1, p. 012114, 2011.

[54]   E. Stern, A. Vacic, N. K. Rajan, J. M. Criscione, J. Park, B. R. Ilic, D. J. Mooney, M. a Reed, and T. M. Fahmy, "Label-free biomarker detection from whole blood.," *Nature nanotechnology*, vol. 5, no. 2, pp. 138–42, Feb. 2010.

[55]   A. Vacic, J. M. Criscione, N. K. Rajan, E. Stern, T. M. Fahmy, and M. a Reed, "Determination of molecular configuration by debye length modulation.," *Journal of the American Chemical Society*, vol. 133, no. 35, pp. 13886–9, Sep. 2011.

[56]   K.-I. Chen, B.-R. Li, and Y.-T. Chen, "Silicon nanowire field-effect transistor-based biosensors for biomedical diagnosis and cellular recording investigation," *Nano Today*, vol. 6, no. 2, pp. 131–154, Apr. 2011.

[57]   H. K. Chang, F. N. Ishikawa, R. Zhang, R. Datar, R. J. Cote, M. E. Thompson, and C. Zhou, "Rapid, Label-Free, Electrical Whole Blood Bioassay Based on Nanobiosensor Systems," *ACS nano*, 2011.

[58]   V. Krivitsky, L.-C. Hsiung, A. Lichtenstein, B. Brudnik, R. Kantaev, R. Elnathan, A. Pevzner, A. Khatchtourints, and F. Patolsky, "Si Nanowires Forest-Based On-Chip Biomolecular Filtering, Separation and Preconcentration Devices: Nanowires Do it All," *Nano Letters*, vol. 12, no. 9, pp. 4748–4756, Oct. 2012.

[59]   S. J. Tans, A. R. M. Verschueren, and C. Dekker, "Room-temperature transistor based on a single carbon nanotube," vol. 393, no. 6680, pp. 49–52, May 1998.

[60]   A. D. Franklin, M. Luisier, S.-J. Han, G. Tulevski, C. M. Breslin, L. Gignac, M. S. Lundstrom, and W. Haensch, "Sub-10 nm Carbon Nanotube Transistor," *Nano Letters*, vol. 12, no. 2, pp. 758–762, 2012.

[61]   F. Schwierz, "Graphene transistors.," *Nature nanotechnology*, vol. 5, no. 7, pp. 487–96, Jul. 2010.

[62]   Y. Cui, Q. Wei, H. Park, and C. M. Lieber, "Nanowire Nanosensors for Highly Sensitive and Selective Detection of Biological and Chemical Species," *Science*, vol. 293, no. 5533, pp. 1289–1292, Mar. 2001.

[63]   G. Zheng, F. Patolsky, Y. Cui, W. U. Wang, and C. M. Lieber, "Multiplexed electrical detection of cancer markers with nanowire sensor arrays.," *Nature Biotechnology*, vol. 23, no. 10, pp. 1294–1301, 2005.

[64]   F. Patolsky, G. Zheng, and C. M. Lieber, "Fabrication of silicon nanowire devices for ultrasensitive, label-free, real-time detection of biological and chemical species," *Nature Protocols*, vol. 1, no. 4, pp. 1711–1724, Mar. 2006.

[65]   F. Patolsky, G. Zheng, O. Hayden, M. Lakadamyali, X. Zhuang, and C. M. Lieber, "Electrical Detection of Single Viruses," *Proceedings of the National Academy of Sciences of the United States of America*, vol. 101, no. 39, pp. 14017–14022, Mar. 2004.

[66]   E. Stern, J. F. Klemic, D. a Routenberg, P. N. Wyrembak, D. B. Turner-Evans, A. D. Hamilton, D. a LaVan, T. M. Fahmy, and M. a Reed, "Label-free immunodetection with CMOS-compatible semiconducting nanowires.," *Nature*, vol. 445, no. 7127, pp. 519–22, Feb. 2007.

[67]   N. S. Ramgir, Y. Yang, and M. Zacharias, "Nanowire-Based Sensors," *Small*, vol. 6, no. 16, pp. 1705–1722, 2010.

[68] M. Curreli, R. Zhang, F. N. Ishikawa, H.-K. Chang, R. J. Cote, C. Zhou, and M. E. Thompson, "Real-Time, Label-Free Detection of Biological Entities Using Nanowire-Based FETs," *IEEE Transactions on Nanotechnology*, vol. 7, no. 6, pp. 651–667, May 2008.

[69] A. Liu, "Towards development of chemosensors and biosensors with metal-oxide-based nanowires or nanotubes.," *Biosensors & bioelectronics*, vol. 24, no. 2, pp. 167–77, Oct. 2008.

[70] G. S. Kulkarni and Z. Zhong, "Detection beyond the Debye Screening Length in a High-Frequency Nanoelectronic Biosensor," *Nano Lett.*, vol. 12, no. 2, pp. 719–723, 2012.

[71] G. Zheng, X. P. a Gao, and C. M. Lieber, "Frequency domain detection of biomolecules using silicon nanowire biosensors.," *Nano letters*, vol. 10, no. 8, pp. 3179–83, Aug. 2010.

[72] I. Park, Z. Li, A. P. Pisano, and R. S. Williams, "Top-down fabricated silicon nanowire sensors for real-time chemical detection.," *Nanotechnology*, vol. 21, no. 1, p. 015501, Jan. 2010.

[73] M. M. A. Hakim, M. Lombardini, K. Sun, F. Giustiniano, P. L. Roach, D. E. Davies, P. H. Howarth, M. R. R. de Planque, H. Morgan, and P. Ashburn, "Thin Film Polycrystalline Silicon Nanowire Biosensors," *Nano Lett.*, 2012.

[74] S. Chen, J. G. Bomer, W. G. van der Wiel, E. T. Carlen, and A. van den Berg, "Top-Down Fabrication of Sub-30 nm Monocrystalline Silicon Nanowires Using Conventional Microfabrication," *ACS Nano*, vol. 3, no. 11, pp. 3485–3492, 2009.

[75] S. Choi, I. Park, Z. Hao, H.-Y. N. Holman, and A. P. Pisano, "Quantitative studies of long-term stable, top-down fabricated silicon nanowire pH sensors," *Applied Physics A*, Mar. 2012.

[76] O. Knopfmacher, D. Keller, M. Calame, and C. Schönenberger, "Dual Gated Silicon Nanowire Field Effect Transistors," *Procedia Chemistry*, vol. 1, no. 1, pp. 678–681, Sep. 2009.

[77] O. Knopfmacher, a Tarasov, W. Fu, M. Wipf, B. Niesen, M. Calame, and C. Schönenberger, "Nernst limit in dual-gated Si-nanowire FET sensors.," *Nano letters*, vol. 10, no. 6, pp. 2268–74, Jun. 2010.

[78] M.-P. Lu, C.-Y. Hsiao, W.-T. Lai, and Y.-S. Yang, "Probing the sensitivity of nanowire-based biosensors using liquid-gating," *Nanotechnology*, vol. 21, no. 42, Apr. 2010.

[79] S. Kim, T. Rim, K. Kim, U. Lee, E. Baek, H. Lee, C.-K. Baek, M. Meyyappan, M. J. Deen, and J.-S. Lee, "Silicon nanowire ion sensitive field effect transistor with integrated Ag/AgCl electrode: pH sensing and noise characteristics," *Analyst*, vol. 136, no. 23, pp. 5012–5016, Jan. 2011.

[80] A. Tarasov, W. Fu, O. Knopfmacher, J. Brunner, M. Calame, and C. Schönenberger, "Signal-to-noise ratio in dual-gated silicon nanoribbon field-effect sensors," *Applied Physics Letters*, vol. 98, no. 1, Feb. 2011.

[81] G.-J. Zhang, K. T. C. Chai, H. Z. H. Luo, J. M. Huang, I. G. K. Tay, A. E.-J. Lim, and M. Je, "Multiplexed detection of cardiac biomarkers in serum with nanowire arrays using readout ASIC," *Biosensors & bioelectronics*, vol. 35, no. 1, pp. 218–223, May 2012.

[82] S. Reza, G. Bosman, S. Member, M. S. Islam, T. I. Kamins, S. Sharma, and R. S. Williams, "Noise in Silicon Nanowires," vol. 5, no. 5, pp. 523–529, 2006.

[83] A. Bid, A. Bora, and A. Raychaudhuri, "1/f noise in nanowires," *Nanotechnology*, pp. 1–5, 2005.

[84] M. Crescentini, M. Bennati, and M. Tartagni, "Recent Trends for (Bio)Chemical Impedance Sensor Electronic Interfaces," *Electroanalysis*, vol. 24, no. 3, pp. 563–572, Mar. 2012.

[85] *About Lock-In Amplifiers*, no. 408. Stanford Research Systems.

154

[86]   Y.-S. Yang, "The electrical signals measurement for nanowire field effect transistors," *2011 Fifth International Conference on Sensing Technology*, pp. 599–602, Nov. 2011.

[87]   W. C. Maki, N. N. Mishra, E. G. Cameron, B. Filanoski, S. K. Rastogi, and G. K. Maki, "Nanowire-transistor based ultra-sensitive DNA methylation detection.," *Biosensors & bioelectronics*, vol. 23, no. 6, pp. 780–7, Jan. 2008.

[88]   Y. Zhao, S. Inayat, D. a Dikin, J. H. Singer, R. S. Ruoff, and J. B. Troy, "Patch clamp technique: review of the current state of the art and potential contributions from nanoengineering," *Proceedings of the Institution of Mechanical Engineers, Part N: Journal of Nanoengineering and Nanosystems*, vol. 222, no. 1, pp. 1–11, Jan. 2008.

[89]   H. T. Tien, *Bilayer lipid membranes (BLM): theory and practice*. New York: Marcer Dekker, 1974.

[90]   B. Hille, *Ion Channels of Excitable Membranes*. Sinauer, 2001, p. 814.

[91]   J. P. Overington, B. Al-Lazikani, and A. L. Hopkins, "How many drug targets are there?," *Nature reviews. Drug discovery*, vol. 5, no. 12, pp. 993–6, Dec. 2006.

[92]   Dr. Schulze GmbH, *EPC 10 / EPC 10 USB Patch Clamp Amplifier*. HEKA Elektronik, 2011.

[93]   J. Dunlop, M. Bowlby, R. Peri, D. Vasilyev, and R. Arias, "High-throughput electrophysiology: an emerging paradigm for ion-channel screening and physiology," *Nature reviews. Drug discovery*, vol. 7, no. 4, pp. 358–68, Apr. 2008.

[94]   F. Thei, M. Rossi, M. Bennati, M. Crescentini, F. Lodesani, H. Morgan, and M. Tartagni, "Parallel Recording of Single Ion Channels: A Heterogeneous System Approach," *IEEE Transactions on Nanotechnology*, vol. 9, no. 3, pp. 295–302, May 2010.

[95]   M. Rossi, F. Thei, H. Morgan, and M. Tartagni, "A Disposable Microfluidic Array Platform for Automatic Ion Channel Recording," *Proceedings of the MicroTAS 2010*, pp. 1913–1915, 2010.

[96]   M. Bennati, F. Thei, M. Rossi, M. Crescentini, G. D'Avino, A. Baschirotto, and M. Tartagni, "A Sub-pA ΔΣ Current Amplifier for Single-Molecule Nanosensors," in *Solid-State Circuits Conference - Digest of Technical Papers, 2009. ISSCC 2009. IEEE International*, 2009, pp. 348–349.

[97]   F. Thei, M. Rossi, and E. Giordano, "A Multichannel Electrophysiology Workbench for Single Ion Channel Screening," *Biophysical Journal*, vol. 102, no. 3, p. 581a–582a, 2012.

[98]   M. E. Sandison, M. Zagnoni, and H. Morgan, "Air-exposure technique for the formation of artificial lipid bilayers in microsystems.," *Langmuir : the ACS journal of surfaces and colloids*, vol. 23, no. 15, pp. 8277–84, Jul. 2007.

[99]   V. C. Stimberg, J. G. Bomer, I. van Uitert, A. van den Berg, and S. Le Gac, "High Yield, Reproducible and Quasi-Automated Bilayer Formation in a Microfluidic Format.," *Small (Weinheim an der Bergstrasse, Germany)*, no. iv, pp. 1–10, Nov. 2012.

[100]   M. Montal and P. Mueller, "Formation of Bimolecular Membranes from Lipid Monolayers and a Study of their Electrical Properties," *Proceedings of the National Academy of Sciences*, vol. 69, no. 12, pp. 3561–3566, Dec. 1972.

[101]   A. Hirano-Iwata, T. Nasu, A. Oshima, Y. Kimura, and M. Niwano, "Lipid bilayer array for simultaneous recording of ion channel activities," *Applied Physics Letters*, vol. 101, no. 2, p. 023702, 2012.

[102]   "Society for Laboratory Automation and Screening - ANSI/SLAS Microplate Standards." [Online]. Available: http://www.slas.org/education/microplate.cfm. [Accessed: 27-Dec-2012].

[103] F. Thei, M. Rossi, M. Bennati, M. Crescentini, and M. Tartagni, "An automatic offset correction platform for high-throughput ion-channel electrophysiology," in *Procedia Engineering*, 2010, vol. 5, no. 0, pp. 816–819.

[104] S. Furini, C. Domene, M. Rossi, M. Tartagni, and S. Cavalcanti, "Model-based prediction of the alpha-hemolysin structure in the hexameric state.," *Biophysical journal*, vol. 95, no. 5, pp. 2265–74, Sep. 2008.

[105] L. Q. Gu and H. Bayley, "Interaction of the noncovalent molecular adapter, beta-cyclodextrin, with the staphylococcal alpha-hemolysin pore.," *Biophysical journal*, vol. 79, no. 4, pp. 1967–75, Oct. 2000.

[106] D. A. Kelkar and A. Chattopadhyay, "The gramicidin ion channel: a model membrane protein.," *Biochimica et biophysica acta*, vol. 1768, no. 9, pp. 2011–25, Sep. 2007.

[107] A. Finkelstein and O. S. Andersen, "The gramicidin A channel: a review of its permeability characteristics with special reference to the single-file aspect of transport.," *The Journal of membrane biology*, vol. 59, no. 3, pp. 155–71, Apr. 1981.

[108] G. Andrew Woolley and B. A. Wallace, "Model ion channels: Gramicidin and alamethicin," *The Journal of Membrane Biology*, vol. 129, no. 2, Aug. 1992.

[109] S. B. Hladky and D. A. Haydon, "Ion transfer across lipid membranes in the presence of gramicidin A," *Biochimica et Biophysica Acta (BBA) - Biomembranes*, vol. 274, no. 2, pp. 294–312, Aug. 1972.

[110] D. D. Busath, C. D. Thulin, R. W. Hendershot, L. R. Phillips, P. Maughan, C. D. Cole, N. C. Bingham, S. Morrison, L. C. Baird, R. J. Hendershot, M. Cotten, and T. A. Cross, "Noncontact dipole effects on channel permeation. I. Experiments with (5F-indole)Trp13 gramicidin A channels.," *Biophysical journal*, vol. 75, no. 6, pp. 2830–44, Dec. 1998.

[111] T. W. Allen, O. S. Andersen, and B. Roux, "Energetics of ion conduction through the gramicidin channel.," *Proceedings of the National Academy of Sciences of the United States of America*, vol. 101, no. 1, pp. 117–22, Jan. 2004.

[112] M. Lee, K. Y. Baik, M. Noah, Y.-K. Kwon, J.-O. Lee, and S. Hong, "Nanowire and nanotube transistors for lab-on-a-chip applications," *Lab on a Chip*, vol. 9, no. 16, May 2009.

[113] G.-J. Zhang, K. T. C. Chai, H. Z. H. Luo, J. M. Huang, I. G. K. Tay, A. E.-J. Lim, and M. Je, "Multiplexed detection of cardiac biomarkers in serum with nanowire arrays using readout ASIC.," *Biosensors & Bioelectronics*, vol. 35, no. 1, pp. 218–23, May 2012.

[114] T. G. Kang, H. M. Ji, G. Zhang, A. Agarwal, Y. Chen, and M. Chip, "BACK-TO-BACK INTEGRATED NANOWIRE BIOSENSOR WITH MICROFILTRATION DEVICE FOR APPLICATION TO THE CARDIAC BIOMARKER DETECTION FROM BLOOD SAMPLE," *Most*, no. October, pp. 1427–1429, 2010.

[115] A. Manickam, C. A. Johnson, S. Kavusi, and A. Hassibi, "Interface Design for CMOS-Integrated Electrochemical Impedance Spectroscopy (EIS) Biosensors," *Sensors*, vol. 12, no. 11, pp. 14467–14488, Oct. 2012.

[116] J. Xu, P. Offermans, G. Meynants, H. Duy Tong, C. J. M. van Rijn, and P. Merken, "A low-power readout circuit for nanowire based hydrogen sensor," *Microelectronics Journal*, vol. 41, no. 11, pp. 733–739, Nov. 2010.

[117] P. Offermans, H. D. Tong, C. J. M. van Rijn, P. Merken, S. H. Brongersma, and M. Crego-Calama, "Ultralow-power hydrogen sensing with single palladium nanowires," *Applied Physics Letters*, vol. 94, no. 22, p. 223110, Jun. 2009.

[118] M. Grassi, P. Malcovati, and A. Baschirotto, "A 141-dB Dynamic Range CMOS Gas-Sensor Interface Circuit Without Calibration With 16-Bit Digital Output Word," *IEEE Journal of Solid-State Circuits*, vol. 42, no. 7, pp. 1543–1554, Jul. 2007.

[119] M.-K. Joo, P. Kang, Y. Kim, G.-T. Kim, and S. Kim, "A dual analyzer for real-time impedance and noise spectroscopy of nanoscale devices.," *The Review of scientific instruments*, vol. 82, no. 3, p. 034702, Mar. 2011.

[120] Y. Cui, Z. Zhong, D. Wang, W. U. Wang, and C. M. Lieber, "High Performance Silicon Nanowire Field Effect Transistors," *Nano Letters*, vol. 3, no. 2, pp. 149–152, Feb. 2003.

[121] "Low-Cost, Bus-Powered Multifunction DAQ for USB - Data Sheet - National Instruments." [Online]. Available: http://sine.ni.com/ds/app/doc/p/id/ds-218/lang/en. [Accessed: 15-Jan-2013].

[122] "AD822 datasheet and product info - Analog Devices, Inc., Norwood, MA, USA." [Online]. Available: http://www.analog.com/en/all-operational-amplifiers-op-amps/operational-amplifiers-op-amps/ad822/products/product.html. [Accessed: 08-Jan-2013].

[123] "AD630 datasheet and product info - Analog Devices, Inc., Norwood, MA, USA." [Online]. Available: http://www.analog.com/en/rfif-components/modulatorsdemodulators/ad630/products/product.html. [Accessed: 08-Jan-2013].

[124] *Agilent Impedance Measurement Handbook: A guide to measurement technology and techniques*, 4th ed. Agilent Technologies, Inc., 2009.

[125] "Alpha-A , Alpha and Beta High Performance Dielectric , Conductivity and Electrochemical Impedance Analyzers - Datasheet." Novocontrol Technologies GmbH & Co. KG, Hundsangen, Germany.

[126] A. Lasia, "Electrochemical impedance spectroscopy and its applications," *Modern aspects of electrochemistry*, vol. 32, pp. 143–248, 2002.

[127] J.-G. Guan, Y.-Q. Miao, and Q.-J. Zhang, "Impedimetric biosensors.," *Journal of bioscience and bioengineering*, vol. 97, no. 4, pp. 219–26, Jan. 2004.

[128] E. Katz and I. Willner, "Probing Biomolecular Interactions at Conductive and Semiconductive Surfaces by Impedance Spectroscopy: Routes to Impedimetric Immunosensors, DNA-Sensors, and Enzyme Biosensors," *Electroanalysis*, vol. 15, no. 11, pp. 913–947, Jul. 2003.

[129] "SEI Connector datasheet and product info - Samtec ." [Online]. Available: https://www.samtec.com/technical-specifications/Default.aspx?seriesMaster=sei. [Accessed: 24-Jan-2013].

[130] "0900 - Brass Alloy Spring-Loaded Pin datasheet- Mill-Max Mfg. Corp." [Online]. Available: http://www.mill-max.com/pin_rec_catalog/productinfo.cfm?webpartnumber=0900&start=1&leaddiameterrange=&pin_or_rec=&PartDescription=Spring-Loaded Pin&taildiameter=NO TAIL&tailtype=NONE&mountingfeature=SURFACE MOUNT&mountinghole=&bodylength=&search=0900&pr=pin&stagecode=&usersearch=. [Accessed: 25-Jan-2013].

[131] "SYLGARD® 184 SILICONE ELASTOMER KIT - Dow Corning." [Online]. Available: http://www.dowcorning.com/applications/search/default.aspx?r=131en. [Accessed: 25-Feb-2013].

[132] O. S. Knopfmacher, "Oren S . Knopfmacher - Sensing with Silicon Nanowire Field-Effect Transistors Sensing with Silicon Nanowire Field-Effect Transistors," *Ph.D. dissertation, University of Basel, Basel, CH*, 2011.

[133] P. Bergveld, "Development of an ion-sensitive solid-state device for neurophysiological measurements," *Biomedical Engineering, IEEE Transactions on*, 1970.

[134] N. Elfström, R. Juhasz, and I. Sychugov, "Surface charge sensitivity of silicon nanowires: Size dependence," *Nano letters*, 2007.

[135] S. Chen, J. G. Bomer, E. T. Carlen, and A. van den Berg, "Al2O3/silicon nanoISFET with near ideal nernstian response.," *Nano letters*, vol. 11, no. 6, pp. 2334–41, Jun. 2011.

[136] E. Vandenberg and L. Bertilsson, "Structure of 3-aminopropyl triethoxy silane on silicon oxide," *Journal of colloid and interface science*, 1991.

[137] J. Kim, P. Seidler, L. S. Wan, and C. Fill, "Formation, structure, and reactivity of amino-terminated organic films on silicon substrates.," *Journal of colloid and interface science*, vol. 329, no. 1, pp. 114–9, Jan. 2009.

[138] U. Jönsson, G. Olofsson, M. Malmqvist, and I. Rönnberg, "Chemical vapour deposition of silanes," *Thin Solid Films*, vol. 124, no. 2, pp. 117–123, Feb. 1985.

[139] Q. Gu and X. Cheng, "Tribological behaviors of self-assembled 3-aminopropyltriethoxysilane films on silicon," *Current Applied Physics*, vol. 8, no. 5, pp. 583–588, Aug. 2008.

[140] P. M. Krämer, M. Keß, E. Kremmer, and S. Schulte-Hostede, "Multi-parameter determination of TNFα, PCT and CRP for point-of-care testing," *The Analyst*, vol. 136, no. 4, Mar. 2011.

[141] J. Faraudo and A. Travesset, "The many origins of charge inversion in electrolyte solutions: effects of discrete interfacial charges," *The Journal of Physical Chemistry C*, pp. 1–22, 2007.

[142] L. De Vico, L. Iversen, M. H. Sørensen, M. Brandbyge, J. Nygård, K. L. Martinez, and J. H. Jensen, "Predicting and rationalizing the effect of surface charge distribution and orientation on nano-wire based FET bio-sensors," *Nanoscale*, vol. 3, no. 9, pp. 3635–3640, Feb. 2011.

[143] M. Waleed Shinwari, M. Jamal Deen, and D. Landheer, "Study of the electrolyte-insulator-semiconductor field-effect transistor (EISFET) with applications in biosensor design," *Microelectronics Reliability*, vol. 47, no. 12, pp. 2025–2057, Dec. 2007.

[144] M. W. Shinwari, M. J. Deen, and P. Selvaganapathy, "Analytic modelling of biotransistors," *IET Circuits, Devices & Systems*, vol. 2, no. 1, pp. 158–165, Apr. 2008.

[145] L. De Vico, M. H. Sørensen, L. Iversen, D. M. Rogers, B. S. Sørensen, M. Brandbyge, J. Nygård, K. L. Martinez, and J. H. Jensen, "Quantifying signal changes in nano-wire based biosensors.," *Nanoscale*, vol. 3, no. 2, pp. 706–17, Feb. 2011.

[146] E. Gnani, A. Gnudi, S. Reggiani, and G. Baccarani, "Effective Mobility in Nanowire FETs Under Quasi-Ballistic Conditions," *IEEE Transactions on Electron Devices*, vol. 57, no. 1, pp. 336–344, 2010.

[147] P. R. Nair and M. a Alam, "Screening-limited response of nanobiosensors.," *Nano letters*, vol. 8, no. 5, pp. 1281–5, May 2008.

[148] S. Martinoia, G. Massobrio, and L. Lorenzelli, "Modeling ISFET microsensor and ISFET-based microsystems: a review," *Sensors and Actuators B: Chemical*, vol. 105, no. 1, pp. 14–27, Feb. 2005.

[149] R. Ulbricht, R. Kurstjens, and M. Bonn, "Assessing charge carrier trapping in silicon nanowires using picosecond conductivity measurements.," *Nano letters*, vol. 12, no. 7, pp. 3821–7, Jul. 2012.

[150] A. Tarasov, M. Wipf, R. Stoop, and K. Bedner, "Understanding the Electrolyte Background for Biochemical Sensing with Ion-Sensitive Field-Effect Transistors," *ACS …*, no. 10, pp. 9291–9298, 2012.

[151] J. O. Bockris and A. K. N. Reddy, *Modern Electrochemistry 2B: Electrodics in Chemistry, Engineering, Biology and Environmental Science, Volume 2*. Springer, 2001, p. 514.

[152] H. Morgan and N. G. Green, *AC Electrokinetic: Colloids and Nanoparticles*. Research Studies Pr, 2002, p. 250.

[153] H. Helmholtz, "Studien über electrische Grenzschichten," *Annalen der Physik und Chemie*, vol. 243, no. 7, pp. 337–382, 1879.

[154] M. Gouy, "Sur la constitution de la charge electrique a la surface d'un electrolyte," *J. Phys. Theor. Appl.*, 1910.

[155] D. Chapman, "LI. A contribution to the theory of electrocapillarity," *The London, Edinburgh, and Dublin Philosophical …*, 1913.

[156] W. U. Wang, C. Chen, K.-H. Lin, Y. Fang, and C. M. Lieber, "Label-Free Detection of Small-Molecule–protein Interactions by Using Nanowire Nanosensors," *Proceedings of the National Academy of Sciences of the United States of America*, vol. 102, no. 9, pp. 3208–3212, Mar. 2005.

[157] C. Berggren, B. Bjarnason, and G. Johansson, "Capacitive Biosensors," *Electroanalysis*, vol. 13, no. 3, pp. 173–180, Mar. 2001.

[158] "Missouri S&T Microstrip Impedance Calculator." [Online]. Available: http://emclab.mst.edu/pcbtlc2/microstrip/index.html. [Accessed: 07-Feb-2013].

[159] "Design guide for the packaging of high speed electronic circuits," IPC, Illinois, 2003.

[160] H. H. Park, P. S. Kang, G. T. Kim, and J. S. Ha, "Effect of gate dielectrics on the device performance of SnO[sub 2] nanowire field effect transistors," *Applied Physics Letters*, vol. 96, no. 10, p. 102908, 2010.

[161] W. Franks, I. Schenker, P. Schmutz, and A. Hierlemann, "Impedance characterization and modeling of electrodes for biomedical applications.," *IEEE transactions on bio-medical engineering*, vol. 52, no. 7, pp. 1295–302, Jul. 2005.

[162] A. M. Johnson, D. R. Sadoway, M. J. Cima, and R. Langer, "Design and Testing of an Impedance-Based Sensor for Monitoring Drug Delivery," *Journal of The Electrochemical Society*, vol. 152, no. 1, p. H6, 2005.

[163] P. Bergveld, "Thirty years of ISFETOLOGY: What happened in the past 30 years and what may happen in the next 30 years," *Sensors and Actuators B: Chemical*, vol. 88, pp. 1–20, 2003.

[164] C.-C. Tsai, P.-L. Chiang, C.-J. Sun, T.-W. Lin, M.-H. Tsai, Y.-C. Chang, and Y.-T. Chen, "Surface potential variations on a silicon nanowire transistor in biomolecular modification and detection.," *Nanotechnology*, vol. 22, no. 13, p. 135503, Apr. 2011.

[165] M. G. Nikolaides, S. Rauschenbach, S. Luber, K. Buchholz, M. Tornow, G. Abstreiter, and A. R. Bausch, "Silicon-on insulator based thin-film resistor for chemical and biological sensor applications.," *Chemphyschem : a European journal of chemical physics and physical chemistry*, vol. 4, no. 10, pp. 1104–6, Oct. 2003.

[166] N. Clément, K. Nishiguchi, J. F. Dufreche, D. Guerin, and A. Fujiwara, "A silicon nanowire ion-sensitive field-effect transistor with elementary charge sensitivity," *Applied Physics Letters*, vol. 1, no. 1, 2011.

[167] S. Srinivasan, "ELECTRODE/ELECTROLYTE INTERFACES: STRUCTURE AND KINETICS OF CHARGE TRANSFER," *Fuel Cells*, 2006.

[168] M. Crescentini, M. Bennati, and M. Tartagni, "Design of integrated and autonomous conductivity–temperature–depth (CTD) sensors," *AEU - International Journal of Electronics and Communications*, vol. 66, no. 8, pp. 630–635, Aug. 2012.

[169] R. Schreier and G. C. Temes, *Understanding Delta-Sigma Data Converters*. Piscataway, NJ: Wiley-IEEE press, 2004.

[170] A. Manickam, A. Chevalier, M. McDermott, A. D. Ellington, and A. Hassibi, "A CMOS Electrochemical Impedance Spectroscopy (EIS) Biosensor Array," *IEEE Transactions on Biomedical Circuits and Systems*, vol. 4, no. 6, pp. 379–390, Dec. 2010.

[171] F. Gozzini, G. Ferrari, and M. Sampietro, "An Instrument-on-Chip for Impedance Measurements on Nanobiosensors with attoFarad Resolution," *IEEE International Solid-State Circuits Conference*, pp. 346–348, 2009.

[172] F. Francesconi, V. Liberali, P. Magani, and F. Maloberti, "Design of a 10.7 MHz band-pass ΣΔ modulator: a comparison between CMOS and BiCMOS technologies," in *Proceedings of 40th Midwest Symposium on Circuits and Systems. Dedicated to the Memory of Professor Mac Van Valkenburg*, 1997, vol. 1, pp. 281–284.

[173] G. Palmisano and F. Montecchi, "Simplified pseudo-N-path cells for z to -z/sup N/ transformed SC active filters," *IEEE Transactions on Circuits and Systems*, vol. 36, no. 3, pp. 461–463, Mar. 1989.

[174] "BF245A/BF245B/BF245C N-Channel Amplifiers - BF245A datasheet - Fairchild Semiconductor." [Online]. Available: http://www.fairchildsemi.com/ds/BF/BF245A.pdf. [Accessed: 21-Feb-2013].

[175] "IR0515S datasheet - IR Series - XP Power." [Online]. Available: http://www.xppower.com/orderPriceList2.php?seriesid=100644&lang=EN. [Accessed: 22-Feb-2013].

[176] M. Oljaca and T. Hendrick, "Combining the ADS1202 with an FPGA digital filter for current measurement in motor control applications," *Application report. Literature number SBAA094*, no. June, pp. 1–22, 2003.

[177] "DLP-FPGA Datasheet - DLP Design." [Online]. Available: http://www.dlpdesign.com/fpga/dlp-fpga-ds-v14.pdf. [Accessed: 24-Feb-2013].

List of publications

[1]   M. Rossi, M. Bennati, F. Thei and M. Tartagni, "A Low-cost, Portable System for Real-time Impedimetric Measurements and Impedance Spectroscopy of Sensors", SENSORDEVICES 2012, August 19-24, 2012 – Rome, Italy.

[2]   M. Rossi, F. Thei and M. Tartagni, "A Parallel Sensing Technique for Automatic Bilayer Lipid Membrane Arrays Monitoring", Sensors & Transducers Journal 2012.

[3]   F. Thei, M. Rossi, E. Giordano, S. Severi and M. Tartagni, "A Multichannel Electrophysiology Workbench for Single Ion Channel Screening", 56th Annual Biophysical Meeting, February 25-29, 2012 – San Diego, California, USA.

[4]   M. Rossi, F.Thei and M. Tartagni, "An Automatic System for Bilayer Lipid Membrane Formation and Monitoring", SENSORDEVICES 2011, August 21-27, 2011 – Nice/Saint Laurent du Var, France. "Best Paper Award".

[5]   F. Thei, M. Rossi, M. Bennati, M. Crescentini, M. Tartagni, "An Automatic Offset Correction Platform for High-Throughput Ion-Channel Electrophysiology", EUROSENSORS XXIV, Linz, 2010.

[6]   M. Rossi, F. Thei, H. Morgan, M. Tartagni, "A Disposable Microfluidic Array Platform for Automatic Ion Channel Recording", MicroTAS, Groningen, 2010

[7]   F. Thei, M. Bennati, M. Rossi, M. Crescentini, M. Tartagni, "Concurrent Acquisition Approach for High Resolution Sensor Arrays", SENSORDEVICES 2010, Venice, 2010.

[8]   F. Thei, M. Rossi, M. Bennati, M. Crescentini, F. Lodesani, H. Morgan, M. Tartagni, "Parallel Recording of Single Ion Channels: A Heterogeneous System Approach", IEEE Transaction on Nanotechnology, 1536-125X, May, 2010, 0, 9, 3, 295-302.

[9]   M. Crescentini, M. Rossi, M. Bennati, F. Thei, A. Baschirotto, M. Tartagni, "A Nanosensor Interface based on Delta-Sigma arrays", 3rd IEEE International Workshop on Advances in Sensors and Interfaces, IWASI, Trani, Jun, 2009.

[10] M. Bennati, F. Thei, <u>M. Rossi</u>, M. Crescentini, G. D'Avino, A. Baschirotto, M. Tartagni, "A Sub-pA Delta-Sigma Current Amplifier for Single Molecule Nanosensors", International Solid State Circuit Conference, ISSCC 2009, San Francisco, Feb, 2009, 0, 52, 0, 348—350.

[11] H. V. B. Achar, <u>M. Rossi</u>, S. Cavalcanti, E. Giordano, E. Sangiorgi and M. Tartagni, "Single particle counter using nanopores: Multiphysics simulations and experiments", proceeding the IASTED International Conference on Nanotechnology and Applications - NANA 2008, Creta, Greece.

[12] S. Furini, C. Domene, <u>M. Rossi</u>, M. Tartagni, S. Cavalcanti, "Model-based prediction of the α-Hemolysin structure in the hexameric state", Biophysical Journal, 2008.

[13] <u>M. Rossi</u>, M. Bennati, F. Lodesani, S. Branchetti, M. Tartagni, "A compact system for single ion channel recording" proceeding IEEE Sensors 2007, Atlanta, Georgia, USA.

[14] PATENT: M. Tartagni, <u>M. Rossi</u>, N. Manaresi, "Apparatus and Method for Counting and Identifying Particles of Interest in a Fluid", WO2009098582, 2009.